Dear Readers!

This issue of *Acoustical Physics* is devoted to Corresponding Member of the Russian Academy of Sciences, Professor Vitaliĭ Anatol'evich Zverev—a prominent scientist and the author of many original ideas and designs. His works have initiated the development of a number of areas of research in physical acoustics and adjacent fields of science. They include signal processing and image formation, antennas, wave propagation in inhomogeneous and random media, and nonlinear acoustics.

Almost all papers presented in this issue of the journal and reflecting the problems of modern acoustics are more or less related to Zverev's works, either in their topics or ideas or in that they simply develop the approaches and methods proposed by him. Among the publications by Zverev in *Acoustical Physics*, one should especially note the pioneering experimental studies of parametric arrays and receivers of sound. The subsequent works by Zverev on the development of new methods for the reception and processing of acoustic signals resulted in the elaboration of the forward-scattering location technique and the related acoustic dark-field method for detecting inhomogeneities in the ocean.

Zverev's work in science is characterized by enthusiasm for new directions of research and also by deep physical intuition and ingenuity, which help him to find new approaches in solving complicated problems. Zverev's professional features are purposefulness and ability to bring an original idea not only to a test experiment but also to its practical implementation as a new technical means or instrument.

It is important to note that most of the authors of publications included in this issue are representatives of the Nizhni Novgorod school in acoustics: the role of Zverev in its formation was quite important. The editorial board also decided to include papers that were written by authors from other scientific centers but that were concerned with subjects close to Zverev's scientific interests.

For years, Zverev has collaborated with the editorial board of *Acoustical Physics* as an author and as a member of the Editorial Council of the journal. Not many of the recent issues have appeared without a paper written by Zverev. This fact testifies to his creative activity and can be a good example for young scientists. Therefore, we are especially glad to congratulate Vitaliĭ Anatol'evich Zverev on the anniversary of his interesting life full of scientific achievements. We wish him good health and new creative ideas.

Editorial Board

Nonlinear Acoustics in Nizhni Novgorod (A Review)

L. A. Ostrovsky*, S. N. Gurbatov**, and J. N. Didenkulov*

* Institute of Applied Physics, Russian Academy of Sciences, ul. Ul'yanova 46, Nizhni Novgorod, 603950 Russia
e-mail: Lev.A.Ostrovsky@noaa.gov
** Nizhni Novgorod State University, pr. Gagarina 23, Nizhni Novgorod, 603950 Russia
e-mail: gurb@rf.unn.ru
Received November 8, 2004

Abstract—This article reviews the development of nonlinear acoustics in Nizhni Novgorod from the days when the idea of parametric transmission and reception was conceived until the present time. © *2005 Pleiades Publishing, Inc.*

THE BEGINNING: PARAMETRIC ARRAYS

The history of nonlinear acoustics in Nizhni Novgorod began as early as in the 1950s. Presumably, its beginning should be associated with the first study carried out by V.A. Zverev [1]. The subject of this study was proposed to Zverev by Professor G.S. Gorelik as the topic of Zverev's candidate dissertation. Zverev theoretically considered and, most importantly, experimentally implemented a relatively simple but previously unknown effect of a periodic transformation of an amplitude modulation into a phase modulation and vice versa when a spectral triplet consisting of a strong carrier and two weak side components propagates in a medium with dispersion. The experiment was performed using an ultrasonic wave propagating on a string [1, 2].

It would be natural to surmise that this study helped Zverev to invent and to implement, together with A.I. Kalachev, the widely known idea of parametric arrays. The basic idea of these arrays is simple and elegant. If a low-frequency (Ω) signal is incident on a high-frequency (ω) intense narrow acoustic beam propagating in a medium (in air or in water), their interaction caused by the nonlinearity of the medium gives rise to side components $\omega + \Omega$ and $\omega - \Omega$, which serve as received signals. This is the so-called parametric receiver. If, by contrast, the high-frequency signal consists of two or three close frequencies (which form frequency beats in the first case and an amplitude-modulated wave in the second case), the medium serves as a detector that generates a low-frequency field and emits it as an end-fire array.

The main advantage of such devices is the possibility of receiving or transmitting a narrow-beam low-frequency signal without using large antenna arrays. Indeed, the directivity of the initial high-frequency beam is formed by medium-size transducers, while the low-frequency signal is received and transmitted by a "virtual" antenna of the end-fire array type that is formed by the high-frequency beam itself, which is sufficiently long to produce directional radiation. Another advantage is that the width of the initial beam is smaller than the low-frequency wavelength, and this beam produces no side lobes causing stray reflections, e.g., in a shallow sea. The main disadvantage of such antennas is their low efficiency and, hence, low signal-to-noise ratio. The latter fact has imposed limitations on the use of these devices in ocean acoustics at low frequencies and long ranges. However, more local applications, such as sonars used for fishing or bottom profiling, proved to be rather promising for experimental investigations and for commercial production of parametric sonars.

The history of parametric arrays is somewhat dramatic. The first publication describing the principle of a parametric radiator belongs to P. Westervelt, who introduced the term "parametric" for these devices [3]. (In fact, it would be more correct to use the term "nonlinear arrays," because the word parametric is conventionally associated with the case of a parametric resonance, when low-frequency signals are generated owing to an instability and may exponentially grow from noise, whereas, in arrays whose operation is based on the principle of nonlinear acoustics, new frequencies are formed owing to the interaction of waves of other frequencies.) Later, in the 1960s–1970s, the number of publications concerned with this subject considerably increased and many experiments were carried out, including those in ocean acoustics. Zverev began studying the problems of the nonlinear interaction of acoustic waves as early as in the mid-1950s. His first paper devoted to this problem appeared in 1955 [4] (co-authored with G.S. Gorelik), and the second paper, in 1958 (co-authored with A.I. Kalachev). In these papers, for calculating the effect of the nonlinear interaction of

two sound waves, the authors used a method based on taking into account the sound velocity variation caused by the low-frequency wave in the medium and on calculating the additional phase shift of the high-frequency wave. Work in this area of research continued, but the next publication did not appear until as late as in 1967 [6]. The parametric radiator and receiver were proposed by Zverev and Kalachev in 1959; however, according to the rules of that time, they were not allowed to publish the results of their work but only received a number of secret patents. Finally, in the late 1960s, the idea of the parametric receiver and the corresponding laboratory experiment could be disclosed and published [7, 8]. Nevertheless, today, when discussing parametric arrays, even acousticians from western countries refer not only to Westervelt's but also to Zverev and Kalachev's publications.

Now, we consider the subsequent contribution of the Nizhni Novgorod scientists to this area of research. One result was concerned with the limiting modes of operation of parametric radiators, when an intense pumping beam forms saw tooth shock waves [9, 10]. This result is important because the efficiency of such arrays increases with pumping intensity. The intensity of the detected signal is proportional to the square of the pumping amplitude up to the point where shock waves are formed; then, the pumping signal is strongly attenuated. In addition, the formation of shock waves leads to a broadening of the directivity pattern of the transmitted signal, which removes the main advantage of the system. The generation of low-frequency noise by parametric arrays under the nonlinear limitation of the radiation intensity and the effect of fluctuations on the characteristics of parametric arrays were studied in [11, 12]. A nonlinear attenuation of the pumping wave also limits the low-frequency signal gain in the parametric reception. For example, in the degenerate case of parametric interaction, when the pumping frequency is twice as great as the frequency ω_0 of the weak signal, the maximal gain of the weak signal is equal to $4/\pi \approx 1.27$. In [13], it was shown that the use of higher combination frequencies $\omega_{1+2m} = \omega_0(1 + 2m)$ allows one to considerably increase the efficiency of the parametric interaction of waves for extracting weak acoustic signals. This is related to the fact that, at the stage of discontinuity, the harmonic amplitudes at these frequencies are equal to the amplitude of the amplified signal at the frequency ω_0 for a very large number of combination frequencies. In this mode of operation, the effect also occurs for the case when the pumping frequency is much higher than the frequency of the weak signal [14]. In [15], it was shown that the use of focusing for the pumping wave also considerably increases the efficiency of the parametric reception. In [16], the efficiency of parametric reception was studied in a moving medium with velocity fluctuations and a method for reducing the effect of these fluctuations was proposed.

One more result was obtained for the acoustics of nonlinear media with dispersion, when the pumping energy is not spent for the higher harmonic generation and one can avoid the formation of shock waves, which makes the system more efficient. One of these possibilities is to use the interaction of modes in waveguides. Indeed, a waveguide may contribute to the radiation of parametric arrays (like any other sources) through the concentration of radiation in the vertical plane [17]. However, here, we consider the case when the nonlinear process itself is subjected to the influence of the waveguide as a medium with dispersion in which only several specific modes interact. In the early papers [18, 19], a parametric (in this case, actually parametric) sound generator was presented. The use of oceanic waveguides for selection of individual modes was proposed in [20].

Many of the works published by the representatives of the Nizhni Novgorod school are devoted to the analysis of the operation of parametric radiators and receivers in inhomogeneous media: in a shallow sea and in refraction waveguides (including those with random inhomogeneities) [21–28]. These works are partially reflected in the review [29]. It was shown that, under specific conditions of waveguide propagation, parametric radiating arrays can be used to form a preset space–time structure of the acoustic field, in particular, for a selective excitation of modes of the oceanic waveguide. In addition to theoretical studies, a series of model experiments were performed in the tank of the Acoustics department of the Nizhni Novgorod State University. In these experiments, the mode composition of the field produced by a parametric radiator in a range-independent waveguide was studied [30, 31] and the formation of the characteristics of a parametric radiator near a statistically rough surface was investigated [32]. The results of experimental studies carried out in field conditions together with the Acoustics Institute are presented in [33, 34].

Another factor that influences the nonlinear acoustic effects is the presence of gas bubbles in water. In the 1970s, it became clear that a small concentration of bubbles may increase the nonlinearity of water by several orders of magnitude. This suggested the idea of using bubbles of one size for amplifying the radiation of parametric arrays; this idea was put forward by Zabolotskaya and Soluyan [35]. Under actual conditions, bubbles strongly vary in radius, and the main contribution is made by those bubbles that are resonant at the given frequencies. In Nizhni Novgorod, a parametric radiation with the use of a bubble layer was realized in a laboratory tank [36]. The problems concerned with parametric arrays, including those in dispersion systems, are considered in detail in [37].

NONLINEAR ARRAYS AND BEAMS

Many of the Nizhni Novgorod scientists involved in research in nonlinear acoustics were educated as specialists in electromagnetic or optical studies. In particular, they carried out research projects in laser physics

and nonlinear optics that were originally related to nonlinear phenomena in wave beams, such as harmonic generation, self-focusing, etc. Therefore, their interest in the problems concerned with beams and rays in acoustics is quite natural. The interest in these problems was also quickened by the popularity of acoustic parametric arrays and by some problems of astrophysics. The main theoretical difficulty in solving these problems is the smallness of dispersion in acoustics, which results in the accumulation of nonlinear deformations of waves up to the shock-front formation. Thus, the approximation of quasi-harmonic waves, which is predominantly used in nonlinear optics (especially before the present time, when ultrashort laser pulses have become feasible), often fails in acoustics.

The early theoretical studies in this area of research belonged to nonlinear geometrical acoustics (NGA), in which diffraction could be ignored and the shape of a ray and the deformation of the wave profile along the ray were considered in terms of the short-wave approximation. Actually, the term NGA was introduced by Gubkin in 1958 [38], although nonlinear rays and ray tubes were discussed earlier by Whitham [39]; presumably, these works were concerned with waves from explosions in the atmosphere. In 1963, one of the authors of this review published a paper on the generalization of the NGA approach to the case of nonstationary waves [40].

Subsequent studies in this direction, which were carried out by a group from the Institute of Applied Physics, were partially initiated by the key paper by Khokhlov and Zabolotskaya [41], who derived a parabolic equation for a weakly divergent acoustic beam. Later, this equation was extended to the case of a viscous medium by Kuznetsov. This equation is still difficult for analytical study but is widely used for numerical calculations. Our group used another approach, which is known as the linear-ray method. It assumes that the accumulation of deformations of the wave profile occurs separately within each ray tube determined in the approximation of linear geometrical optics of inhomogeneous media [42]. This approximation was used in different problems, such as shock-wave propagation in the solar chromosphere and heating of the latter by shock waves [43], shock-wave propagation in the upper layers of the ocean [44], and the propagation and attenuation of intense sound waves in an exponential atmosphere [45].

The linear-ray approximation fails when the effect of self-refraction manifests itself because of the dependence of the velocity of a shock wave on its amplitude (this may occur, e.g., for positive pulses). The geometrical acoustics of shock waves was initially developed by Whitham [39] for relatively long shock pulses of arbitrary amplitude, which propagate within ray tubes as in separate channels. A similar approximation was used for solitons [46, 47]. In [48], Whitham's theory, with the use of the weak-nonlinearity approximation,

was extended to short pulses, whose nonlinear deformations were of the same order of magnitude as the amplitude variations due to self-refraction. Note that another case, namely, the thermal self-refraction of shock waves, was studied earlier by a group of scientists from the Moscow State University [49, 50].

Simultaneously, a simplified approach suitable for more than pencil beams was developed. For this purpose, a step-by-step algorithm was elaborated on the basis of the spatial separation of regions where the diffraction effect is small compared to the NGA effect (nonlinear deformations along the ray tube) and regions where the diffraction effect is relatively strong with the subsequent matching of the respective solutions in the space between these regions. In fact, this approximation was used as early as 1972 in the study of the radiation of an intense acoustic source, where, after the formation of the directivity pattern, nonlinear effects due to diffraction began to accumulate up to a possible shock formation followed by a rapid attenuation of waves in a fixed direction [51]. Since the wave amplitude is usually maximal at the radiation axis, attenuation begins from the axial direction and continues in other directions. This leads to an isotropization of radiation: the radiation intensities in different directions become approximately equal. Note that, simultaneously, a similar effect was experimentally observed by Blackstock *et al.* [52], which resulted in long-term contacts between research groups from Nizhni Novgorod and from the United States.

Another challenge was to describe the nonlinear distortions of a wave approaching a caustic when the latter can be described by a Hilbert integral without considering the nonlinearity [53]. After the wave passes the caustic, the NGA approximation again becomes valid for its description. It was shown that, in the NGA approximation, the nonlinear deformations of the wave remain finite until the caustic is reached in spite of the infinite growth of the wave amplitude in this approximation. As a result, a uniform matching with the diffraction zone near the caustic is possible.

Finally, we note that the step-by-step algorithm proves to be also valid for narrow beams obeying the Khokhlov–Zabolotskaya–Kuznetsov (KhZK) equation, although the latter still usually requires a numerical solution. Such beams include the focused intense acoustic beams that are used in remote acoustic surgery and noninvasive diagnostics of organs. The focusing of radiation can be considered in terms of NGA, and the behavior of waves in the focal plane, in terms of the theory of diffraction of a nonharmonic nonlinearly deformed beam. This method was used in [54], which made it possible to analytically derive the following conclusions:

(i) in the focal plane, the profile of a focused harmonic wave becomes asymmetric with positive peaks, whose shape is close to the time derivative of a convergent steepening wave;

(ii) owing to the stronger concentration of higher harmonics, the amplitude of the wave and the mean intensity are additionally amplified at the focus, as compared to linear focusing;

(iii) in the case of shock formation, the field maximum is achieved somewhat nearer than the geometrical focus.

These conclusions were confirmed by numerical calculations performed by other authors [55] and by experiments. A similar algorithm was applied to diffracted beams [56]. In the case of diffraction of a plane nonlinear wave by a hole in a baffle, for the wave profile at the axis, the Kirchhof method yields a profile close to that at the axis of a focused beam; in a fixed transverse plane, the diffracted wave is smoothed out away from the axis.

Note that, for a beam in free space, this approximation yields a result that is only qualitatively correct. A combination of the linear-ray theory and local diffraction in the direction across the ray was considered in [57]. A more rigorous derivation of the nonlinear evolution equations (including the KhZK equation) was performed in 1974 in [58] (see also [59]).

In the recent years, the theory of nonlinear acoustic beams has found wide application, especially in medicine. The applications use more complex numerical calculations, which are often based on the KhZK equation, and the results often become more popular than the relatively simple models described above. However, these models remain useful not only for constructing a clear qualitative model of the process but also for obtaining fairly accurate quantitative estimates.

NONCLASSICAL NONLINEAR ACOUSTICS OF SOLIDS

Historically, "classical" nonlinear acoustics was formed as a weak-nonlinearity branch of gas dynamics and elasticity theory. It included acoustic waves in liquids and crystalline solids that were usually represented as dispersionless or weakly dispersive media with a nonlinearity caused by the properties of interatomic and intermolecular potentials. In such media, the nonlinearity is small (in most cases, quadratic) if the external forces produced by pressure in an acoustic wave are much smaller than the interatomic forces.

However, many media and materials have complex structures that include grains, pores, cracks, and other elements suppressing the internal bonds; as a result, the acoustic nonlinearity may considerably increase. Such a "structural nonlinearity" is typical of a wide class of media with low volume contents of bonds and defects. A well-known example is water with gas bubbles: when the volume ratio of bubbles is 10^{-3}–10^{-4} or less, the effective nonlinear parameter of the gas–liquid mixture may increase by several orders of magnitude. The same is true for solids with grains, pores, or cracks.

Experiments with ultrasound in metals have been carried out since the 1950s, but, initially, they were mainly concerned with specific properties of samples of materials rather than with their acoustic nonlinearity and the effects related to it. Apparently, the first observations of nonlinear waves with the aim of studying the aforementioned effects were performed the Institute of Applied Physics [60]. A harmonic excitation of an aluminum ring resonator resulted in the observation of a broad spectrum of harmonic and subharmonic frequencies (i.e., a parametric generation). It was shown that the parametric generation threshold was far below the estimate obtained from the reference data on the characteristics of the given metal. In addition, the material exhibited the property of a prolonged relaxation (which is now called "slow dynamics"): after an intense acoustic impact, the threshold value changed and then recovered within an hour or more.

Intensive experimental and theoretical studies of these phenomena in metals and, especially, in rock were started in the 1980s by two research groups: one from the Institute of Applied Physics and the other from the Los Alamos National Laboratory. Experiments were mainly carried out with bars made of different materials, in which resonant longitudinal modes were excited. Many specific effects were observed and measured. They included the following:

(i) harmonic generation. In most cases, the third-harmonic amplitude exceeded the second-harmonic amplitude. The fact of special importance is that the typical dependence of the third-harmonic amplitude on the fundamental signal amplitude was quadratic rather than cubic. This clearly disagrees with any analytical equation of state (the stress–strain dependence) that allows a Taylor series expansion. This fact alone testifies to the presence of singularities in the equation of state, in particular, to the presence of hysteresis;

(ii) nonlinear frequency shift. The amplitude–frequency characteristic of a single mode is characterized by a strong dependence of the quality factor on the wave amplitude, which is typical of media with hysteresis. The frequency corresponding to the resonance maximum is shifted (usually to lower frequencies) as the amplitude increases, and this shift is usually proportional to the amplitude. Note that, for any "normal" oscillator with a cubic nonlinearity, which is described by the Duffing equation, the shift is proportional to the amplitude squared. This difference also testifies to a nonclassical (nonanalytical) nature of the dependence.

In addition, these phenomena are characterized by a considerable inertia. For example, under the action of an intense oscillation packet, the resonant frequency of a weak (linear) signal decreased and recovered to its original value within approximately an hour. It is worth noting that the corresponding frequency shift decreased with time according to a logarithmic law rather than an exponential one;

(iii) modulation. These experiments are of special interest from the point of view of diagnostics. A sample is subjected to the effect of signals with two frequencies: a high frequency and a low frequency. The nonlinearity of the material gives rise to side components represented by the sum and difference frequencies; i.e., the high-frequency field is modulated by the low-frequency one;

(iv) effect of a liquid. Water saturation is known to affect the linear properties of substances. Studies performed at Los Alamos showed that water saturation also considerably affects nonlinear phenomena, such as the nonlinear frequency shift. A 100% saturation reduces the nonlinearity (which is natural, because water fills the cavities and makes the material harder), whereas a relatively low or medium water content (e.g., up to 30%) leads to a considerable increase in the nonlinearity. Presumably, this occurs because of the effects of the surface tension and Van der Waals forces on the grain coupling.

In Nizhni Novgorod, these effects were observed for a number of materials, including metals [61–63], rock (sandstone, limestone, etc.) [64], sand [65], ice [66], and concrete [67].

A theoretical study of acoustical phenomena in strongly nonlinear media and, especially, in media with hysteresis, presents a complex problem, which has not yet been fully investigated. One of the mechanisms that may be responsible for a strong nonlinearity is related to the interaction between grains, which can be represented as Hertzian contacts with the displacement (strain) being proportional to the force (stress) to the 2/3 power. At the Institute of Applied Physics, the application of such models to acoustic phenomena has been studied since the early 1990s [68], and the theoretical conclusions derived from these studies were confirmed by experiments with lead balls and tufa grains [69]. Later, this theory was used to obtain estimates in more realistic situations, for example, in the case of a nonideal packing of grains or in the case of depth-dependent parameters of rock [70–72]. Another model refers to the type of cracks with rough edges, where Hertzian-type contacts occur within a crack and the distributions of cracks in size and orientation are taken into account in the derivation of the "macroscopic" stress–strain dependence [73, 74].

These models account for strong nonlinearity but not for hysteresis. Most of the existing hysteresis models are more or less phenomenological (except possibly for the Granato–Lucke model proposed in the 1950s for describing dislocations in metals). In [62, 64, 75], the aforementioned experimental data were used as a basis to propose some hysteretic stress–strain dependences that simultaneously agreed with the results of different types of measurements (harmonic generation, loss, and frequency shift). Among the hysteresis models, we select two main ones: with a loop around the zero point (the so-called inelastic hysteresis, whose name origi-

nates in the residual stress at zero displacement) and with a double loop returning to zero (the so-called elastic hysteresis). Since the nonlinearity is still weak (the nonlinear terms of the equation are much smaller than the linear ones), any continuous portion of the hysteresis curve can be represented by a combination of linear and quadratic terms. Note that these models can be obtained by representing a medium in the form of a set of hysteretic elements with different parameters and by averaging their contributions to the stress–strain dependence [76].

Wave processes that occur in such systems were theoretically studied with the use of the two aforementioned basic models. According to [77, 78], at the beginning, a travelling harmonic wave considered in the framework of the inelastic model may acquire a triangular or saw tooth shape, which radically differs from the wave profile in a classical medium with a quadratic nonlinearity. Then, on the basis of the classical "elastic" model, a shock-wave front may be formed in addition to the singular peaks (jumps of derivative). This theory was applied to traveling-wave modes in a ring resonator [79]. However, most of the recent experiments were performed on bars with free ends. This situation corresponds to a more complex problem of the interaction of waves propagating in opposite directions. For a classical quadratic nonlinearity, this problem was solved in 1974 [80] (see also [81]). For hysteretic media, it was considered in application to a single example of harmonic oscillations and was only recently generalized to the case of counter-propagating waves of arbitrary shape [82, 83].

One of the practically important branches of nonlinear acoustics of solids is the nonlinear vibroacoustics of thin-walled structures (bars, plates, and shells). In Nizhni Novgorod, these studies were mainly performed at the Nizhni Novgorod Branch of the Institute of Mechanical Engineering, Russian Academy of Sciences, and at the Nizhni Novgorod State University. In particular, nonlinear processes in a thin-walled ring resonator were studied with allowance for the self-consistent interaction of longitudinal and flexural waves [84, 85]. It was found that, as a result of decay instability, energy from an intense longitudinal wave can be transferred to flexural waves. Processes of a cascade transfer of oscillation energy up and down the spectrum in distributed elastic systems were considered in the absence of simple and multiple resonances. Conditions for the formation of envelope solitons were revealed along with the conditions for the resonance interaction of long and short waves in the presence of a group synchronism and for self-modulation effects [86–88]. Between 1984 and 1986, what were presumably the first studies of the influence of diffraction effects on the nonlinear evolution of quasi-plane longitudinal and shear waves in a thin plate were carried out; the instability of nonlinear plane waves was demonstrated along with the possibility of the formation of two-dimensional longitudinal-strain solitons in a plate and the

possibility of the self-focusing of a two-dimensional shear-wave beam [89].

Research carried out at the Nizhni Novgorod Branch of the Institute of Mechanical Engineering included some other aspects of the nonclassical nonlinear acoustics of materials consisting of nonpoint particles coupled by complex interaction forces. The particles may be large molecules, domains, nanocrystallites, etc. Historically, one of the first models of a medium to take into account internal rotations is the Cosserat continuum consisting of solid undeformable bodies with not only translational but also rotational degrees of freedom. In [90–95], the propagation and interaction of nonlinear waves in such media are investigated and, in particular, the formation of stationary longitudinal spin waves and the nonlinear self-modulation of helical shear waves are studied along with different variants of resonance interactions between longitudinal, spin, and shear waves.

The rapid development of nanocrystal technologies in recent years has attracted considerable interest to studies of the nonlinear dynamics of complex crystal lattices, such as molecular polymers or liquid crystals. In the long-wave approximation, the theory of such systems is equivalent to the nonlinear acoustics of media with a microstructure. Nonlinear self-consistent models that describe the propagation and interaction of translational and spin waves in quasi-one-dimensional and quasi-two-dimensional crystals with lattices of a molecular type were considered in [96, 97].

One more remarkable achievement was the development of the theory of thermal parametric excitation of nonlinear transverse vibrations in current-carrying structures (bars and strings) in the presence of convective and radiative heat transfer to the surrounding medium [98, 99]. It should be noted that the formulation of the problem was first put forward by L.I. Mandel'shtam in the late 1920s as an example of parametric instability in an electromechanical system. Similar effects of flexural vibration excitation in current-carrying bars were observed, in particular, in electric-arc melting plants and in experiments with current-carrying tungsten bars simulating the operation of fuel elements in nuclear reactors.

A keen interest in the problems described in this section is stimulated by the prospects of using nonlinear methods for diagnostics of materials and for nondestructive testing of structures. Indeed, small defects, such as cracks, or the fatigue of a material may cause no considerable effect on the linear properties of a given material or structure (e.g., the velocity of sound) but may noticeably (by several orders of magnitude) increase the manifestation of nonlinear processes. Some aspects of the use of nonlinear acoustic methods for the diagnostics of different media and materials are described below.

STATISTICAL PROBLEMS OF NONLINEAR ACOUSTICS

Active theoretical studies in statistical nonlinear acoustics began in the USSR in the mid-1970s, simultaneously at the Moscow State University and in Nizhni Novgorod (Nizhni Novgorod State University and Institute of Applied Physics, Russian Academy of Sciences). These studies were concerned with the analysis of plane intense noise waves described by the Riemann or Burgers equations. In the theory of turbulence, the Burgers equation is widely used in model descriptions of hydrodynamic turbulence [100], and the solution to this equation with random initial conditions is called Burgers turbulence (sometimes, even Burgulence [101]) or acoustic turbulence. Therefore, many of the papers on the Burgers turbulence that were published by the Nizhni Novgorod specialists in nonlinear waves were closely related to statistical nonlinear acoustics. The most important results obtained by Nizhni Novgorod scientists in this area of research were summarized in the monographs [102–106] and the reviews [107–110], which contain extensive lists of references. Some of the original problems were included in the university manual [111] prepared by the Acoustics departments of the Moscow and Nizhni Novgorod universities.

In describing acoustic waves, one can usually ignore their dispersion in a broad frequency range. In a dispersionless medium, an effective interaction occurs between a great number of harmonics, and this interaction leads to a strong phase coherence of the harmonics involved in it. Therefore, in this class of problems, one cannot use the method of slowly varying amplitudes, which is rather efficient in nonlinear optics, where it is possible to limit consideration to a small number of linear interacting modes because of strong dispersion. The strong coherence of spectral components also does not allow one to use the chaotic phase approximation, which is used in the weak turbulence theory, where the description of the interaction of a great number of linear modes can be reduced to kinetic equations for the mode intensities.

For plane nonlinear waves, the evolution of the particle velocity $v(t, z)$ is described by the nonlinear diffusion equation, i.e., the Burgers equation. For acoustic noise, the statement of the problem is reduced to a search for the statistical characteristics of the field $v(t, z)$ in a cross section z from the known statistics of the field $v_0(t)$ at the source at $z = 0$. Although the nonlinear Burgers equation can be reduced, via the Hopf–Cole substitution, to a linear diffusion equation, a direct application of the exact solution is of little use for statistical problems, where averaging over an ensemble of realizations is required. This problem becomes especially difficult at large Reynolds numbers, when approaches based on the perturbation method are inapplicable. However, when the viscosity coefficient is small, the dissipation is significant in only a narrow

vicinity of shock fronts, which, in the limiting case of a vanishingly small viscosity, allows one to reduce the solution of the Burgers equation to the so-called principle of maximum or principle of particle selection [102, 103]. In this case, the solution of a homogeneous Burgers equation is reduced to a search for the maximum of a functional of the initial field.

In the limiting case of a vanishingly small viscosity, at the initial stage where the formation of discontinuities can be neglected, the Burgers equation transforms into the Riemann equation. The latter, in its turn, is reduced to a set of characteristic equations in terms of ordinary derivatives, i.e., to the free motion of particles. Using the statistical relations between the Lagrangian description (statistics of particles) and the Eulerian description (statistics of the field at a given space–time point), exact expressions were determined for the probability distributions of the Riemann waves [112, 113]. In particular, it was shown that, despite the strong distortions of the profile, the one-point probability distribution of a Riemann wave is conserved. In the course of the evolution of a wave with initially Gaussian statistics, the one-dimensional distribution remains Gaussian, while the higher probability distributions are distorted. The use of higher order spectra in the diagnostics of intense acoustic noise allows one to determine the direction of the energy flux along the spectrum from the measurements in a single cross section [114, 115]. In practical applications, an important problem is to obtain information on the spectrum of a random acoustic wave. Expressions for the energy spectra of Riemann waves were almost simultaneously obtained at the Moscow State University and at the Nizhni Novgorod State University [116–118]. On the basis of these expressions, characteristic features of transformation of both broadband and quasi-monochromatic signals were studied. In particular, it was shown that a nonlinear interaction leads to a universal behavior (proportional to the square of frequency) of the spectrum in the low-frequency region. For a Riemann wave, the energy should be conserved; however, from the expressions obtained for the spectra in [116–118], it follows that the energy, when calculated as the integral over the spectrum, decreases with distance from the input. This is related to the fact that, in the case of Gaussian statistics, the regions of ambiguity of the Riemann wave occur at arbitrarily small distances, and the passage from the Eulerian description to the Lagrangian one in the spectral representation is equivalent to the replacement of the multivalued solution by a single-flux one, which is obtained by an alternating-sign summation of the branches of the Riemannian solution [109].

The appearance of discontinuities leads to a universal asymptotics of the spectrum $\propto \omega^{-2}$ in the high-frequency region. The effect of discontinuities can be analytically calculated either for the initial stage, where their number on the characteristic time scale is small [119], or for long distances, where, because of the multiple confluence of discontinuities, the characteristic

time scale of the wave $\tau(z)$ far exceeds the initial correlation time τ_0 [102, 103, 120, 121]. At these distances, the wave represents a sequence of saw tooth pulses with the same slope $\partial v/\partial t \propto -1/z$ and with random positions of discontinuities. The confluence of discontinuities occurs according to the law of coalescence of perfectly inelastic particles and leads to the growth of the characteristic time scale $\tau(z)$. The multiple confluence of discontinuities leads to a loss of information on the fine structure of the initial signal, and, at long distances, a self-similar spectrum $E(\omega, z) \propto \tau^3(z)z^{-2}\tilde{E}(\omega\tau(z))$ is formed, whose evolution in time is determined by a single time scale $\tau(z) \propto z^{1/2}\ln^{-1/4}(z)$ [102, 103, 120]. In the high-frequency and low-frequency regions, the spectrum has universal asymptotics $E(\omega, z) \propto \omega^{-2}z^{-3/2}$ and $E(\omega, z) \propto \omega^2 z^{1/2}$, respectively. Because of the confluence of discontinuities, the energy spectrum is shifted towards low frequencies and the decay of noise occurs more slowly, $\langle v^2 \rangle \propto \tau^2(z)/z^2 \propto z^{-1}$, than that of a periodic signal, $\langle v^2 \rangle \propto \tau_0^2/z^2 \propto z^{-2}$. A nonlinear decay of complex deterministic signals (of a fractal type and with a Weierstrass–Mandelbrot spectrum), whose behavior reflects the main features of the noise-field evolution, was considered in [122, 123].

At finite but rather large Reynolds numbers, the shock fronts are of a finite width $\tau_{shock}(z) \propto z/\tau(z)$ and the power law describing the spectrum decay, $E(\omega, z) \propto \omega^{-2}z^{-3/2}$, is replaced by the exponential decay law $E(\omega, z) \propto \exp[-\omega\tau_{shock})^{2/3}]$. This behavior of the high-frequency part is related to fluctuations in the width of discontinuities of the noise wave (for a periodic wave, $E(\omega, z) \propto \exp[-n\omega_0\tau_{shock}]$). Because of the multiple confluence of discontinuities, the distance z_{lin} at which the plane noise wave reaches the linear stage is large: $z_{lin} \propto \exp(\mathrm{Re}_0^2)$, where Re_0 is the Reynolds number of the input noise [102, 103, 120, 124]. The analytical theory adequately explains the results of the field experiments on the propagation of intense acoustic noise [125]. In [126–128], the decay of noise characterized by a power law $E(\omega, z = 0) \propto \omega^n$ in the low-frequency region was studied. It was shown that, when $1 < n < 2$, a loss of self-similarity occurs with the evolution of the energy spectrum, and, when $n < 1$, the asymptotic behavior of the spectrum, as well as the behavior of individual realizations, only weakly depends on the high-frequency components.

For applications, it is important to study the evolution of quasi-monochromatic signals $v_0(t) = a(t)\cos(\omega_0 t + \varphi(t))$ with random amplitude and phase modulations, and the first studies were carried out for such signals. In [129], the probability distribution of the discontinuity development length was determined, and it was found that discontinuities may appear in a randomly modulated wave earlier than in a deterministic wave with the same energy. For a quasi-monochromatic signal with Gaussian statistics and zero spectrum width, the proba-

bility distribution of the field was first calculated by researchers from the Moscow State University [130]. It was shown that, for an amplitude-modulated signal, a nonlinear medium is a perfect limiter and that, at long distances, the initial Gaussian distribution transforms into a uniform one. In [131–133], it was shown that, in a nonlinear medium, a frequency modulation of the input signal is transformed into an amplitude modulation of a saw tooth wave, which results in a spread of the boundaries of the uniform distribution. If the input spectrum has a finite width, the amplitude modulation gives rise to motion of the shock fronts, i.e., to an additional phase modulation of the saw tooth wave. Physically, the motion of the shock fronts is related to the interaction of the high-frequency quasi-periodic saw tooth wave with the low-frequency wave $v_{LF}(t, z)$ caused by the nonlinear detection of the input signal. As the order number of harmonic increases, spectral lines broaden until a continuous power-law spectrum is formed. This effect was observed experimentally in [133]. The same experiments demonstrated the disappearance of the fine structure of intense broadband acoustic noise. The fundamental difference between the nonlinear propagation of a quasi-monochromatic wave and that of a tone signal lies in the parametric generation of slowly decaying low-frequency components $v_{LF}(t, z)$. In [131, 132, 134], the statistical characteristics of low-frequency components were studied and, in particular, it was shown that, for small Reynolds numbers, the detected component is characterized by a Rayleigh-type distribution, and, for large Reynolds numbers, by a Gaussian distribution.

Another class of problems is related to the propagation of modulated noise, when nonlinear processes lead to the generation of coherent noise components with zero mean. In [135–137], it was shown that, as a result of the multiple confluence of discontinuities, a pulse with a noise carrier is transformed into an N-wave; if the time scale of the noise carrier is much smaller than the pulse duration, the positions of the shock fronts of the N-wave in different realizations are virtually deterministic. The generation of a tone signal from noise with a harmonic intensity modulation was studied in [138]. It was shown that the efficiency of the generation of a signal with a noise carrier is higher than that of a signal with a tone carrier.

Pioneering studies of the nonlinear interaction of noise with regular signals were performed at the Moscow State University (see [117] and the literature cited therein). A series of publications [14, 139, 140] reported on the interaction of noise with signals at later stages, when the formation of continuities radically changes the spectral composition of the wave and, in particular, noise components appear in a broad frequency range. Here, we limit our consideration to the example of interaction between an intense high-frequency harmonic wave and low-frequency noise $v_N(t, z)$. In this case, one can assume that noise only causes a quasi-static phase shift of the high-frequency signal. At

distances at which the nonlinear distortion of noise $v_{N, 0}(t)$ can be ignored, the expression for the nth harmonic of the signal can be represented as $v_n(t, z) = A_n(z)\cos(n\omega_0 t + \varphi_n(t, z))$, where $A_n(z)$ is the amplitude of the nth harmonic of the regular signal and $\varphi_n(t, z) \approx n\omega_0 z\beta v_{N, 0}(t)$ is the phase shift. As long as the phase modulation index is small, for the noise component we have $\tilde{v}_n(t, z) \approx A_n(z)n\omega_0 z\beta v_{N, 0}(t)\sin(n\omega_0 t)$ and, hence, the spectrum of the nth component reproduces the spectrum of the low-frequency noise. At the discontinuity stage, where $A_n \approx 1/n\omega_0 z\beta$, the amplitude of the noise component does not depend on distance z and is equal to the amplitude of the low-frequency noise for a large number of harmonics. This effect can be called the effect of an anomalous amplification of noise. In its turn, the noise leads to the decay of the regular signal. In [142], it was shown that the interaction of a pulse with intense noise can be described by introducing an effective viscosity for the mean field. The evolution of the mean field of a nonlinear wave in a medium with random inhomogeneities was studied in [143].

The statistics of the velocity and density fields for counter-propagating waves was considered in [144] for different values of the Mach number.

THE USE OF NONLINEAR ACOUSTIC METHODS IN DIAGNOSTICS

The discovery of new physical effects usually stimulates a quest for their practical application. Therefore, it is no wonder that the rapid development of nonlinear acoustics gave rise to studies aimed at the application of new methods in nondestructive testing and different types of diagnostics. The advantages of nonlinear acoustic methods are primarily related to their high sensitivity to structure disturbances in substances, such as the appearance of bubbles in a liquid or cracks and foliations in solids. The area of application of these methods is wide and includes diagnostics of liquids, testing of large-size structures, seismic prospecting, and medicine. Since we cannot consider all aspects of nonlinear acoustical diagnostics in this section, we dwell on the main areas of application in which practical achievements are evident.

Presumably, one of the first examples is the diagnostics of gas bubbles in liquids. The detection of bubbles in a liquid and the measurement of their size distribution is important, e.g., for underwater acoustics and oceanography, for the operation of power plants (nuclear reactors), and for the treatment of the decompression disease. In Nizhni Novgorod, research in this area was mainly carried out at the Institute of Applied Physics and at the Department of Acoustics of the Nizhni Novgorod State University. For bubble diagnostics, different methods were used, including the second-harmonic method [145–147], the combination-frequency method [148–152], and the subharmonic and ultraharmonic method [153, 154]. The first two meth-

ods were successfully applied to measurements of the bubble distribution in the subsurface layer of the sea. The second-harmonic method allowed the use of commercial sonars. In this method, the signal was recorded at the second harmonic frequency of the transmitted pumping signal. In the combination-frequency method, the signal was recorded at the sum or difference frequency when a bubble fell into a relatively small working volume of the measuring system. Measurements carried out in different seas and oceans during expeditions provided information on the bubble distributions in space and size. In addition to the data on the mean concentration, it was found that bubbles are nonuniformly distributed not only in depth but also in the horizontal direction and form so-called bubble clouds [147, 150]. On the basis of the difference-frequency method, an instrument was designed for detecting bubbles in the heat-transfer medium of the cooling system of a nuclear reactor [152].

Experiments performed together with colleagues from Poland in the shallow-water areas of the Baltic Sea using high-power sonar made it possible to use the combination-frequency method at a distance of about 10 m for the diagnostics of both the subsurface bubble layer and the gas-saturated bottom sediments [160]. To measure the spatial distribution of nonlinear scatterers, the pulsed tomography method was proposed in [161].

The subharmonic and ultraharmonic methods have found application in the diagnostics of decompression states of divers and astronauts [153, 154]. The generation of subharmonic and ultraharmonics is of a threshold character, as in the case of the classical parametric effect, and, hence, it requires fairly large pumping amplitudes at the bubble resonance frequencies.

With a certain geometry of two pumping beams (when they are directed toward each other), the difference-frequency signal scattered from a moving bubble acquires a considerable Doppler frequency shift, whose value is mainly determined by the Doppler shifts at the pumping frequencies [155]. This allows one to measure the velocities of moving bubbles with a high accuracy and, hence, to measure the distribution of the velocity of liquid in a flow [156]. If the concentration of bubbles is high and prevents the use of the approximation of preset pumping amplitudes within the whole cross section of the liquid flow, the determination of the flow velocity distribution is made possible by the tomographic reconstruction method [157, 158].

It should be noted that the use of transmitting or receiving scanning acoustic systems allows one to obtain spatial images of the distribution of nonlinear scatterers. For bubbles in water, this problem was solved using a scanning focusing system operating at the difference frequency. With the difference-frequency method, images of a liquid jet in the cavitation regime and images of metal samples were obtained in [159]. In the latter case, for the samples to acquire the properties of nonlinear scatterers, a controlled voltage was applied

to them, so that the samples were covered with small gas bubbles due to electrolysis.

Sometimes, new ideas arise not from theoretical considerations but from attempts to solve specific problems encountered in practice. An example is the case in which specialists from Moscow asked V.A. Zverev to assist in the development of a method for testing the strength of the heat-protection coating of a space vehicle. The conventional linear high-frequency echo-sounding method had failed in this case because of the strong damping of sound. After many attempts were made to solve this problem, a new idea involving low-frequency vibrations of samples was put forward, so that the sizing defects could be detected by their "chatter" manifesting itself in the spectrum as the appearance of higher harmonics [162]. The experiment verifying this idea can be considered as the beginning of the studies concerned with the development of methods of the nonlinear acoustical diagnostics of solid materials and structures at the Institute of Applied Physics. A major contribution to this area of research was made by A.M. Sutin. The higher harmonic method and the modulation method were used to demonstrate the potentialities of nonlinear acoustical diagnostics of metals with cracks and steel samples with fatigue [63, 163, 164]. The higher harmonic method was also used to test large graphite electrodes for cracks [165]. The modulation method is as follows: an acoustic wave is introduced in the sample under test conditions, and, simultaneously, the sample is subjected to low-frequency vibrations. The presence of cracks in the sample leads to the modulation of the high-frequency wave by the low-frequency vibrations. Later on, this method was widely used in nondestructive testing of different structures (concrete, metal, etc.) [67, 166, 167]. The advantage of this method is the possibility of exciting fairly intense vibrations in a structure. In solving the problems of diagnostics, it is also possible to use other nonlinear acoustic effects, such as the shift of the resonance frequency of a sample depending on the pumping-field amplitude [168], the "slow dynamics," the cross-modulation, etc.

Often, it is important not only to determine which sample has a defect but also to locate the defect in the sample. In this case, the simplest way is to use the echo-sounding method [169–171]. This method is based on the modulation of the acoustic echo pulses that are scattered from the crack by low-frequency vibrations of the sample. One can use modulation within a single pulse [170] or modulation of a pulse sequence [169–171]. In the second case, much shorter pulses are used, which increases the spatial resolution of the method. In this method, the echo signals reflected from stable defects (cavities, saw kerfs, etc.) have no modulation, which allows one to distinguish them from cracks. However, if the sample contains several cracks or stable defects, errors in their identification are possible.

Another approach to solving the problem of crack location is based on the use of the resonant eigenmodes of the sample. It is evident that the deformation of a crack under vibrations of the sample depends on the position of the crack with respect to the nodes and antinodes of the resonant modes, and, hence, the effect of modulation of the high-frequency wave propagating in the sample also depends on the crack position. This method of nonlinear mode modulation tomography allows one to reconstruct the position of the crack from measurements of the coefficient of modulation of high-frequency acoustic waves by low-frequency resonance vibrations of the sample for different modes [172, 173]. The advantage of the method is the possibility of using continuous acoustic signals and relatively low frequencies (compared to the pulsed method), which is important for the diagnostics of materials with a strong sound absorption. A further development of this method in application to complex structures is possible if the problems of calculation and identification of their vibrations are solved. This actually presents an acoustic spectroscopy problem. At the Institute of Applied Physics of the Russian Academy of Sciences, research in this area is carried out with the aim of achieving the highest possible measurement accuracy [174].

Studies in the nonlinear acoustical diagnostics of solid media and materials were being carried out at the Radiophysical Research Institute even before the establishment of the Institute of Applied Physics. At that time, the phenomenon of the much stronger dependence of nonlinear elastic parameters, as compared to the linear ones, on the degree of fatigue of a material was revealed [175].

The use of the parametric modulation of a high-frequency acoustic wave by a low-frequency field excited in a solid resonator proved to be an efficient method for measuring the quadratic nonlinearity parameter. Specifically, a strong dependence of the quadratic nonlinearity parameter on electric and magnetic external fields was revealed and acoustoelectronic devices with a controlled nonlinearity were proposed [176].

Later on, a series of theoretical and experimental studies of the nonlinear interactions of acoustic waves in solids were carried out with allowance for cubic nonlinearity. In particular, the effect of cross-modulation was experimentally observed [177], and a new method of measuring the cubic nonlinearity was developed on the basis of this effect [178]. The Radiophysical Research Institute and the All-Russia Research Institute for Standardization and Certification in Mechanical Engineering in cooperation with the Institute of Mechanics and Paton Electric Welding Institute of the Academy of Sciences of Ukraine developed a standard procedure for the determination of the nonlinear elastic constants of structural materials by the acoustic method [179].

Since the late 1970s, studies of seismic nonlinear acoustic effects have been being carried out at the Radiophysical Research Institute [180]. The development of these studies culminated in the testing of a number of new nonlinear methods of geological prospecting. In particular, the method of nonlinear interwell sounding based on the modulation of sound by sound was implemented in a working pilot system [181–183]. A further development of well technologies for the nonlinear diagnostics of geological media resulted in the design of a new type of well sources, namely, focusing well arrays [184]. On the basis of the diffraction scattering that occurs at the focus of the pumping field of the detected signal, a method of studying the nonlinear characteristics of the near-well region was developed.

The phenomenon of acoustoelasticity was experimentally discovered in 1959, and, in the 1970s–1980s, various nondestructive acoustoelastic methods for determining mechanical stresses in structures were developed. The corresponding research was mainly carried out at the three institutes of Nizhni Novgorod: the All-Russia Research Institute for Standardization and Certification in Mechanical Engineering, the Nizhni Novgorod Branch of the Institute of Mechanical Engineering, Russian Academy of Sciences, and the Institute of Applied Physics, Russian Academy of Sciences. Methodical foundations were elaborated for the pulsed acoustic method of determining biaxial stresses from measurements of the travel time of longitudinal and shear elastic waves, and a standard procedure of determining the residual stresses in elements of commercial structures was developed and approved by the corresponding State Standard Institute [185–187].

Today, research aimed at developing methods of nonlinear acoustical diagnostics for specific applications is carried out in many countries and laboratories. Twenty years ago, there were only a few places where such investigations were initiated. One of those places was Nizhni Novgorod. Unfortunately, for reasons of space, we cannot consider many other aspects of nonlinear acoustical diagnostics. Therefore, in this review, we have narrowed the limits of this notion and concentrated on practical achievements.

CONCLUSIONS

Even from the brief description of ideas and works that was given above, one can see the great progress in nonlinear acoustics that took place over several decades and the important role that was played by the scientists from Nizhni Novgorod in this progress. Today, several dozen researchers are working in this area of research at different institutes in Nizhni Novgorod. Unfortunately, for space reasons, it was impossible to mention all publications and their authors in this review. Therefore, above, we tried to outline the main stages of the development of nonlinear acoustics in Nizhni Novgorod, from the first ideas to the basic fundamental and applied studies that are being carried out at the present time.

We note that the 80th birthday of Vitaliĭ Anatol'evich Zverev virtually coincides with the 50th anniversary of his first ideas and studies in nonlinear acoustics. Within these 50 years, Zverev also worked in other areas of research and gave much of his time and energy to solving many other scientific problems, for example, in underwater acoustics. However, he returned to the problems of nonlinear acoustics several times, and each time he made new contributions to this area of research. In particular, this occurred when he worked on the application of superpower parametric systems in underwater acoustics (this work was carried out in tandem by scientists from the Institute of Applied Physics and the Acoustics Institute). The history of nonlinear acoustics once more confirms the statement that each field of science develops on the basis of several key ideas. The generation of such ideas is the quality that is characteristic of Zverev, and it is an inspiring example for younger scientists.

ACKNOWLEDGMENTS

REFERENCES

1. V. A. Zverev, Dokl. Akad. Nauk SSSR **91**, 791 (1953).

2. V. A. Zverev, Akust. Zh. **2**, 142 (1956) [Sov. Phys. Acoust. **2**, 144 (1956)].

3. P. J. Westervelt, J. Acoust. Soc. Am. **35**, 935 (1963).

4. G. S. Gorelik and V. A. Zverev, Akust. Zh. **1**, 339 (1955) [Sov. Phys. Acoust. **1**, 353 (1955)].

5. V. A. Zverev and A. I. Kalachev, Akust. Zh. **4**, 321 (1958) [Sov. Phys. Acoust. **4**, 331 (1958)].

6. V. A. Zverev, A. I. Kalachev, and N. S. Stepanov, Akust. Zh. **13**, 380 (1967) [Sov. Phys. Acoust. **13**, 324 (1967)].

7. V. A. Zverev and A. I. Kalachev, Akust. Zh. **14**, 214 (1968) [Sov. Phys. Acoust. **14**, 173 (1968)].

8. V. A. Zverev and A. I. Kalachev, Akust. Zh. **15**, 369 (1969) [Sov. Phys. Acoust. **15**, 322 (1969)].

9. A. M. Sutin, Akust. Zh. **24**, 104 (1978) [Sov. Phys. Acoust. **24**, 55 (1978)].

10. S. N. Gurbatov, I. Yu. Demin, and A. M. Sutin, Akust. Zh. **25**, 515 (1979) [Sov. Phys. Acoust. **25**, 294 (1979)].

11. S. N. Gurbatov, I. Yu. Demin, and A. N. Malakhov, Akust. Zh. **26**, 399 (1980) [Sov. Phys. Acoust. **26**, 217 (1980)].

12. S. N. Gurbatov and I. Yu. Demin, Akust. Zh. **28**, 32 (1982) [Sov. Phys. Acoust. **28**, 19 (1982)].

13. S. N. Gurbatov and A. N. Malakhov, Akust. Zh. **25**, 53 (1979) [Sov. Phys. Acoust. **25**, 28 (1979)].

14. S. N. Gurbatov, Akust. Zh. **26**, 551 (1980) [Sov. Phys. Acoust. **26**, 302 (1980)].

15. D. M. Donskoĭ and A. M. Sutin, Akust. Zh. **27**, 151 (1981) [Sov. Phys. Acoust. **27**, 83 (1981)].

16. I. N. Didenkulov and D. M. Donskoy, in *Advances in Nonlinear Acoustics*, Ed. by H. Hobak (World Sci., Singapore, 1993), pp. 289–294.

17. V. Yu. Zaĭtsev, L. A. Ostrovskiĭ, and A. M. Sutin, Akust. Zh. **33**, 37 (1987) [Sov. Phys. Acoust. **33**, 21 (1987)].

18. L. A. Ostrovskiĭ, I. A. Papilova, and A. M. Sutin, Pis'ma Zh. Éksp. Teor. Fiz. **15**, 456 (1972) [JETP Lett. **15**, 322 (1972)].

19. L. A. Ostrovskiĭ and I. A. Papilova, Akust. Zh. **19**, 67 (1973) [Sov. Phys. Acoust. **19**, 45 (1973)].

20. N. S. Gorskaya, L. A. Ostrovskiĭ, and A. M. Sutin, Akust. Zh. **29**, 451 (1983) [Sov. Phys. Acoust. **29**, 269 (1983)].

21. D. M. Donskoĭ and A. M. Sutin, Akust. Zh. **27**, 876 (1981) [Sov. Phys. Acoust. **27**, 485 (1981)].

22. S. N. Gurbatov and N. V. Pronchatov-Rubtsov, Akust. Zh. **28**, 770 (1982) [Sov. Phys. Acoust. **28**, 456 (1982)].

23. D. M. Donskoĭ, V. A. Zverev, and A. I. Kalachev, Akust. Zh. **29**, 181 (1983) [Sov. Phys. Acoust. **29**, 106 (1983)].

24. V. Yu. Zaĭtsev, L. A. Ostrovskiĭ, and A. M. Sutin, Akust. Zh. **33**, 37 (1987) [Sov. Phys. Acoust. **33**, 21 (1987)].

25. S. N. Gurbatov, A. G. Kosterin, and N. V. Pronchatov-Rubtsov, Akust. Zh. **35**, 809 (1989) [Sov. Phys. Acoust. **35**, 471 (1989)].

26. S. N. Gurbatov, V. Yu. Zaĭtsev, and N. V. Pronchatov-Rubtsov, Akust. Zh. **35**, 620 (1989) [Sov. Phys. Acoust. **35**, 358 (1989)].

27. V. Yu. Zaĭtsev and M. A. Raevskiĭ, Akust. Zh. **36**, 288 (1990) [Sov. Phys. Acoust. **36**, 156 (1990)].

28. V. Yu. Zaĭtsev and N. V. Pronchatov-Rubtsov, Izv. Vyssh. Uchebn. Zaved., Radiofiz. **36**, 752 (1993).

29. S. N. Gurbatov, V. Yu. Zaĭtsev, A. G. Kosterin, *et al.*, in *Acoustics in the Ocean*, Ed. by L. M. Brekhovskikh and I. B. Andreeva (Nauka, Moscow, 1992), pp. 208–227 [in Russian].

30. V. Yu. Zaĭtsev, V. V. Kurin, and A. M. Sutin, Akust. Zh. **35**, 266 (1989) [Sov. Phys. Acoust. **35**, 160 (1989)].

31. S. N. Gurbatov, S. A. Egorychev, V. V. Kurin, *et al.*, Akust. Zh. **46**, 192 (2000) [Acoust. Phys. **46**, 153 (2000)].

32. S. N. Gurbatov, V. V. Kurin, V. M. Loktev, *et al.*, Izv. Vyssh. Uchebn. Zaved., Radiofiz. **38** (1–2), 82 (1995).

33. V. Yu. Zaĭtsev, A. I. Kalachev, K. A. Naugol'nykh, and Yu. S. Stepanov, Akust. Zh. **34**, 470 (1988) [Sov. Phys. Acoust. **34**, 273 (1988)].

34. I. B. Esipov, S. V. Zimenkov, A. I. Kalachev, and V. E. Nazarov, Akust. Zh. **39**, 173 (1993) [Acoust. Phys. **39**, 89 (1993)].

35. E. A. Zabolotskaya and S. I. Soluyan, Akust. Zh. **18**, 472 (1972) [Sov. Phys. Acoust. **18**, 396 (1972)].

36. L. M. Kustov, V. E. Nazarov, L. A. Ostrovsky, and A. M. Sutin, Acoust. Lett. **6** (2), 15 (1982).

37. K. A. Naugol'nykh and L. A. Ostrovskiĭ, *Nonlinear Wave Processes in Acoustics* (Nauka, Moscow, 1990) [in Russian].

38. K. E. Gubkin, Prikl. Mat. Mekh. **22**, 561 (1958).

39. G. B. Whitham, Commun. Pure Appl. Math. **6**, 3 (1953).

40. L. A. Ostrovskiĭ, Prikl. Mat. Mekh. **27**, 924 (1963).

41. E. L. Zabolotskaya and R. V. Khokhlov, Akust. Zh. **15**, 40 (1969) [Sov. Phys. Acoust. **15**, 35 (1969)].

42. A. Ostrovsky, Int. J. Nonlinear Mech. **11**, 401 (1976).

43. S. A. Kaplan, L. A. Ostrovskiĭ, N. S. Petrukhin, and V. E. Fridman, Astron. Zh. **49**, 1267 (1972) [Sov. Astron. **16**, 1013 (1972)].

44. L. A. Ostrovskiĭ, E. N. Pelinovskiĭ, and V. E. Fridman, Akust. Zh. **25**, 103 (1979) [Sov. Phys. Acoust. **25**, 55 (1979)].

45. L. A. Ostrovskiĭ and V. E. Fridman, Akust. Zh. **31**, 625 (1985) [Sov. Phys. Acoust. **31**, 374 (1985)].

46. L. A. Ostrovskiĭ and V. I. Shrira, Zh. Éksp. Teor. Fiz. **71**, 1412 (1976) [Sov. Phys. JETP **44**, 738 (1976)].

47. V. I. Shrira, Zh. Éksp. Teor. Fiz. **79**, 87 (1980) [Sov. Phys. JETP **52**, 44 (1980)].

48. V. E. Fridman, Wave Motion **4**, 151 (1982).

49. A. A. Karabutov, O. V. Rudenko, and O. A. Sapozhnikov, Akust. Zh. **34**, 644 (1988) [Sov. Phys. Acoust. **34**, 371 (1988)].

50. A. A. Karabutov, O. V. Rudenko, and O. A. Sapozhnikov, Akust. Zh. **35**, 67 (1989) [Sov. Phys. Acoust. **35**, 40 (1989)].

51. L. A. Ostrovskiĭ and V. E. Fridman, Akust. Zh. **18**, 584 (1972) [Sov. Phys. Acoust. **18**, 478 (1972)].

52. D. T. Blackstock, J. C. Lockwood, and T. J. Muir, J. Acoust. Soc. Am. **53**, 1148 (1973).

53. L. A. Ostrovskiĭ, E. N. Pelinovskiĭ, and V. E. Fridman, Akust. Zh. **22**, 914 (1976) [Sov. Phys. Acoust. **22**, 516 (1976)].

54. L. A. Ostrovskiĭ and A. M. Sutin, Dokl. Akad. Nauk SSSR **221**, 1300 (1975) [Sov. Phys. Dokl. **20**, 275 (1975)].

55. N. S. Bakhvalov, Ya. M. Zhileĭkin, and E. A. Zabolotskaya, *Nonlinear Theory of Sound Beams* (Nauka, Moscow, 1982; Am. Inst. Phys., New York, 1987).

56. L. A. Ostrovskiĭ and A. M. Sutin, Akust. Zh. **22**, 93 (1976) [Sov. Phys. Acoust. **22**, 49 (1976)].

57. E. N. Pelinovskiĭ and I. A. Soustova, Akust. Zh. **25**, 631 (1979) [Sov. Phys. Acoust. **25**, 359 (1979)].

58. L. A. Ostrovskiĭ and E. N. Pelinovskiĭ, Prikl. Mat. Mekh. **38** (1), 121 (1974).

59. E. N. Pelinovskiĭ, V. E. Fridman, and Yu. K. Éngel'brekht, *Nonlinear Evolution Equations* (Valgus, Tallinn, 1984) [in Russian].

60. L. A. Ostrovsky, I. A. Soustova, and A. M. Sutin, Acustica **39** (5), 298 (1978).

61. V. E. Nazarov, L. A. Ostrovsky, I. A. Soustova, and A. M. Sutin, Phys. Earth Planet. Inter. **50** (1), 65 (1988).

62. V. E. Nazarov, Fiz. Met. Metalloved., No. 3, 172 (1991).

63. A. S. Korotkov, M. M. Slavinskiĭ, and A. M. Sutin, Akust. Zh. **40**, 84 (1994) [Acoust. Phys. **40**, 71 (1994)].

64. S. V. Zimenkov and V. E. Nazarov, Izv. Ross. Akad. Nauk, Fiz. Zemli, No. 1, 13 (1993).

65. V. E. Nazarov, A. B. Kolpakov, and V. Yu. Zaitsev, Acoust. Lett. **21** (9), 182 (1998).

66. A. É. Ekimov, A. V. Lebedev, L. A. Ostrovskiĭ, and A. M. Sutin, Akust. Zh. **42**, 61 (1996) [Acoust. Phys. **42**, 51 (1996)].

67. I. N. Didenkulov, A. É. Ekimov, V. V. Kazakov, and A. M. Sutin, in *Nonlinear Acoustics of Solid State*, Ed. by V. I. Erofeev (Intelservis, Nizhni Novgorod, 1998), pp. 265–268 [in Russian].

68. I. Yu. Belyaeva, V. Yu. Zaĭtsev, and L. A. Ostrovskiĭ, Akust. Zh. **39**, 25 (1993) [Acoust. Phys. **39**, 11 (1993)].

69. I. Yu. Belyaeva, L. A. Ostrovsky, and E. M. Timanin, Acoust. Lett. **15** (11), 221 (1992).

70. I. Yu. Belyaeva, V. Yu. Zaĭtsev, and E. M. Timanin, Akust. Zh. **40**, 893 (1994) [Acoust. Phys. **40**, 789 (1994)].

71. V. Yu. Zaĭtsev, Akust. Zh. **41**, 439 (1995) [Acoust. Phys. **41**, 385 (1995)].

72. I. Yu. Belyaeva and V. Yu. Zaĭtsev, Izv. Vyssh. Uchebn. Zaved., Radiofiz. **38** (1–2), 94 (1995).

73. A. M. Sutin and V. E. Nazarov, Izv. Vyssh. Uchebn. Zaved., Radiofiz. **38** (3–4), 169 (1995).

74. V. E. Nazarov and A. M. Sutin, J. Acoust. Soc. Am. **102**, 3349 (1997).

75. V. E. Nazarov, Akust. Zh. **46**, 228 (2000) [Acoust. Phys. **46**, 186 (2000)].

76. G. D. Meegan, P. A. Johnson, R. A. Guer, and K. R. McCall, J. Acoust. Soc. Am. **94**, 3387 (1993).

77. V. E. Nazarov, Akust. Zh. **43**, 225 (1997) [Acoust. Phys. **43**, 192 (1997)].

78. V. Gusev, C. Glorieux, J. Lauriks, and W. Thoen, Phys. Lett. A **232**, 77 (1997).

79. V. E. Nazarov, L. A. Ostrovsky, I. A. Soustova, and A. V. Radostin, in *Nonlinear Acoustics at the Turn of the Millenium*, Ed. by W. Lauterborn and T. Kurtz (Am. Inst. Phys., Melville, N.Y., 2000), pp. 299–302.

80. L. A. Ostrovskiĭ, Akust. Zh. **20**, 140 (1974) [Sov. Phys. Acoust. **20**, 88 (1974)].

81. L. A. Ostrovsky and P. A. Johnson, Riv. Nuovo Cimento **24** (7), 1 (2001).

82. V. Gusev, J. Acoust. Soc. Am. (2004) (in press).

83. L. A. Ostrovsky, J. Acoust. Soc. Am. **116** (6) (2004) (in press).

84. D. A. Kovrigin and A. I. Potapov, Dokl. Akad. Nauk SSSR **305**, 803 (1989) [Sov. Phys. Dokl. **34**, 330 (1989)].

85. D. A. Kovrigin and A. I. Potapov, Prikl. Mekh. **25** (3), 76 (1989).

86. D. A. Kovriguine and A. I. Potapov, Eur. J. Mech. A/Solids **15**, 1049 (1996).

87. D. A. Kovriguine, G. A. Maugin, and A. I. Potapov, Int. J. Solids Struct. **39**, 5571 (2002).

88. D. A. Kovriguine, G. A. Maugin, and A. I. Potapov, Sound Vibr. **263**, 1055 (2003).

89. A. I. Potapov and I. N. Soldatov, Akust. Zh. **30**, 819 (1984) [Sov. Phys. Acoust. **30**, 486 (1984)].

90. A. I. Potapov and V. I. Erofeev, *Problems in Nonlinear Acoustics* (Novosibirsk, 1987), Part 2, pp. 108–111 [in Russian].

91. V. I. Erofeyev and A. I. Potapov, in *Nonlinear World* (World Sci., Singapore, 1990), Vol. 2, pp. 1197–1209.

92. V. I. Erofeev and A. I. Potapov, Akust. Zh. **37**, 477 (1991) [Sov. Phys. Acoust. **37**, 244 (1991)].

93. V. I. Erofeyev and A. I. Potapov, Int. J. Nonlinear Mech. **28** (4), 483 (1993).

94. V. I. Erofeev, *Wave Processes in Solids with Microstructure* (Mosk. Gos. Univ., Moscow, 1999) [in Russian].

95. V. I. Erofeyev, *Wave Processes in Solids with Microstructure* (World Sci., Singapore, 2003).

96. S. A. Lisina, A. I. Potapov, and S. F. Nesterenko, Akust. Zh. **47**, 685 (2001) [Acoust. Phys. **47**, 598 (2001)].

97. A. I. Potapov, I. S. Pavlov, K. A. Gorshkov, and G. A. Maugin, Wave Motion **34** (1), 83 (2001).

98. A. I. Potapov and V. V. Stupin, Prikl. Mekh. Tekh. Fiz., No. 5, 142 (1985).

99. I. A. Kadinskaya and A. I. Potapov, Prikl. Mekh. **24** (12), 100 (1988).

100. U. Frisch, *Turbulence: The Legacy of A.N. Kolmogorov* (Cambridge Univ. Press, Cambridge, 1995).

101. U. Frisch and J. Bec, nlin.CD/0012033; in *Les Houches 2000: New Trends in Turbulence*, Ed. by M. Lesieur, A. Yaglon, and F. David (Springer, Heidelberg, 2001), Vol. 74.

102. S. N. Gurbatov, A. N. Malakhov, and A. I. Saichev, *Nonlinear Random Waves in Nondispersive Media* (Nauka, Moscow, 1990) [in Russian].

103. S. N. Gurbatov, A. N. Malakhov, and A. I. Saichev, *Nonlinear Random Waves and Turbulence in Nondispersive Media: Waves, Rays, Particles* (Manchester Univ. Press, New York, 1991).

104. K. A. Naugol'nykh and L. A. Ostrovskiĭ, *Nonlinear Wave Processes in Acoustics* (Nauka, Moscow, 1990) [in Russian].

105. K. Naugolnykh and L. Ostrovsky, *Nonlinear Wave Processes in Acoustics* (Cambridge Univ. Press, New York, 1998).

106. S. Gurbatov and O. Rudenko, in *Nonlinear Acoustics* (Academic, New York, 1998), pp. 377–398.

107. S. N. Gurbatov and A. I. Saichev, in *Nonlinear Acoustics: Theoretical and Experimental Results*, Ed. by V. A. Zverev and L. A. Ostrovskiĭ (Inst. Prikl. Fiz. Akad. Nauk SSSR, Gorki, 1980), pp. 108–142 [in Russian].

108. S. N. Gurbatov, A. I. Saichev, and I. G. Yakushkin, Usp. Fiz. Nauk **141** (2), 221 (1983) [Sov. Phys. Usp. **26**, 857 (1983)].

109. S. N. Gurbatov and A. I. Saichev, Chaos **3** (3), 333 (1993).

110. S. N. Gurbatov and A. I. Saichev, Izv. Vyssh. Uchebn. Zaved., Radiofiz. **36**, 687 (1993).

111. *Acoustics in Problems*, Ed. by S. N. Gurbatov and O. V. Rudenko (Nauka, Moscow, 1996) [in Russian].

112. A. N. Malakhov and A. I. Saichev, Izv. Vyssh. Uchebn. Zaved., Radiofiz. **17**, 699 (1974).

113. A. N. Malakhov and A. I. Saichev, Zh. Éksp. Teor. Fiz. **67**, 940 (1974) [Sov. Phys. JETP **40**, 467 (1975)].

114. S. N. Gurbatov, A. N. Malakhov, and N. V. Pronchatov-Rubtsov, Izv. Vyssh. Uchebn. Zaved., Radiofiz. **29**, 691 (1986).

115. S. N. Gurbatov, A. N. Malakhov, and N. V. Pronchatov-Rubtsov, Akust. Zh. **33**, 944 (1987) [Sov. Phys. Acoust. **33**, 549 (1987)].

116. O. V. Rudenko and A. S. Chirkin, Dokl. Akad. Nauk SSSR **214**, 1045 (1974) [Sov. Phys. Dokl. **19**, 64 (1974)].

117. O. V. Rudenko and S. I. Soluyan, *Theoretical Foundations of Nonlinear Acoustics* (Nauka, Moscow, 1975; Consultants Bureau, New York, 1977).

118. A. I. Saichev, Izv. Vyssh. Uchebn. Zaved., Radiofiz. **17**, 1025 (1974).

119. S. N. Gurbatov, Izv. Vyssh. Uchebn. Zaved., Radiofiz. **20** (1), 112 (1977).

120. S. N. Gurbatov and A. I. Saichev, Zh. Éksp. Teor. Fiz. **80**, 689 (1981) [Sov. Phys. JETP **53**, 347 (1981)].

121. S. N. Gurbatov, I. Yu. Demin, and A. I. Saichev, Zh. Éksp. Teor. Fiz. **87** (2), 497 (1984) [Sov. Phys. JETP **60**, 284 (1984)].

122. S. N. Gurbatov and D. G. Crighton, Chaos **5** (3), 524 (1995).

123. S. N. Gurbatov and A. V. Troussov, Physica D (Amsterdam) **145**, 47 (2001).

124. S. N. Gurbatov, A. A. Dubkov, and A. N. Malakhov, Zh. Éksp. Teor. Fiz. **72** (2), 456 (1977) [Sov. Phys. JETP **45**, 239 (1977)].

125. F. M. Pestorius and D. J. Blackstock, *Finite-Amplitude Wave Effects in Fluids* (IPC Science and Technology, London, 1974), p. 24.

126. E. Aurell, S. N. Gurbatov, and I. I. Wertgeim, Phys. Lett. A **182**, 109 (1993).

127. S. N. Gurbatov, S. Simdyankin, E. Aurell, *et al.*, J. Fluid Mech. **344**, 339 (1997).

128. S. N. Gurbatov and G. V. Pasmanik, Zh. Éksp. Teor. Fiz. **115**, 564 (1999) [JETP **88**, 309 (1999)].

129. E. N. Pelinovskiĭ and V. E. Fridman, Akust. Zh. **18**, 590 (1972) [Sov. Phys. Acoust. **18**, 482 (1972)].

130. O. V. Rudenko and A. S. Chirkin, Dokl. Akad. Nauk SSSR **214**, 1045 (1974) [Sov. Phys. Dokl. **19**, 64 (1974)].

131. S. N. Gurbatov and A. N. Malakhov, Akust. Zh. **23**, 569 (1977) [Sov. Phys. Acoust. **23**, 325 (1977)].

132. S. N. Gurbatov and L. G. Shepelevich, Izv. Vyssh. Uchebn. Zaved., Radiofiz. **21**, 1627 (1978).

133. S. N. Gurbatov and C. M. Hedberg, Acta Acust. **84** (3), 414 (1998).

134. L. Björnö and S. N. Gurbatov, Akust. Zh. **31**, 303 (1985) [Sov. Phys. Acoust. **31**, 179 (1985)].

135. S. N. Gurbatov, A. A. Dubkov, and A. N. Malakhov, Akust. Zh. **23**, 260 (1977) [Sov. Phys. Acoust. **23**, 146 (1977)].

136. S. N. Gurbatov and I. Yu. Demin, Akust. Zh. **28**, 634 (1982) [Sov. Phys. Acoust. **28**, 375 (1982)].

137. S. N. Gurbatov, B. O. Enflo, and G. V. Pasmanik, Acust. Acta Acust. **85** (2), 181 (1999).

138. S. N. Gurbatov, B. O. Enflo, and G. V. Pasmanik, Acust. Acta Acust. **87** (2), 16 (2001).

139. S. N. Gurbatov, I. Yu. Demin, and G. V. Pasmanik, Akust. Zh. **47**, 474 (2001) [Acoust. Phys. **47**, 405 (2001)].

140. S. N. Gurbatov, Akust. Zh. **27**, 859 (1981) [Sov. Phys. Acoust. **27**, 475 (1981)].

141. S. N. Gurbatov, Izv. Vyssh. Uchebn. Zaved., Radiofiz. **26** (3), 283 (1983).

142. S. N. Gurbatov, I. Yu. Demin, and N. V. Pronchatov-Rubtsov, Zh. Éksp. Teor. Fiz. **91** (4), 1352 (1986) [Sov. Phys. JETP **64**, 797 (1986)].

143. S. N. Gurbatov, E. Pelinovskiĭ, and A. I. Saichev, Izv. Vyssh. Uchebn. Zaved., Radiofiz. **21**, 1458 (1978).

144. S. N. Gurbatov and A. I. Saichev, Izv. Vyssh. Uchebn. Zaved., Radiofiz. **31**, 1451 (1988).

145. L. A. Ostrovskiĭ and A. M. Sutin, in *Ultrasonic Diagnostics* (Inst. Prikl. Fiz. Akad. Nauk SSSR, Gorki, 1983), pp. 139–150 [in Russian].

146. L. A. Ostrovsky and A. M. Sutin, in *Proceedings of 11th International Congress on Acoustics* (Paris, 1983), Vol. 2, pp. 137–140.

147. L. A. Ostrovsky and A. M. Sutin, in *Sea Surface Sound*, Ed. by B. Kerman (Kluwer Academic, Dordrecht, 1993), pp. 363–370.

148. V. A. Zverev, B. M. Sandler, D. A. Selivanovskiĭ, and A. Yu. Sokolov, Zh. Tekh. Fiz. **50**, 1544 (1980) [Sov. Phys. Tech. Phys. **25**, 897 (1980)].

149. B. M. Sandler, D. A. Selivanovskiĭ, and A. Yu. Sokolov, Dokl. Akad. Nauk SSSR **260**, 1474 (1981).

150. I. N. Didenkulov, S. I. Muyakshin, and D. A. Selivanovsky, Proc. Inst. Acoust. **23**, 220 (2001).

151. A. M. Sutin, S. W. Yoon, E. J. Kim, and I. N. Didenkulov, J. Acoust. Soc. Am. **103**, 2377 (1998).

152. S. N. Aleksandrov, Yu. A. Kobelev, V. V. Kulikov, *et al.*, in *Ultrasonic Diagnostics* (Inst. Prikl. Fiz. Akad. Nauk SSSR, Gorki, 1983), pp. 166–172 [in Russian].

153. A. D. Mansfel'd and A. M. Reĭman, in *Ultrasonic Diagnostics* (Inst. Prikl. Fiz. Akad. Nauk SSSR, Gorki, 1983), pp. 151–161 [in Russian].

154. A. D. Mansfel'd, D. A. Mansfel'd, and A. M. Reĭman, Akust. Zh. (2005) (in press).

155. I. N. Didenkulov, S. W. Yoon, A. M. Sutin, and E. J. Kim, J. Acoust. Soc. Am. **106**, 2431 (1999).

156. I. N. Didenkulov, L. M. Kustov, A. I. Mart'yanov, *et al.*, in *Proceedings of 11th Session of the Russian Acoustical Society* (GEOS, Moscow, 2001), Vol. 1, pp. 299–302.

157. I. N. Didenkulov, L. M. Kustov, A. I. Martyanov, *et al.*, in *Nonlinear Acoustics at the Beginning of the 21st Century*, Ed. by O. V. Rudenko and O. A. Sapozhnikov (Moscow State Univ., Moscow, 2003), Vol. 2, p. 999.

158. N. I. Didenkulov, A. I. Martyanov, D. A. Selivanovsky, and N. V. Pronchatov-Rubtsov, Hydroacoustics **4**, 43 (2001).

159. I. Didenkulov, L. Kustov, A. Martyanov, and N. Pronchatov-Rubtsov, in *Acoustical Imaging*, Ed. by W. Arnold and S. Hirsekorn (Kluwer Academic/Plenum, Dordrecht, 2004), Vol. 27, pp. 349–356.

160. Z. Klusek, A. M. Sutin, A. L. Matveev, and A. I. Potapov, Acoust. Lett. **18** (11), 198 (1995).

161. I. A. Soustova, A. M. Sutin, and S. V. Yun, Akust. Zh. **42**, 254 (1996) [Acoust. Phys. **42**, 222 (1996)].

162. V. A. Antonets, D. M. Donskoĭ, and A. M. Sutin, Mekh. Kompoz. Mater. **15**, 934 (1986).

163. A. S. Korotkov and A. M. Sutin, Acoust. Lett. **18** (4), 59 (1994).

164. A. M. Sutin and V. E. Nazarov, Izv. Vyssh. Uchebn. Zaved., Radiofiz. **38** (3–4), 109 (1995).

165. A. M. Sutin, C. Delclos, and M. Lenclud, in *Proceedings of the 2nd Symposium on Acoustical and Vibratory Surveillance Methods and Diagnostic Techniques* (Senlis, France, 1995), pp. 725–735.

166. D. M. Donskoy and A. M. Sutin, J. Intell. Mater. Syst. Struct. **9**, 765 (1998).

167. D. Donskoy, A. Sutin, and A. Ekimov, NDT & E Int. **34**, 231 (2001).

168. K. Van Den Abeele, A. M. Sutin, J. Carmeliet, and P. A. Johnson, NDT & E Int. **34**, 239 (2001).

169. V. V. Kazakov, A. É. Ekimov, A. M. Sutin, and I. N. Didenkulov, in *Nonlinear Acoustics of Solid State: Proceedings of 8th Session of the Russian Acoustical Society*, Ed. by V. I. Erofeev (Intelservis, Nizhni Novgorod, 1998), pp. 247–250.

170. I. N. Didenkulov, A. M. Sutin, V. V. Kazakov, *et al.*, in *Nonlinear Acoustics at the Turn of the Millenium*, Ed. by W. Lauterborn and T. Kurz (Melville, New York, 2000), pp. 329–332.

171. V. V. Kazakov, A. M. Sutin, and P. A. Johnson, Appl. Phys. Lett. **81** (4), 646 (2002).

172. I. N. Didenkulov, N. V. Kurochkin, A. A. Stromkov, and V. V. Chernov, in *Methods of Acoustical Diagnostics of Inhomogeneous Media* (Inst. Prikl. Fiz. Ross. Akad. Nauk, Nizhni Novgorod, 2002), pp. 188–195 [in Russian].

173. I. N. Didenkulov, N. V. Kurochkin, A. A. Stromkov, and V. V. Chernov, in *Proceedings of the Tenth International Congress on Sound and Vibration* (Int. Inst. of Acoustics and Vibration, Stockholm, 2003), pp. 3565–3572.

174. A. V. Lebedev, L. A. Ostrovskiĭ, I. A. Soustova, *et al.*, Akust. Zh. **49**, 92 (2003) [Acoust. Phys. **49**, 81 (2003)].

175. I. D. Gits, V. V. Gushchin, V. A. Zverev, *et al.*, in *Proceedings of VII All-Union Acoustical Conference* (Leningrad, 1971), pp. 57–60.

176. B. A. Konyukhov and G. M. Shalashov, Izv. Vyssh. Uchebn. Zaved., Radiofiz. **17**, 1313 (1974).

177. G. M. Shalashov, Akust. Zh. **30**, 386 (1984) [Sov. Phys. Acoust. **30**, 227 (1984)].

178. B. A. Konyukhov and G. M. Shalashov, USSR Inventor's Certificate No. 517732, Byull. Izobret., No. 33 (1977).

179. *Method for the Diagnostics of Structural Materials: Determination of the Third-Order Elasticity Constants by the Acoustic Method* (Gf VNIINMASh, Gorki, 1976) [in Russian].

180. V. V. Gushchin and G. M. Shalashov, in *Studies of the Earth by Nonexplosive Seismic Sources* (Nauka, Moscow, 1981), pp. 144–155 [in Russian].

181. G. M. Shalashov, Izv. Akad. Nauk SSSR, Fiz. Zemli, No. 3, 95 (1985).

182. D. A. Kas'yanov and G. M. Shalashov, USSR Inventor's Certificate No. 1520461, Byull. Izobret., No. 41 (1989).

183. A. L. Groshkov, R. R. Kalimulin, G. M. Shalashov, and V. A. Shemagin, Dokl. Akad. Nauk SSSR **313** (1), 63 (1990).

184. D. A. Kas'yanov and G. M. Shalashov, Izv. Vyssh. Uchebn. Zaved., Radiofiz. **45** (2), 170 (2002).

185. N. E. Nikitina, Probl. Mashinostr. Nadezhnosti Mash., No. 4, 70 (1999).

186. N. Ye. Nikitina and L. A. Ostrovsky, Ultrasonics **35**, 605 (1998).

187. *Methods: Calculations and Strength Tests in Mechanical Engineering; Experimental Methods for Determining the Stress–Strain State of Machine and Structure Elements; Acoustical Methods for Determining the Residual Stresses in Structural Materials* (VNIINMASh, Moscow, 1980) [in Russian].

Translated by E. Golyamina

Acoustic Cavitation Thresholds of Sea Water in Different Regions of the World Ocean

V. A. Akulichev and V. I. Il'ichev[†]

Il'ichev Pacific Oceanological Institute, Far-East Division, Russian Academy of Sciences,
Baltiiskaya ul. 43, Vladivostok, 690041 Russia
e-mail: akulich@poi.dvo.ru
Received October 18, 2004

Abstract—Results of experimental measurements of acoustic cavitation thresholds are presented for the waters of the Atlantic Ocean, Pacific Ocean, Indian Ocean, Arctic Ocean, and some other parts of the World Ocean, including the Arabian Sea, Baltic Sea, East Siberian Sea, North Sea, Philippine Sea, Black Sea, Sea of Japan, Sea of Okhotsk, and South China Sea. The measurements were carried out by many oceanic expeditions between 1963 and 1987. General laws governing the variations in the cavitation strength of sea water over the World Ocean are revealed. © 2005 Pleiades Publishing, Inc.

INTRODUCTION

Cavitation occurs in water or in other liquids under decreasing pressure and manifests itself as a discontinuity of the medium. It is conventional to distinguish between acoustic and hydrodynamic cavitation.

Acoustic cavitation arises in sea water or any other liquid under the action of an intense acoustic field when the acoustic pressure amplitude P_m exceeds some threshold value P_m^*, which is commonly called the acoustic cavitation threshold or the tensile strength of water. The value of P_m^* in sea water depends on many hydrophysical and hydrochemical parameters. The influence of hydrostatic pressure P_0, linearly growing with depth, is an important factor. The quantities P_m^* and P_0 are related by the formula $P_m^* = P_0 - P_c$, where P_c is the hydrodynamic cavitation threshold pressure at which cavitation arises. Cavitation nuclei are usually represented by microscopic (most often gaseous) inclusions in a liquid. For liquids with large cavitation nuclei, the value of P_c is usually equal to the saturated vapor pressure P_v. However, for very pure liquids with small cavitation nuclei, P_c can be much smaller than P_v and in some cases can even be negative. The value of the acoustic cavitation threshold pressure P_m^* is always positive.

Hydrodynamic cavitation is induced by the pressure fluctuations arising in sea water due to the rotation of screw propellers or due to flows around different moving bodies. The corresponding threshold value of the pressure variation $(P_0 - P_c)$ is conventionally called the hydrodynamic tensile strength or the cavitation threshold of sea water. This quantity is virtually equal to the acoustic cavitation strength when the frequency of the acoustic field is equal or close to the frequency of hydrodynamic pressure fluctuations.

The acoustic cavitation threshold P_m^* for ocean water is connected with many hydrophysical parameters of the water medium and with the parameters of acoustic sources, including the acoustic field frequency f, which can be much higher than the frequency of hydrodynamic fluctuations caused by flows around different bodies in sea water. However, at low frequencies of acoustic cavitation excitation, the frequency f may only slightly differ from characteristic frequencies of hydrodynamic fluctuations. In this case, the quantity P_m^* measured for acoustic cavitation will be approximately equal to the hydrodynamic cavitation strength of the same water under the same conditions. This allows one to use the results of acoustic cavitation measurements to determine the cavitation thresholds of sea water for hydrodynamic cavitation.

CAVITATION NUCLEI

Usually, the tensile strength of sea water P_m^* grows with sea water depth. However, this growth may obey different laws, which are determined by the depth dependence of the size and concentration of phase inclusions serving as cavitation nuclei.

[†] Deceased.

In the upper sea water layer, the most characteristic cavitation nuclei are gas bubbles. Their sizes and concentration are determined by the surface roughness and by hydrophysical parameters governing the formation and dissolution of gas bubbles in water. Depending on these conditions, gas bubbles in the upper ocean layer may vary in size from 10^{-5} to 10^{-1} cm.

Cavitation in sea water can also arise at phase inclusions represented by zooplankton or phytoplankton. The sizes of zooplankton range from several microns for nanoplankton to several centimeters for macroplankton. The sizes of phytoplankton vary over an even wider range. On the whole, the size and concentration of plankton in sea water depends on the biological condition of the medium in a given region, which is characterized by both spatial and temporal variability governed by complex laws and which is an object of special studies.

Cavitation can also originate in solid nuclei, which get into sea water from the atmosphere, from rivers, and from other sources, including anthropogenic ones. Solid nuclei may have different sizes (10^{-6} to 10^{-2} cm), shapes, and degrees of wetting with water.

In sea water, cavitation nuclei in the form of small vapor bubbles may also be generated by high-energy particles caused by cosmic rays or radioactivity. Primary cosmic rays composed mainly of protons and alpha particles are transformed into secondary particles mainly consisting of electrons and μ-mesons at the sea level. Electrons are intensively absorbed in water, while μ-mesons possess a high penetrating power and are poorly absorbed in water. Electrons and μ-mesons interact with sea water atoms and knock out electrons, thus spending energy for the ionization of the medium. If the resulting electrons have a sufficiently high energy, they may in their turn cause ionization. Such secondary electrons are called δ electrons. The local heat release by δ electrons leads to the formation of vapor bubbles smaller than 10^{-6} cm in size. Their lifetime is small, but their concentration may vary depending on the intensity of cosmic rays.

The effect of radioactivity on sea water may manifest itself as a neutron flux, which interacts only with atomic nuclei on passing through the sea water medium. In this case, free radicals and atoms of oxygen and hydrogen can arise in water. They can form bubbles owing to the coagulation of gas molecules. Similar effects may be caused by such a primary cosmic particle as the neutrino.

All the aforementioned cavitation nuclei appear in the sea water medium under the effect of external forces and disturbances. However, even in the case of a complete isolation from external effects, the formation of vapor bubbles in water is possible due to the manifestation of thermodynamic heterophase fluctuations. The size of such cavitation nuclei is deter-
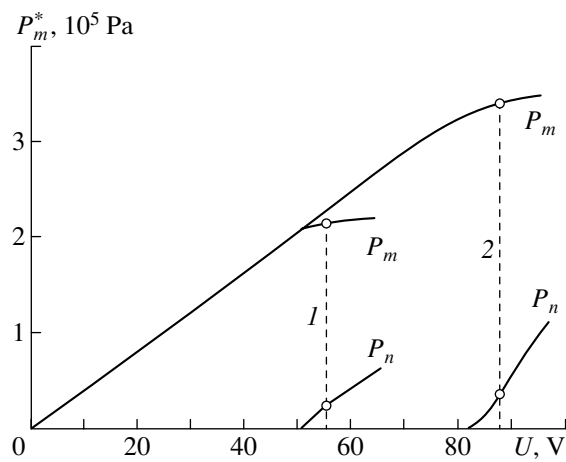
Fig. 1. Dependence of the initial acoustic signal P_m and cavitation noise signal P_n on the voltage U applied to the source for different depths: (*1*) 5 and (*2*) 10 m.

mined by the absolute temperature of the medium and, for water under normal conditions, does not exceed 10^{-7} cm. Under usual conditions in sea water, the effect of these cavitation nuclei is negligibly small compared to the effects of gas bubbles, plankton, and solid particles.

MEASUREMENT TECHNIQUE

The determination of the tensile strength of sea water was performed by specially designed technical means on the basis of measuring the acoustic field threshold amplitude P_m^*, the excess over which causes the development of cavitation.

The measurement technique was first proposed in [1], and its essence was as follows. Acoustic cavitation was excited by an intense tonal acoustic signal with a fundamental frequency f and with an increasing amplitude P_m. The onset of cavitation corresponded to the rise of an acoustic cavitation noise signal with a summary pressure P_n, which contained discrete harmonic spectral components with frequencies nf, where $n = 2, 3, \ldots$, and also a continuous spectrum component of the received signal. The ratio of the acoustic cavitation noise signal P_n to the amplitude of the basic tonal signal P_m determines the coefficient K of nonlinear distortion of the acoustic signal at the beginning of acoustic cavitation: $K = P_n/P_m$.

Figure 1 shows an example of an experimental measurement of the initial acoustic signal P_m and the cavitation noise signal P_n in sea water as a function of the electric voltage V applied to the high-power acoustic source with an excitation frequency of 10 kHz. Figure 2 shows the summary acoustic signal and the cavitation noise signal. These measurements were carried out in
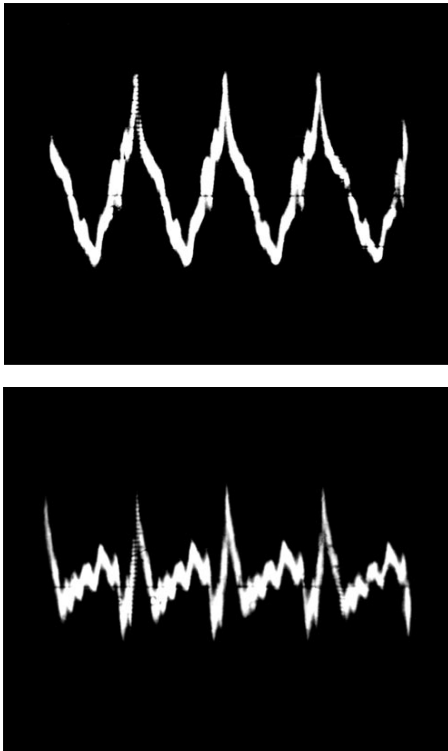
Fig. 2. Summary signal (top) and cavitation noise signal (bottom) for the case of cavitation excitation at a frequency of 10 kHz at a depth of 10 m.

September 1982 in the Sea of Japan, at depths of 5 and 10 m, at the point with a latitude of 42° N and a longitude of 132° E.

Experimental studies of the onset of acoustic cavitation in sea water with different physical and chemical characteristics (temperature, salinity, gas content,

etc.) at different depths showed that the cavitation threshold corresponds to the acoustic pressure amplitude P_m^* at which the value of the coefficient of nonlinear distortion due to cavitation is $K = 0.1$. In Fig. 1, the pressure values of the fundamental tone signal P_m and cavitation noise P_n that correspond to the acoustic cavitation threshold P_m^* are marked with empty circles.

In our measurements of the cavitation strength of sea water at different depths, we used water-filled cylindrical acoustic sources, which in fact were cylindrical focusing systems and which allowed us to stimulate cavitation in water at a given distance from the inner radiating surface without perturbing the physicochemical characteristics of water. Figures 3 and 4 show two different systems used for measuring the acoustic cavitation thresholds P_m^* in sea water.

The system presented in Fig. 3 is based on the application of a high-power cylindrical acoustic source. Usually, such sources are made of piezoceramic active materials. The resonance frequency f of such an acoustic source is connected with the diameter of the cylinder d by the formula $f = c_p/\pi d$, where c_p is the speed of sound in the piezoceramic material. Such sources are suitable for frequencies f of more than 1 kHz. For measurements at lower frequencies f, an excessive increase in d is required, which leads to technical difficulties. To excite cavitation in sea water at low frequencies f on the order of hundreds of hertz, it is more convenient to apply sound sources in the form of resonance metal tubes open at one end and excited at the other by an acoustic vibrator. Figure 4 shows a scheme of the system with a resonance tube for measuring the acoustic
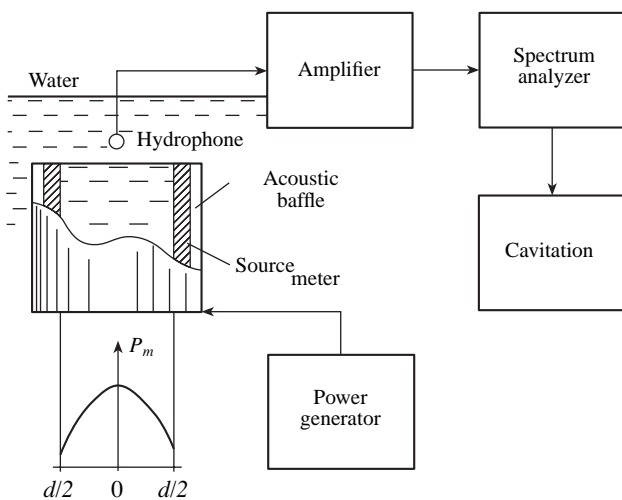
Fig. 3. Schematic representation of the system for measuring the acoustic cavitation thresholds with the use of a water-filled cylindrical piezoceramic acoustic source.
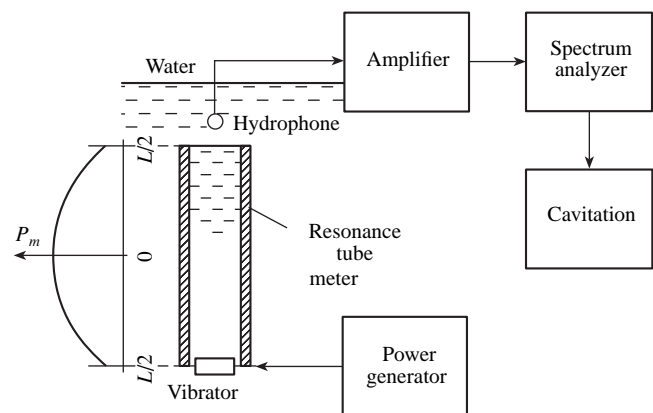
Fig. 4. Schematic representation of the system for measuring the acoustic cavitation thresholds with the use of a resonance metal tube excited at one end by an acoustic vibrator.

cavitation thresholds P_m^*. In such a system, the coefficient of nonlinear distortion of the signal and, hence, the acoustic cavitation threshold is determined by a cavitation meter. This technique for measuring the acoustic cavitation thresholds in sea water was suggested in [2]. The resonance frequency of such an acoustic source f is connected with the tube length L by the formula $f = c_v/2L$, where c_v is the sound speed in sea water. The aforementioned spectral feature of measuring the acoustic cavitation thresholds P_m^* can be successfully used with both piezoceramic cylindrical sources and resonance tubes.

The proposed technique was used by us for measuring the cavitation strength of sea water in different regions of the ocean [1–3]. Similar techniques were used later by other researchers [4, 5].

ACOUSTIC CAVITATION THRESHOLDS IN DIFFERENT REGIONS OF THE WORLD OCEAN

Below, we present the results of experimental measurements of acoustic cavitation thresholds in different regions of the World Ocean. The measurements were performed between 1963 and 1987.

Figure 5 presents the results of measuring the cavitation thresholds of sea water P_m^* depending on the depth h according to the data obtained in September 1982 in the Sea of Japan at a latitude of 42° N and a longitude of 132° E. Acoustic sources with different frequencies from 230 Hz to 10 kHz were used to excite the cavitation. The measurements at a low frequency of 230 Hz were conducted using resonance acoustic steel tubes in accordance with Fig. 4. The measurements at other, higher, frequencies were conducted using water-filled cylindrical piezoceramic acoustic sources in accordance with Fig. 3.

As follows from Fig. 5, the values of acoustic cavitation thresholds P_m^* increase on the average linearly with increasing depth h. However, at some depths h, one can see deviations of P_m^* from the hydrostatic pressure level P_0, which is shown by the dashed line. In some cases, the acoustic cavitation thresholds prove to be lower than the hydrostatic pressure values. According to [6], this may occur because of the so-called rectified gas diffusion under the effect of the periodic acoustic field, when the cavitation nuclei in water grow into bubbles whose resonance frequency is close to the frequency of the exciting acoustic field.

In 1968, measurements of acoustic cavitation thresholds P_m^* were carried out in the northern part of the Atlantic Ocean, including the North Sea and the
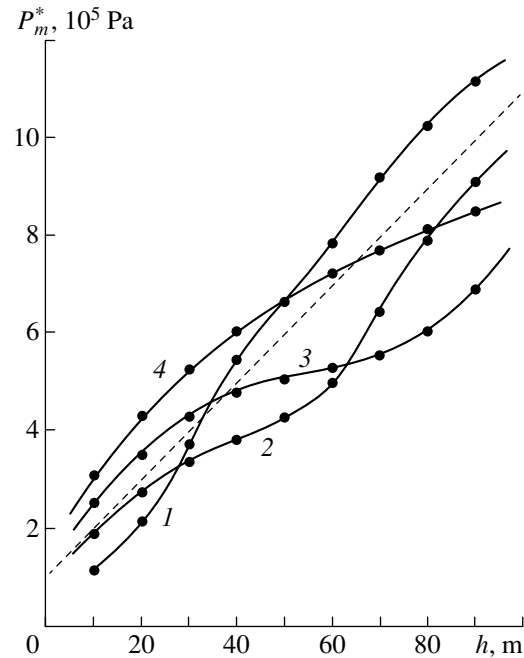
Fig. 5. Acoustic cavitation thresholds P_m^* versus the depth for different frequencies $f = (1)$ 230 Hz, (2) 750 Hz, (3) 4.5 kHz, and (4) 10 kHz.

Baltic Sea. Figure 6 shows the sites of the measurements for two different seasons. The crosses correspond to the spring season (March–April 1968), and the crosses in circles correspond to the summer season (June–July 1968). From general considerations, it follows that the seasonal variability of weather and the related variability of both meteorological parameters in the near-water layer of the atmosphere and hydrological parameters in the upper water layer of the ocean should be most pronounced away from the equator, that is, at higher latitudes. Therefore, we expected that the values of the acoustic cavitation thresholds P_m^* measured in the near-equator zone of the ocean should not noticeably vary from season to season. However, the results of measurements proved to be unexpected.

Figure 7 presents the experimental results of acoustic cavitation thresholds P_m^* as a function of latitude in the Atlantic Ocean, from the equator to the North Sea and the Baltic Sea. Cavitation was excited at depths of 10 and 20 m by a continuous tonal signal at a frequency of 10 kHz. It is seen from Fig. 7 that, in the northern part of the Atlantic Ocean, cavitation thresholds vary depending on the latitude. The acoustic cavitation thresholds P_m^* have higher values near the equator and decrease with increasing latitude. This effect is more pronounced at a depth of 20 m compared to at a depth of 10 m. In Figs. 6 and 7, the point with a latitude of
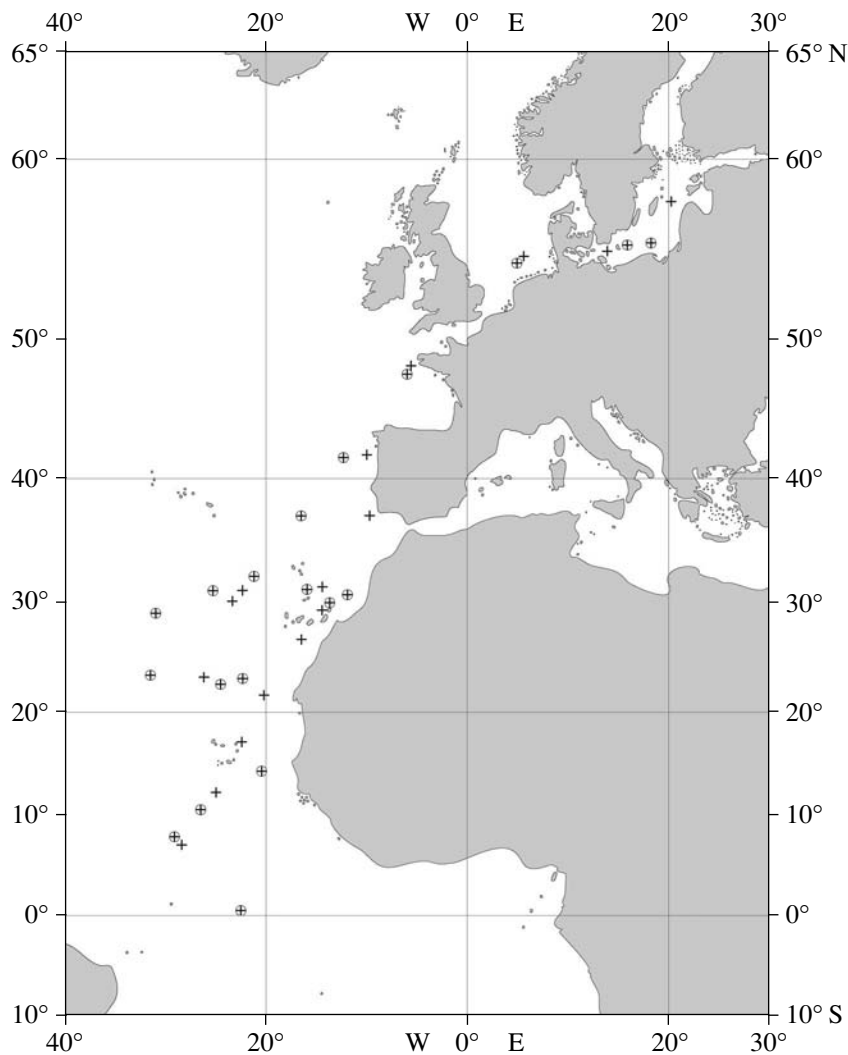
Fig. 6. The measurement sites in the Atlantic Ocean for (+) the spring season (March–April 1968) and (⊕) the summer season (June–July 1968).

54°30′ N (and a longitude of 4°52′ E) corresponds to the measurements in the North Sea. Two points with latitude 55°33′ N (longitude 15°55′ E) and latitude 57°46′ N (longitude 20°09′ E) correspond to the measurements in the Baltic Sea. In the North Sea and Baltic Sea, the thresholds P_m^* were measured in March and July with maximum separation in time. From Fig. 7, one can see that, in the aforementioned high-latitude seas, the cavitation thresholds P_m^* in July are higher than in March. This trend manifests itself to one or another extent in all high-latitude measurements to the north of latitude 40° N. To the south of this latitude down to the equator, another trend is observed: the cavitation thresholds are higher in spring and lower in summer.

Figure 8 shows the data on temperature, salinity, and dissolved gas and oxygen at the sites of acoustic measurements at the aforementioned depths. From Fig. 7, it follows that the cavitation strength of water in the equatorial Atlantic proved to be higher in spring compared to summer. According to Fig. 8, in this part of the Atlantic Ocean in these seasons no considerable difference was observed between the measured hydrological parameters. In the regions lying to the north of 40° N, the picture was different. According to Fig. 7, the cavitation thresholds in summer (in July) proved to be higher than those in spring (in March). At the same time, according to Fig. 8, in summer, because of the increase in temperature, a decrease was observed in the concentrations of dissolved gas and dissolved oxygen. The latter decrease may lead to a decrease in the concentration and size of gaseous cavitation nuclei in sea water. According to the existing physical concepts [6, 7], such changes in the hydrology should definitely lead to an increase (see Fig. 7) in the cavita-

tion strength of water in summer (July) compared to that in spring (March) in subarctic waters.

A comparison of Figs. 7 and 8 shows that, in the northern Atlantic, the cavitation strength decreased as the latitude increased from the equatorial part of the ocean with tropical waters to high-latitude regions with subarctic waters. The passage from the equator to high latitudes was accompanied by the characteristic temperature decrease, a very small change in salinity (except for the well-known salinity drop in the Baltic Sea), and an increase in the concentrations of dissolved gas and oxygen.

The tendency towards the decrease in acoustic cavitation thresholds in ocean water on moving from the equator to higher latitudes also proved to be typical of other parts of the World Ocean.

Figure 9 shows the points where acoustic cavitation thresholds were measured in the Pacific Ocean. The measurements were carried out in different years from 1964 through 1985. The most extensive measurements were carried out from September to November 1982, when data were obtained for both the northern and southern parts of the Pacific Ocean. At that time, it was autumn in the northern part and spring season in the southern part of the ocean. Figure 10 shows the acoustic cavitation thresholds P_m^* as a function of latitude for the Pacific Ocean, from a latitude of about 49° N near the Kamchatka Peninsula to latitude 15°30′ S in the Coral Sea. Cavitation was excited at depths of 10 m and 20 m by tone signals at a frequency of 10 kHz. Figure 10 shows that, in the Pacific Ocean, the cavitation thresholds also vary depending on the latitude. It turned out that the acoustic cavitation thresholds P_m^* were higher near the equator and decreased with increasing latitude in the directions from the equator to the northern subarctic waters and to the southern subtropic waters of the Pacific Ocean. This dependence of the cavitation strength of water P_m^* on latitude in the Pacific Ocean proved to be as clearly pronounced as in the Atlantic Ocean.

The measurements of acoustic cavitation thresholds in the Indian Ocean were carried out in March–April 1987. Figure 11 shows the measurement sites from a latitude of about 20° N in the Arabian Sea to a latitude of about 45° S in the southern part of the Indian Ocean. Figure 12 presents the measured cavitation thresholds P_m^* as a function of latitude. Cavitation was excited at depths of 10 and 20 m by continuous tonal signals at a frequency of 10 kHz. In the Indian Ocean, the cavitation thresholds had higher values near the equator and decreased with increasing latitude in the northern (toward subtropic waters) and southern (toward subantarctic waters) directions. The measurements were performed in late autumn in the southern
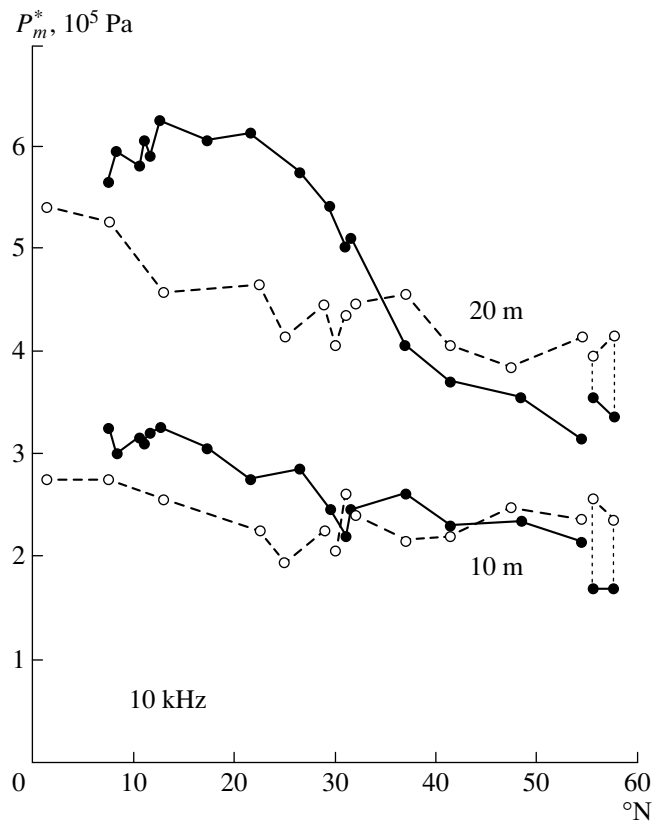
Fig. 7. Acoustic cavitation thresholds P_m^* in the Atlantic Ocean as a function of latitude at depths of 10 and 20 m for different seasons of 1968: (●) spring and (○) summer.

part of the Indian Ocean. With the passage from the equator to the south to latitude 45° S, the water temperature decreased from 30°C in the tropical region to 10°C in the subantarctic region. The surface roughness in the ocean varied in the southern direction from 1 m near the equator to 6.5 m at the point with latitude 45° S. An increase in the sea surface roughness usually leads to breaking of surface waves, which, in its turn, causes an increase in the concentration and characteristic size of gas bubbles serving as cavitation nuclei in the upper ocean layer [7]. This explains the decrease in the cavitation thresholds P_m^* with increasing latitude in the southern part of the Indian Ocean (see Fig. 12).

It should be noted that the increase in the surface roughness with growing latitude is a general feature of all oceans except for those regions with an ice cover. Presumably, it is this feature that explains the decrease observed in the acoustic cavitation thresholds P_m^* with the passage from the equator to higher latitudes in the Atlantic, Pacific, and Indian oceans.

Measurements in the Arctic Ocean proved to be important for understanding the relations between the acoustic cavitation thresholds and the hydrome-
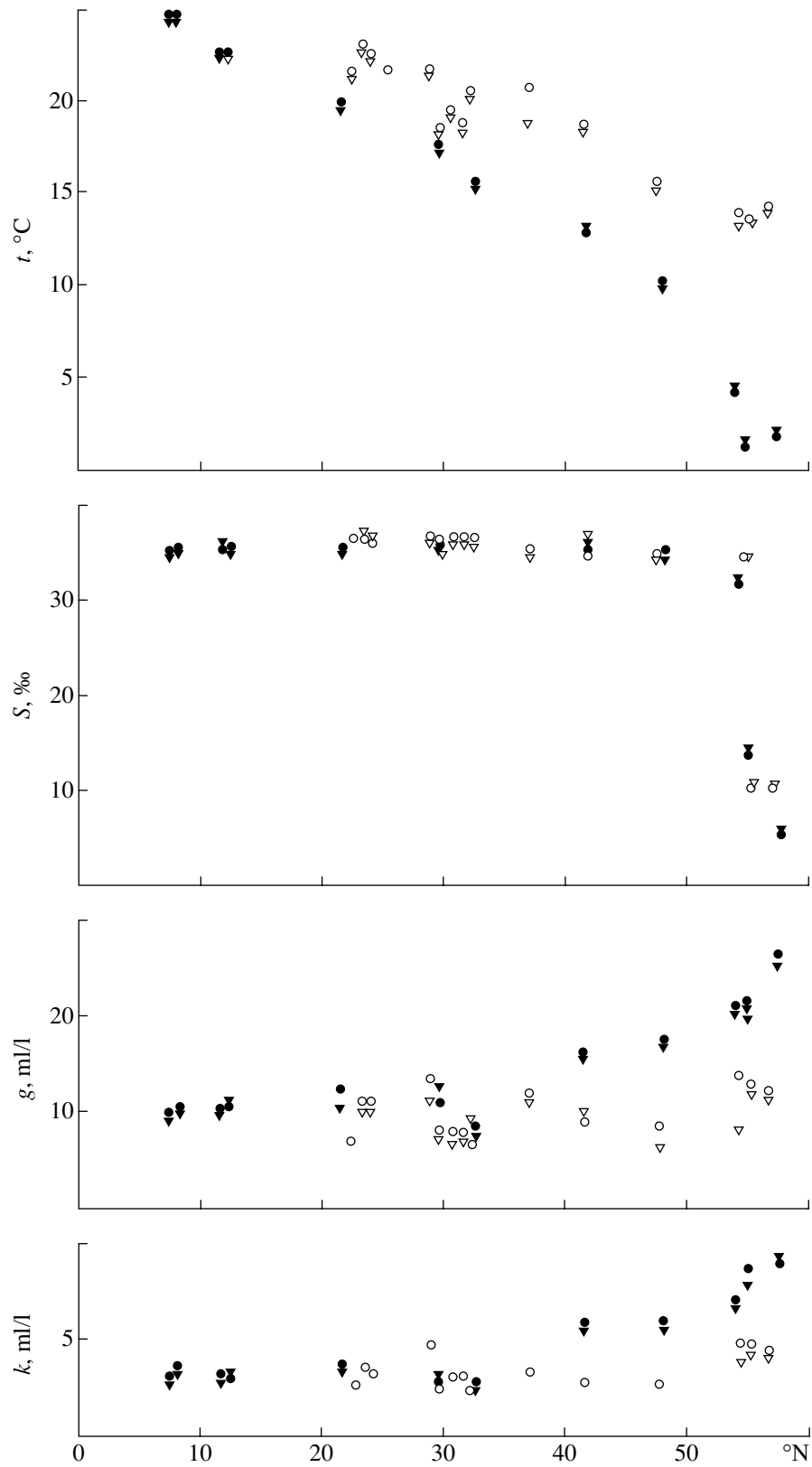
Fig. 8. Temperature, salinity, and dissolved gas and oxygen concentrations at different points in the Atlantic Ocean at a depth of 10 m in (●) spring and (○) summer and at a depth of 20 m in (▼) spring and (▽) summer.
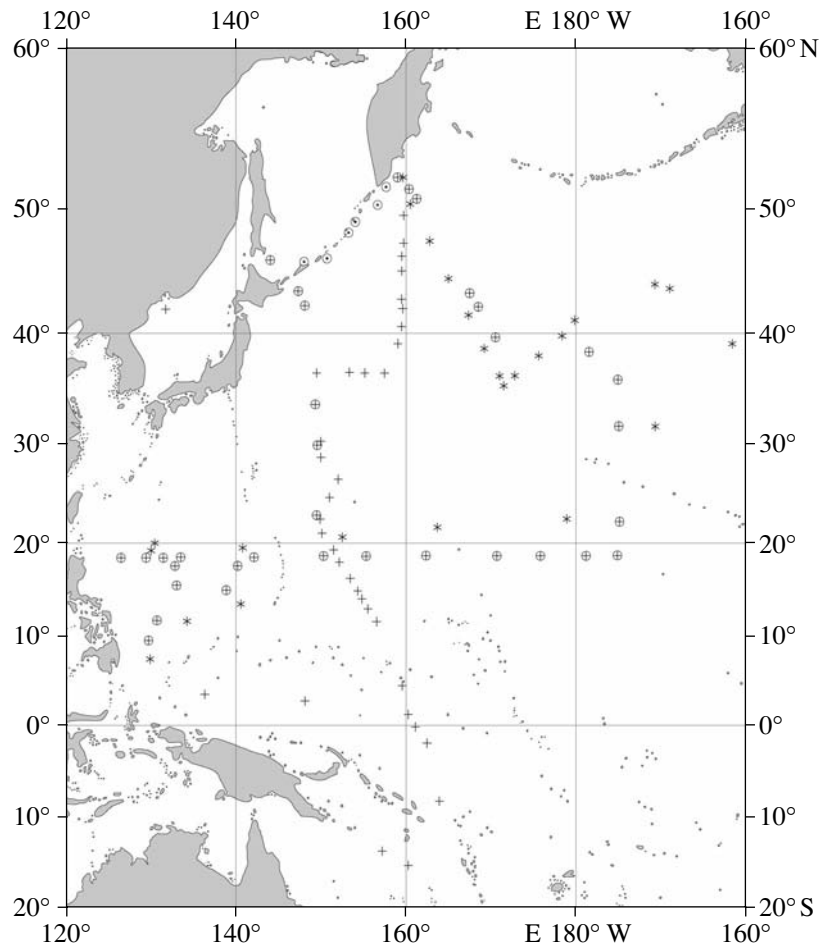
Fig. 9. The sites of cavitation measurements in the Pacific Ocean in different years: (⊙) September 1964, (+) September–November 1982, (⊕) October–November 1983, and (∗) August–October 1985.

teorological and hydrological conditions. These measurements were carried out in May 1969 from a drifting block of ice in the East Siberian Sea (one of the ice bases belonging to the North Pole-18 drifting arctic station). Figure 13 shows the point (the cross in the plot) with coordinates 76° N and 164° E where the measurements of acoustic cavitation thresholds were carried out. The ice thickness was about 3 m. The air temperature was –12°C, and the water temperature varied from –1.68°C near the water surface to –1.55°C at a depth of 50 m. The ice cover prevented surface roughness, and the upper water layer contained almost no cavitation nuclei in the form of gas bubbles, which usually occur in the open ocean due to the breaking of waves. Presumably, this fact is responsible for the very high values of cavitation strength of water P_m^* that were obtained under these conditions, as compared to the values obtained in other ocean regions.

Table 1 presents the data on the acoustic cavitation thresholds P_m^* for the arctic conditions under the ice
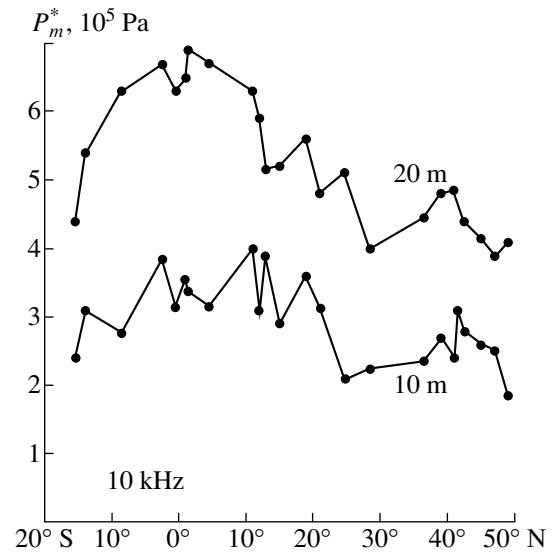
Fig. 10. Acoustic cavitation thresholds P_m^* in the Pacific Ocean as a function of latitude at depths of 10 and 20 m in September–November 1982.
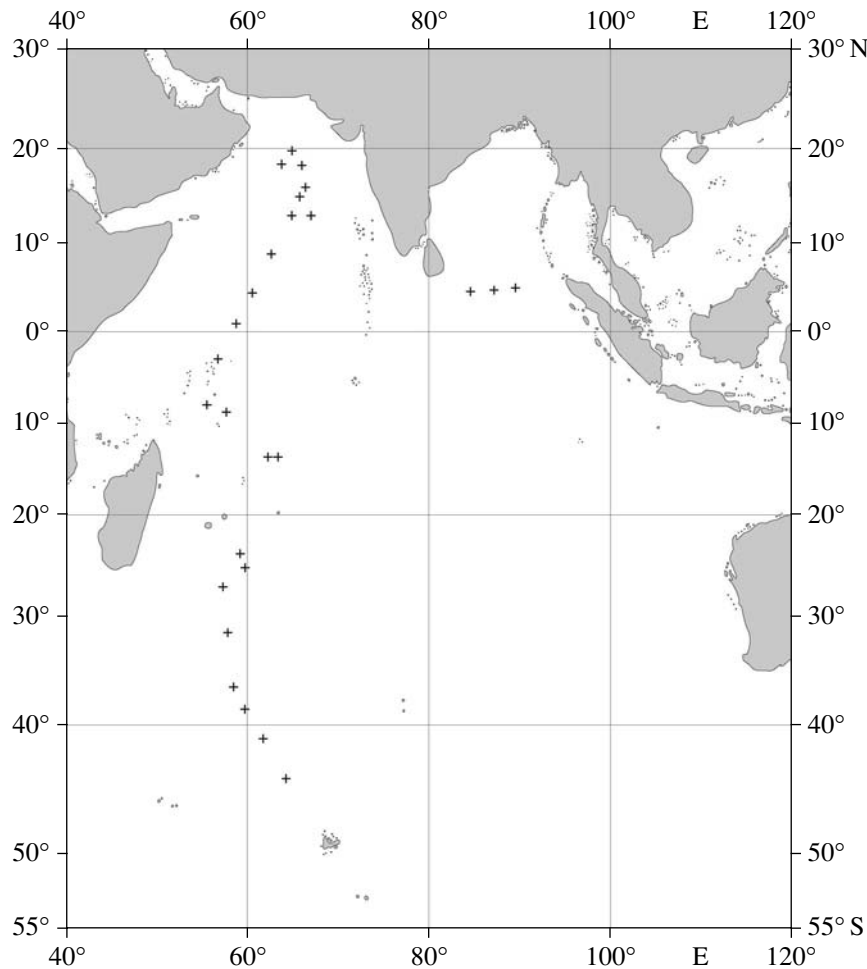
Fig. 11. The sites of cavitation measurements in the Indian Ocean (+) in March–April 1987.

cover at a depth of 10 m and for different frequencies from 2.0 to 15.0 kHz. One can see that, at a frequency of 10 kHz at a depth of 10 m, the value of the cavitation threshold P_m^* is 5.6×10^5 Pa, which noticeably exceeds the values of P_m^* obtained at the same frequency and depth in other regions of the World Ocean. From Table 1, it also follows that the acoustic cavitation thresholds P_m^* increase as the excitation frequency f increases. This tendency manifests itself to some extent in all regions of the World Ocean.

It is of interest to compare the cavitation strength of sea water in different regions of the World Ocean. This

Table 1. Acoustic cavitation thresholds P_m^* at different frequencies f in the Arctic Ocean

Frequency f, kHz	2.0	4.0	6.0	8.0	10.0	15.0
Cavitation threshold, 10^5 Pa	1.9	2.9	3.8	4.7	5.6	6.9

problem is not a simple one, because, even at one given point of the ocean, the cavitation threshold may vary with time over wide limits depending on weather conditions and on the seasonal and climate variability of those hydrophysical parameters of the water medium that determine the threshold and the development of cavitation, with all other technical conditions being the same. However, we can speculate on some average values of acoustic cavitation thresholds P_m^* obtained at a certain frequency f at the same depth in each of the ocean regions under study.

Table 2 presents the results of measuring the acoustic cavitation thresholds P_m^* in different regions of the World Ocean within 1963 to 1987. These results refer to measurements at a standard depth of 10 m and at a frequency of 10 kHz. The measurements were carried out in the equatorial parts of the Atlantic Ocean, the Indian Ocean, and the Pacific Ocean. The values obtained for the Arctic Ocean correspond to the measurements in the East Siberian Sea. The lowest acous-
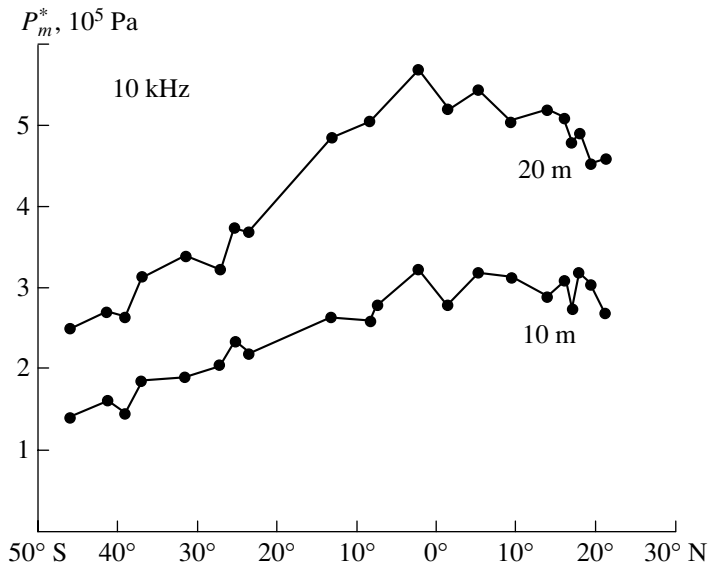
Fig. 12. Acoustic cavitation thresholds P_m^* in the Indian Ocean as a function of latitude at depths of 10 and 20 m in March–April 1987.
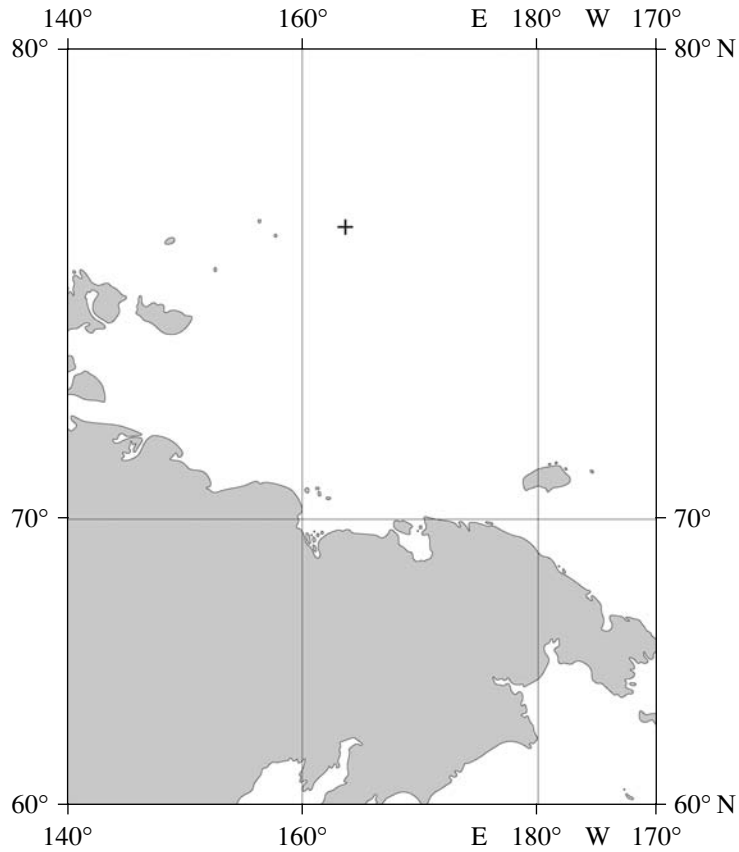
Fig. 13. (+) Site of cavitation measurements in the East Siberian Sea in May 1969.

Table 2. Acoustic cavitation thresholds P_m^* in different regions of the World Ocean

Region	Threshold P_m^*, 10^5 Pa	Time of measurement
Atlantic Ocean	3.2	April 1968
Indian Ocean	2.8	March 1987
Arctic Ocean	5.6	May 1969
Pacific Ocean	3.6	October 1982
Arabian Sea	2.8	March 1987
Baltic Sea	2.3	June 1968
East Siberian Sea	5.6	May 1969
Sea of Okhotsk	2.2	September 1964
North Sea	2.4	June 1968
Philippine Sea	2.5	October 1985
Black Sea	1.8	September 1963
South China Sea	2.4	September 1985
Sea of Japan	2.6	September 1982

tic cavitation thresholds were found to occur in the Indian Ocean, and the highest, in the Arctic Ocean. The cavitation thresholds obtained for waters of different seas vary over wide limits. The lowest values were observed in the Black Sea, and the highest values, in the East Siberian Sea.

CONCLUSIONS

The results presented above show that acoustic cavitation thresholds P_m^* have different values in different regions of the World Ocean. This fact should be taken into account when using high-power acoustic sources in sea water. The value of the cavitation threshold P_m^* determines the limiting level of acoustic intensity J_C that can be emitted by an acoustic source:

$$J_C = K_a (P_m^*)^2,$$

where K_a is the coefficient that determines the type of the acoustic field; for a plane acoustic wave, $K_a = (1/2\rho c)$, where ρ is the density of sea water and c is the sound velocity in it.

Moreover, the value of the cavitation threshold P_m^* allows one to estimate the critical speed V_C for bodies moving in sea water, i.e., the speed limit beyond which a moving body gives rise to cavitation. For a streamlined spheroidal body moving in sea water, the following formula is valid:

$$V_C = K_h (P_m^*)^{1/2},$$

where the coefficient $K_h = (2/\rho K_f K_p)^{1/2}$ characterizes the hydrodynamic flow around the body; here, the coefficient K_f is determined by the shape of the body and the coefficient K_p is determined by the hydrodynamic fluctuations of the flow around the body.

In closing, it should be noted that studies of the cavitation strength of sea water in different regions of the World Ocean began in the early 1960s, when the authors of this paper worked at the Sukhumi Marine Research Station of the Acoustics Institute of the Academy of Sciences of the USSR [1]. Later, in the 1970s and 1980s, these studies were continued at the Pacific Oceanological Institute, Far-East Division, Russian Academy of Sciences [2, 3, 8–15].

REFERENCES

1. V. A. Akulichev and V. I. Il'ichev, Akust. Zh. **9**, 158 (1963) [Sov. Phys. Acoust. **9**, 128 (1963)].
2. V. A. Akulichev, S. I. Penkin, and D. N. Shekhovtsev, in *Proceedings of the 10th International Symposium on Nonlinear Acoustics*, Ed. by Akira Nakamura (Teikohsha, Osaka, 1984), pp. 185–188.
3. V. A. Akulichev and V. I. Il'ichev, in *Proceedings of the International Symposium on Propeller and Cavitation* (Editorial Office of Shipbuilding of China, Shanghai, 1986), pp. 201–205.
4. J. S. M. Rusby, J. Sound Vibr. **13** (3), 257 (1970).
5. V. P. Elistratov and V. L. Korets, in *Proceedings of IX All-Union Acoustical Conference* (Inst. of Acoustics, Moscow, 1977), Sect. D, pp. 77–79.
6. E. A. Neppiras, Ultrasonics **18**, 201 (1980).
7. V. A. Akulichev and V. A. Bulanov, in *Progress in Underwater Acoustics*, Ed. by H. D. Merclinger (Plenum, New York, 1987), pp. 85–92.
8. V. I. Il'ichev, V. P. Elistratov, V. L. Korets, *et al.*, Dokl. Akad. Nauk SSSR **312**, 974 (1990).
9. V. I. Il'ichev, V. P. Elistratov, V. L. Korets, and N. P. Mel'nikov, Dokl. Akad. Nauk SSSR **315**, 206 (1990).
10. V. I. Il'ichev, V. L. Korets, and N. P. Mel'nikov, Dokl. Akad. Nauk SSSR **317**, 458 (1991).
11. V. I. Il'ichev, V. P. Elistratov, V. L. Korets, and N. P. Mel'nikov, Dokl. Akad. Nauk **324**, 458 (1992).
12. V. A. Akulichev, in *Bubble Dynamics and Interface Phenomena*, Ed. by J. R. Blake, J. M. Boulton-Stone, and N. H. Thomas (Kluwer Academic, Dordrecht, 1994), pp. 171–178.
13. V. A. Akulichev, in *Proceedings of the Second International Symposium on Cavitation*, Ed. by H. Kato (Univ. of Tokyo, Tokyo, 1994), pp. 343–348.
14. V. A. Akulichev and V. I. Il'ichev, in *Problems in Continuum Mechanics*, Ed. by V. A. Levin (IAPU DVO RAN, Vladivostok, 1996), pp. 68–79 [in Russian].
15. V. A. Akulichev and V. I. Il'ichev, Vestn. Dal'nevost. Otd. Ross. Akad. Nauk, No. 4, 26 (1997).

Translated by the authors

Active Control of Normal Particle Velocity at a Boundary between Two Media

V. V. Arabadzhi

Institute of Applied Physics, Russian Academy of Sciences, ul. Ul'yanova 46, Nizhni Novgorod, 603950 Russia
e-mail: v.arab@hydro.appl.sci-nnov.ru
Received July 2, 2004

Abstract—A spatially one-dimensional model of a plane active double layer between two homogeneous elastic half-spaces is studied analytically. The layer synthesizes a preset smooth trajectory of the controlled boundary between the media without any mechanical support. The outer layer of the coating is a piezoelectric, and the inner layer is a polymer that is transparent for low-frequency sound and opaque for high-frequency sound because of dissipation. An algorithm for controlling the piezoelectric elements of the layer on the basis of signals from surface particle-velocity sensors is proposed, and a method for measuring the particle velocity is developed. Conditions of stability and efficiency of the synthesis are formulated. It is shown that the active layer thickness can be much smaller than the wavelength corresponding to the minimal time scale of the boundary trajectory to be formed. The accuracy of the trajectory synthesis depends on the accuracy of measuring, computing, and actuating elements of the system but does not depend on the vibroacoustic characteristics of the half-spaces separated by the active layer or on the presence of smooth waves in these half-spaces. For the synthesis to be efficient, the operating frequency band and the dynamic range of sensors and actuators should be many times greater than the frequency band and the dynamic range of the trajectory to be formed. © 2005 Pleiades Publishing, Inc.

INTRODUCTION

Many problems of controlling vibroacoustic fields are reduced to the formation of a preset space–time distribution of normal particle displacements $u_{\otimes}(\vec{r}, t)$ or velocities (DNPV) $\{u_{\otimes}(\vec{r}, t)\}_t$ at the boundary S between two elastic media (or, for instance, at the outer surface S of a closed shell in a liquid, Fig. 1b). One of these media is inside S and has arbitrary vibroacoustic properties. The external medium is supposed to be infinite, homogeneous, and isotropic with a density ρ_w and a sound speed c_w. The zero DNPV corresponds to the solution to the problem of soundproofing and suppression of radiation [1–4]. An arbitrary nonzero DNPV may be, for example, the solution to the problem of the formation of a preset radiation field at the boundary S or the problem of matching the distribution to incident waves (suppression of scattering) [3]. The instrument commonly used for solving such problems is an active piezoelectric layer [4] (Fig. 1c) of a controlled thickness $\ell(\vec{r}, t)$ separating the two media and lying between the outer surface S_V and the inner surface $S_{\overline{V}} = S$. The prescribed DNPV $u_{\otimes}(\vec{r}, t)$ should be created on the outer surface S_V. The solution of the aforementioned problems, as a rule, is complicated by the fact that $u_{\otimes}(\vec{r}, t)$ should be formed in real time, i.e., by knowing only the past and current values of the prescribed DNPV and the degree of its smoothness in

space and time. For this purpose, exhaustive and periodically updated information on the vibroacoustic characteristics of the boundaries $S_{\overline{V}}$ and S_V separated by the layer is needed.

In the simplest case, it may be assumed that the surface $S_{\overline{V}}$ is immobile, i.e., that this surface is in contact with a stationary mechanical support. This suggests that the impedance $Z_{\perp}$ for waves of normal stresses of surface S_V (in the absence of contact with the external medium) is negligible compared to the impedance of
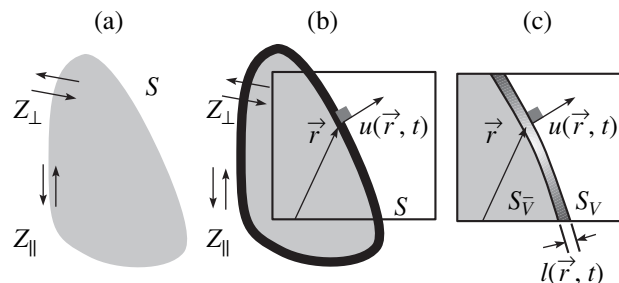
Fig. 1. Geometry of a three-dimensional problem of controlling the DNPV $u(\vec{r}, t)$ (a) on the surface S of a homogeneous elastic body and (b) on a shell surface; $Z_{\perp}$ and $Z_{\parallel}$ are the impedances for waves of normal and tangential stresses of the shell and $\ell(\vec{r}, t)$ is the thickness of the controlled layer.

the external medium, which simplifies the solution [5–7] of noise control problems for, e.g., steel shells in air, when $|Z_\perp| \gg \rho_w c_w$. However, for a steel shell in water, $|Z_\perp| \ll \rho_w c_w$ (Fig. 1b); in this case, the surface $S_{\bar{V}} = S$ cannot play the role of an acoustically rigid mechanical support for the active layer. In addition, under the condition of neutral buoyancy of the shell in the liquid, even a perfect rigidity of the shell does not provide a sufficient support for the active layer. Such a perfectly rigid shell should oscillate under the action of the active layer as a monolithic body whose mass is limited by the condition of neutral buoyancy.

In the general case, it is necessary to determine an integral impedance operator [3] of the surfaces $S_{\bar{V}}$ and S_V, because only in this case is it possible to rigorously formulate the problem of stability and efficiency of the active system. In the cases of practical interest, the volume of required information is so large that the process of learning (or updating the information) for an adaptive control system [8] in many cases lags behind the natural drift of parameters of the boundary-value problem under the effect of changes in temperature, hydrostatic pressure, ageing of materials, and so on. In addition, the linear operator modeling normal-to-surface vibrations of a closed shell disregards the factor of "nonextensibility" of its walls, when the impedance $Z_\parallel$ of waves of tangential stresses on the shell surface is much greater in absolute value than the impedance $Z_\perp$ of waves of normal stresses; i.e., $|Z_\parallel| \gg |Z_\perp|$. This makes the fundamental difference between vibrations of a shell and vibrations of a homogeneous elastic body (Fig. 1a), where $|Z_\parallel| \sim |Z_\perp|$. The smallness of changes in the perimeters of the shell compared to its normal deformations imparts nonlinear properties to the model system and severely complicates the control of its vibrations. As a result, the sound-field control system of interest cannot be based on the interaction with the shell.

CHARACTERISTIC SCALES

A fundamental feature of the approach presented in this paper is the absence of any requirements imposed on the rigidity of the surface $S_{\bar{V}}$ (support) or on any information about its vibroacoustic characteristics [9]. It is required on the surface S_V to form a prescribed DNPV $u_\otimes(\vec{r}, t)$, the spectral power of which is mainly concentrated in the frequency range

$$\omega_{min} \le |\omega| \le \omega_{max}. \tag{1}$$

The DNPV $u_\otimes(\vec{r}, t)$ is characterized by the minimal $\tau_{min} = \pi/\omega_{max}$ and maximal $\tau_{max} = \pi/\omega_{min}$ time scales and by the displacement amplitude $u_\otimes \sim A_w$. The thickness $\ell(\vec{r}, t)$ of the active layer should be much smaller than the wavelength corresponding to the upper boundary of

frequency range (1) and much greater than the displacement amplitude A_w; i.e.,

$$A_w \ll \ell(\bar{r}, t) \ll 2\pi c_w/\omega_{max}. \tag{2}$$

To form the DNPV $u_\otimes(\vec{r}, t)$ on S_V, we use a periodic stepped change of space distributions $u(\vec{r}, t_n) = u_n(\vec{r})$ of normal displacements of surface S_V at the instants $t = t_n = nT$ ($n = 1, 2, \ldots$) with the period

$$T \ll 2\pi/\omega_{max}. \tag{3}$$

The jump like change of distributions $u_n(\vec{r})$ takes place as a result of impact-control actions of duration

$$\tau_c \ll T. \tag{4}$$

Hence, it is necessary to remove the restriction on possible radiation in the range $|\omega| > \omega_{max}$. Thus, we try to minimize the deviation $u - u_\oplus$ of the surface S from the trajectory $u_\otimes$ prescribed in the interval $(-\infty, t)$ (but unknown beforehand) in frequency range (1); i.e.,

$$\int_{|\omega| \in [\omega_{min}, \omega_{max}]} |\tilde{u} - \tilde{u}_\otimes|^2 d\omega \longrightarrow \min,$$

where

$$\tilde{u} = \int_{-\infty}^{+\infty} u(\vec{r}, t)\exp(-i\omega t)dt$$

and

$$\tilde{u}_\oplus = \int_{-\infty}^{+\infty} u_\oplus(\vec{r}, t)\exp(-i\omega t)dt$$

are the spectra of the actual and prescribed trajectories. Beyond range (1), it is sufficient to require that the vibration power be bounded,

$$\int_{|\omega| \notin [\omega_{min}, \omega_{max}]} |\tilde{u} - \tilde{u}_\otimes|^2 d\omega < \infty,$$

to provide for the stability of the system. For the one-dimensional case considered below, this means the formation of a prescribed trajectory of displacement $u(0, t) = u_\otimes(t)$ of a certain plane boundary, the equilibrium position of which corresponds to the point $x = 0$. The time derivative $u(0, t)_t$ of the displacement represents the particle velocity, whose spectrum should be made close to the spectrum of the function $[u_\otimes]_t$ in frequency range (1), while outside this range, it is only restricted by the finiteness of the displacement.

THE BOUNDARY-VALUE PROBLEM

We consider a one-dimensional problem involving the displacements $u(x, t)$ of particles in an elastic medium ($-\infty < x < +\infty$) and assume that these displace-

ments are described by the equation $u_{tt} = c^2 u_{xx}$, where c is the sound speed in the medium. A homogeneous medium with density ρ_w and sound speed c_w corresponds to the domains $x < -h_r - h_c$ and $x > 0$. The intervals $x \in [-h_c, 0]$ and $x \in [-2h_c, -h_c]$ (Fig. 2) are separated by metallized surfaces, electrically independent of one another, and filled with longitudinally polarized piezoelectric with density ρ_c, sound speed c_c, and Young's modulus E_c. The domain $-h_r - h_c < x < -h_c$ is filled with a polymer material (for example, rubber with density $\rho = \rho_r$ and sound speed $c = c_r$) transparent at low frequencies (1) and opaque at high frequencies $|\omega| \gg \omega_{max}$ due to dissipation characterized by the space attenuation factor $\sim \exp[-\alpha_r(\omega)x]$ (where $\alpha_r = \alpha_1 |\omega|^{\alpha_2}$ and $\alpha_1, \alpha_2 = \text{const} \geq 0$). We assume that the boundaries $x = 0$, $x = -h_c$, and $x = -2h_c$ are sound-transparent; i.e.,

$$|\rho_r c_r - \rho_c c_c|/(\rho_c c_c) \ll 1,$$
$$|\rho_w c_w - \rho_c c_c|/(\rho_c c_c) \ll 1, \quad \alpha_r(\omega_h) \ll \omega_h/c_r, \quad (5)$$

where $\omega_h = \pi/T \gg \omega_{max}$. Some polymer piezoelectric materials have impedances close to the impedance of water [10]. The impedances of various types of rubber may also vary over wide limits. The points $x = -h_r - h_c$ and $x = 0$ are the one-dimensional analogs of surfaces $S_{\bar{V}}$ and S_V, and the quantity $(2h_c + h_r)$ is the analog of the active layer thickness $\ell(\vec{r}, t)$.

A RECTANGULAR ELECTRIC PULSE

If, in the absence of incident waves, a constant electric voltage φ_0 is applied to one piezoelectric layer (for instance, to $x \in [-h_c, 0]$) of thickness h_c, then the surface (along the plane $x = 0$) energy density of mechanical deformation

$$W_{mech} = E_c h_c^{-1} \psi^2(\infty)/2$$

and the surface density of electrostatic energy

$$W_{e\ell} = \varepsilon_0 \varepsilon_c h_c^{-1} \varphi_0^2/2$$

are connected by the electromechanical coupling coefficient $\eta = W_{mech}/W_{e\ell}$ characterizing this piezoelectric material (typically, $\eta \sim 0.2$–0.7), where ε_c is the relative dielectric permittivity of vacuum and ε_0 is the value of static (compression–tension) deformation of the layer $x \in [-h_c, 0]$ of thickness h_c. For $\psi(\infty)$, we obtain the expression $\psi(\infty) = (\varepsilon_0 \varepsilon \eta/E_c)^{1/2} \varphi_0$, which is independent of the layer thickness. With fixed layer boundaries $x \in [-h_c, 0]$, we obtain the relationship $P(\infty) = \mu_c \varphi_0$ between the piezoelectric pressure $P(\infty)$ and the applied voltage φ_0, where $\mu_c = h_c^{-1} (\varepsilon_0 \varepsilon \eta E_c)^{1/2}$. Now, we assume that, during the time interval $t \in [0, \tau_c]$ and in the absence of incident waves, the electric voltage
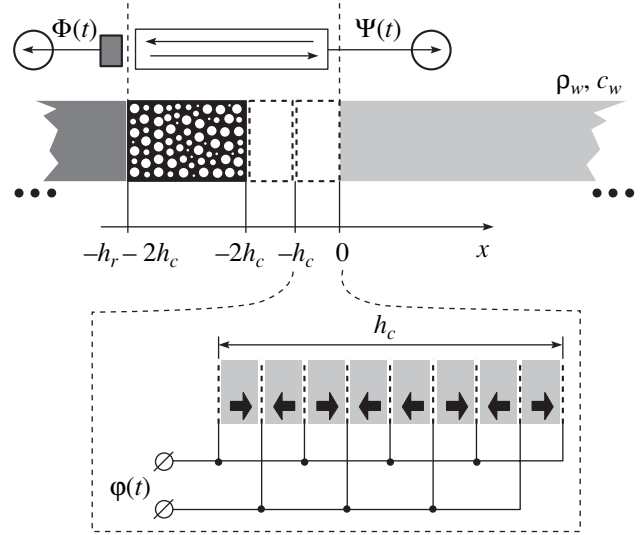

Fig. 2. Modification of the boundary-value problem with piezoelectric layers $-h_c \leq x \leq 0$ and $-2h_c \leq x < -h_c$ in the form of an echelon of thin layers with opposite polarization and metallized boundaries electrically connected in parallel.

$\varphi(t) = \varphi_0 U(t)$ is applied to the layer $x \in [-h_c, 0]$, where $U(t) = 1$ for $t \in [0, \tau_c]$, $U(t) = 0$ for $t \notin [0, \tau_c]$, and φ_0 is the pulse amplitude. Due to the symmetry of the boundary-value problem, the displacements $u(0, t)$ and $u(-h_c, t)$ of the boundaries $x = 0$ and $x = -h_c$ are connected by the relation $u(0, t) = -u(-h_c, t) = \psi(t)$ at $\psi(0) = 0$. If, within the time τ_c of action of the electric pulse, the displacement $\psi(t)$ of the boundaries of the segment $x \in [-h_c, 0]$ is much smaller than the static limit, i.e., $|\psi(\tau_c)|/|\psi(\infty)| \ll 1$, then the action of all piezoelectric layers is equivalent to pressure (compression or tension). This pressure is instantaneously (with the light velocity) and uniformly distributed over the segment $x \in [-h_c, 0]$ and is equal to zero outside it. According to the Euler equation for a continuous medium, the particles are subjected to a force proportional to the gradient of this pressure. Therefore, the boundary-value problem is reduced to a simultaneous impact action of pressure $P(t) = \mu_c \varphi(t)$ on the boundary $x = -h_c$ and pressure $-P(t) = \mu_c \varphi(t)$ on the boundary $x = 0$. In this case, the boundary displacement $\psi(t)$ for $0 \leq t \leq \tau_c$ is described by the integral

$$\psi(t) = (z_w/2)^{-1} \int_0^t P(\xi) d\xi,$$

which yields the "plasticity" of the boundaries $x = -h_c$ and $x = 0$ with respect to short pulses (impacts) of local pressure: after termination of the pulse $P(t)$, the displacement of every boundary under the effect of the pulse persists until the arrival of waves from the other boundary. Below, we assume that the duration of the electric pulses satisfies the condition

$$\tau_c \ll h_c/c_c. \quad (6)$$
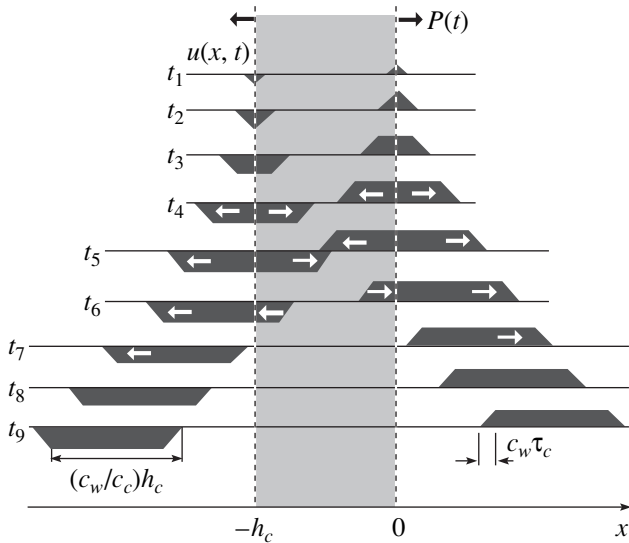
Fig. 3. Instantaneous distributions of the particle displacements $u(x, t)$ in the medium at the instants $0 < t_1 < t_2 < t_3 < t_4 < 2^{-1}h_c c_c^{-1}$, $t_5 = 2^{-1}h_c c_c^{-1}$, $2^{-1}h_c c_c^{-1} < t_6 < h_c c_c^{-1}$, and $h_c c_c^{-1} < t_7 < t_8 < t_9$ under the effect of one voltage pulse of duration $\tau_c \ll h_c c_c^{-1}$.

Transient processes (and proper time scales) do not manifest themselves in this system because of condition (3) of the transparency of the boundaries $x = 0$, $x = -h_c$, and $x = -2h_c$.

Figure 3 shows the spatial distributions $u(x, t)$ of particle displacements in the medium under the effect of a single short (see relation (6)) pulse of electric volt-age $\varphi(t)$ within the interval $x \in [-h_c, 0]$ at various instants of time.

A HUYGENS SOURCE

In the section concerning the scales, the formation of the trajectory $u(0, t) = u_{\otimes}(t)$ of the boundary $x = 0$ was assumed to occur within the time $\sim T \ll 2\pi/\omega_{max}$ in the absence of interaction of the active layer with the underlying surface $S_{\bar{V}}$ (support) or with the boundary $x = -h_r - 2h_c$. Therefore, below, we will try to find the shortest time combination of the voltages $b\bar{\varphi}(t)$ and $b\bar{\bar{\varphi}}(t)$ (Fig. 4b) applied to the piezoelectric layers $x \in [-h_c, 0]$ and $x \in [-2h_c, -h_c]$ (Fig. 4a) that provides a zero field $u(x, t) = 0$ in the domain $x < -2h_c$ and a nonzero field $u(x, t) \neq 0$ in the domain $x > 0$ for any coefficients b. We confine the class of desired voltages $\bar{\varphi}_B(t)$ and $\bar{\bar{\varphi}}_B(t)$ to rectangular pulses

$$\bar{\varphi}_B(t) = \bar{b}\varphi_0 U(t - \bar{\tau}), \quad \bar{\bar{\varphi}}_B(t) = \bar{\bar{b}}\varphi_0 U(t - \bar{\bar{\tau}})$$

of duration τ_c satisfying condition (4). Now, it is easy to make certain that the above-mentioned goals can be achieved only for $\bar{\bar{\tau}} - \bar{\tau} = h_c/c_c = \tau_V$ and $\bar{b} = -\bar{\bar{b}}$, as is shown in Fig. 4a. Trying to provide for $u = 0$ in the domain $x < -2h_c$, we obtain a unique combination of delays $\bar{\tau}$, $\bar{\bar{\tau}}$ and amplitudes $\bar{b}$, $\bar{\bar{b}}$, which, in turn, produces a bipolar rectangular wave of displacements propagating rightward in the domain $x > 0$:

$$u(x, t) = \psi_B[t - (x/c_w)].$$
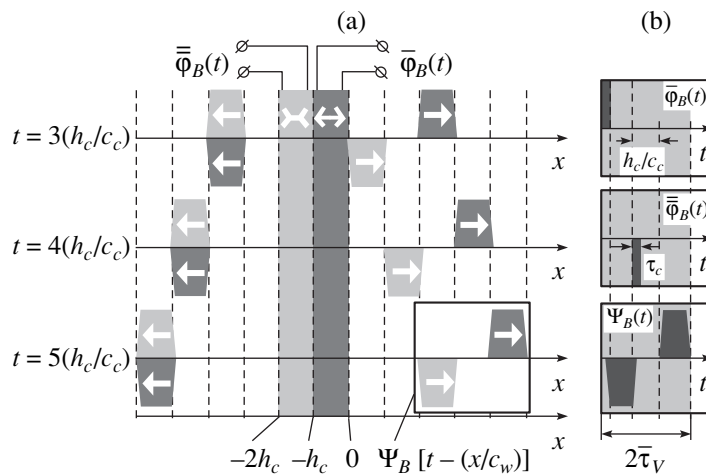
Fig. 4. (a) Instantaneous spatial distributions of particle displacements in the medium under the effect of piezoelectric layers: black pulses are produced by the voltage $\bar{\varphi}_B(t)$ across the layer $x \in [-h_c, 0]$, and gray pulses are produced by the voltage $\bar{\bar{\varphi}}_B(t)$ across the layer $x \in [-2h_c, -h_c]$; (b) diagrams of the base voltage pulses $\bar{\varphi}_B(t)$ and $\bar{\bar{\varphi}}_B(t)$ and of the base pulse $\psi_B(t)$ of mechanical displacement $u(0, t)$ of the boundary $x = 0$.

Here, $\psi_B(t)$ is characterized by the following properties:

    (i) $\psi(t) = 0$ for $t < 0$;

    (ii) $\psi_B(t) = \text{const} > 0$ for $0 < t \le \tau_V$;

    (iii) $\psi_B(t) = 0$ for $\tau_V < t \le 2\tau_V$;

    (iv) $\psi_B(t) = \text{const} < 0$ for $2\tau_V < t \le 3\tau_V$;

    (v) $\psi_B(t) = 0$ for $t > 3\tau_V$, where $\tau_V = h_c/c_c$.

The function $\psi_B(t)$ also satisfies the integral relations

$$\int_0^{\tau_V} \psi_B(t)dt = +\psi_0\tau_V, \quad \int_{2\tau_V}^{3\tau_V} \psi_B(t)dt = -\psi_0\tau_V$$

inside the finite interval $0 < t \le 3\tau_V$, and, outside this interval, it equals zero. The functions $\bar{\varphi}_B(t)$ and $\bar{\bar{\varphi}}_B(t)$ satisfy the relation

$$\int_0^{\tau_c} \bar{\varphi}_B(t)dt = -\int_{\tau_V}^{\tau_V + \tau_c} \bar{\bar{\varphi}}_B(t)dt = \varphi_0\tau_c,$$

where $\varphi_0 = 2\rho_w c_w \tau_c^{-1} \mu_c^{-1} \psi_0$. The system described above represents a pulsed version of a classical Huygens wave source [1, 2] characterized by one-sided radiation with the sound energy concentrated at the jumps of the function ψ_B. The equality

$$\int_{-\infty}^{+\infty} \psi_B(t)dt = \int_0^{3\tau_V} \psi_B(t)dt = 0 \qquad (7)$$

is a consequence of the momentum conservation law for the medium of wave propagation. Note that the wave radiated only to the right (a wavelet [11]) $\psi_B[t - (x/c_w)]$ of minimal duration $3\tau_V$ necessarily has a pause τ_V between the maxima of different polarities.

It is important to note that, in the effect of one-sided radiation, a role of fundamental significance is played by the wave deformations of the layers $x \in [-h_c, 0]$ and $x \in [-2h_c, -h_c]$. For example, in the case of $\rho_c c_c \gg \rho_w c_w$ (unlike relations (5)), the layers $x \in [-h_c, 0]$ and $x \in [-2h_c, -h_c]$ are perfectly rigid bodies, into which no waves penetrate from the external medium ($x < -2h_c$, $x > 0$). Such bodies (layers) have the given thicknesses $d(t) = |u(-2h_c, t) - u(-h_c, t)|$ and $\bar{d}(t) = |u(-h_c, t) - u(0, t)|$ and a common boundary $u(-h_c, t)$. In this case, none of the combinations of the functions $\bar{d}(t)$ and $\bar{\bar{d}}(t)$ can provide the desired effect of one-sided radiation.

BASE PULSES

As was shown above, in the absence of incident waves, the displacement $u(0, t) = \psi_B(t)$ of the boundary $x = 0$ is a result of the action of the voltage pulses $\bar{\varphi}_B(t)$ and $\bar{\bar{\varphi}}_B(t)$ connected by the relation

$$\bar{\bar{\varphi}}_B(t) = -\bar{\varphi}_B(t - \tau_V) \qquad (8)$$

and applied to the layers $x \in [-h_c, 0]$ and $x \in [-2h_c, -h_c]$. Now, we represent the current voltages

$$\bar{\varphi}(t) = \sum_n B_n\bar{\varphi}_B(t - nT), \quad \bar{\bar{\varphi}}(t) = \sum_n B_n\bar{\bar{\varphi}}_B(t - nT) \ (9)$$

across the layers $x \in [-h_c, 0]$ and $x \in [-2h_c, -h_c]$ as a sum of base voltage, pulses $\bar{\varphi}_B(t)$ and $\bar{\bar{\varphi}}_B(t)$, where $T = 2\tau_V$ is the pulse repetition period. The current displacement of the controlled boundary $x = 0$,

$$\psi(t) = u(0, t) = \sum_n B_n\psi_B(t - nT), \qquad (10)$$

is represented as a sum of base pulses of displacement $\psi_B(t)$. The coefficients B_n of expansions (9), (10) (or the amplitudes of pulses $\bar{\varphi}_B$, $\bar{\bar{\varphi}}_B$, and ψ_B) are determined by the control algorithm.

THE ALGORITHM FOR CONTROLLING THE BOUNDARY PROBLEM

The purpose of the algorithm for controlling the piezoelectric layers is the synthesis of the prescribed trajectory $u_\otimes(t)$ of displacement of the boundary $x = 0$ on the basis of a sequence of bipolar antisymmetric pulses $\psi_B(t)$ with the left third part of every subsequent pulse being superimposed on the right third part of every preceding pulse. The novelty of the proposed approach is determined by the fact that, usually, the prescribed trajectory is approximated by a sequence of nonoverlapping pulses with nonzero mean value of every pulse (for example, by a sequence of delta-pulses), whereas, in the algorithm described below, intersecting (Figs. 5a–5c) bipolar base pulses with zero mean (see Eq. (7)) are used to synthesize the prescribed trajectory.

The algorithm averages the difference $u(0, t) - u_\otimes(t)$ between the desired $u_\otimes(t)$ and actual $u(0, t)$ displacements of the boundary $x = 0$ over the time interval $t \in [\tau_V(n - \Im), \tau_V n]$ and tends to compensate for this error signal on the average within the interval $t \in [nT, (n + 1)T]$. For this purpose, at the instant $t = nT$, the algorithm begins to generate the base pulse $\psi_B(t - nT)$ of displacement of the boundary $x = 0$ with the amplitude

$$B_n = (\psi_0 T_V/2)^{-1} \int_{\tau_V n - T_V}^{\tau_V n} \hat{F}^\varepsilon [u_\oplus - u_\otimes]dt, \qquad (11)$$

where $\hat{F}$ is the operator of action of one differentiating network (see below), ε is a positive integer (see inequality (16)), $u_\oplus(t)$ is the measured displacement of the boundary $x = 0$, $u_\otimes(t)$ is the prescribed trajectory of the boundary $x = 0$, $\psi_0 = \tau_V^{-1}\int_0^{\tau_V} \psi_B(t)dt$, and T_V is the duration of the interval of averaging.
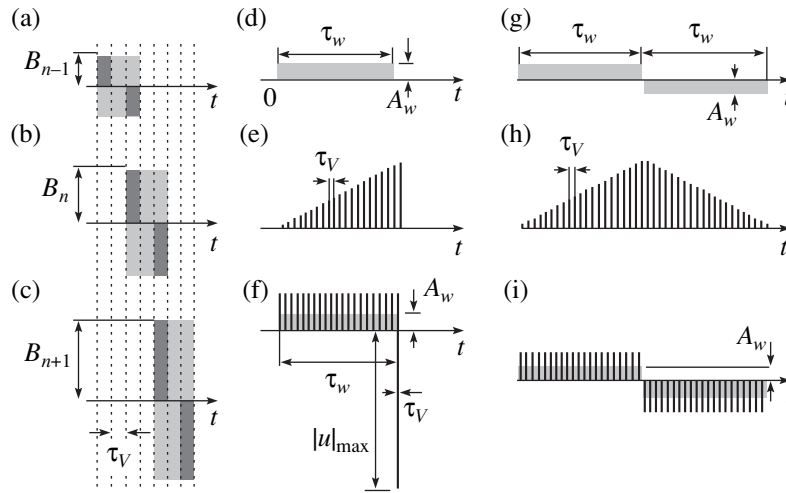
Fig. 5. Examples of synthesis of the prescribed displacement trajectory of the boundary $x = 0$ by means of controlling the amplitudes B_n of sequence (10) of base pulses at zero noise and $\Im = 1$:

(a), (b), (c) successive superposition in time of the base pulses $\psi_B(t)$ with the amplitudes B_{n-1}, B_n, B_{n+1};

(d) the desired displacement $u_\otimes(t)$ with a nonzero mean value;

(e) amplitudes B_n of sequence (10) of the base pulses $\psi_B(t)$ that approximates the prescribed displacement $u_\otimes(t)$ of the boundary $x = 0$;

(f) the resulting displacement $u(0, t)$ of the boundary $x = 0$;

(g) the desired displacement $u_\otimes(t)$ with a zero mean value;

(h) amplitudes B_n of sequence (10) of the base pulses $\psi_B(t)$ that approximates the prescribed displacement $u_\otimes(t)$ of the boundary $x = 0$; and

(i) the resulting displacement $u(0, t)$ of the boundary $x = 0$.

STABILITY OF THE SYSTEM

Let us formulate the stability condition for a damping system to prevent the unlimited growth of the impact amplitude. The origin of instability may be both internal (connected with the compensation for the system's own inevitable random errors) and external (connected with the special features of the synthesized trajectory $u_\otimes(t)$ preset from outside).

(i) *Internal source of instability.* We assume that, for a zero preset displacement $u_\otimes(t) = 0$, one "wrong" base pulse of displacement $\psi_B(t)$ with the amplitude $\xi_1 \neq 0$ accidentally appears at the instant $t = 0$; then, algorithm (11) tends to provide for $u(0, t) = 0$. Sequence of pulses (9), which serves to compensate for the disturbance of the form $\xi_1\psi_B(t)$ according to algorithm (11), has the amplitude distribution

$$B_n(\xi_1) = \xi_1(\psi_0\Im/2)^{-1}(-1)^n\Im^{-n}, \qquad (12)$$

where $\Im = T_V/(3\tau_V) = 1, 2, 3, \ldots$. From Eq. (12) it follows that, for

$$\Im \geq 1, \qquad (13)$$

the conditions $\lim_{n \to \infty} |B_n| = 0$ and $\lim_{n \to \infty} \sum_{k=1}^{n} |B_k| < \infty$ are satisfied and the system is stable. The value of the averaging interval being a multiple of $3\tau_V$ is needed for the most efficient suppression of the oscillating component in the error signal $u_\oplus - u_\otimes$.

(ii) *External source of instability.* Assume that noise in the system is absent, $\Im = 1$, and $u_\otimes(t) \neq 0$. The time average value of every base pulse $\psi_B(t - nT)$ equals zero. Then, for the synthesis of a constant displacement A_w (Fig. 5d), during the characteristic maximum interval $\tau_{max} = \pi/\omega_{min}$ of sign constancy of the function $u_\otimes(t)$, the amplitude of base pulses B_n should increase linearly from $A_w\psi_0^{-1}$ at $t = 0$ to

$$(B_n)_{max} = (1 + \tau_{max}\tau_V^{-1})A_w\psi_0^{-1} \qquad (14)$$

at $t = \tau_{max}$ (see Fig. 5e). In addition, after the termination of algorithm (10), (i.e., at $B_n = 0$ and $t > \tau_{max}$), a powerful reverse displacement (Fig. 5f) of the boundary with the amplitude

$$|u(0, \tau_{max} + \tau_V)|_{max} = |B_n|_{max}\psi_0$$
$$= (1 + \tau_{max}\tau_V^{-1})A_w \gg A_w \qquad (15)$$

is inevitable.

The large amplitude of reverse displacement is caused by the necessity of obtaining the zero value of the integral $\int_0^{\tau_{max} + \tau_V} u(0, t)dt = 0$, where the function $u(0, t)$ consists of the pulses $\psi_B(t - nT)$ with zero mean in time. The presence of a nonzero constant component in the signal $u_\otimes(t)$ is equivalent to the tendency $\tau_{max} \longrightarrow \infty$ and, correspondingly, $|u(0, \tau_{max} + \tau_V)|_{max} \longrightarrow \infty$ and

$|B_n|_{max} \longrightarrow \infty$, which implies instability of the system. Figures 5d–5f illustrate the incorrectness of the synthesis of a function with nonzero mean using the function combination $\psi_B(t-nT)$ (Fig. 5d) with a zero time-averaged value. Figures 5d–5f also show the process of synthesis of the trajectory $u_\otimes(t)$ with a zero mean value by algorithm (11). In this case, the result of synthesis (Fig. 5i) and the sequence of amplitudes B_n (Fig. 5h) of base pulses are fully adequate to the stated problem. The prescribed rectangular trajectories $u_\otimes$ shown in Fig. 5 are not smooth (as was supposed above) but, all the more, they demonstrate the efficiency of algorithm (11). For $\tau_V \ll \tau_{min}$, the amplitude of the nth base pulse may be approximately evaluated as

$$B_n \approx (\psi_0 \tau_V/2)^{-1} \int_0^{\tau_V n} u_\otimes(t)dt,$$

which yields an unlimited increase in B_n with $n \longrightarrow \infty$. Therefore, for stability of the system (or, for the finiteness of the quantities $|B_n| < \infty$ and $|u(0, t)| < \infty$), it is necessary to exclude a constant component from the signal $u_\oplus(t) - u_\otimes(t)$. For this purpose, it is sufficient at the input of algorithm (11) to insert

$$\varepsilon \geq 1 \qquad (16)$$

series-connected differentiating RC networks with a time constant $\tau_D \gg \tau_{max}$, which are described by the operator $\hat{F}$ (see Eq. (11)). Such networks with large time constants suppress the Fourier components in the error signal $u_\oplus(t) - u_\otimes(t)$ in a narrow frequency band $|\omega| < 2\pi/\tau_D$ near the zero frequency but do not distort the signal at the frequencies $2\pi/\tau_D \ll |\omega| < \omega_{min}$. As was mentioned above (see relation (1)), we consider the trajectories $u_\otimes(t)$ with a zero power at zero frequency.

Estimates (14) and (15) of the quantities $(B_n)_{max}$ and $|u(0, \tau_{max} + \tau_V)|_{max}$ imply stronger requirements on the dynamic range of compression (expansion) of the piezoelectric material. However, if, instead of one homogeneous piezoelectric layer of thickness h_c, we use an echelon (Fig. 2) of $N_c \gg 1$ layers that have a thickness h_c/N_c and opposite polarizations and are electrically connected in parallel, then, their static expansion (compression) under the action of the same voltage will be N_c times greater. This is possible because the absolute value of linear expansion (compression) of a piezoelectric is proportional to the applied electric voltage but does not depend on the layer thickness. However, in this multilayer piezoelectric system, the recharging current is greater by a factor of N_c.

THE EFFICIENCY OF CONTROL

If conditions (13) and (16) determining the stability of the system are satisfied, the efficiency of the system is characterized by the closeness of the measured coordinate $u_\oplus(t)$ of the displacement of the boundary $x = 0$

to the prescribed trajectory $u_\otimes(t)$. We take into account such disturbing factors as the following: (i) random noise (an additive factor) with the relative value $\delta_1 \ll 1$ in measuring and actuating units of the system and (ii) hardware distortions (a multiplicative dynamic factor) with the relative value $\delta_2 \ll 1$ in measuring and actuating units.

(i) *Random noise.* We consider a sequence of "improper" (to be suppressed by the algorithm) pulses $\xi_n \psi_B(t - nT)$ with the random amplitudes ξ_n, where $-\infty < n < +\infty$. We assume that the amplitudes ξ_n have a zero mean value $\langle \xi_n \rangle = 0$ and are uncorrelated; i.e., $\langle \xi_n \xi_m \rangle = \chi^2 \delta_{nm}$, where $\chi = const > 0$, $\delta_{nm} = 0$ for $n \neq m$, and $\delta_{nm} = 1$ for $n = m$. Every nth pulse beginning at the instant $t = nT$ generates a sequence $\sum_{m=n}^{\infty} B_m (\xi_n) \psi_B(t - mT)$ of compensating base pulses with the coefficients $B_m(\xi_n) = \xi_n(\psi_0 \Im/2)^{-1}(-1)^m \Im^{-m}$ ($m = 0, 1, 2, \ldots$) (see Eq. (12)). Then, we obtain the estimate of total average noise power $\langle \psi^2(\tilde{t}) \rangle = (1 - \Im^{-2})^{-1}\chi^2$ of the trajectory $u(0, t)$ at the instant $\tilde{t}$ due to the random errors ξ_n of amplitudes of the base pulses started at the instants $-\infty < t < \tilde{t}$ without taking into account the averaging over the interval $\tilde{t} - T_V < t < \tilde{t}$. With allowance for the interval T_V of time averaging in algorithm (11), the relative noise error δ_1 of the trajectory synthesis is

$$\delta_1 \leq (1 - \Im^{-2})^{-1/2} \Im^{-1/2} \delta_\oplus \ll 1,$$

where $\delta_\oplus = \chi/A_w \ll 1$ is the total relative error of measuring and actuating units of the system (see the next section).

(ii) *Hardware distortions.* With the increase in T_V (or $\Im$), the noise error δ_1 decreases, but the relative inertial dynamic distortion $\delta_2 \approx T_V/\tau_{min} \ll 1$ of the trajectory $u_\otimes(t)$ grows. If both δ_1 and δ_2 are small, then the total relative error $[\delta_\Sigma]$ of the synthesis can be represented as the sum $\delta_\Sigma \approx \delta_1 + \delta_2$. An increase in T_V leads to a decrease in δ_1 and an increase in δ_2. Then, there is a certain value of T_V for which $(\delta_\Sigma)_{T_V} = 0$ and δ_Σ is minimal.

MEASUREMENT OF THE COORDINATE OF THE CONTROLLED BOUNDARY

We represent the measured coordinate $u_\oplus(t)$ of the boundary $x = 0$ in the form

$$u_\oplus = \Psi(t) + \int_0^t d\zeta \int_0^\zeta \Phi(\xi)d\xi,$$

where $\Phi(t) \sim M\{u(-2h_c - h_r, t)\}_{tt}$ is the signal of an inertial accelerometer with a mass M (Fig. 2) and with a sensing element located at the point $x = -2h_c - h_r$; $\Psi(t) \sim u(0, t) - u(-2h_c - h_r, t)$ is the signal of the sensor measuring the distance between the boundaries $x = -2h_c - h_r$ and $x = 0$ (for instance, a miniature optical

interferometer). A rather large mass of the inertial body of the accelerometer provides for its sensitivity to a relatively weak slow signal $\Phi(t)$. A powerful component of the signal $u_\oplus(t)$ at technological frequencies cannot be represented adequately by the accelerometer because of the propagation of sound waves in its inertial body. However, the source of high-frequency radiation is positioned at the point $x = -2h_c$ at a distance h_r from the accelerometer and, owing to the high-frequency attenuation factor

$$\delta_A = \exp[-\alpha(\pi/\tau_V)h_r] \ll 1, \tag{17}$$

influences the signal $\Phi(t)$ much less than $u_\otimes(t)$. Condition (17) is compatible with smallness (2) of the active layer thickness

$$\ell = h_r + 2h_c \ll c_w\tau_{\min}$$

only when

$$h_r \gg c_r\tau_V.$$

It is easy to see that neither the inertial accelerometer nor the optical interferometer taken separately can provide the measurement of displacement of the boundary $x = 0$ relative to the inertial reference system in such a wide frequency band and in the absence of a mechanical support.

CONCLUSIONS

We considered a one-dimensional system consisting of piezoelectric layers $x \in [-h_c, 0]$, $x \in [-2h_c, -h_c]$ and a layer of a high-frequency absorbing polymer in a homogeneous elastic isotropic medium occupying the regions $x < -2h_c - h_r$ and $x > 0$. The boundaries $x = 0$, $x = -h_c$, and $x = -2h_c$ were assumed to be transparent to sound.

The minimal-duration configuration of voltage pulses $\bar{\varphi}_B(t)$ and $\bar{\bar{\varphi}}_B(t)$ applied to the layers $x \in [-h_c, 0]$ and $x \in [-2h_c, -h_c]$ is determined, for which the field at the left (for $x < -2h_c - h_r$) is absent and, at the right (for $x > 0$), a wave (wavelet) of particle displacements $u(x, t) = \psi_B[t - (x/c_w)]$ propagates in the medium with an amplitude proportional to the amplitude of the electric pulses $\bar{\varphi}_B$ and $\bar{\bar{\varphi}}_B$. The function $\psi_B(t)$ has the duration $3h_c/c_c$ and consists of two rectangular pulses of different polarity and the same duration h_c/c_c separated by a pause of the same length h_c/c_c. The momentum conservation law for the medium in the absence of the field at the left determines the zero mean value of this wave.

A wavelet approximation of the prescribed smooth trajectory $u_\otimes(t)$ of the boundary $x = 0$ by bipolar pulses $B_n\psi_B(t - nT)$ of displacement with a repetition period $T = 2h_c/c_c$ $(n = 1, 2, \ldots)$, which are produced by the corresponding sequence of electric pulses $B_n\bar{\varphi}_B(t - nT)$ and $B_n\bar{\bar{\varphi}}_B(t - nT)$, is considered. Every pulse of the sequence is partially superimposed on the preceding one.

A control algorithm determining the amplitudes B_n of the pulses $\psi_B(t - nT)$ on the basis of the error signal measurement within the preceding time interval T_V is formulated. It is shown that, for stability of the synthesis, it is necessary to do the following: (a) to average the error signal over the interval T_V that is a multiple of the duration $3h_c/c_c$ of the function $\psi_B(t)$ (to suppress the oscillatory component) and (b) to eliminate the zero frequency from the error signal. The accuracy of the trajectory synthesis is evaluated.

A technique for measuring the displacement of the boundary $x = 0$ with respect to an inertial reference system in a wide frequency range in the absence of mechanical support is suggested.

The system of synthesis of a prescribed trajectory of a controlled boundary is a version of a Huygens source [1, 2]; it has the form of a thin continuous active coating on the protected surface and is considered in the temporal (pulse) representation.

REFERENCES

1. *Active Methods of Acoustic Field Control (Based on Huygens Surfaces)* (TsNII Rumb, Moscow, 1982) [in Russian].

2. A. I. Boĭko and V. V. Tyutekin, Akust. Zh. **50**, 5 (2004) [Acoust. Phys. **50**, 1 (2004)].

3. Yu. I. Bobrovnitskiĭ, Akust. Zh. **49**, 731 (2003) [Acoust. Phys. **49**, 620 (2003)].

4. T. R. Howart, V. K. Varadan, X. Bao, and V. V. Varadan, J. Acoust. Soc. Am. **91**, 823 (1992).

5. J. B. Fahnline and G. H. Koopmann, J. Acoust. Soc. Am. **100**, 3539 (1996).

6. S. J. Elliott, P. Gardonio, T. Sors, and M. J. Brennan, J. Acoust. Soc. Am. **111**, 908 (2002).

7. P. Gardonio, Y.-S. Lee, S. J. Elliott, and S. Debost, J. Acoust. Soc. Am. **110**, 3025 (2001).

8. B. Widrow, IEEE Trans. Antennas Propag. **24**, 615 (1976).

9. V. V. Arabadzhi, J. Low Freq. Noise Vibr. Active Control **16** (2), 89 (1997).

10. H. Kawai, Jpn. J. Appl. Phys., No. 8, 975 (1969).

11. I. Daubechies, *Ten Lectures on Wavelets* (Society for Industrial and Applied Mathematics, Philadelphia, 1992; RKhD, Moscow–Izhevsk, 2001).

Translated by A. Svechnikov

Nonlinear Generation of Airborne Sound by Waves of Ultrasonic Frequencies

N. S. Vinogradov, M. S. Dorofeev, A. I. Korobov, S. G. Mikhaĭlov, O. V. Rudenko, A. V. Shanin, and A. O. Shilkin

Faculty of Physics, Moscow State University, Vorob'evy gory, Moscow, 119992 Russia
e-mail: rudenko@acs366.phys.msu.ru
Received September 22, 2004

Abstract—The results of research into the design and optimization of laboratory sources of intense airborne ultrasound are reported. Two types of sources are studied: multielement arrays of small-size piezoelectric radiators and single membrane transducers of a capacitor type. The measured characteristics of the ultrasound fields and the audible sound fields generated in air due to the nonlinear interaction of high-frequency waves are presented. Applications of nonlinear acoustic problems in air are discussed. © *2005 Pleiades Publishing, Inc.*

INTRODUCTION

Ideas about the possibility of a directional low-frequency radiation caused by the interaction of intense high-frequency waves and the possibility of receiving low-frequency signals modulating an intense high-frequency beam were put forward by V.A. Zverev (together with A.I. Kalachev) and P. Westervelt more than 40 years ago. The history of these ideas and their experimental verification and implementation in the original devices was described by Zverev in a historic essay under the title "How the Idea of a Parametric Acoustic Array Was Conceived" [1].

Parametric arrays operating in a fluid were studied in detail and, owing to their unique characteristics, have found wide application in underwater acoustics [2]. Arrays operating in air [3–7] appeared later than their underwater analogs and could not find wide application for a long time. Presumably, this was related to the fact that nonlinear problems of airborne acoustics were not as topical (at that time) and, hence, the development of sources of intense coherent airborne ultrasound was of no particular interest.

Today, interest in the problem of nonlinear radiation of airborne sound has quickened in connection with some applications. These primarily include the possibility of detecting inhomogeneities in the atmosphere by sounding the latter with a narrow-beam sound signal of tunable frequency [3, 4]. Considerable interest is also being expressed in "parametric" loudspeakers [5–7], which produce unusual acoustic effects (e.g., selectively transmit a speech signal to an individual listener or form a moving localized source of sound) and offer commercial success to the designers of the corresponding audio systems. The advantages of parametric microphones are described in [1].

From our point of view, the use of intense sources of narrow-beam sound and ultrasound offers considerable promise for acoustic diagnostics and nondestructive testing. As is known, the ratio of the energy flux through a boundary between gas and a condensed medium to the incident energy flux is fairly small: about 10^{-3}–10^{-4} (see, e.g., [8]). This means that, for a reliable detection of the scattered signal in the remote nondestructive testing of solid articles, it is necessary to use high-intensity ultrasound. In this case, the signal may have a combination frequency and originate from a structural inhomogeneity (e.g., near the tip of an internal crack, whose vicinity is characterized by strongly nonlinear properties [9]). The use of such narrow-beam tunable sources as parametric radiators provides the possibility to determine the frequency response of a scattering inhomogeneity. In addition, one can selectively excite specific types of vibrations, for example, Lamb waves or Brillouin modes, in a plane-parallel plate by irradiating it with a narrow beam incident under a certain angle to the surface [10, 11].

ANTENNA ARRAYS

In view of the aforementioned applications, we developed multielement antenna arrays for the excitation of intense airborne ultrasound.

Each array consisted of small-size radiators represented by stock-produced radio-electronic devices. The active element of each of these devices was a bimorph piezoelectric plate 10.6 mm in diameter. At the center of each plate, where the displacement was maximal, a conic horn made of a light metal with a diameter of 7 mm was welded to provide a better matching with air. The whole structure was placed in a cylindrical casing and emitted radiation through the end of the cylinder, which was closed by an acoustically transparent net.

The measured amplitude–frequency response of a single radiator is shown in Fig. 1. The frequency depen-

P, dB
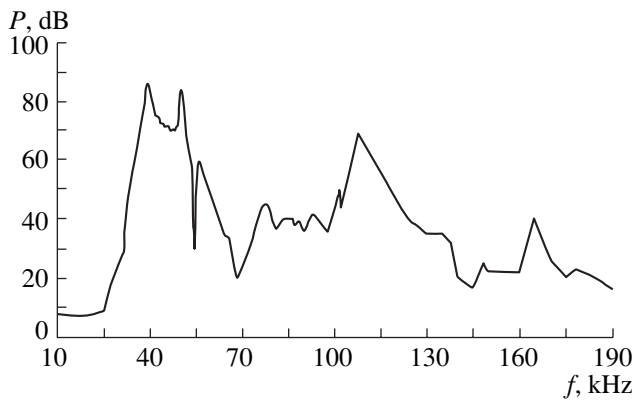
Fig. 1. Amplitude–frequency response of a single radiator.
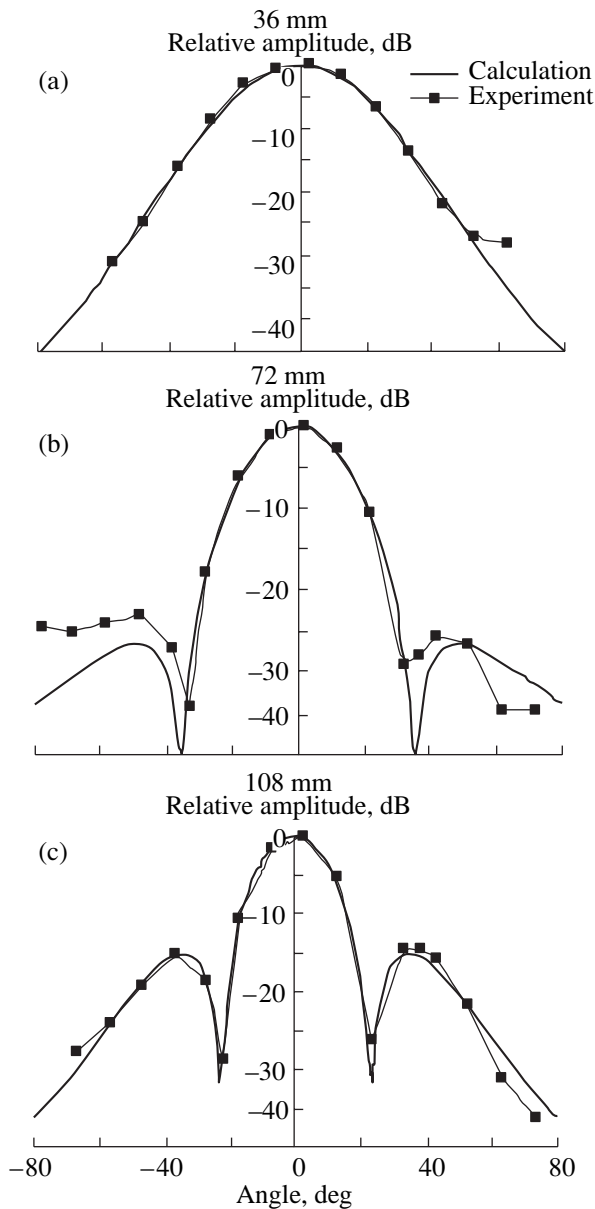
Fig. 2. Directional patterns of two vertical rows of small-size radiators for different distances between the rows: (a) 36, (b) 72, and (c) 108 mm. The difference frequency is 4 kHz.

dence of the acoustic pressure level exhibits many resonance maxima. The highest of them is observed at a frequency of 39 850 Hz. Therefore, we choose the operating frequencies in the vicinity of 40 kHz with the aim of providing for an efficient generation of ultrasonic waves and, hence, of nonlinear signals in the audible frequency range. The radiator operated in the linear mode when the amplitudes of the alternating voltage supplied to it varied from 1 to 20 V. At the maximum voltage of 20 V, the ultrasound level measured at a distance of 30 cm was 120 dB.

In the first series of experiments, the frame of the array was a rectangular fabric-based laminate plate, in which holes were drilled to fix the small-size piezoelectric radiators. On this plate, it was possible to mount 49 radiators forming a 7×7 square pattern. In this case, the radiators were almost immediately adjacent to each other, with the distance between their centers being equal to 18 mm. The experiments were carried out with an array completely filled with radiators and also with an array containing only two vertical rows of seven radiators each. In the latter case, the rows were spaced at different distances from each other, specifically, from 18 to 108 mm.

The signal supplied to the radiators of the array was a two-frequency one formed as a sum of two harmonics with frequencies close to 40 kHz and amplitudes up to 10 V. We studied the directional patterns in the horizontal plane for the difference-frequency wave (DFW) generated by such an array. The measurements were performed at a distance of 3.3 m from the plane of the plate.

Figures 2a–2c show the directional patterns obtained for the DFW signal of frequency 4 kHz that was produced by two vertical rows of radiators spaced at 36, 72, and 108 mm, respectively. Calculations were performed by representing each radiator as a point source with a directional pattern approximating the one measured for a single radiator in the angular range from –60° to +60°. Figure 2 demonstrates a fairly good agreement between the calculated and measured patterns near the axis. For large angles, the accuracy of the main lobe approximation increases with the distance between the rows of radiators.

Directional patterns obtained with the completely filled plate (with 49 small-size piezoelectric radiators) are shown in Figs. 3a and 3b for DWF frequencies of 500 Hz and 4 kHz.
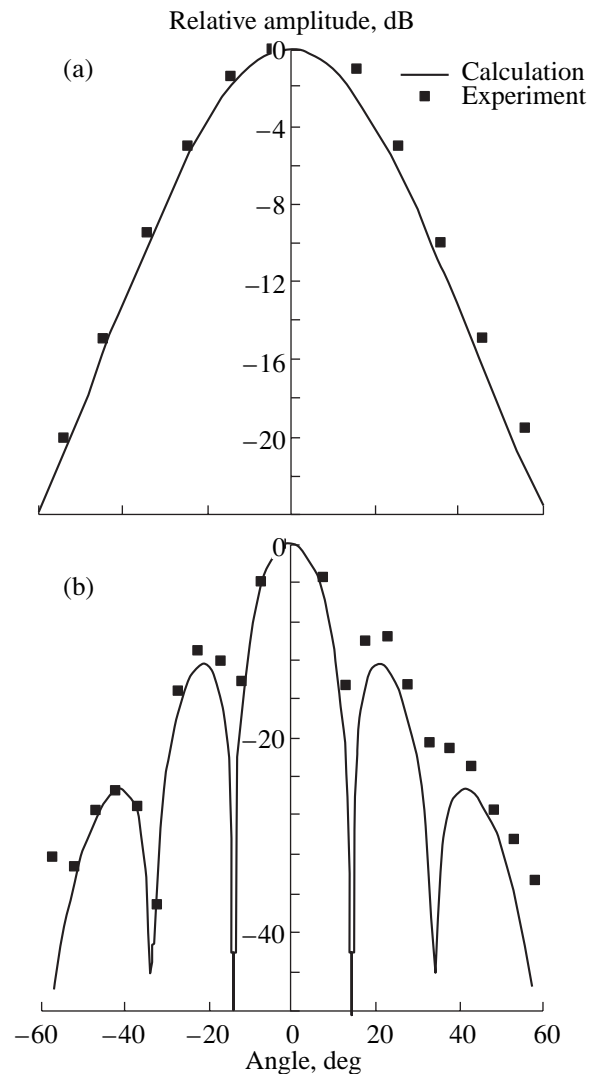
The second series of measurements was carried out with a ring-shaped array. It consisted of a fabric-based laminate ring 360 mm in diameter with 48 small-size radiators fixed on it at regular intervals. Figures 4a and 4b show the angular dependences of the DFW amplitude measured for difference frequencies of 500 Hz and 3 kHz at a distance of 4 m from the ring. At this distance, the ultrasound pressure level remained relatively high (124 dB), while the DFW divergence law was close to spherical.
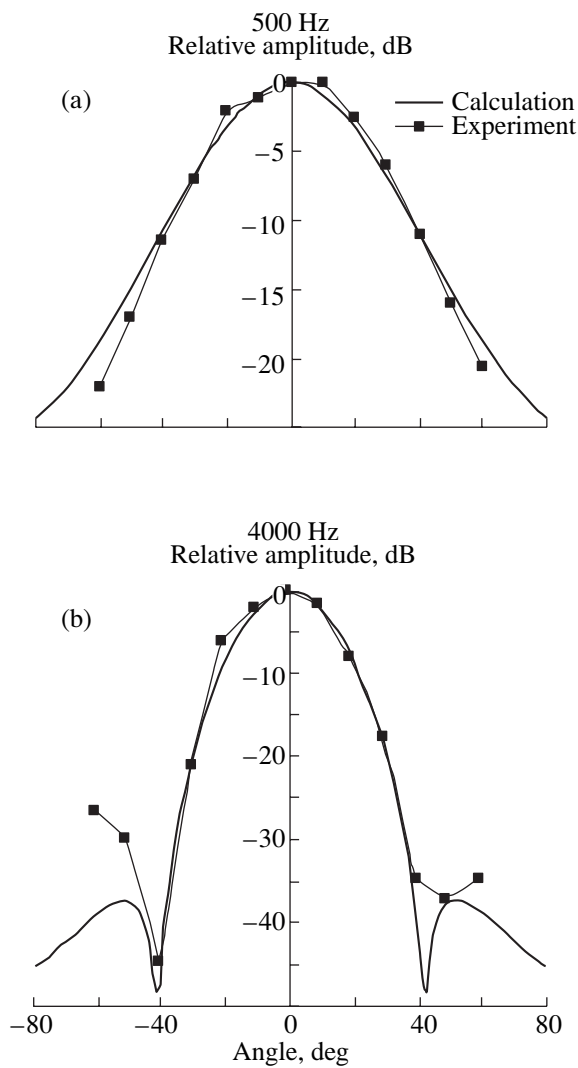
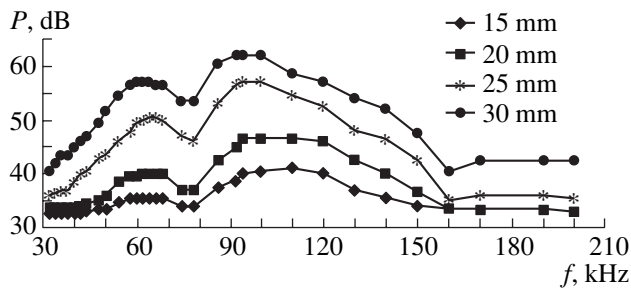**Fig. 3.** Directional patterns of a square array. The difference frequency is (a) 500 Hz and (b) 4 kHz.

Fig. 4. Directional patterns for the DFW obtained with a ring-shaped array. The frequency of the signal is (a) 500 Hz and (b) 3 kHz.

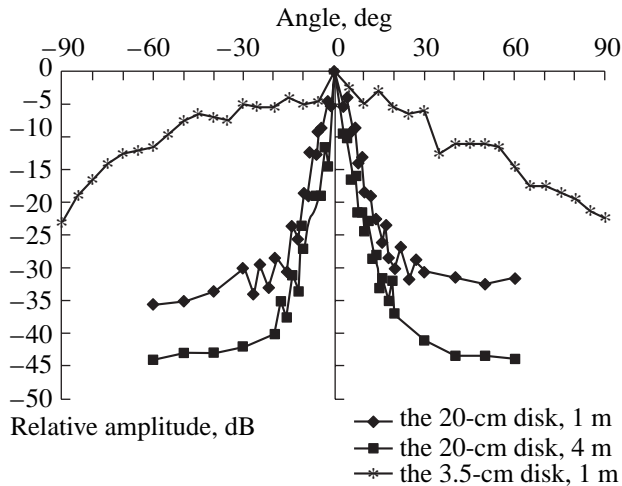The third series of experiments was carried out with a focusing array. It consisted of a disk with groups of small-size radiators fixed on it. The groups were arranged as rings whose radii approximately corresponded to the boundaries of the Fresnel zones. The electric signals supplied to neighboring rings had a phase shift of π between them. The structure was carefully optimized to obtain the maximal intensities of ultrasound in the focal region for a given focal length and the limitations imposed on the diameter of the array and the number of radiators. In addition, it was necessary to obtain a sufficiently smooth field distribution along the beam axis.

Two identical arrays containing 90 radiators each were manufactured. We plan to later use these arrays at different but close frequencies in the confocal position

to obtain a pronounced nonlinearity and to generate low (audio) frequencies near their common focus.

The focus of each of these arrays was at a distance of about 32 cm from the plane of the source of radiation, and the diameter of the focal spot was 2–3 cm. At reasonable loads allowing for an almost infinitely long operation of the device, the maximal intensity level near the focus reached 152 dB. However, for safety reasons, the experiments were performed with lower intensities.

We measured the profile of the ultrasonic signal immediately before the focus and behind it. We observed typical nonlinear diffraction distortions associated with the formation of steep wave fronts and the asymmetric distortion of half-periods of different polarity. A detailed comparison of the experimental data with the theory is planned to be performed later.

Fig. 5. Amplitude–frequency response of the membrane transducer for disks of different diameters.

Fig. 6. Directional patterns of membrane transducers.
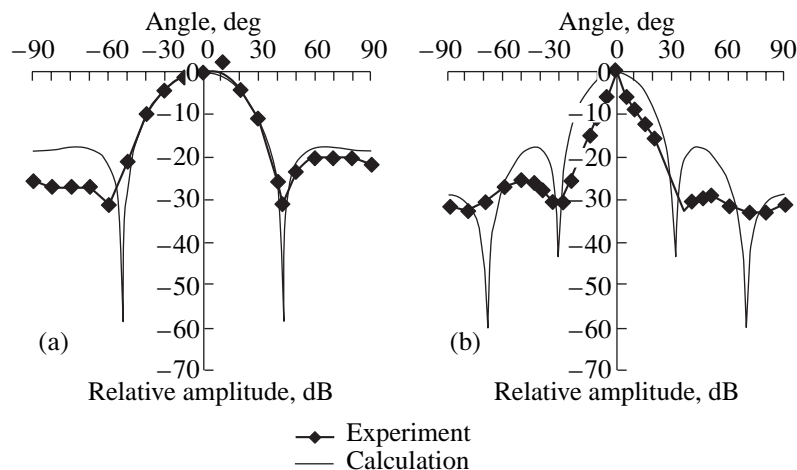
MEMBRANE TRANSDUCERS

Along with the radiating arrays, we fabricated a family of radiating membrane transducers of the type described in [12]. The principle of their operation is as follows. A light metallized polymer film (membrane) is slightly stretched over a rough surface of a conducting disk. A constant voltage component induces charges of opposite signs on the membrane and on the disk. As a result, the membrane is pressed to the rough surface. Under the action of an alternating voltage component, parts of the membrane that lie over depressions of the surface begin to vibrate. In this case, the air in the depressions plays the role of an elastic load, and each of these small areas operates as a small capacitor-type radiator.

First, we studied the amplitude–frequency responses with the use of four disks of different diameters. Grooves on their surfaces were scratched by a rough abrasive cloth. The polarization voltage was equal to 200 V, and the amplitude of the alternating voltage was 50 V. A microphone was placed at the axis, at a distance of 1 m from the membrane surface. The dependences obtained in the experiment are shown in Fig. 5. The curves corresponding to different diameters have the same shape with two smooth maxima and a minimum between them. The positions of the extrema on the frequency axis are approximately the same for all curves. The sound pressure level increases with increasing diameter because of the increase in the working area of the radiator and, hence, in the radiation power.

In the next experiment, we measured the ultrasound pressure levels at the maxima of the amplitude–frequency response for three disks with the same diameter of 30 mm but with grooves scratched by different abrasive cloths: rough, intermediate, and fine. The frequencies corresponding to the extrema varied within narrow limits, but the radiator with rough grooves proved to be

Here, we note only that the evolution of the profiles and spectra of waves produced by the arrays differs from the well-investigated evolution of periodic signals excited in a nonlinear medium by single radiators.

Fig. 7. Angular dependences of the radiation levels for ultrasound modulation frequencies of (a) 3 and (b) 4 kHz.

the most efficient one: it provided a 10-dB-higher pressure level compared to the two other radiators.

Then, we measured the level of the first maximum as a function of the groove depth (from 0.2 to 0.6 mm) for grooves that were cut by a milling machine at a constant step. The highest ultrasound pressure level was obtained for the smallest groove depth (0.2 mm). This level also was 18 dB higher than the pressure level achieved with the disk with grooves made by the rough abrasive cloth. Thus, we determined the parameters that provided for the generation of ultrasound with maximal intensity by the membrane transducers of the aforementioned type.

In the following experiments, we used a large source 20 cm in diameter with 0.1-mm-deep grooves. Figure 6 shows the angular dependences of the normalized ultrasound level obtained with this source of radiation at distances of 1 and 4 m at the first maximum (62 kHz). For comparison, in the same figure, we present the corresponding dependence obtained for a disk 35 mm in diameter at a frequency of 48 kHz at a distance of 1 m. In the latter case, the diffraction length is about 14 cm; i.e., we have a completely formed directional pattern at this distance. Its angular width is evidently much greater than that for the disk with the diameter of 20 cm.

The large source (20 cm) was loaded with an electric signal generated at a frequency of 62 kHz (corresponding to the first resonance) and modulated at a frequency of 3–4 kHz. In air, a nonlinear demodulation takes place, which results in the generation of an audio-frequency wave. At a distance of 1 m, its level was 55 dB for the frequency of 3 kHz and 60.5 dB for the frequency of 4 kHz. The level of the high frequency signal was 130 dB at the same distance. The angular dependences of the sound pressure levels measured at a distance of 4 m for frequencies of 3 and 4 kHz are shown in Figs. 7a and 7b.

CONCLUSIONS

Arrays of small-size piezoelectric radiators and membrane transducers generating intense airborne ultrasound have a number of characteristic features, which include both advantages and drawbacks. Therefore, their use in experiments and applications may be advantageous or inappropriate, depending on the specific problem to be solved.

The sound pressure levels that were achieved in the experiments described above can be noticeably increased with the use of more advanced materials and technologies.

REFERENCES

1. V. A. Zverev, Akust. Zh. **45**, 685 (1999) [Acoust. Phys. **45**, 611 (1999)].
2. B. K. Novikov, O. V. Rudenko, and V. I. Timoshenko, *Nonlinear Underwater Acoustics* (Sudostroenie, Leningrad, 1981; American Inst. of Physics, New York, 1987).
3. M. B. Bennett and D. T. Blackstock, J. Acoust. Soc. Am. **57**, 562 (1975).
4. S. N. Kulichkov, Izv. Akad. Nauk SSSR, Fiz. Atmos. Okeana **15** (4) (1979).
5. M. Yoneyama, J. Fujimoto, Y. Kawamo, and S. Sasabe, J. Acoust. Soc. Am. **73**, 1532 (1983).
6. T. Kite, J. T. Post, and M. F. Hamilton, in *Proceedings of 16th International Congress on Acoustics*, Ed. by P. K. Kuhl and L. A. Crum (Acoust. Soc. Am., New York, 1998), Vol. 2, pp. 1091–1092.
7. F. J. Pompei, J. Audio Eng. Soc. **47**, 726 (1999).
8. M. A. Isakovich, *General Acoustics* (Nauka, Moscow, 1973) [in Russian].
9. O. V. Rudenko, Russ. J. Nondestr. Test. **29** (8), 583 (1993).
10. I. Solodov, K. Pfleiderer, H. Gerhard, and G. Busse, Ultrasonics **42**, 1011 (2004).
11. E. M. Ballad, S. Yu. Vezirov, K. Pfleiderer, *et al.*, Ultrasonics **42**, 1031 (2004).
12. M. A. Kallistratova, Tr. Inst. Fiz. Atmos. Akad. Nauk SSSR **4**, 203 (1962).

Translated by E. Golyamina

Physical Modeling of Nonlinear Sound Wave Propagation in Oceanic Waveguides of Variable Depth

S. N. Gurbatov, V. V. Kurin, L. M. Kustov, and N. V. Pronchatov-Rubtsov

Lobachevski State University, pr. Gagarina 23, Nizhni Novgorod, 603950 Russia
e-mail: nikvas@rf.unn.ru; kurin@rf.unn.ru; gurb@rf.unn.ru
Received June 23, 2004

Abstract—Results of laboratory experiments aimed at studying the spatial distribution of the difference-frequency acoustic wave field in a shallow-water waveguide with a sloping bottom are presented. It is shown that, in an inhomogeneous waveguide, the direction toward the radiation maximum in the angular spectrum of the low-frequency wave continuously varies as the rib of the wedge is approached, whereas, in a homogeneous waveguide, the angular spectrum is shaped. A spatial filtering of low-frequency modes produced by a parametric radiator and reflected from the coastal wedge is experimentally realized. The results of the experiment are confirmed by numerical modeling. Problems of the physical adequacy of the experimental results obtained under actual and laboratory conditions are discussed. © 2005 Pleiades Publishing, Inc.

INTRODUCTION

The study of acoustic wave propagation in shelf zones of the ocean presents a fairly complex problem because of the difficulties involved in the determination of the sound field characteristics when the parameters of the medium depend not only on the depth of the waveguide but also on the horizontal coordinates. For the first time, the solution to the problem of wave diffraction by a wedge was obtained in a general form by Sommerfeld. However, this solution often does not allow one to represent the physical picture of the field without intricate additional transformations. Therefore, at present, the problems of sound propagation in almost stratified media, i.e., in media whose properties slowly vary in the horizontal direction, are in most cases theoretically solved by using one of the two following approaches.

One of them is based on the well-known theory of horizontal rays and vertical modes [1, 2] with the assumption that no interaction occurs between them. In this method, taking into account the variations of both sound velocity and waveguide depth in both space and time, a combination of normal modes and horizontal rays is used. The other approach is based on the ray representations of high-frequency sound fields in media whose parameters depend on three coordinates. For example, in [3], an approximate relationship (called ray invariant or Weston invariant) was derived, which then was used in [4] to construct horizontal projections of ray paths with multiple reflections from the bottom and the surface of the sea. Expressions for "horizontal rays" were obtained in the form of definite integrals for the case of a sea depth depending on a single horizontal coordinate. Using the relations between rays and modes, Weston also considered the possibility of applying Snell's law to describing the "horizontal refraction" of rays multiply reflected from the bottom and the surface. In connection with this, one should note the publications by Komissarova [5, 6]: in addition to theoretical studies, she gave detailed descriptions of numerical and field experiments on sound propagation in actual oceanic conditions, where the depth of the water layer depended on both horizontal coordinates in an arbitrary way.

The experiments described in [5, 6] were performed with linear point sources of sound. A selective control over the mode composition of the sound field can be achieved with the use of horizontal and vertical phased linear transmitting arrays of considerable length or with the use of parametric sources of sound. The latter possibility is of special interest for oceanographic investigations. This is related to the unique properties of parametric radiators, specifically, to the extremely narrow directional pattern at a low radiation frequency. The use of intense sources that have a fairly long region of interaction of the initial pumping waves makes it necessary to take into account the waveguide nature of sound propagation and the inhomogeneities of the medium in the region where the difference-frequency wave is formed.

However, in the literature available to us, we did not encounter any information on experimental studies of parametric sound radiation in waveguides whose parameters smoothly vary along the sound propagation path. With the aim of partially filling this gap, we carried out experimental studies of the sound fields produced by parametric sound sources in waveguides that modeled a shelf zone of the ocean.

The laboratory modeling of nonlinear acoustic wave propagation has some distinctive features compared to

the scaled physical modeling of linear wave propagation. Let us consider this issue in more detail [7].

SPECIFIC FEATURES OF THE SCALED PHYSICAL MODELING OF NONLINEAR ACOUSTIC WAVE PROPAGATION

A method often used at the Department of Acoustics of the Nizhni Novgorod State University for studying the propagation of sound in an oceanic medium is laboratory physical modeling. The department's wide experience in the physical modeling of sound propagation in the ocean was summarized in a monograph by Professor A.N. Barkhatov, which was published in 1982 [8]. Since the mid-1980s, this method has been successfully used in studying the nonlinear effects that manifest themselves in the underwater propagation of intense acoustic waves [9–11].

The physical modeling of linear problems in the acoustics of ideal inhomogeneous media should be performed with a retention of the similarity between the model and the phenomenon under study. This is possible when the condition kL = const is satisfied for the field and laboratory experiments, where k is the wave number and L is the respective spatial scale. In addition, the so-called modeling parameter Q is introduced [8]:

$$L_i/l_i = f/F = \Lambda/\lambda = Q,$$

where L_i represents the microscales of the field physical experiment (the characteristic size of inhomogeneities, the ocean depth, the propagation path, etc.), l_i represents the corresponding scales of the laboratory experiment, f and λ are the frequency and wavelength in the laboratory experiment, and F and Λ are the corresponding parameters of the field experiment.

As is known, the velocity of sound in the ocean varies much faster with depth than in the horizontal direction. This allows one to approximately describe the ocean as a horizontally layered medium, whose parameters vary only slightly along the horizontal [12].

For a correct scaled physical modeling of the underwater sound channel, it is necessary to leave the same absolute velocity drop but scale down the macroscopic parameters of the problem (the waveguide depth) and increase the radiation frequency by a corresponding factor. However, under laboratory conditions, it is not always possible to observe the formation of convergence zones (zones of enhanced illumination) that lie at distances of 50–70 km from the source in field conditions. For example, when the modeling parameter is $Q = 10^4$ and the depth of the underwater sound channel axis is $z_{oc} = 1.5$ km under field conditions, the distance to the first convergence zone under laboratory conditions is $L_{con} = 5$–7 m, which exceeds the size of our laboratory tanks. Therefore, in the laboratory experiments, it is necessary to reduce the cycle length of sound rays by a disproportionate increase in the vertical gradients of sound velocity.

It should also be noted that, in modeling the sound propagation in a shallow sea under laboratory conditions, it is impossible to retain the same value of the parameter D/H, where D is the aperture of the sound source and H is the depth of the waveguide. This violates the similarity of the angular characteristics of radiation in the field and laboratory experiments.

In the modeling of nonlinear effects in an ideal medium, the processes will be physically identical if the similarity parameter Q holds for the characteristic nonlinear length $L_r = 1/k\varepsilon M$, where ε is the nonlinear parameter and M is the Mach number. This condition is satisfied if M has a constant value in the field and laboratory experiments.

In the case of studying the propagation of acoustic waves in linear dissipative media, the method of a scaled physical modeling is, generally speaking, unrealizable, because the sound absorption coefficient nonlinearly depends on frequency. This leads to a disproportionately high attenuation in the modeling of sound propagation under laboratory conditions. However, for linear problems, it is possible to introduce corrections compensating for the attenuation and then take into account this difference in the numerical processing of experimental results [8].

In analyzing nonlinear problems, the relative role of nonlinear and dissipative effects is also characterized by a similarity number represented by the acoustic Reynolds number Re, which is inversely proportional to the radiation frequency [13]. This does not allow one to obtain a simultaneous equality of the similarity numbers M and Re in the laboratory and field experiments when considering the nonlinear interaction of sound waves in inhomogeneous dissipative media. In particular, since the attenuation is one of the decisive factors in the formation of the directional patterns of parametric radiators [14], the physical modeling gives only a qualitative picture of the parametric source operation in an oceanic medium.

However, despite these circumstances, the method of laboratory modeling allows one to carry out unique experimental studies in physical underwater acoustics under strictly controlled laboratory conditions. With all the aforementioned disadvantages, it remains a powerful instrument for studying sound fields in the ocean.

LABORATORY ACOUSTIC SYSTEM

The physical modeling was performed using the acoustic system of the Department of Acoustics of Nizhni Novgorod University. Earlier, this system was used to study the nonlinear generation and scattering of sound waves in a homogeneous space and under the conditions of waveguide propagation [15] and also to study the diffraction of sound waves by smooth and discrete inhomogeneities of a medium [16]. In addition, a physical modeling of the low-frequency sound propagation in an oceanic medium was carried out [17] and
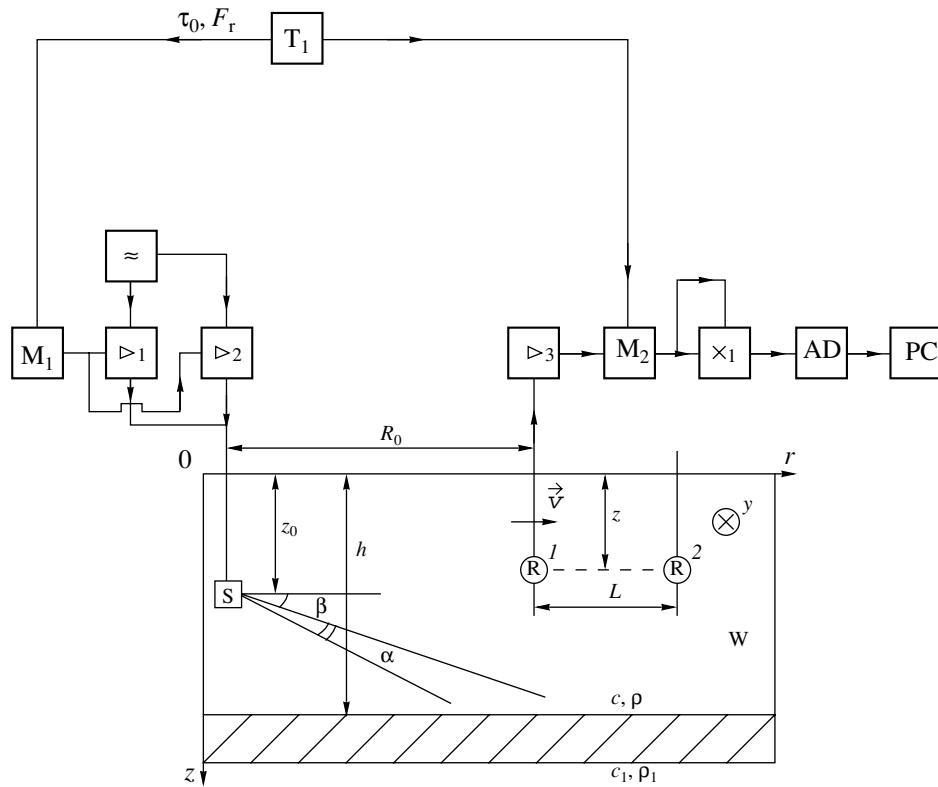
Fig. 1. Flow chart of the experimental system.

methods for the acoustical diagnostics of the underlying surfaces of shallow-water oceanic waveguides were developed [18].

The experiments were performed in a laboratory tank (W) with anechoic walls. The tank was 500 cm in length with a width of 65 cm and a depth of 55 cm. It was filled with water (characterized by sound velocity c and the density ρ) and had a suspended bottom (with a sound velocity c_1 and a density ρ_1), which could be moved by screws in the vertical plane from 0 to 17 cm, the desired depth being set with an accuracy of ±2 mm. Thus, it was possible to model a plane waveguide and a waveguide with a sloping bottom.

A simplified flow chart of the experimental system is shown in Fig. 1, where the relative positions of the source and receiver are indicated.

Below, we briefly describe the operation of the main parts of the experimental system.

High-frequency oscillations were produced by two high-power amplifiers ($\triangleright_1$ and $\triangleright_2$), to the inputs of which continuous sinusoidal signals of frequencies f_1 and f_2 were supplied from the reference frequency unit ($\approx$). To reduce the level of reverberation noise due to the boundaries of the volume under study, a pulsed radiation mode was used in the experiments. The duration of the pulses τ_0 satisfied the condition $f_1\tau_0 \geqslant 2\pi$, which ensured the quasi-monochromatic radiation mode.

The modulation pulses were produced by a generator (T_1) of rectangular video pulses with a controlled duration τ_0 and a repetition rate $F_r = 64$ Hz. These pulses, via a pulse amplifier (M_1), were supplied to the modulation inputs of the amplifiers ($\triangleright_1$ and $\triangleright_2$), where the formation and amplification of radio pulses took place. The signal formed in this way was supplied to the acoustic transducer of pumping waves (S).

The source of the signal (S) was a circular piston-type piezoceramic transducer with diameter $D = 2.8$ cm, which formed a weakly divergent acoustic beam at the frequency $F_1 = 200$ kHz (the pumping frequencies were $f_1 = 3.2$ MHz and $f_2 = 3.0$ MHz). With this transducer, the angular width α of the low-frequency beam of the difference-frequency wave was 1.5°. The transducer was mounted on a rod that allowed for the positioning of the source in depth z_0 (with an error no greater than 1 mm), as well as for the orientation of the axis of the parametric source radiation in the vertical plane (angle β) with an accuracy of 1° or better.

To determine the mode of operation of the pumping transducer, we performed preliminary experiments in the unbounded space. The attenuation length determined experimentally was $l_a = 1.47$ m. As is known [14], the mode of operation of a parametric source is determined by the parameter $\eta = \dfrac{l_a}{R_f}\left(\dfrac{\Omega_1}{\omega_j}\right)$, where R_f is the diffraction divergence length of the transducer at a

high frequency, $\Omega_1 = 2\pi F_1$, and $\omega_j = 2\pi f_j$ ($j = 1, 2$). In our case, we had $\eta \ll 1$, so that the formation of the characteristics of the difference-frequency wave radiation was close to the Westervelt regime.

The synchronization of the operation of the whole system was provided by a sync pulse produced by the same generator (T_1).

When it had been transmitted through the medium under study, the signal was received by an omnidirectional piezoceramic receiver (R). The distribution of acoustic fields (in all three coordinates (r, y, z)) was measured by a piezoceramic receiver whose size was small compared to the wavelength. The receiver was mounted on a carriage that could uniformly move in three perpendicular directions (along the length, width, and depth of the tank). The velocity of the receiver motion along the hydroacoustic tank was $V = 1.8$ cm/s in all experiments. The uncontrolled velocity fluctuations did not exceed ± 0.005 cm/s. In Fig. 1, the initial distance between the source and the receiver of sound is denoted R_0, and the base of the receiver motion, L. The accuracy of the receiver positioning along any of the coordinate axes was within 1 mm.

After two-stage amplification and filtering performed by an amplifier ($\triangleright_3$), the pulsed received signal was supplied to the gate unit (M_2) controlled by the gate pulse generator (T_1). Pulses produced by this generator, which were characterized by a duration τ_1 and a controlled delay time with respect to the onset of the transmitted pulse, allowed us, first, to suppress the pulsed reverberation noise and, second, to measure the amplitude at any point of the received signal. The gated pulse was supplied in parallel to both inputs of a multiplier ($\times_1$), which made it possible to measure the intensity of the signal. As a result, at the output of the multiplier ($\times_1$), video pulses were formed with a duration τ_1 and an amplitude depending on the amplitude of the received signal. The transformed signal was supplied to an integrator (not shown in Fig. 1) controlled by the pulse from the gate generator. Thus, the voltage formed at the output of the integrator had an amplitude proportional to the square of the amplitude of the pulsed input signal. This voltage, in its turn, was converted to a digital code by an A/D converter and recorded on the disk of a PC for a further processing. The sampling rate in the A/D conversion was 50 Hz for all experiments.

Now, let us discuss the experimental results.

EXPERIMENTAL STUDY OF THE ANGULAR CHARACTERISTICS OF THE DIFFERENCE-FREQUENCY WAVE FIELDS IN A PLANE WAVEGUIDE AND IN A WAVEGUIDE WITH A SLOPING BOTTOM

In the experiment, we compared the angular (in the horizontal plane) dependences of the difference-frequency wave field in a plane waveguide and in a waveguide with a sloping bottom at different fixed distances R_0 between the source and the receiver.

The waveguide under study is schematically represented in Fig. 2. It has the form of a homogeneous water layer of variable depth with sound velocity $c = 1475$ m/s and density $\rho = 1$ g/cm^3. The water layer lies on a sloping aluminum substrate with longitudinal wave velocity $c_1 = 6200$ m/s and density $\rho_1 = 2.72$ g/cm^3; the wedge angle Φ is approximately equal to $0.78°$. The depth at the source site was the same as that in the reference waveguide and was equal to 38 mm. The distance r_0 between the source and the rib of the wedge was 280 cm.

The plane reference waveguide has the form of a homogeneous water layer of thickness $H = 38 \pm 2$ mm, which overlies a metal substrate parallel to the free surface of the layer.

The orientation of the axis of the parametric source radiation in the vertical plane, i.e., the angle β, provided the best excitation of the first three propagating modes. The experimental studies of the mode structure of acoustic field in the plane waveguide with the same bottom model showed that the vertical structure of the low-number mode field virtually corresponds to the field in a waveguide with two acoustically soft boundaries. The eigenmodes of this waveguide are described in terms of the simplest Pekeris model, namely, a waveguide with a liquid bottom [9].

In [19], directional patterns of single modes of the difference-frequency wave in the horizontal plane were calculated for an ideal waveguide with a free surface and a rigid bottom. An expression was obtained for the main maxima of the directional pattern of the mth mode:

$$\theta_{m\max} \cong \pi \pm \sqrt{\frac{2\pi\beta}{KH} - (\beta - \zeta_m)^2}, \tag{1}$$

where K is the wave number of the difference-frequency wave, H is the depth of the plane waveguide, and $\zeta_m = \zeta_m(H)$ is the grazing angle of Brillouin waves of the mth mode. From Eq. (1), it follows that, at some preset slope angle of the source β, the field is formed by different modes whose radiation maxima correspond to different angles in the azimuth plane. This theory agrees well with the results of the model experiment carried out for a range-independent waveguide [9].

The analysis of Eq. (1) in the adiabatic approximation shows that the angle $\theta_{m\max}$ characterizing the direction toward the radiation maximum of the mth mode should increase if the depth of the waveguide decreases along the path of sound propagation. Hence, in studying the horizontal distributions of acoustic fields in range-dependent waveguides, one should expect a broadening of the angular spectrum of the fields generated by the source, as compared to the corresponding characteristics measured in the plane waveguide.

The source depth z_0 and the angle β were fixed and were the same in both experiments; in addition, $z_0 = H/2$.

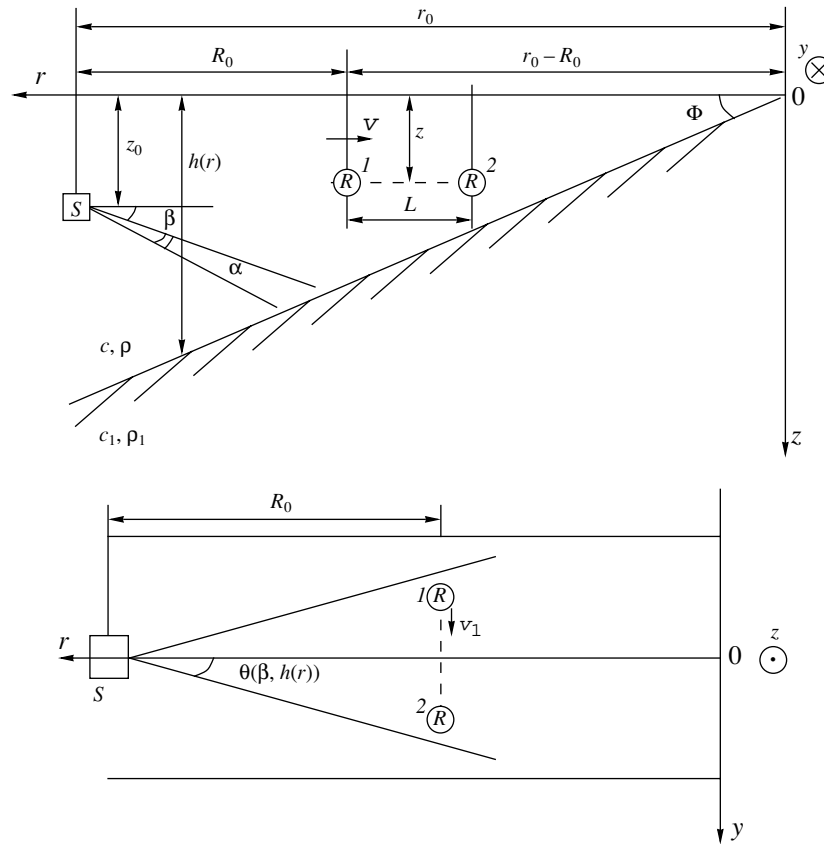The technique used for the measurements in the waveguide with a variable depth is worth noting. In the

Fig. 2. Geometry of the experimental problem.

experiments with the reference waveguide, the source depth was fixed ($z = H/2$) for all distances R_0, at which the field sections were considered. The position of the receiver in the middle of the water layer ensured the reception of the first and third modes of this waveguide.
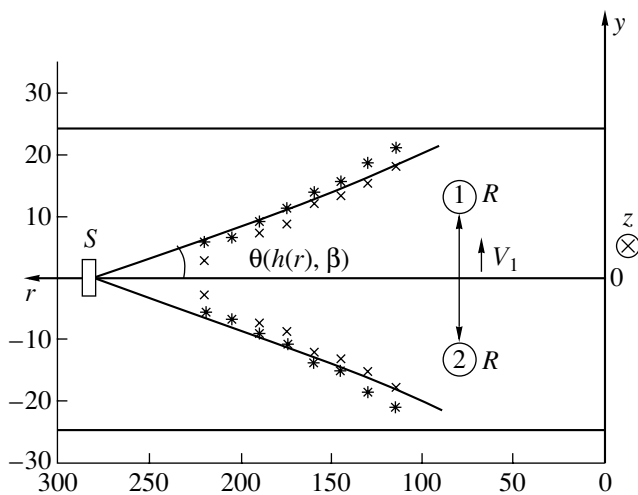

Fig. 3. Directions toward the difference-frequency wave radiation maximum determined experimentally in the plane waveguide and in the waveguide with a sloping bottom.

In the waveguide with variable depth, the receiver depth varied from section to section with distance from the source toward the rib of the wedge in such a way that the quantity $z/H = 1/2$ remained constant; here, H is the depth of the waveguide (wedge) at a distance r from the rib. As one can see from Fig. 2, this depth linearly depends on r: $H = H_s \dfrac{r}{r_0}$, where H_s is the depth of the wedge at the source site. This technique was used with the aim of retaining the amplitude ratios between the normal modes forming the difference-frequency wave field at different distances from the wedge rib. The relative contributions of individual normal modes to the resulting field remained invariable at different distances from the source.

Figure 3 shows the experimental data on the spatial positions of the radiation maxima of the difference-frequency wave produced by the parametric radiator operating in the plane waveguide (crosses) and in the waveguide with a linearly varying depth (asterisks) for different source–receiver distances. The solid line shows the theoretically determined direction toward the radiation maxima of the first propagating mode of the waveguide with variable depth. The calculations were performed using formula (1).

From Fig. 3, one can see that the angular spectrum of radiation in the plane waveguide is shaped, whereas, in the wedge, the angular distribution of the maxima noticeably broadens as the rib is approached.

Thus, the experiment confirmed the assumption that, in a waveguide with a sloping bottom in the case of difference-frequency wave propagation in the direction of decreasing thickness of the water layer, the angular spectrum of parametric radiation broadens compared to the angular spectrum of the field in the reference waveguide.

MODE COMPOSITION OF THE REFRACTED DIFFERENCE-FREQUENCY WAVE FIELD IN A WAVEGUIDE WITH A SLOPING BOTTOM

According to the method of solving the problem of sound propagation in an almost stratified medium, which is called horizontal rays–vertical modes [2], the field in the wedge can be represented as a superposition of normal modes. The distribution of the field of a normal mode in the plane $\varphi = \text{const}$ in the waveguide zone is determined by the two-dimensional wave equation for a layered inhomogeneous medium:

$$\frac{\partial^2 W}{\partial r^2} + \frac{\partial^2 W}{\partial y^2} + k^2 n^2(r) W = 0. \qquad (2)$$

From Eq. (2), it follows that the field of a single normal mode in the horizontal plane (r, y) can be studied by the methods developed in the waveguide problems for smoothly inhomogeneous media, e.g., by the methods of geometrical acoustics. In this case, the refraction index of the medium can be represented in the form

$$\tilde{n}_m(r) = \sqrt{1 - \frac{\mu_m^2(r)}{k^2 r^2}}, \qquad (3)$$

where m is the order number of the normal mode and the quantity μ_m depends on r according to the transcendental equation

$$\tan \mu_m \Phi = \frac{\rho_1}{\rho} \frac{\mu_m}{\sqrt{k^2 r^2 (1 - n^2) - \mu_m^2}}, \qquad (4)$$

where $n = c/c_1$ and $k = \omega/c$.

From Eq. (3), it follows that each single mode propagates in the medium with a varying refraction index, and each of the refracted mode rays has its own path in the horizontal plane. As the wedge rib is approached, the effective propagation velocity of the mth mode increases. With respect to the normal mode of a given order m, the whole wedge region falls into two subregions separated by the straight line

$$r_m = \frac{(2m-1)\pi}{2k\Phi\sqrt{1-n^2}}. \qquad (5)$$
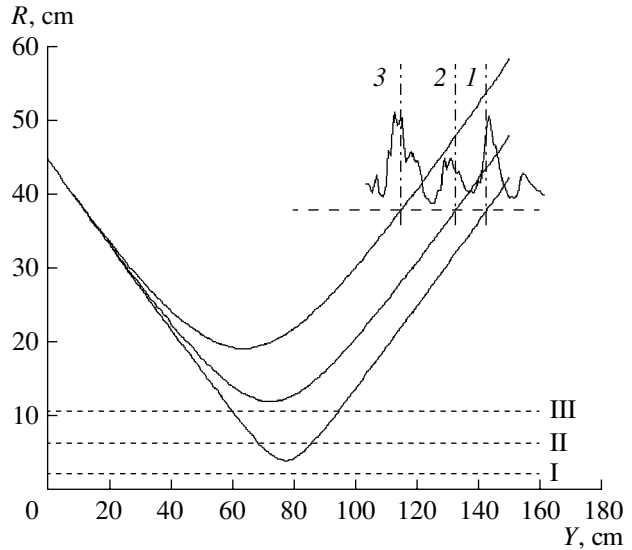
Fig. 4. Horizontal distribution of the refracted sound field in the waveguide.

In the subregion where $r > r_m \mu_m$, the quantity μ_m takes on real values. In this subregion, the waveguide propagation of sound takes place. As the wedge rib is approached, μ_m decreases and the maximum of the normal mode profile moves toward the lower boundary. At the same time, the exponential part of the profile grows within the limits of the half-space. The normal mode seems to be gradually immersed in the half-space. This phenomenon was called the vertical refraction of normal modes.

Thus, in the given acoustic waveguide, along with the refraction of a normal mode in the horizontal plane, which is determined by Helmholtz equation (2), a displacement of the normal mode in the vertical plane takes place; under certain conditions, this displacement leads to the emission of the wave energy into the half-space. However, in this paper, we investigate only the horizontal refraction of individual mode rays in the waveguide zone.

The waveguide under study is an isovelocity liquid wedge of angle $\Phi = 5.07°$ overlying a metal substrate. The parameters of the waveguide layer and the bottom were described in the previous section. The depth of the waveguide at the source site was 40 mm. The parametric radiator was placed at a distance of 45 cm from the wedge rib. The axis of its radiation in the horizontal plane made an angle $\theta_0 = 34°$ with the normal to the wedge rib. In the experiment, we measured the distribution of the sound field intensity by a receiver uniformly moving parallel to the wedge rib (the y coordinate). The distance between the wedge rib and the receiver varied from 20 to 36 cm for different experiments. The receiver depth was three-fourths of the waveguide depth at a given distance from the rib for all measurements. This configuration of the transmitting–receiving
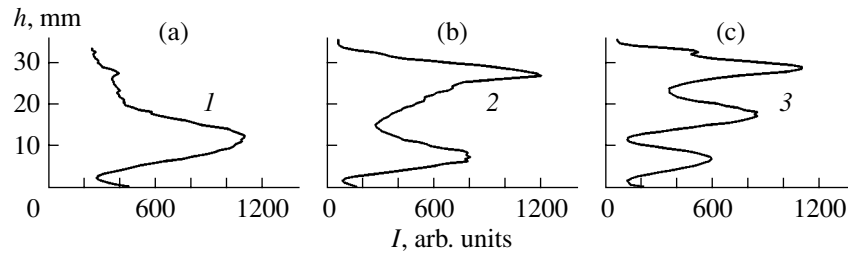
Fig. 5. Vertical intensity distributions for the first, second, and third modes.

system ensured the reception of all three propagating modes.

Figure 4 shows the experimental results for the case of the field intensity measurement by a receiver moving at a distance of 36 cm from the wedge rib. The same figure shows the paths of the refracted mode rays in the horizontal plane for the first three propagating waveguide modes of the difference-frequency wave. These ray paths (marked with numbers *1*, *2*, and *3* in the plot) were determined with the help of a computer program using the MatLab package and the vertical modes–horizontal rays computational algorithm [2]. The horizontal lines (marked as I, II, and III) indicate the boundaries of the waveguide and nonwaveguide zones for modes of respective numbers. One can see from Fig. 4 that different modes with the same launch angle θ_0 in the horizontal plane are refracted in different ways. The highest order mode is the first to be reflected, and mode number one is reflected last.

The theory describes the propagation of monochromatic waves in the linear approximation. However, in the experiments, we use a nonlinear traveling-wave source. Evidently, the presence of soft boundaries in the region of interaction of high-frequency pumping waves should distort the angular characteristics of the sound field produced by the parametric radiator. In addition, the sloping boundaries of the waveguide lead to a situation where each of the propagating modes of the difference-frequency wave, as well as the high-frequency pumping waves, propagate over their own paths in the horizontal plane. Naturally, in this case, the synchronism between the pumping wave and the difference-frequency wave characterized by a limited mode composition is violated. The synchronism is affected by the loss of collinearity of the initial pumping beam and the modes parametrically generated at the difference frequency. This mechanism deteriorates the directional properties of the parametric radiator.

However, experimental studies have shown that, in the waveguide under study, the directivity of the parametric source at the difference frequency remained sufficiently high so as to allow for the selection of normal modes in the refracted sound field with respect to the spatial *y* coordinate. At the top right of Fig. 4, the intensity distributions experimentally measured at distances of 90 to 150 cm from the source are represented. One

can see that the spatial positions of the field intensity maxima that correspond to individual refracted mode rays agree well with the theoretical calculations. At each of these maxima, the intensity of the difference-frequency wave field was measured along the depth of the waveguide. The results of these measurements are shown in Fig. 5. One can see that the vertical distribution of the sound field intensity measured at each of the detected maxima (*1*, *2*, and *3*) corresponds to the intensity distribution of the first three propagating modes.

Thus, the application of the narrow-beam low-frequency radiation produced by a nonlinear sound source allowed us to demonstrate the filtering properties of smoothly inhomogeneous media.

CONCLUSIONS

In conclusion, we will formulate the main results of this study:

(i) We discussed the problems of the physical adequacy of the experimental results obtained under actual and laboratory conditions. We noted that, in modeling the nonlinear effects in dissipative media, the method of scaled physical modeling is, strictly speaking, unrealizable, because it is impossible to achieve a simultaneous equality of the Reynolds and Mach similarity numbers in the laboratory and field experiments.

(ii) We presented experimental results on the spatial distributions of difference-frequency sound wave fields in a waveguide with a sloping bottom. We showed that, in a waveguide of variable depth, the angular spectrum differs from that in a plane reference waveguide. In an inhomogeneous waveguide, the direction toward the radiation maximum in the angular spectrum of the difference-frequency wave continuously varies as the rib of the wedge is approached, whereas, in a homogeneous waveguide, the angular spectrum is shaped.

(iii) A spatial filtering of the difference-frequency wave modes reflected from the coastal wedge was experimentally realized. The results of the experiment were confirmed by numerical modeling.

ACKNOWLEDGMENTS

REFERENCES

1. A. D. Pierce, J. Acoust. Soc. Am. **37**, 19 (1965).

2. R. Burridge and H. Weinberg, in *Wave Propagation and Underwater Acoustics*, Ed. by J. B. Keller and J. S. Papadakis (Springer, New York, 1977; Mir, Moscow, 1980).

3. D. E. Weston, Proc. Phys. Soc. London **73**, 365 (1959).

4. D. E. Weston, Proc. Phys. Soc. London **78**, 46 (1961).

5. N. N. Komissarova, Akust. Zh. **41**, 617 (1995) [Acoust. Phys. **41**, 542 (1995)].

6. N. N. Komissarova, Akust. Zh. **44**, 801 (1998) [Acoust. Phys. **44**, 698 (1998)].

7. S. N. Gurbatov, S. A. Egorychev, V. V. Kurin, and N. V. Pronchatov-Rubtsov, in *Proceedings of 5th Scientific Conference on Radio Physics*, Ed. by A. V. Yakimov (Nizhegor. Gos. Univ., Nizhni Novgorod, 2001), p. 248.

8. A. N. Barkhatov, *Modeling of Sound Propagation in the Ocean* (Gidrometeoizdat, Leningrad, 1982) [in Russian].

9. V. Yu. Zaĭtsev, V. V. Kurin, and A. M. Sutin, Akust. Zh. **35**, 266 (1989) [Sov. Phys. Acoust. **35**, 160 (1989)].

10. S. N. Gurbatov, V. Yu. Zaĭtsev, A. G. Kosterin, *et al.*, in *Acoustics in the Ocean*, Ed. by L. M. Brekhovskikh and I. B. Andreeva (Komiss. Probl. Mirovogo Okeana Ross. Akad. Nauk, Moscow, 1992), pp. 208–227 [in Russian].

11. I. Yu. Gryaznova, S. N. Gurbatov, S. A. Egorychev, *et al.*, Izv. Vyssh. Uchebn. Zaved., Prikl. Nelin. Din. **9** (4–5), 175 (2001).

12. L. M. Brekhovskikh and Yu. P. Lysanov, *Fundamentals of Ocean Acoustics* (Gidrometeoizdat, Leningrad, 1982; Springer, New York, 1991).

13. O. V. Rudenko and S. I. Soluyan, *Theoretical Foundations of Nonlinear Acoustics* (Nauka, Moscow, 1975; Consultants Bureau, New York, 1977).

14. B. K. Novikov, O. V. Rudenko, and V. I. Timoshenko, *Nonlinear Underwater Acoustics* (Sudostroenie, Leningrad, 1981; Acoustical Society of America, New York, 1987).

15. S. N. Gurbatov, S. A. Egorychev, V. V. Kurin, *et al.*, Akust. Zh. **46** (2), 192 (2000) [Acoust. Phys. **46**, 153 (2000)].

16. N. V. Gorskaya, S. M. Gorskiĭ, V. A. Zverev, *et al.*, Akust. Zh. **34**, 55 (1988) [Sov. Phys. Acoust. **34**, 29 (1988)].

17. O. V. Lebedev, V. V. Kurin, and N. V. Pronchatov-Rubtsov, Akust. Zh. **40**, 486 (1994) [Acoust. Phys. **40** (1994)].

18. S. N. Gurbatov, S. A. Egorychev, D. A. Zakharov, *et al.*, in *Nonlinear Acoustics at the Turn of the Millennium: Proceedings of 15th International Symposium on Nonlinear Acoustics, Goettingen, Germany, 1999*, Ed. by W. Lauterborn and T. Kurz (American Inst. of Physics, 2000), pp. 173–176.

19. V. Yu. Zaĭtsev, L. A. Ostrovskiĭ, and A. M. Sutin, Akust. Zh. **33**, 37 (1987) [Sov. Phys. Acoust. **33**, 21 (1987)].

Translated by E. Golyamina

Optoacoustic Conversion in Suspensions: The Competition of Mechanisms and Statistical Characteristics

S. V. Egerev, O. B. Ovchinnikov, and A. V. Fokin

Andreev Acoustics Institute, Russian Academy of Sciences, ul. Shvernika 4, Moscow, 117036 Russia
e-mail: sergey_egerev@mtu-net.ru
Received November 8, 2004

Abstract—Optoacoustic conversion in diluted suspensions under the effect of nanosecond laser pulses is considered. The mode of operation with moderate values of the laser fluence is studied theoretically and experimentally. In this mode, a competition of the thermooptical and cavitation mechanisms of sound conversion is observed, which leads to considerable fluctuations of the acoustic response from one laser pulse to another. Analytical expressions for the basic characteristics of the acoustic signal are obtained. A simulation of the statistical characteristics of the cavitation contribution to the signal is performed using the Monte Carlo method. The experiment is based on the use of second harmonic pulses of a YAG laser and test suspensions. The histograms of the amplitudes of acoustic signals can be used to discriminate between the mechanisms of optoacoustic conversion and also can serve as the basis for diagnosing a low content of an insoluble phase in a liquid. © *2005 Pleiades Publishing, Inc.*

INTRODUCTION

In studying sound generation by laser radiation, one sometimes has to deal with the probabilistic nature of the effect. For example, studies of the random acoustic field generated in the sea by laser irradiation of a rough sea surface were conducted in the presence of a randomly inhomogeneous heterophase subsurface layer [1, 2].

A striking example of the statistical nature of optoacoustic conversion is the effect of sound generation due to irradiation of liquid suspensions and inhomogeneous solutions by laser pulses. This effect is the subject of the present paper. We restrict our consideration to strongly diluted suspensions, and, hence, the effect is considered under the approximation of a single scattering of light (the optoacoustics of strongly scattering heterogeneous media is another rapidly developing area of research [3]).

Studying the statistical characteristics of the mechanisms underlying the optoacoustic conversion in diluted suspensions is important from both fundamental and applied points of view. For example, it is possible to give at least two examples of important medical suspensions, the application of optoacoustic diagnostics to which is very promising: suspensions of lipopolysaccharides (the particle size is about several microns) [4] and suspensions of gold nanoparticles [5].

FORMULATION OF THE PROBLEM

Apparently, the first studies of the probabilistic nature of optoacoustic conversion in weakly absorbing inhomogeneous liquids were conducted about 15 years ago [6, 7]. At that time, optoacoustic spectroscopy basically provided an opportunity to attain a record sensitivity in the determination of small admixture concentrations in biological and medical solutions and suspensions. The basis for the spectroscopy was the effect of linear thermooptical generation of sound in liquids, which were considered to be homogeneous solutions. The quantitative basis of the measurements was the well-known formula [8] for the peak level of the sound signal observed in the direction perpendicular to the beam axis in the case of liquid excitation by a short (usually nanosecond) laser pulse:

$$p_m \approx (\mu\beta c^2 E)/(\pi a_0^{3/2} c_p r^{1/2}), \tag{1}$$

where μ is the coefficient of optical absorption, β is the coefficient of cubic thermal expansion, c is the sound velocity, E is the energy of the laser pulse, a_0 is the diameter of the beam cross section, r is the distance from the beam axis to the observation point, and c_p is the specific heat of the solvent. This formula played an important role in the analysis of homogeneous solutions.

Experiments with optoacoustic conversion in inhomogeneous liquids revealed the nonstationary nature of the sound response even at very moderate values of the laser fluence. The intense signals arising in the series and exceeding the thermooptical contribution suggested that a new contribution from cavitation nature appeared because of the heating of inhomogeneities.
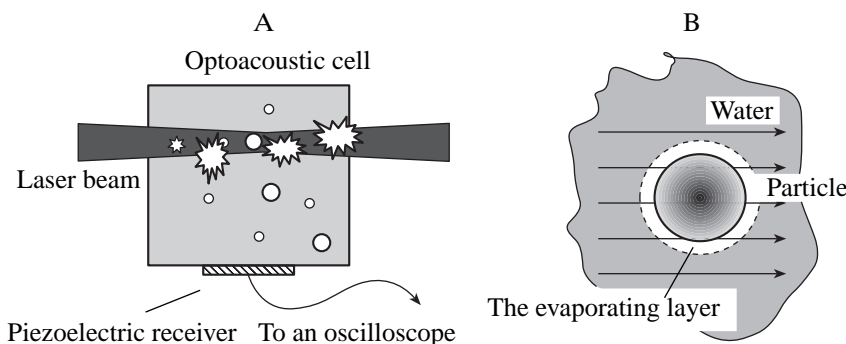
Fig. 1. Simplified scheme of the experiment. Scheme A is a general geometry. A laser beam is focused in an optoacoustic cell with a low-concentration suspension of particles. Circles show the particles constituting the suspension. Stars are for the particles for which the threshold of boiling of the surrounding liquid is attained at a given pulse. Scheme B demonstrates what happens around a particle satisfying the threshold condition. The expanding vapor layer is an effective source of sound.

Thus, the question of the applicability of Eq. (1) to the optoacoustic analysis of suspensions is mainly a question of the optical contrast of the inhomogeneities present in a sample against the surrounding liquid. In its turn, this optical contrast depends on the wavelength of the laser radiation and on the characteristics of both the solvent and the solid phase. If this contrast is high, then, starting from a certain energy of the laser pulse, Eq. (1) describes only the regular component of the overall signal at best. It is possible to assume the presence of a certain competition between the common thermooptical and the nonstationary cavitation contributions to the optoacoustic conversion in suspensions. It is evident that the investigation into the nature of this random process primarily implies taking into account the threshold of the energy that any particle should receive to stimulate the growth of a single cavitation cavity.

A simplified scheme of laser generation of sound in suspensions is given in Figs. 1a and 1b. The interaction of a laser beam with a weakly absorbing inhomogeneous liquid containing suspended absorbing particles initiates an optoacoustic conversion within the region shaped as an elongated cylinder. An emitted acoustic signal is usually detected in the direction perpendicular to the axis of the laser beam (below, we consider just this signal). The liquid itself (solvent) is almost transparent to the radiation, but the suspended particles are heated effectively by the laser pulse. In the case of a low laser fluence, the acoustic signal is caused by the thermal expansion of the liquid, which is (a) directly heated by the laser beam and (b) receives thermal energy from heated particles.

The role of particles increases when the energy of the laser pulse reaches a certain threshold value. Single particles are heated over the boiling temperature of the liquid. Such a particle is surrounded by a rapidly expanding vapor layer. The energy of the laser pulse that is evolved into the expanding region is converted into both the energy of cavity fluctuations and the energy entrained by an acoustic wave. Under these conditions, the total signal has a random amplitude and

profile, since the sources with different intensities and positions changing from one pulse to another contribute to it.

The analysis of the absolute amplitude value of the cavitation contribution is a difficult problem. However, for a qualitative statistical analysis of the contribution of the cavitation signal component, it is possible, according to [7], to assume that the amplitude of the signal emitted by an elementary cavity is proportional to the difference between the absorbed energy and the energy necessary to heat a particle to the boiling temperature of the liquid.

Experiments demonstrate that, in the case of a further growth of the laser fluence, the signal again becomes stable (the mode of a developed laser spark). Historically, this mode was investigated in the 1960s and 1980s in parallel with the study of thermooptical sound generation [9]. For example, shadow pictures of bubble fluctuations were obtained in [10], and, in [11], a description of acoustical–hydrodynamic phenomena under a laser breakdown in a liquid is given. No interesting statistical effects were revealed in this case.

Thus, the amplitude instability of the sound signal under irradiation of real liquids characterizes only a limited range of laser fluence. As was demonstrated in the aforementioned papers [6, 7], the amplitude histograms are an important instrument for studying the acoustic responses in the instability range. In [12], the histogram method was studied from the point of view of its diagnostic potential by using latex suspensions as test objects.

In the present paper, detailed amplitude histograms are obtained, first, as the result of computer simulations and, second, as an experimental result.

THEORY

The phenomenological model described above is taken as the basis for studying the nonstationary cavitation component of the acoustic signal. From the quan-
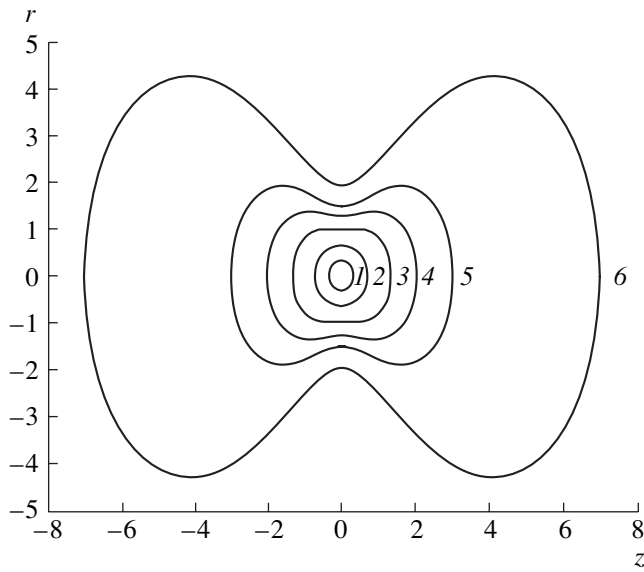
Fig. 2. Determination of the focal region configuration that is used for the calculations. The curves define the regions with the energy flux density ε satisfying the relation $\varepsilon_b \leq \varepsilon \leq \varepsilon_m$ for $\zeta = \varepsilon_m/\varepsilon_b =$ (*1*) 1.1, (*2*) 1.5, (*3*) e (= 2.72…), (*4*) 5, (*5*) 10, and (*6*) 50, where ε_m is the energy flux density at the focal spot center.

titative point of view, it is based on the following assumptions.

First, the suspension is assumed to be monodisperse, and only the cavitation component of the signal is taken into account. The amplitude of the signal from one particle is nonzero only if the density of the optical energy flux ε at the point of the particle position is higher than the threshold density of the energy flux ε_{th} necessary for the formation of an expanding bubble. The signal amplitude is assumed to be proportional to the difference between the absorbed and threshold energies [7]. We normalize the signal amplitude to the signal amplitude of the particle that has absorbed twice the threshold energy. In this case, the normalized (dimensionless) signal amplitude $p(\varepsilon)$ is given by the expression

$$p(\varepsilon) = (\varepsilon - \varepsilon_{th})/\varepsilon_{th}. \qquad (2)$$

Second, we assume that the total amplitude of the cavitation contribution to the signal generated in a monodisperse suspension is the sum of the signal amplitudes from single particles. This is true if the difference of the arrival times of sound pulses at the receiver is small in comparison to the characteristic length of a signal from one particle, which is determined by the upper frequency of the reception band.

Third, we simulate a typical experimental situation, where the longitudinal dimension of the focal spot l is greater than the transverse dimension of the focal spot a (the dimension of the beam waist).

Moreover, we assume that the suspension has a small concentration, so that the influence of absorption and scattering of optical radiation by particles on the density distribution of the energy flux is negligible. In this case, the density distribution of the energy flux in the vicinity of the focus can be calculated within the framework of the quasi-optical approximation. In the cylindrical coordinates r and z, it has the form [13]

$$\varepsilon(z, r) = \frac{\varepsilon_m}{1 + (z/l)^2} \exp\left\{-\frac{(r/a)^2}{1 + (z/l)^2}\right\}, \qquad (3)$$

where ε_m is the density of the energy flux at the center of the focal spot.

Within the model under consideration, it is possible to calculate such important characteristics of the process of signal generation as the average number of particles above the threshold $\langle N_{th} \rangle$ and the average value of the signal amplitude $\langle p_N \rangle$ in a series of tests with irradiation of a monodisperse suspension containing N particles.

Let us preliminarily calculate an important quantity, namely, the volume of the region $V(\varepsilon_b)$ where the density of the radiation energy flux exceeds ε_b ($\varepsilon_b \leq \varepsilon \leq \varepsilon_m$). The boundary of this region is determined by the equation

$$r^2 = (1 + z^2) \ln \frac{\varsigma}{1 + z^2}, \qquad (4)$$

where $\zeta = \varepsilon_m/\varepsilon_b$ and the longitudinal and transverse coordinates are measured in the units of the longitudinal and transverse dimensions of the focal spot, respectively. The shape of the boundary depends on the ratio between the value of the parameter ζ and the number e (see Fig. 2). When $\zeta > e$, the boundary point most distant from the axis is located at the point $z = \pm\sqrt{\zeta/e - 1}$ at the distance $r = \sqrt{\zeta/e}$. After simple integration, we obtain the following expression for the desired volume:

$$V(\varepsilon_b)$$
$$= \frac{8\pi}{3} a^2 l \left(\frac{1}{6}(\varsigma - 1)^{3/2} + \sqrt{\varsigma - 1} - \arctan\sqrt{\varsigma - 1}\right). \qquad (5)$$

Since the particles are distributed over the volume randomly and independently of each other, the average number of particles above the threshold is determined by the product of the particle concentration n by the volume $V(\varepsilon_{th})$ of the region where the density of the radiation energy flux exceeds the threshold:

$$\langle N_{th} \rangle = nV(\varepsilon_{th})$$
$$= \frac{8\pi}{3} na^2 l \left(\frac{1}{6}(\Delta\varepsilon)^{3/2} + \sqrt{\Delta\varepsilon} - \arctan\sqrt{\Delta\varepsilon}\right), \qquad (6)$$

$$\Delta\varepsilon = \frac{\varepsilon_m - \varepsilon_{th}}{\varepsilon_{th}}.$$

Let us note useful asymptotic relations following from Eq. (6):

$$\langle N_{th} \rangle \approx \frac{4\pi}{3} n a^2 l (\Delta\varepsilon)^{3/2}, \quad \Delta\varepsilon \ll 1,$$

$$\langle N_{th} \rangle \approx \frac{4\pi}{9} n a^2 l (\Delta\varepsilon)^{3/2}, \quad \Delta\varepsilon \gg 1.$$

The signal amplitude is represented by the sum of independent responses from single particles; therefore, the relation

$$\langle p_N \rangle = \int_{\varepsilon_m}^{\varepsilon_{th}} p(\varepsilon_b) n \, dV(\varepsilon_b) \tag{7}$$

is valid. Using Eqs. (2) and (5), from Eq. (7) we obtain an equation for the average value of the signal amplitude:

$$\langle p_N \rangle = \frac{8\pi}{3} n a^2 l \left(\frac{1}{3} (\Delta\varepsilon)^{3/2} - \sqrt{\Delta\varepsilon} + \arctan \sqrt{\Delta\varepsilon} \right). \tag{8}$$

The following asymptotic forms are valid:

$$\langle p_N \rangle \approx \frac{8\pi}{15} n a^2 l (\Delta\varepsilon)^{5/2}, \quad \Delta\varepsilon \ll 1,$$

$$\langle p_N \rangle \approx \frac{8\pi}{9} n a^2 l (\Delta\varepsilon)^{3/2}, \quad \Delta\varepsilon \gg 1.$$

In the case where only one particle occurs in a sample, it is even possible to obtain an analytical expression for the density of the probability distribution for the normalized signal amplitude p_1, which takes on random values p determined by Eq. (2), depending on the particle position at the instant of irradiation. Let this particle be present in a cell with volume V. In this case, the distribution density $\varphi_{p_1}(p)$ is determined by the expression

$$\varphi_{p_1}(p) = \left(1 - \frac{V_{th}}{V} \right) \delta(p) + \left| \frac{1}{V} \frac{dV(\varepsilon_b)}{dp(\varepsilon_b)} \right|, \tag{9}$$

where $\delta(p)$ is the delta function and $V_{th} = V(\varepsilon_{th})$ is the volume of the region where the density of the energy flux exceeds the threshold value. We assume that $\varepsilon_m \geq \varepsilon_{th}$ and, in addition, that the "over-threshold" range $\varepsilon_m \geq \varepsilon \geq \varepsilon_{th}$ is fully contained in the cell region. The distribution given by Eq. (9) is of a discrete–continuous character. The first addend formally determines the finite probability of the fact that the signal amplitude acquires a zero value; i.e., the particle is located in the region where the density of the energy flux is below threshold. The second addend describes the distribution density in the range $0 < p < \gamma - 1$, corresponding to the situation where the particle is in the "over-threshold" region.

Substituting Eqs. (2) and (5) into Eq. (9), we finally obtain

$$\varphi_{p_1}(p) = \left(1 - \frac{V_{th}}{V} \right) \delta(p)$$

$$+ \frac{2\pi}{3} \frac{a^2 l}{V} \left(1 + \frac{\gamma}{p+1} - 2\frac{p+1}{\gamma} \right) \frac{\gamma}{(p+1)^2} \left(\frac{\gamma}{p+1} - 1 \right)^{-1/2}, \tag{10}$$

$$0 \leq p < \gamma - 1,$$

where the parameter $\gamma = \varepsilon_m / \varepsilon_{th}$ is the density of the energy flux at the center of the focal spot when normalized to the threshold density of the energy flux. It is interesting to note that, at $\gamma \gg 1$, there is a sufficiently broad range of values of the signal amplitude $p \ll \gamma - 1$ within which the distribution density is of a power character: $\varphi_{p_1}(p) \propto (p+1)^{-7/2}$.

NUMERICAL SIMULATION WITH THE MONTE CARLO METHOD

To verify the analytical results obtained above and to analyze the statistical characteristics of the cavitation component of the sound signal formed by a large number of particles, we conducted a simulation with the Monte Carlo method. The simulation was based on the assumption that N_p particles of equal size were distributed randomly in a cylindrical cell with diameter D and length L. The distribution of the density of the energy flux in the cell was described by Eq. (3). In this case, the center of the focal spot was located at the cell center, and the density of the energy flux ε_m at this center was given in the units of the threshold energy density ε_{th}, which was the same for all particles (i.e., the dimensionless parameter γ was preset). We performed N_t tests, which corresponded to the actual experimental situation of sample irradiation by a series of laser pulses. In each new test, the particle coordinates had new random values.
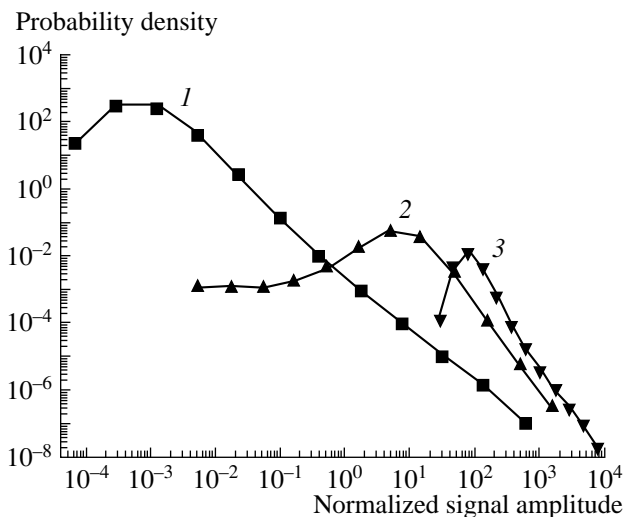
The normalized signal amplitude for each of the N_t tests was calculated as the sum of the normalized signal amplitudes from each of N_p particles, which were described by Eq. (2).

The ratio of the focal spot dimensions corresponded to a typical experimental situation, wherein the longitudinal dimension of the spot exceeds the transverse one by a factor of 10 to 100. To simplify calculations, as the cell dimensions, we used the minimal dimensions satisfying the condition that, in the range of interest of the energy density of optical radiation ($\gamma = \varepsilon_m / \varepsilon_{th}$ varies from 1 to 10^4), outside the cell, the density of the energy flux of optical radiation was below the threshold. Correspondingly, the following dimensions of the focal spot and the cylinder (in the units of the transverse dimension of the focus) were adopted: $a = 1$, $l = 30$, $L = 6000$, and $D = 125$.

Probability density
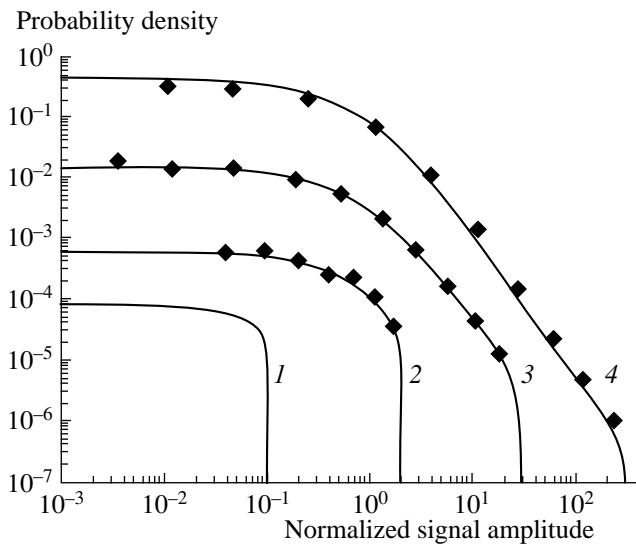
Fig. 3. Cavitation component of the signal. The probability distribution density of the normalized signal amplitude in double logarithmic coordinates for the series obtained with the values of the energy parameter $\gamma = $ (*1*) 1.1, (*2*) 3, (*3*) 30, and (*4*) 300. The number of particles is $N_p = 100$. The average number of particles above the threshold is less than unity. The solid curves correspond to analytical calculation by Eq. (10), and the diamonds correspond to numerical simulation.

Two situations were considered, and, for each situation, several series of irradiation experiments were simulated. The number of tests in each series was $N_t = 300\,000$.

Probability density

Fig. 4. Cavitation component of the signal (results of numerical simulation). The probability distribution density of the normalized signal amplitude in double logarithmic coordinates for the series obtained with the values of the energy parameter $\gamma = $ (*1*) 1000, (*2*) 3000, and (*3*) 10^4. The number of particles is $N_p = 100$. The average number of particles above the threshold is 1.8, 9.4, and 57.

First, we investigated the form of the probability distribution density for the amplitude of the sound signal at a fixed particle concentration and different values of the density of laser energy. The number of particles was taken to be 100, and the normalized density of the energy flux at the center of the focal spot, $\gamma = \varepsilon_m/\varepsilon_{th}$, varied from one series to another within the range $3–10^4$.

Second, the form of the same function at a fixed energy and different values of particle concentration in the suspension was studied. The value of γ was fixed at 10^4, and the number of particles varied from 10 to 10^4.

For each series of tests, we calculated the probability distribution density for different values of the signal amplitude. To do this, from the array of amplitude values we excluded the zero values with nonzero probability, which were only formally described by the probability density (the first addend in Eq. (2)). Then, the array of amplitude values was nonuniformly broken into several intervals, and the distribution density was approximated by the quantity $(\Delta n(i)/N)/\Delta p(i)$, where $\Delta n(i)$ was the number of events with amplitudes falling within the ith interval of width $\Delta p(i)$.

Figures 3 and 4 show the results obtained by simulating the energy dynamics of the signal amplitude distribution for a suspension with 100 particles for different densities of the energy flux of optical radiation. Figure 3 presents the results of numerical simulation for the range of the energy densities corresponding to the case where the average number of particles above the threshold is smaller than unity. The results of calculations according to Eq. (10), where only the second addend was taken into account, are also presented in this figure. The results of analytical calculations coincided with the results of numerical simulations. At small values of the energy parameter γ, the distribution density is almost constant within the whole range and sharply decreases to zero at $p = \gamma - 1$. As γ grows, a region appears where, as was mentioned above, the distribution has a power-law character with an index of 7/2. The results of numerical simulations at large energies γ, when the average number of particles above the threshold is greater than unity, are given in Fig. 4. In this case, the distribution density becomes nonmonotonic and is not described by Eq. (10). More illustratively, the change in the form of the distribution density with the growth of the average number of particles above the threshold is demonstrated by the simulation results for the concentration dynamics of the amplitude distribution, which are shown in Fig. 5. Thus, when the average number of particles above the threshold becomes greater than unity, a local maximum arises in the distribution density in the range of small values of p, and a long power tail persists in this case. When the average number of particles above the threshold is small, the distribution density has a complex form and may have a local minimum apart from the maximum (curve *1* in Fig. 5). If the average number of particles

above the threshold grows, the distribution density acquires the form of a normal distribution.

EXPERIMENT

In contrast to the model situation considered above, in experimental practice, in the case of irradiation of suspensions, one has to deal with several competing mechanisms of optoacoustic conversion simultaneously. The experiment consisted in the irradiation of samples by the focused second harmonic radiation of a YAG laser with a pulse energy from 0.3 to 20 mJ and a pulse length of 10 ns. A cell with a volume of 80 ml was used as the sample container. The cell was equipped with a piezoelectric pressure sensor with a sensitivity of 30 μV/Pa in a measuring band of 1 MHz. The geometry of optoacoustic conversion corresponded to Fig. 1, and the distance from the beam axis to the pressure receiver was 7 mm. The beam diameter before the focusing lens was 10 mm. The irradiation was conducted in several series of 2000 pulses with a subsequent statistical processing. Within each series, the energy of the laser pulses was constant.

The signal from the receiver output was fed to the first channel of a 12-digit two-channel A/D converter (with a maximum sampling frequency of 40 MHz). A signal from a photodiode was fed to the second channel to monitor the energy of laser pulses. The amplitude of each sound signal was multiplied by the ratio of the laser pulse energy averaged over the series to the current energy. As the result of processing, the histograms demonstrating the amplitude distribution of sound pulses in a series were plotted.

Figure 6 shows histograms in double logarithmic coordinates, which correspond to optoacoustic conversion in the case of irradiation of singly purified distilled water. Such water can be considered as a model of a diluted suspension.

Figure 7 demonstrates the histograms obtained in the case of irradiation of the same water sample with the addition of particles of black Indian ink with a typical diameter of 3 μm. Here, the thermooptical sound generation is more pronounced in comparison with Fig. 6. The histogram shape is approximately the same; however, to observe the realizations corresponding to different mechanisms (sections *2* and *3*), it was necessary to increase to a certain extent the focal length of the lens in this situation as well.

The presence of rectilinear sections in the plots in both Figs. 6 and 7, which was predicted in the theoretical part of the paper, is evidence of the fact that the flat "tails" of the distributions are characterized by decreasing power functions, with the indices depending on the energy in a series and on the particle concentration. This is especially characteristic of the realizations with prevailing cavitation contributions. In section *2*, the values of these indices vary from 1 to 4.5 (remember that, in the theoretical part of this paper, we obtained a
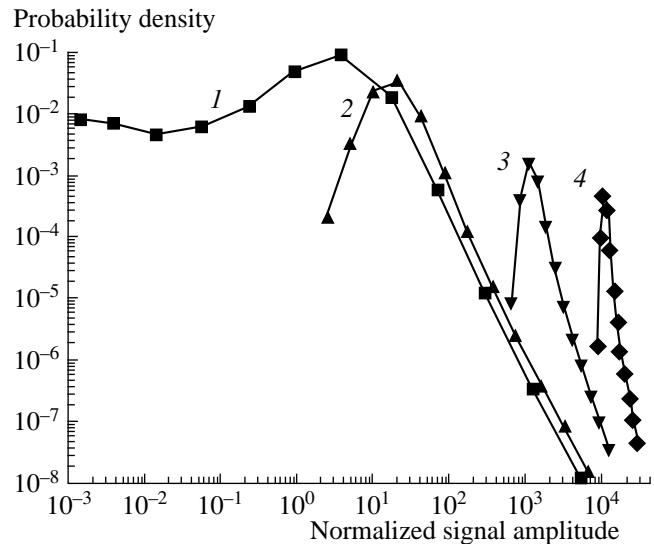
Fig. 5. Cavitation component of the signal (results of numerical simulation). The probability distribution density of the normalized signal amplitude in double logarithmic coordinates for the series obtained with the values of the energy parameter $\gamma = 10^4$ and the number of particles in the suspension $N_p = $ (*1*) 10, (*2*) 30, (*3*) 1000, and (*4*) 10^4. The average number of particles above the threshold is 5.7, 17, 570, and 5700.
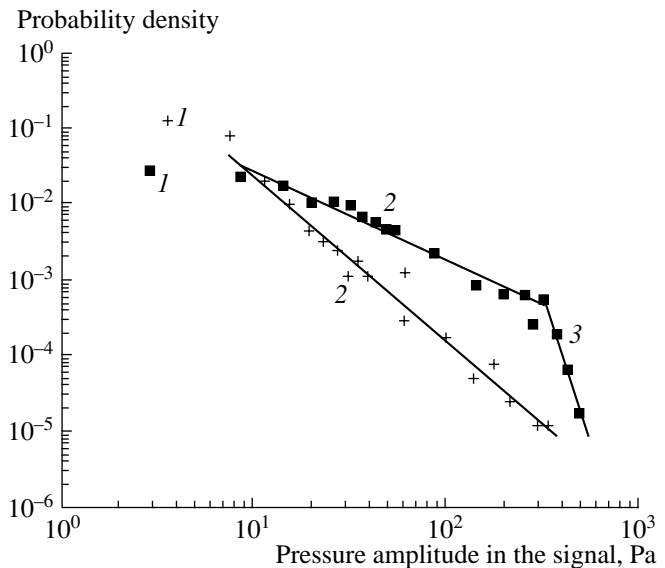
Fig. 6. Experiment. The density of the probability distribution for the amplitude in a series of sound pulses. Two series of irradiation of singly purified distilled water with energy values of 0.3 mJ (crosses) and 1 mJ (squares). The focal distance of the lens is equal to 10 cm. (*1*) Realizations where the thermooptical mechanism of sound generation prevails, (*2*) realizations where the main contribution into sound generation belongs to the cavitation phenomena with a relatively small number of "participant" particles, and (*3*) realizations where the threshold is exceeded for a large number of particles (in these realizations, luminescence is observed in the focal region).

Probability density
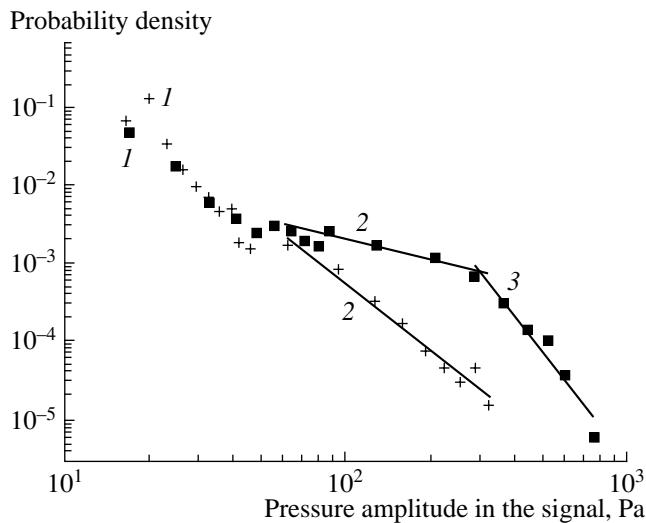
Fig. 7. Experiment. The density of the probability distribution for the amplitude of sound signals. Two series of irradiation of a suspension with Indian ink particles (volume concentration of 10^{-6}) with the energy values of 13 mJ (crosses) and 17 mJ (squares). The focal distance of the lens is 14 cm. Notations are the same as in the previous figure.

value of 7/2 for the analogous index in the case of irradiation of a monodisperse suspension). Sharp bends of rectilinear sections clearly indicate the realizations corresponding to the change of the optoacoustic conversion mechanisms.

CONCLUSION

The flat tails of the amplitude distributions observed in the optoacoustics of suspensions are apparently manifestations of both the fractal nature of phase transformations in disperse media [14] and certain fractal properties of wave processes [15]. In particular, it is known that fractal effects in radiation may occur already in the case of an aggregate of independent point radiators with a fractal distribution in space (which corresponded to the conditions of optoacoustic experiments with low-concentration suspensions).

The shapes of the histograms for the amplitude of the acoustic signals obtained by irradiating the test samples of suspensions with several series of laser pulses demonstrate the change of the competing conversion mechanisms and, in a certain way, depend on the energy density of a laser pulse and on the concentration of the suspension particles, which opens up possibilities for an optoacoustic diagnostics suitable for very small particle concentrations.

REFERENCES

1. S. V. Egerev and A. E. Pashin, Izv. Akad. Nauk SSSR, Fiz. Atmos. Okeana **27** (3), 259 (1991).
2. S. V. Egerev, O. B. Ovchinnikov, and A. E. Pashin, Pis'ma Zh. Tekh. Fiz. **18** (21), 71 (1992) [Sov. Tech. Phys. Lett. **18**, 715 (1992)].
3. A. A. Karabutov, I. M. Pelivanov, N. B. Podymova, and S. E. Skipetrov, Kvantovaya Élektron. (Moscow) **29** (3), 215 (1999).
4. W. Beatty, S. Meresse, and P. Gounon, J. Cell Biol. **145**, 689 (1999).
5. A. A. Karabutov and E. Savateeva, Proc. SPIE **4256**, 179 (2003).
6. S. V. Egerev, Ya. O. Simanovskii, and A. E. Pashin, in *Advances in Nonlinear Acoustics* (World Sci., Singapore, 1993), pp. 436–442.
7. S. S. Alimpiev, Ya. O. Simanovskii, S. V. Egerev, and A. E. Pashin, Laser Chem. **16**, 63 (1995).
8. A. C. Tam, Rev. Mod. Phys. **58** (2), 381 (1986).
9. T. Autrey, S. Egerev, N. Foster, and A. Fokin, Rev. Sci. Instrum. **74** (1), 628 (2003).
10. L. M. Lyamshev, *Laser Thermooptical Excitation of Sound* (Nauka, Moscow, 1979) [in Russian].
11. S. V. Egerev and A. E. Pashin, Zh. Tekh. Fiz. **51** (1), 226 (1981) [Sov. Phys. Tech. Phys. **26**, 138 (1981)].
12. T. A. Dunina, S. V. Egerev, and L. M. Lyamshev, Akust. Zh. **28**, 192 (1982) [Sov. Phys. Acoust. **28**, 116 (1982)].
13. M. B. Vinogradova, O. V. Rudenko, and A. P. Sukhorukov, *The Theory of Waves*, 2nd ed. (Nauka, Moscow, 1990) [in Russian].
14. M. L. Lyamshev, Pis'ma Zh. Tekh. Fiz. **26** (8), 56 (2000) [Tech. Phys. Lett. **26**, 341 (2000)].
15. V. V. Zosimov and L. M. Lyamshev, Usp. Fiz. Nauk **165**, 361 (1995) [Phys. Usp. **38**, 347 (1995)].

Translated by M. Lyamshev

Acoustic Testing of the Vortex Structure Produced by an Air Flow about an Array of Cylinders

A. B. Ezerskiĭ, P. R. Gromov, P. L. Soustov, and V. V. Chernov

Institute of Applied Physics, Russian Academy of Sciences, ul. Ul'yanova 46, Nizhni Novgorod, 603950 Russia
e-mail: vcher@appl.sci-nnov.ru
Received August 4, 2003

Abstract—Results of experiments on the scattering of a plane ultrasonic wave from a vortex wake formed in an air flow behind a lattice of vertical cylinders are presented. The lattice is periodic in the direction perpendicular to the oncoming flow. The experiments are performed in a wind tunnel for two values of the Reynolds number, namely, Re = 75 and 500, and for lattices with different numbers of cylinders and with different lattice periods $g = (2.5-15)d$ (where d is the diameter of the cylinders). The measured parameters of the scattered waves are used to estimate the degree of transverse correlation between the vortex wakes formed behind the cylinders for flows with different Reynolds numbers. The results obtained from an analysis of the characteristics of the scattered sound are compared with the results of direct hot-wire anemometer measurements and with the data obtained by other researchers. © 2005 Pleiades Publishing, Inc.

By now, remote acoustic testing of vortex and temperature fluctuations in air flows has been demonstrated on a laboratory scale for a number of well-known flow types: a Karman vortex street behind a circular cylinder [1–3], vortex rings [4, 5], vortices behind a heated cylinder [6], buoyancy-driven heated gas flows [7], and a heated jet [8]. The experiments determined the parameters of hydrodynamic flows that could be extracted from the characteristics of scattered sound. The basic idea of these experiments consisted in the comparison between the experimental data obtained for flows with controlled parameters and the theoretical calculations based on models with small numbers of parameters, such as the circulation of vortices, the velocity of their motion, and the amount of heat transferred by them (in the case of vortices behind a heated cylinder).

In the recent years, the object of intensive studies has been the wake behind an array of circular cylinders placed in a plane-parallel air (or water) flow [9–14]. From a practical point of view, the interest taken in these problems can be explained by the fact that sets of such arrays placed in air or water flows are often used as efficient cooling systems in different kinds of reactors. Visualization of such flows (see [9] and the literature cited there) has shown that the vortex wakes formed behind different cylinders may interact with each other. This interaction may lead to a synchronization of oscillations in the flow and to the formation of different kinds of flows [9–11], depending on the parameters of the array (the number of cylinders and the distance g between them) and on the Reynolds number (Re = $U_0 d/\nu$, where U_0 is the velocity of the oncoming flow and ν is the kinematic viscosity of air).

Studies of the vortex structures formed behind arrays of cylinders show that the control parameter of the flow (at a constant Re of the oncoming flow) is the distance g between the cylinders in the direction perpendicular to the oncoming flow. Depending on the value of this parameter, the vortex wakes can be conditionally divided into weakly coupled ($g \geq 4.5d$) and strongly coupled ($g \leq 2.5d$).

For weakly coupled wakes (see, e.g., [9, 11, 12]), the formation of an individual Karman street behind every cylinder is typical. From visualization experiments, it was found that the vortex streets behind different cylinders may be either in phase or in antiphase. However, according to [9], only the state in which $\Delta\varphi = (2n - 1)\pi/2$ (where $\Delta\varphi$ is the phase difference between vortices characterized by the same sign of circulation and belonging to neighboring vortex streets and $n = 1, 2, 3\ldots$) is stable and can persist downstream as long as one likes. A flow with $\Delta\varphi = 2n\pi$ persists within only 1–2 spatial periods of the vortex structure downstream from the cylinders; then, vortices that have the same sign of circulation Γ (where $\Gamma = \int \vec{\upsilon} dl$ and $\vec{\upsilon}$ is the vortex velocity field) but belong to neighboring streets merge forming a single "consolidated" periodic vortex structure behind every pair of cylinders. A visualization of the flow behind an array of 16 cylinders with $g = 5d$ and Re = 75 was described in [16]. The wake behind the cylinders was found to exhibit a spatiotemporal chaos with randomly formed "dislocations" or amplitude holes typical of this regime and also with phase jumps by π in the direction perpendicular to the flow.

Strongly coupled flows are characterized by a strong spatial inhomogeneity across the flow (along the array). For example, the visualization of a wake behind two cylinders with $g = 2.5d$ [11] revealed a strong asymme-
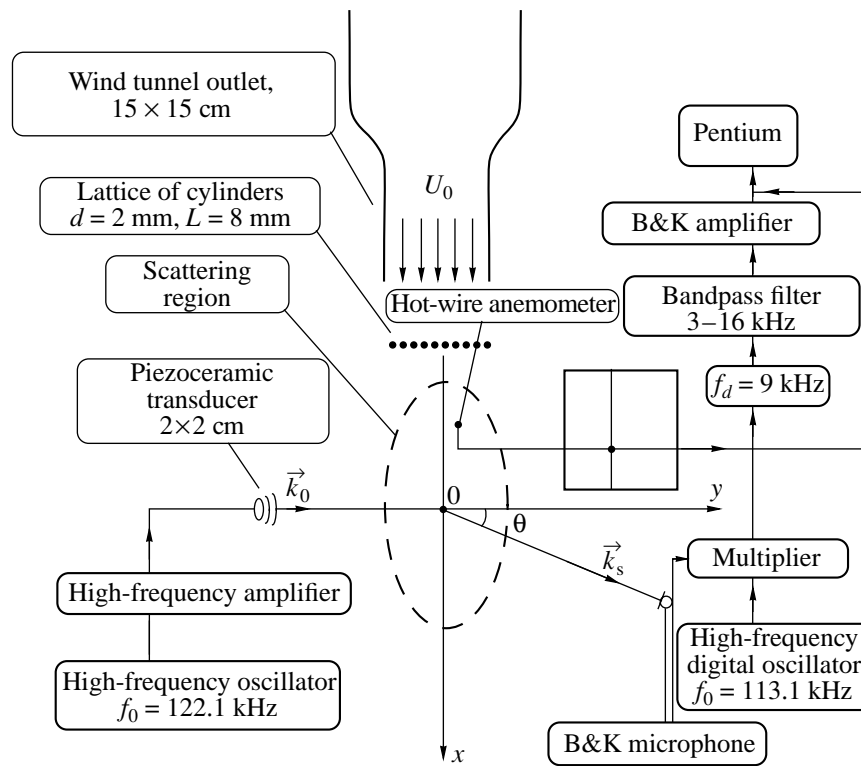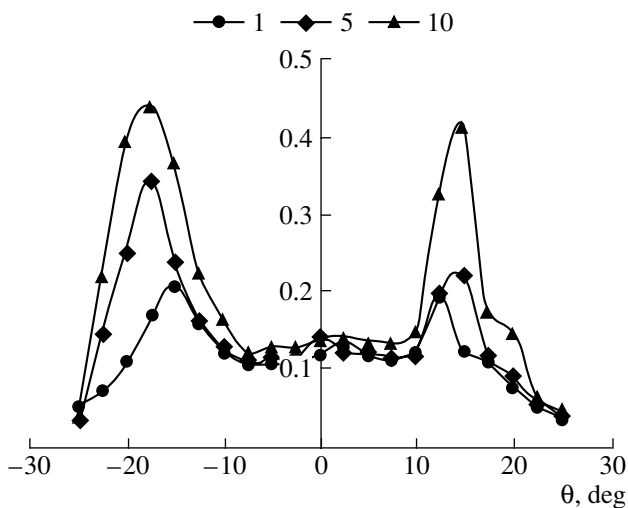
Fig. 1. Schematic diagram of the experiment.

Fig. 2. Amplitudes of scattering into the harmonics of numbers +1 and −1 versus the scattering angle θ for the cases of one, five, and ten cylinders at Re = 75.

try of vortex streets behind different cylinders. One more important feature of such a wake is the possibility of "switching" between the asymmetric states [10], when the width of the wake becomes alternately greater behind the first and the second cylinder. The lifetime of the flow in one of the states is inversely proportional to the Reynolds number and may reach 10^2 time periods

of the vortex structure at Re = 70. A visualization of the flow behind an array of 21 cylinders was performed in [13] for the case of a strong coupling and for different Reynolds numbers. In this experiment, a smooth increase in the Reynolds number resulted in the recirculation zones behind different cylinders beginning to deviate from their positions and combining into the so-called clusters. Then, as the Reynolds number drastically increased to Re = 100, oscillations with the Strouhal frequency ($f_{st} = fd/U_0$, where f is the vortex separation frequency) were initiated in each of these clusters. The flow inside each of the clusters was fully synchronized and represented a set of Karman streets with $\Delta\varphi = 2n\pi$; the number of these streets was approximately two times smaller than the number of cylinders behind which the given cluster was formed. The width of a cluster and the place of its formation varied in a random way depending on the initial conditions. The global modes of oscillation in different clusters were in antiphase, and the flow between them had the form of an alternating mode.

All aforementioned studies of the synchronization of vortex wakes in air or water flows were mainly purely experimental. To prove the presence of synchronization, researchers used instantaneous photographs of the flows. However, from instantaneous photographs, one cannot quantitatively estimate the degree of the flow synchronization behind an array of cylinders. We managed to obtain a quantitative characteristic of

this effect with the help of remote acoustic testing. Varying the number of cylinders and the distance between them, as well as the velocity of the oncoming flow, we studied the scattering from both weakly and strongly coupled flows. We compared the experimental results on sound scattering with the results of direct measurements of vortex fluctuations by hot-wire anemometers. In particular, we measured the coherence length of a vortex wake in the transverse direction for different parameters of the vortex flow. The results of these measurements agree well with the data from acoustic testing.

EXPERIMENTS ON SOUND SCATTERING

Experiments were performed in an air flow produced in the low-turbulence (the turbulent velocity fluctuation level of the oncoming flow was below 0.4%) wind tunnel of the Institute of Applied Physics of the Russian Academy of Sciences with a working section of $30 \times 30 \times 120$ cm. A schematic diagram of the experiment is shown in Fig. 1 (top view).

We studied the scattering of ultrasound of frequency $f_0 = 122.1$ kHz (with wavelength $\lambda_0 = 2.7$ mm) by the vortex flow formed behind an array of vertically oriented cylinders with diameter $d = 2$ mm and a length of 30 cm. The cylinders were rigidly fixed in symmetric holes made in the upper and lower walls of the working section of the wind tunnel in such a way that they were positioned at regular intervals in a row across the flow with the array period $g = 2–24d$ (this value was varied depending on the experimental conditions), at a distance of 30 cm from the confuser outlet. The velocity of the oncoming flow was varied so as to study the scattering of both laminar (Re = 75) and turbulent (Re = 500) vortex flows. The number of cylinders was varied from one to ten. The source of ultrasound was a piezoceramic transducer placed behind a baffle with a square opening of side $a = 2$ cm. The transducer was placed at a distance of 65 cm from the center of the vortex street to provide for the validity of the Fraunhofer zone approximation ($D_\Phi \sim \Lambda^2/\lambda_0 \sim 30$ cm, where Λ is the size of the transducer). To measure the parameters of the ultrasound, we used a B&K 4135 high-frequency microphone, whose signal was heterodyned to a frequency range of 0–20 kHz (the operating range of the A/D converter). The microphone was mounted on a moving rod at a fixed distance of 1.6 m from the center of the scattering region, and its position was varied in the angular range from 45° to –45° with respect to the direction toward the source of ultrasound. The spectral characteristics of the scattered signal were measured using a computer.

As is known (see, e.g., [1]), the amplitude of sound scattered from an "ideal" infinite Karman vortex street is represented by a set of harmonics propagating symmetrically about the direction of incident sound. The amplitude of each of these harmonics is proportional to the vortex circulation Γ in the vortex street. The fre-
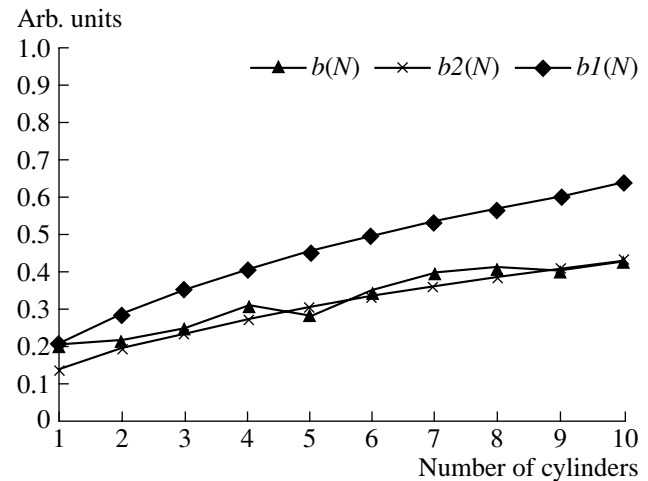

Fig. 3. First harmonic amplitude versus the number of cylinders at Re = 75.

quency of each harmonic is shifted with respect to the frequency of incident sound f_0 by a quantity that is a multiple of the vortex separation frequency (i.e., the Strouhal frequency f_{sh}): $\Delta f_n = n f_{sh}$, where $n = \pm 1, 2\ldots$.

Since every single vortex mainly scatters sound in the forward direction, experimental observation is usually possible only for harmonic nos. +1 and –1. In our experiments, we measured the directional patterns of harmonic nos. +1 and –1 for different numbers of cylinders and for two different values of the Reynolds number. Figure 2 shows the rms amplitudes of these harmonics obtained in a 3-Hz frequency band for the cases of one, five, and ten cylinders at Re = 75. One can see a certain asymmetry in the amplitudes and angles that occurs for the scattering into harmonic nos. +1 and –1 irrespective of the number of cylinders in the array. This asymmetry is caused by the fact that, in our experiment, the angle between the direction of incident sound $\vec{k}_0$ and the direction of the vortex motion differs from $\pi/2$ by ≤3°. Calculations show (see, e.g., [1]) that this deviation leads to the asymmetry observed in the experiment.

An increase in the number of cylinders in the array (i.e., an increase in the number of Karman streets) leads to an increase in the scattered signal amplitude. Figure 3 shows the dependence of the mean amplitude of the first harmonic ($= \dfrac{A_{+1} + A_{-1}}{2}$, where A_{+1} and A_{-1} are the amplitudes of harmonic nos. +1 and –1, respectively) on the number of cylinders in the array at a constant array period $g = 4d$ and a Reynolds number Re = 75.

The same figure shows two approximations of the aforementioned dependence by power laws ($\sqrt{n}$, where n is the number of cylinders in the array). Curve *1* is
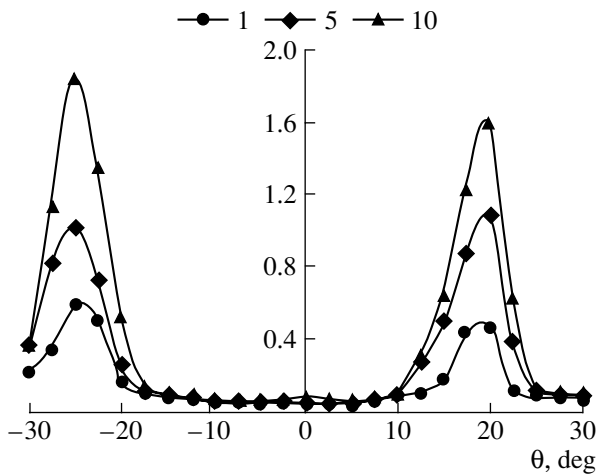
Fig. 4. Amplitudes of scattering into the harmonics of numbers +1 and −1 versus the scattering angle θ for the cases of one, five, and ten cylinders at Re = 500.

Fig. 5. First harmonic amplitude versus the number of cylinders at Re = 500.

plotted according to the formula $a_n = a_1 \sqrt{n}$, where a_1 is the experimentally measured amplitude of sound scattered from the wake behind a single cylinder and curve *2* follows the formula $a_n = a_{10} \sqrt{n/10}$, where a_{10} is the experimentally measured amplitude of sound scattered from the wake behind ten cylinders. From comparison of the experimental results and the theoretical dependence, it follows that, in our experiment, the scattered signal amplitude grows more slowly than the root of the number of scatterers (i.e., the number of vortex wakes). This tendency is most pronounced for small values of *n*: curve *2* gives a much better approximation of the experimental data for the large number of cylinders than does curve *1*.

When the Reynolds number is Re = 500, the dependence of the scattered sound amplitude on the number of cylinders exhibits a different behavior. The results of measuring the characteristics of scattered sound in this case are shown in Figs. 4 and 5. Figure 4 represents the directional patterns of harmonic nos. +1 and −1.

One can see that, as in the case of Re = 75, the scattering into harmonic nos. +1 and −1 exhibits an asymmetry. However, at certain conditions, this effect is much weaker. According to the analytical calculation performed in [1], an increase in the flow velocity (in the experiment, Re was varied by varying the flow velocity at a constant viscosity and a constant diameter of the cylinders) leads to an increase in the scattering amplitude because of the growing circulation Γ of vortices in the vortex streets. Unlike the case of Re = 75, the scattering amplitude is proportional to the number of cylinders in the array.

Figure 5 shows the mean spectral amplitude characterizing the scattering into the first harmonic versus the number of cylinders in the array. This dependence is almost perfectly approximated by a function $\sim \sqrt{n}$.
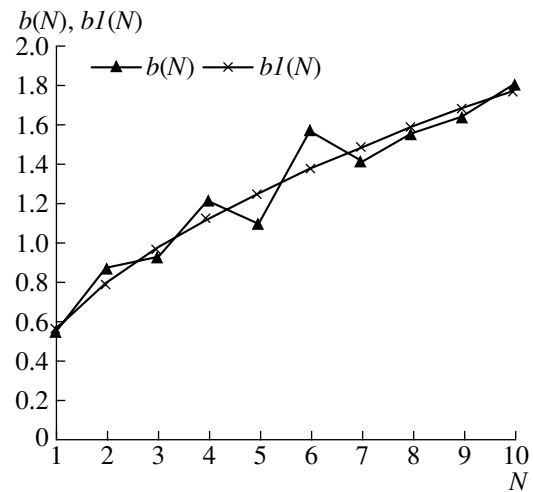
To reveal the origin of the difference in the dependences of the sound amplitude on the number of cylinders, we performed detailed measurements of the velocity fields in the vortex wakes behind the arrays of cylinders.

## MEASUREMENTS OF THE VORTEX VELOCITY FIELD BY HOT-WIRE ANEMOMETERS

Direct measurements of the vortex velocity field were performed by two hot-wire anemometers. The positions of the sensors along and across the flow could be varied by a traverse gear. The signal from the sensors was amplified and filtered and then supplied to a computer, where it was analyzed by a data-processing code. In the experiment, we measured the following characteristics:

(i) the velocity fluctuation profiles in the wake at fixed numbers of cylinders for different distances between them and for Re = 75 and 500 (Figs. 6 and 7);

(ii) the dependence of the velocity fluctuation amplitude on the coordinate across the flow for different numbers of cylinders at a fixed distance between them for two Reynolds numbers Re = 75 and 500 (Figs. 8 and 9); and

(iii) the coherence function obtained with two sensors and the phase difference as functions of the distance between the sensors in the direction perpendicular to the flow for two Reynolds numbers Re = 75 and 500 (Figs. 10–13).

Figure 6a shows the velocity field in the wake behind a single cylinder at Re = 75. Figures 6b–6d represent the dependence of the velocity fluctuation profile in the wake behind three cylinders on the distance between them in the direction across the flow. As seen from the velocity fluctuation profiles obtained for Re = 75 (Fig. 6), when the cylinders become fairly
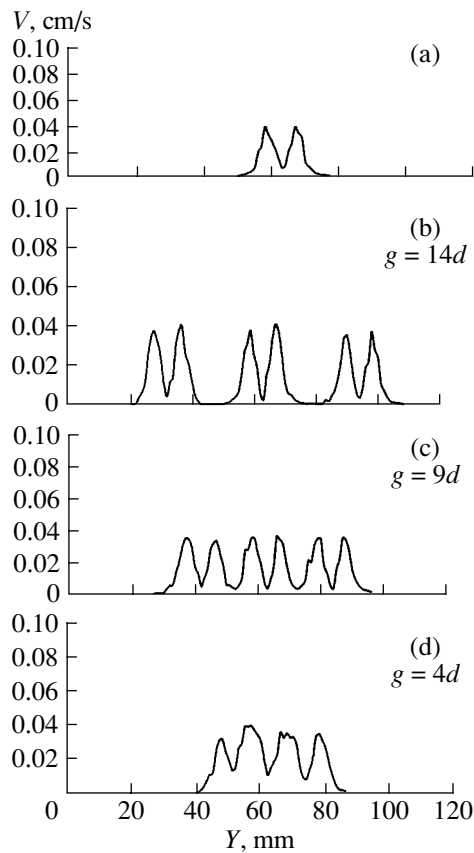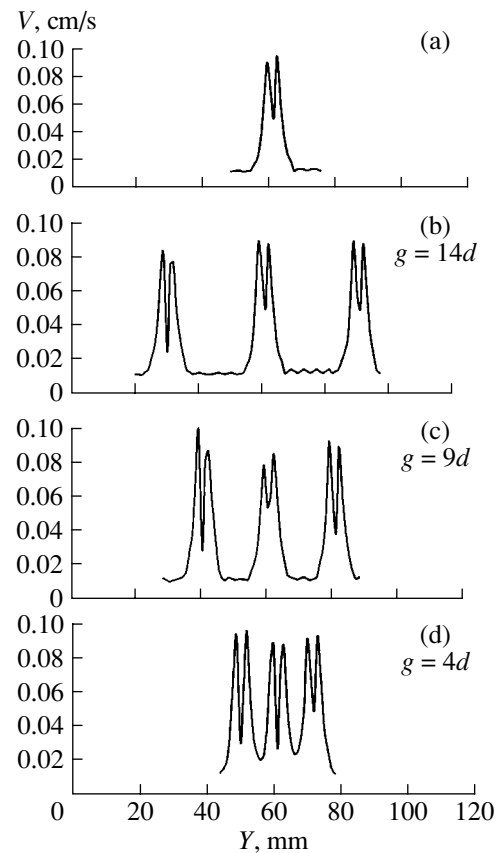
Fig. 6. Fluctuation amplitude of the first harmonic of the vortex velocity field in the wakes behind (a) one cylinder and (b–d) three cylinders for different distances *g* between them at Re = 75.
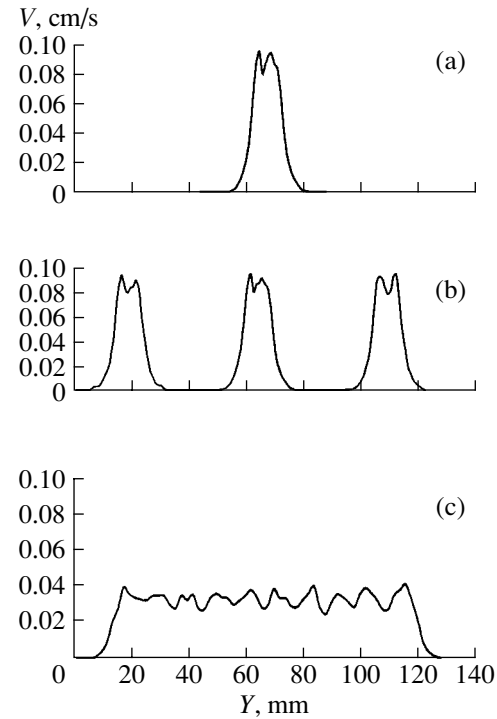

Fig. 7. Fluctuation amplitude of the first harmonic of the vortex velocity field in the wakes behind (a) one and (b–d) three cylinders for different distances *g* between them at Re = 500.

close to each other, the vortex streets merge and, at $g = 4d$, two vortex streets are present instead of three. These plots agree well with the visualization of the confluence of vortex streets formed behind different cylinders with the same parameters of the array and the same Reynolds numbers as in our experiment [8]. For large distances between the cylinders, $g = 9d$ and $14d$, the vortex streets do not merge and the number of maxima in the fluctuation profile is twice as great as the number of cylinders.

Similar measurements (see Fig. 7) performed for the case of Re = 500 show that an increase in the Reynolds number suppresses the effect of the vortex street confluence. For all three periods of the array ($g = 4d$, $g = 9d$, and $14d$), velocity fluctuation profiles typical of a single Karman street are observed behind each of the three cylinders of the array.

From the comparison of the velocity fluctuation profiles obtained for the vortex wakes behind three and ten cylinders at Re = 75 (Fig. 8), it follows that the effect of a pairwise confluence of vortex streets at $g = 4d$ also occurs in extended arrays (see Fig. 8, where 11 maxima and 10 vortex wakes are observed).

The corresponding measurements performed for Re = 500 (Fig. 9) show that, in this case, the vortex streets do not merge. At Re = 500, the width of every vortex street is much smaller then that observed at Re = 75, and the velocity maxima corresponding to different rows of vortices in a single Karman street are much closer to each other (see Figs. 9a and 9b) than at Re = 75. The number of velocity fluctuation maxima observed in Fig. 9c is equal to the number of cylinders; i.e., an individual Karman vortex street is formed behind each of the cylinders.

The fact that vortex streets may merge into pairs or persist separately does not give any definite information on the degree of coherence of the whole vortex wake. To determine the degree of synchronization of the vortex wakes, we measured the coherence function of the signals obtained from two different hot-wire anemometers. The measurements were performed in the wakes behind one, three, and ten cylinders for two values of the Reynolds number, namely, Re = 75 and 500. At first, we determined the maximum of the velocity field fluctuations, which, in our case, was achieved when the sensor position exactly coincided with one of the two vortex rows of the Karman street formed behind
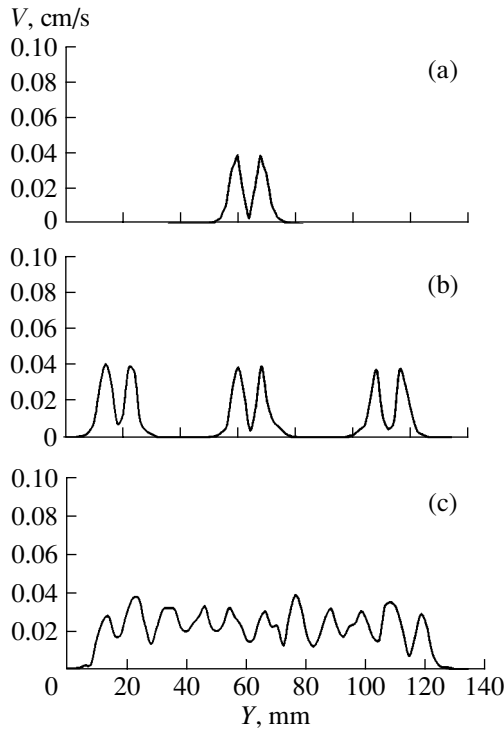
Fig. 8. Fluctuation amplitude of the first harmonic of the vortex velocity field in the wakes behind (a) one, (b) three, and (c) ten cylinders at Re = 75.

Fig. 9. Fluctuation amplitude of the first harmonic of the vortex velocity field in the wakes behind (a) one, (b) three, and (c) ten cylinders at Re = 500.

any of the cylinders. Then, one of the sensors was placed at this maximum and remained fixed, while the other sensor was placed above the first one (the distance along the cylinder axis between the two sensors was less than 2 mm) and then was moved across the wake. We measured the coherence function and the cross-spectrum phase as functions of the distance between the sensors. Such measurements were performed in the wakes behind one, three, and ten cylinders with the same invariable position of the fixed sensor.

The square of the coherence function, γ_{xy}^2, of two signals $x(t)$ and $y(t)$ is determined as (see, e.g., [14])

$\gamma_{xy}^2 = \dfrac{|S_{xy}(f)|^2}{S_x(f)S_y(f)}$, where $S_x(f)$ and $S_y(f)$ are the power spectrum densities of the corresponding signals and $S_{xy}(f)$ is the cross-spectrum density function of the two signals, $x(t)$ and $y(t)$. The latter function is understood as the quantity $S_{xy}(f) = \hat{x}(f)\hat{y}^*(f) = |\hat{x}(f)||\hat{y}(f)|e^{i(\hat{F}x(f) - \hat{F}y(f))}$, where $\hat{x}(f)$ and $\hat{y}(f)$ are the Fourier transforms of the corresponding signals and the asterisk denotes complex conjugation. In elementary statistics, an analog of the coherence function is the square of the correlation coefficient.

The results of measuring the coherence function and the phase difference for the wakes behind one, three, and ten cylinders at Re = 75 are shown in Figs. 10 and 11.

As one can see from Fig. 10a, for one cylinder, the coherence function has two maxima, where it is equal to unity. These maxima exactly correspond to two vortex rows forming the Karman street. As one would expect, the phase difference between the two signals is exactly equal to 180° when the sensors are in two different vortex rows (see, e.g., [15]).

In the case of a three-cylinder lattice, the coherence function broadens and exhibits a single clearly pronounced maximum with $\gamma_{xy}^2 = 1$ and two local maxima with $\gamma_{xy}^2 = 0.85$ and 0.45 on both sides of the maximum $\gamma_{xy}^2 = 1$. At each of the local maxima, the phase difference between the signals of the two sensors has a constant value (see Fig. 11). Presumably, the broadening of the coherence function is related to the confluence–synchronization effect, which was described in the papers reporting on the visualization of wakes.

In the case of a ten-cylinder lattice, the coherence function is symmetric about its maximum at $\gamma_{xy}^2 = 1$. In addition to the central maximum, the coherence function exhibits four local maxima with $\gamma_{xy}^2 = 0.65$ and 0.4, which are positioned symmetrically about the point of $\gamma_{xy}^2 = 1$. Each of the local maxima corresponds to a plateau in the dependence of the cross-spectrum phase on the transverse coordinate (see Fig. 11). These measure-
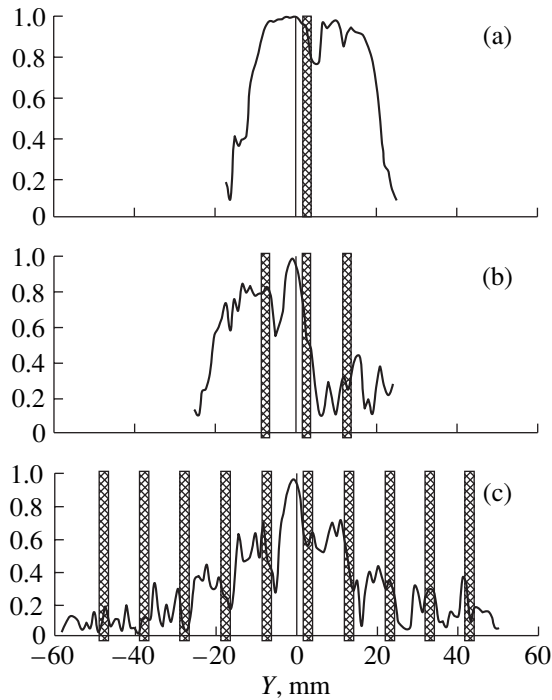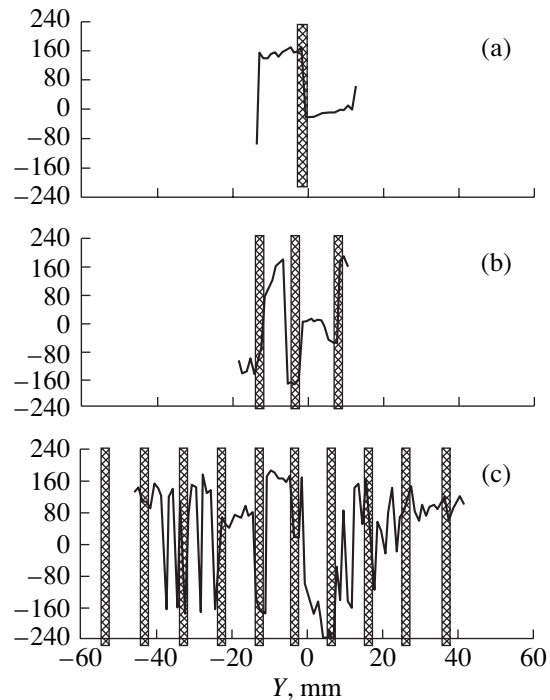
Fig. 10. Coherence function of the signals from two velocity sensors versus the distance between the sensors across the wake for the cases of (a) one, (b) three, and (c) ten cylinders at Re = 75. The cylinders are represented by columns.
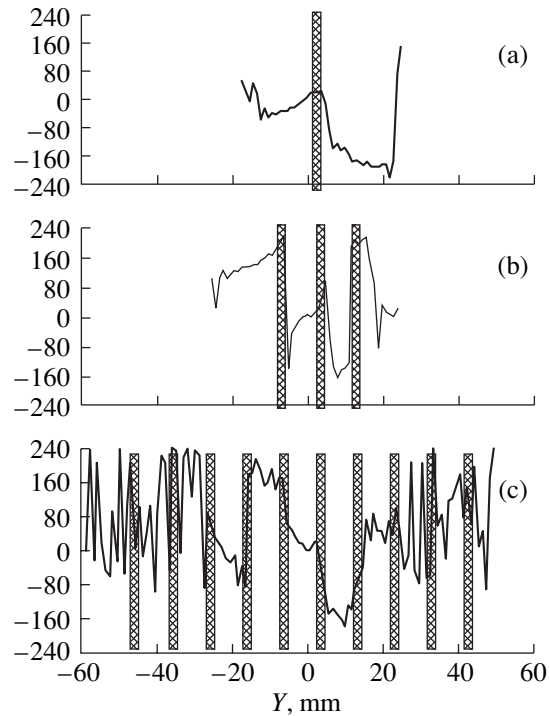
Fig. 11. Phase difference between the signals from two velocity sensors versus the distance between the sensors across the wake for the cases of (a) one, (b) three, and (c) ten cylinders at Re = 75. The cylinders are represented by columns.
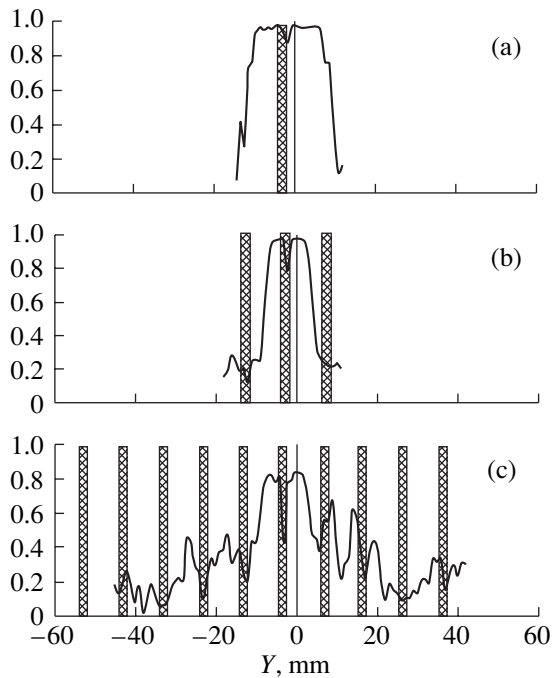
Fig. 12. Coherence function of the signals from two velocity sensors versus the distance between the sensors across the wake for the cases of (a) one, (b) three, and (c) ten cylinders at Re = 500. The cylinders are represented by columns.

Fig. 13. Phase difference between the signals from two velocity sensors versus the distance between the sensors across the wake for the cases of (a) one, (b) three, and (c) ten cylinders at Re = 500. The cylinders are represented by columns.

ments allow us to estimate the characteristic correlation length of the velocity fields in the direction perpendicular to the oncoming flow at Re = 75. Specifically, in the wake behind the ten-cylinder lattice, this length is about 10–11*d*. Hence, in the case of a wake with a total width of 50*d*, we deal with approximately five uncorrelated scatterers ("enlarged" Karman streets), which fully agrees with the result obtained by us at Re = 75 with the use of remote acoustic testing (see Fig. 3).

Figures 12 and 13 show similar results for the case of Re = 500. The main difference from the case of Re = 75 is that all coherence functions are much narrower (in the direction perpendicular to the flow). Specifically, when the lattice consists of ten cylinders, the coherence function has only two closely spaced maxima with $\gamma_{xy}^2 = 0.82$. In this case, the characteristic coherence length is only 5–6*d*, which corresponds to ten uncorrelated scatterers fitting within the wake width of 50*d*. As a result, at Re = 500, the scattered signal amplitude grows according to the law $\sim \sqrt{n}$ (see Fig. 5).

Thus, for both Re = 75 and Re = 500, the synchronization is actually possible only between the vortex streets that are closest to each other, because the coherence function has a finite length in both cases. The difference is only in that, at Re = 75, the vortex streets can merge and, hence, the increase in amplitude with growing *n* occurs more slowly than in the case of Re = 500.

CONCLUSIONS

The results reported in this paper show that remote acoustic testing allows one to quantitatively estimate the degree of synchronization of the vortex flow formed behind a lattice of cylinders. Thus, this method can be used as an alternative to taking instantaneous photographs of a vortex flow, which is the conventional method of proving the presence of synchronization without any quantitative estimates.

For the future, we plan to construct a model of such a vortex flow with allowance for the interaction between the vortex streets. A comparison between theoretical and experimental results should give insight into the manifestation of synchronization effects in scattered sound.

REFERENCES

1. P. R. Gromov, A. B. Ezerskiĭ, and A. L. Fabrikant, Akust. Zh. **28**, 763 (1982) [Sov. Phys. Acoust. **28**, 452 (1982)].
2. C. Baudet, S. Ciliberto, and J. F. Pinton, Phys. Rev. Lett. **67** (2), 193 (1991).
3. A. B. Ezerskii, P. L. Soustov, and V. V. Chernov, Acoust. Phys. **46**, 670 (2000).
4. P. R. Gromov, A. B. Ezerskiĭ, S. V. Kiyashko, and A. L. Fabrikant, Preprint No. 59, IPF AN SSSR (Inst. of Applied Physics, USSR Academy of Sciences, Gorki, 1982), p. 16.
5. A. B. Ezerskiĭ, A. G. Munin, A. A. Potokin, and M. I. Rabinovich, in *Proceedings of 8th Scientific and Technical Conference on Hydroacoustics* (Tsentr. Aerogidrodin. Inst., Moscow, 1990), p. 25.
6. A. B. Ezerskiĭ, A. B. Zobnin, and P. L. Soustov, Izv. Vyssh. Uchebn. Zaved., Radiofiz. **38**, 832 (1995).
7. J. F. Pinton, C. Laroche, and S. Fauve, J. Phys. II **3**, 767 (1993).
8. A. Petrossian and J. F. Pinton, J. Phys. II **7**, 801 (1997).
9. C. H. K. Williamson, J. Fluid Mech. **159**, 1 (1985).
10. H. J. Kim and P. A. Durbin, J. Fluid Mech. **196**, 431 (1988).
11. P. Le Gal, M. P. Chauve, R. Lima, and J. Rezende, Phys. Rev. A **41**, 4566 (1990).
12. I. Peschard and P. Le Gal, Phys. Rev. Lett. **77**, 3122 (1996).
13. P. Le Gal, I. Peschard, M. P. Charve, and Y. Takeda, Phys. Fluids **8**, 2097 (1996).
14. J. F. Ravoux and P. Le Gal, Phys. Rev. E **58**, 5233 (1998).
15. R. Otnes and L. Enochson, *Applied Time Series Analysis* (Wiley, New York, 1978; Mir, Moscow, 1982).
16. M. Okude and T. Matsui, Trans. Jpn. Soc. Aeronaut. Space Sci. **33** (99), 1 (1989).

Translated by E. Golyamina

Determination of the Mode Composition of the Sound Field with a Single-Point Reception in a Shallow Sea

V. A. Zverev, B. M. Salin, and A. A. Stromkov

Institute of Applied Physics, Russian Academy of Sciences, ul. Ul'yanova 46, Nizhni Novgorod, 603950 Russia
e-mail: zverev@hydro.appl.sci-nnov.ru
Received March 17, 2004

Abstract—A possibility of determining the mode composition of the sound field in a shallow sea is considered. The procedure involves the transmission of a short pulse by a point source and the subsequent reception of this pulse at a single point. It is shown that the problem can be solved by using linearly frequency-modulated broadband pulses at relatively short distances (about 20 km), where the attenuation of the signal is rather weak. To take into account the intramode dispersion, it is proposed to use the value of the dispersion typical of a perfect Pekeris waveguide with a stiff bottom. With the use of the calculations and the experimental data obtained in the Barents Sea, it is shown that the proposed approximation is sufficient to determine the mode composition of the sound field. © *2005 Pleiades Publishing, Inc.*

The location of objects in a shallow sea requires special methods of signal processing to be used [1–6]. This problem becomes easier if the mode structure of the wave field is known. A major portion of monograph [1] deals with the technique of determining the mode composition in a shallow sea. In solving this problem, two quite different methods can be used [1]. With the first one, the modes can be selected by a distributed vertical antenna array covering the entire waveguide. Another method consists in separating the modes by their arrival times in view of the fact that the modes propagate with different group velocities. The second method does not imply using a long array, because the separation in time can be implemented with a single hydrophone serving as the signal receiver.

For the signals to be separable in time, they must be localized within a short time interval. Such a localization can be implemented by either using short pulses or compressing a complex signal in time. Both methods imply a broad frequency band. The use of broadband probing signals requires taking into account the intramode dispersion, which causes an initially short pulse to spread, in addition to the intermode dispersion. To avoid such a necessity, the authors of monograph [1] propose to use long sequences of complex (with a high product of the duration and the frequency bandwidth) but sufficiently short pulses. The detailed calculations and experimental data of [1] argue that long distances should be traveled by the wave in the waveguide for the modes to be reliably separated if the intramode dispersion is neglected. Such distances can be impracticable because of the high attenuation of sound waves in a shallow sea.

In this paper, we study the possibility of determining the modes of the waveguides by transmitting and receiving linearly frequency-modulated (LFM) signals, which are characterized by a high value of the product of the duration and the frequency bandwidth because of the large bandwidth. The latter, in turn, offers an opportunity to reach a high time resolution in the signal processing. With such a signal propagating in the waveguide, the processing procedure should necessarily include the intramode dispersion.

It is known [1] that taking into account and even compensating for the intramode dispersion are desirable and, in principle, feasible. However, the difficulty of doing so for the natural waveguide is also well understood. Such a waveguide has too many parameters governing the intramode dispersion for one to be able to estimate them in advance. Furthermore, it is not quite clear how the parameters of the medium (the sea depth varying along the path, the characteristics of the layered bottom, the properties of internal waves, etc.) can be related to the parameters of the waveguide governing the intramode dispersion. In addition, it is unlikely that all the parameters could or should be measured in practice.

In view of the aforementioned considerations, this paper uses an approximation that facilitates the solution of the problem with allowance for the intramode dispersion in an LFM signal. As such an approximation, the value of the intramode dispersion is used that corresponds to the simplest Pekeris waveguide (SPW) with a stiff bottom in the absence of sound absorption. In the SPW, the group velocity of the modes is determined by several parameters: the ordinal number of the mode, the distance, the sound speed, and the thickness of the

waveguide. The same is true for the propagation time of the pulse components with different frequencies. In addition, all of these parameters influencing the mode group velocity can be combined into a single coefficient. This coefficient can be easily fitted by analyzing the experimental data, and one can drop the assumption of the bottom stiffness.

It was found that the aforementioned approximation can be used to satisfactorily interpret the experiment performed in a shallow sea at a distance much shorter than that required for the intramode dispersion to be neglected in transmitting pulsed CW signals. The study showed that, with allowance for the intramode dispersion, one could not select the modes by simply separating them in their arrival times, even in the SPW, where the intramode dispersion can be completely compensated for. To determine the set of modes of the sound field received by a single hydrophone, a special technique of processing and representing the data is required. Such a technique is proposed here.

The experiments on the signal propagation were carried out in the Barents Sea. The sound signals were produced by a broadband transmitter deployed from a drifting research vessel. The hydrophones positioned at different depths operated as self-contained units. The signal received by a single hydrophone was recorded by the digital system [7] with allowance for its amplitude and phase. The distance between the transmitter and the receiver (the path length) varied from 2–3 to 20 km. The transmitted signals were the LFM pulses with a frequency deviation of about 30 Hz/s and a frequency band from 100 to 350 Hz.

The processing of the received signals recalled a preceding modeling of the signal propagation in the SPW similar to a natural waveguide (the distance $R = 17$ km, the waveguide thickness $H = 120$ m, and the sound speed $c = 1500$ m/s). In view of the frequency dependence of the group velocity, the arrival time of a mode in the SPW is determined by the formula [1, 2]

$$\tau(\omega) = \frac{\pi^2 Rc(m - 0.5)^2}{2\omega^2 H^2}, \tag{1}$$

where ω is the cyclic frequency and m is the mode number.

The LFM wave can be represented as

$$A(t) = \cos[\Phi(t)], \tag{2}$$

where the phase $\Phi(t)$ is given by the expression

$$\Phi(t) = \omega_0 t + \alpha \frac{t^2}{2}. \tag{3}$$

To take into account the dispersion of waves in the waveguide, one should introduce delay (1) into Eq. (2).

A problem arises even at this step. If the delay is introduced formally, so that oscillation (2) is delayed according to Eq. (1),

$$AD(t) = A\cos[\Phi(t - \tau(\omega))], \tag{4}$$

the oscillation will be extended in time. Such an extension influences the spectrum of the oscillation in a manner opposite to the delay introduced. Figure 1a shows the running spectrum of the oscillation for $m = 9$. This spectrum is obtained by introducing the delay according to Eq. (4).

To correctly calculate the frequency-modulated oscillation with allowance for the dispersion in the waveguide, one should proceed in the following way. The variation in the frequency of the LFM signal is defined as

$$\omega = \omega_0 + \alpha t \tag{5}$$

for the time interval $[0, t]$.

Into this time dependence, the delay is introduced according to Eq. (1):

$$\omega = \omega_0 + \alpha(t - \tau(\omega)). \tag{6}$$

From Eq. (6), the frequency $\omega(t)$ and phase $\Phi(t)$ of the oscillation is found by integrating the frequency $\omega(t)$ over time from 0 to t:

$$\Phi D(t) = \int_0^t \omega(\xi) d\xi. \tag{7}$$

Thus, an oscillation is obtained that models the amplitude and phase of the LFM signal transmitted through the Pekeris waveguide:

$$AD(t) = \cos[\Phi D(t)]. \tag{8}$$

Figure 1b shows the running spectrum of Eq. (8). As one would expect, the lower frequencies correspond to greater delays, as compared to higher frequencies.

Figure 1 displays the dispersion in an explicit form. This suggests the conclusion that the dispersion can be directly extracted from the experimental running spectrum of the oscillation. It seems that the shape of the curves carries some information on the mode composition of oscillations. However, this is not true, because, for low mode numbers, short distances, and shallow depths (these being the factors that govern the dispersion), the offset of the frequency deviation from the linear law is so small that it cannot be detected in the running spectrum.

Figure 2 confirms the above statement. This figure shows the time dependences of the frequency in the LFM oscillations transmitted through the SPW in view of the dispersion given by Eq. (6). The curves shown are not the current spectra as in Fig. 1 but rather the cal-
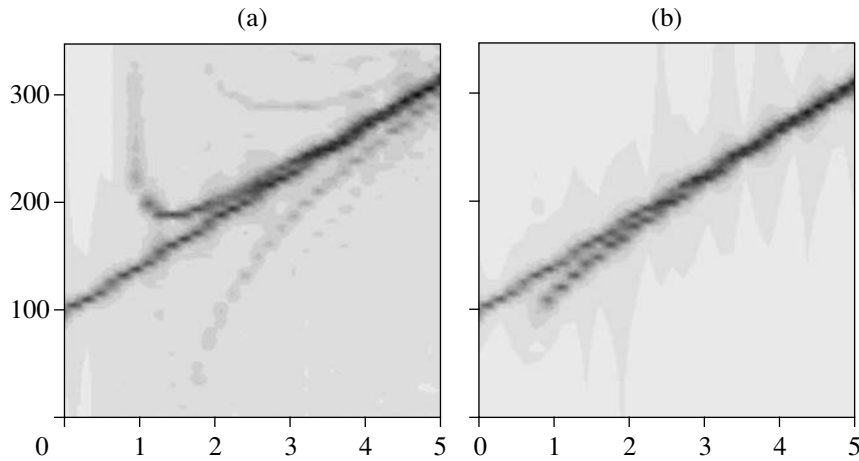
Fig. 1. Dependence of the signal frequency (vertical axis, in hertz) on time (horizontal axis, in seconds) without (straight lines) and with (curves) allowance for the dispersion. The dispersion is taken into account by (a) selectively delaying the entire LFM signal and (b) by delaying the time dependence of the frequency with a subsequent reconstruction of the signal. The distance is 17 km.
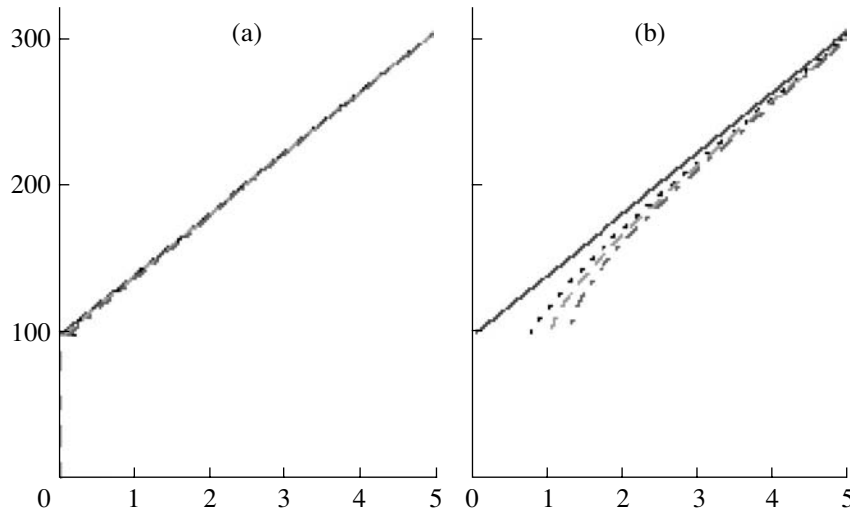

Fig. 2. Dependence of the signal frequency (vertical axis, in hertz) on time (horizontal axis, in seconds) for the LFM signal (solid line) and the LFM signal with allowance for the intramode dispersion of (a) modes 1 to 3 and (b) modes 7 to 9. The distance is 17 km.

culated dependences of the frequency on time. With such a visualization of variations (6) in the frequency of the oscillations, the resolution is incomparably higher than with the analysis of the running spectra. However, in Fig. 2a, which shows the three initial modes, the offset from the linear law is also nearly unnoticeable. Such an offset is clearly pronounced in Fig. 2b, which corresponds to higher modes. Thus, the analysis of the running spectrum (or the running correlation function) cannot lead to the desired result, that is, to the selection of modes with low ordinal numbers at short distances.

The processing of the experimental data may consist in cross-correlating the oscillation received by the hydrophone with a reference oscillation. The latter can be obtained by using a mathematical model allowing for the dispersion of the velocities of the waves propagating in the waveguide. The inclusion of the dispersion in the reference oscillation allows one to compensate for the spread of the maximum in the cross-correlation function of the LFM signal with the reference one and thereby to more accurately measure the arrival time of the signal for each waveguide mode.

To analyze the set of modes, we use the cross-correlation between the received oscillation and the reference one obtained with allowance for the dispersion of waves in the waveguide. At the first stage, a mathematical model of the SPW is used. To do so, we combine
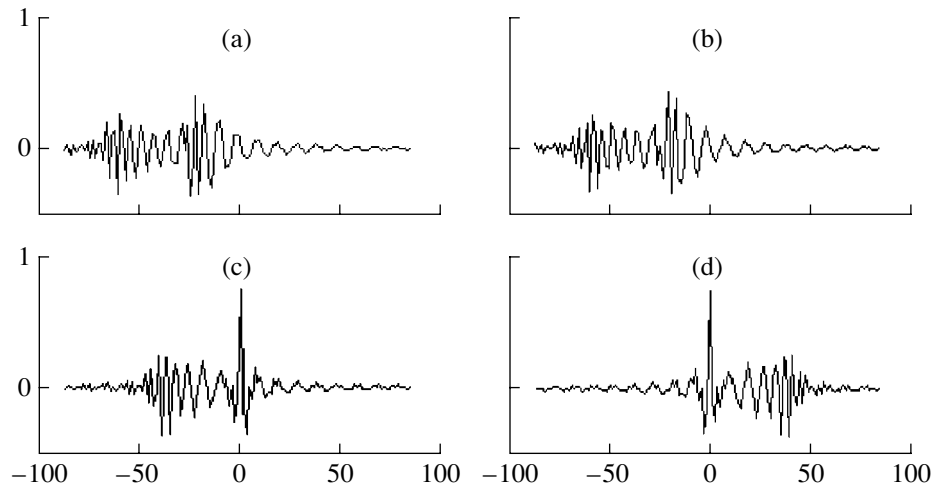
Fig. 3. Coefficients of correlation (vertical axis) of the modeled signal with the LFM signal (a) without and (b–d) with allowance for the dispersion of modes (b) 1, (c) 2, and (d) 3. The horizontal coordinate is time (in milliseconds). The distance is 8 km.

oscillations (8) with a single mode in each summand. For instance, the sum of the second and third modes has the form

$$E(t) = AD(t, 2) + AD(t, 3), \qquad (9)$$

where the characters in parentheses denote the mode numbers used to allow for the dispersion.

Then, the reference oscillation (RO) is constructed. It is advantageous to represent the RO in the form of Eq. (8), where the number m of the mode, whose dispersion is taken into account, can be varied. For brevity, the RO is assigned a subscript denoting the mode number. The cross-correlation functions of signal (9) with the $RO_{0.5}$, RO_1, RO_2, and RO_3 are shown in Figs. 3a–3d, respectively.

The mode with subscript 0.5 corresponds to the LFM signal that is not disturbed in its propagation. Figure 3a shows the cross-correlation for this signal. In Fig. 3a, a correlation response can be seen that manifests itself as a peak spread in time (to the left of zero, with negative delays). The negative delay time corresponds to a lag of signal (9) relative to the reference one. Such a lag indicates that the signal contains higher modes arriving later than the $RO_{0.5}$. The response is spread, because signal (9) and the $RO_{0.5}$ differ in their frequency deviations. Figure 3b is quite similar to Fig. 3a, because the RO_1 slightly differs from the $RO_{0.5}$ used as reference in Fig. 3a. In Fig. 3c, two responses can be seen, one of which is spread as in previous figures and the other of which looks like a narrow well-developed correlation peak. This peak corresponds to the second mode, because the RO_2 is the signal of the second mode, which is also present in signal (9). The spread peak is the response to the higher third mode; therefore, it is at the left of zero. Two responses are also present in Fig. 3d. The first one is a well-pronounced correlation peak at zero. This peak is the correlation of

the RO_3 with the third mode, while the spread response results from the correlation of the RQ_3 with the second mode. The latter mode has a lower number, and, hence, the corresponding response advances the correlation peak (this is the only response in Fig. 3 that exists to the right of zero).

The following general conclusion can be drawn from Fig. 3. Cross-correlating the signal and the RO containing a single known mode allows one to determine the amplitude of the mth mode from the concentrated-in-time response. At the same time, the left- and right-hand spread responses carry information on the presence of modes with numbers higher and lower than m in the signal.

The aforementioned situation of the strong intramode dispersion differs from that considered in [1], where each mode has its correlation maximum observed simultaneously with the maximum of another mode. In our case, one cannot focus the responses on two modes arriving at different times, because these modes correspond to different frequency deviations depending on the intramode dispersion.

Nevertheless, a method exists that allows one to focus all the modes and to represent them in the same plot, even if the intramode dispersion is taken into account. For simultaneously visualizing all the modes existing in the signal, one can calculate the cross-correlation function of the received or modeled signal and the reference one for a single instant and then use the numbers of the modes in the reference signal as the variable required to obtain a plot. In doing so, the mode number m takes not only integral but also fractional values.

The possibility of varying the mode number in the reference signal instead of performing tuning in time is offered by the fact that Eq. (8) automatically separates the LFM signals with different mode numbers in
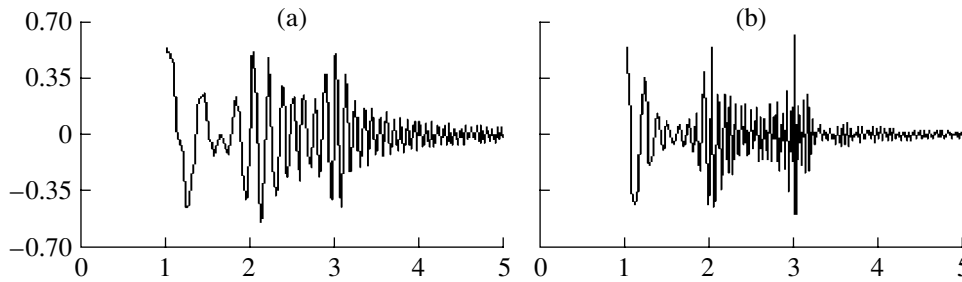
Fig. 4. Coefficients of correlation (vertical axis) between the mathematical model of the LFM oscillation in the form of the sum of modes 1, 2, and 3 and the LFM oscillation constructed with allowance for the SPW dispersion at a zero delay versus the number of the mode taken into account (horizontal axis). The distances are (a) 8 and (b) 17 km.

time. Therefore, if the distance, the parameters of the path, and the initial time are correctly fitted, the maximum of the cross-correlation function of the RO and the signal will correspond to the same instant t for all the modes.

Figure 4 illustrates the results obtained with the proposed technique for the signal numerically modeled as a sum of three modes (signal (9) is complemented with the first mode). The curves shown correspond to distances of 8 and 17 km. In Fig. 4a, three maxima can be seen. Their horizontal coordinates are 1, 2, and 3, according to the ordinal numbers of the modes present in the signal. For other mode numbers, the responses are noticeably lower. As the distance increases, the difference in propagation conditions for different modes becomes greater, and one can expect that, at long distances, the modes will be distinguished better than in Fig. 4b.

The plot shown in Fig. 4 accentuates the difference in the shapes of the correlation functions for different modes, i.e., the difference that could be noticed from Fig. 3. It is true that, in Fig. 4, all the modeled modes are clearly pronounced, and a distance of 8 km is sufficient for the modes to be reliably separated. Thus, the necessary part of the problem is solved: it is shown that the set of modes can be determined for the numerically modeled signal.

In an in-sea experiment, the initial delay time can be estimated from the instant corresponding to the maximum in the correlation response at some mode if such a response is present in the signal. An error in determining this instant leads to both a shift of the mode numbers in the plot and a decrease in the correlation coefficient.

The results of Fig. 4 do not lead to the conclusion that the same situation will take place in an experiment. The reason is not only that, in numerical modeling, a "pure" signal is obtained without noise and interference. The point is also that the natural waveguide differs from the SPW used in generating the reference signal.

An experimental curve plotted with the same technique as Fig. 4 should exhibit individual maxima corre-

sponding to mode numbers indicated on the horizontal axis. However, the dispersion characteristic is governed by both the mode number and the value of the coefficient appearing in Eq. (1). This coefficient depends on the waveguide thickness, which is not known along the path, and on the impedance of the bottom in the natural waveguide (again, along the path). In addition, an uncertainty is caused by the error in measuring the instant of the zero delay between the arrivals of different modes; this delay is determined by the maximum in the cross-correlation of the signal and the RO. The natural waveguide does not have a perfectly stiff bottom, and, hence, the mode numbers can take nonintegral values [1].

The signals received in the experiment were processed with the parameter $H = 136.1$ m, while the sea depth in the vicinity of the receiver was about 120 m. Such a value of H was chosen for the maximum in the figure to correspond to the 3rd mode at a distance of 17 km. In fact, this mode can be number 2, 2.5, or some other. Accordingly, the characters on the horizontal axis in Fig. 5 should be treated as the numbers of modes in the reference signal (NMRS) rather than the mode numbers themselves.

Figure 5 illustrates the results of processing the experimental signals with the aforementioned technique. To obtain the plots in Fig. 5, the same reference signals were used as in Fig. 4. According to Fig. 5, the results obtained are noticeably different for different distances and reception depths. It is characteristic that the maxima are noticeable at certain values of the NMRS in all the plots. However, these maxima are pronounced to different extent. In Fig. 5a (a distance of 8 km, reception near the surface), a well-pronounced maximum exists at NMRS = 3 and less pronounced maxima occur at the NMRS values of 1, 4.5, and 5. In Fig. 5c (the same distance but a different depth), a strong and well-pronounced maximum corresponds to the vicinity of NMRS = 1, while the noticeable peak that corresponds to NMRS = 3 in Fig. 5a is nearly absent in Fig. 5c. At deeper horizons of reception (Fig. 5e), the highest maximum corresponds to NMRS = 5. The sharpness of the maxima in Figs. 5a, 5c, and 5e is
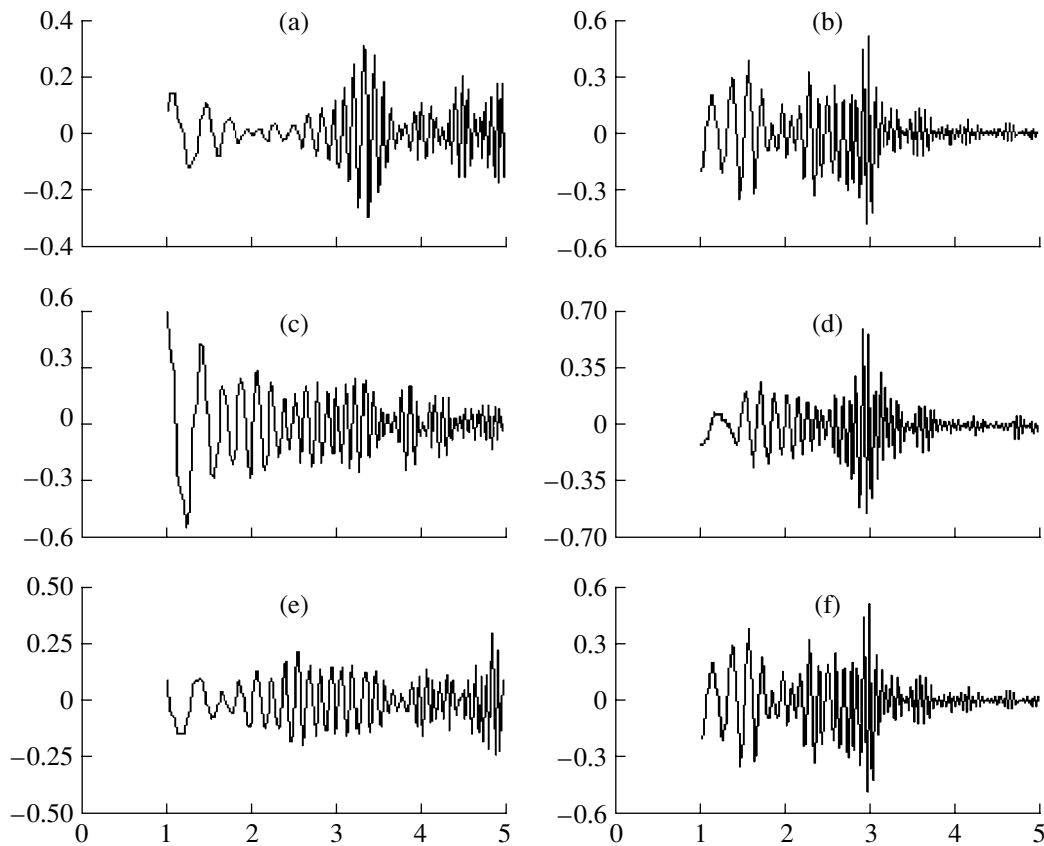
Fig. 5. Coefficients of correlation (vertical axis) between the received LFM oscillation and the LFM oscillation constructed with allowance for the SPW dispersion at a zero delay versus the number of the mode taken into account (horizontal axis). The distances are (a, c, e) 8 and (b, d, f) 17 km. The receivers are (a, b) near the surface, (c, d) at the half-depth of the sea, and (e, f) near the bottom.

nearly the same as in Fig. 4a, corresponding to the same distance.

In Figs. 5b, 5d, and 5f, corresponding to a distance of 17 km, much more pronounced and narrower maxima exist than in Figs. 5a, 5c and 5e. This fact fully agrees with Fig. 4, which also shows a much clearer pattern at a distance of 17 km than at 8 km. At 17 km, there are nearly no maxima at NMRS values greater than 3. Such a situation can be explained by the fact that higher modes attenuate more rapidly than lower ones as the distance increases. This result confirms the fact that the actual modes of the waveguide are observed in Fig. 5. The most pronounced mode is the one that corresponds to an NMRS value of about 3 at a distance of 17 km. This mode is easily detectable at all depths. The main justification of the statement that Fig. 5 yields the actual individual modes of the signal consists in the existence of the pronounced maxima in this figure and in the agreement of their shapes with the results of numerical modeling (Fig. 4).

The comparison of Figs. 5 and 4 shows that the separation of modes also takes place in the experiment and that this separation is almost as definite as in modeling, although the experimental values of the cross-correlation coefficients are substantially lower. The decrease in the experimental cross-correlation coefficients is governed by both factors responsible for the difference between the experiment and the calculations. These are the existence of noise and interference and the difference between the modeled reference signal and the LFM signal propagating in the natural waveguide. The reliable separation of modes in the experiment shows that, for solving the problem at hand (that is, for determining the mode composition in a shallow sea with an intramode dispersion), it is sufficient to use the approximation of a perfect Pekeris waveguide.

Thus, the approximation of a perfect Pekeris waveguide allows one to take into account the intramode dispersion and to determine the approximate mode composition of the broadband oscillation at a distance where the modes can be separated due to the broad frequency band. It is also shown that, to obtain a higher correlation coefficient (and, hence, to increase the noise immunity), the transmitted LFM signal should be correlated with a signal that, in the first approximation, allows for sound propagation in the waveguide rather than with the initial LFM signal.

ACKNOWLEDGMENTS

REFERENCES

1. B. G. Katsnel'son and V. G. Petnikov, *Acoustics of a Shallow Sea* (Nauka, Moscow, 1997) [in Russian].

2. N. S. Ageeva and V. D. Krupin, Akust. Zh. **27**, 669 (1981) [Sov. Phys. Acoust. **27**, 372 (1981)].

3. Ph. Roux and M. Fink, J. Acoust. Soc. Am. **113**, 1406 (2003).

4. L. M. Zurk, N. Lee, and J. Ward, J. Acoust. Soc. Am. **113**, 2719 (2003).

5. H. Bucker, J. Acoust. Soc. Am. **96**, 3809 (1994).

6. L. Zurk and J. Ward, J. Acoust. Soc. Am. **107**, 2889 (2000).

7. V. A. Zverev, P. I. Korotin, A. L. Matveev, *et al.*, Akust. Zh. **47**, 227 (2001) [Acoust. Phys. **47**, 184 (2001)].

Translated by E. Kopyl

Low-Frequency Acoustic Tomography of a Shallow Sea by Low-Mode Pulses

A. G. Luchinin and A. I. Khil'ko

Institute of Applied Physics, Russian Academy of Sciences, ul. Ul'yanova 46, Nizhni Novgorod, 603950 Russia
e-mail: A.khil@hydro.appl.sci-nnov.ru
Received October 9, 2004

Abstract—Possibilities for the observation of randomly distributed and spatially localized inhomogeneities in a shallow sea by the method of low-frequency low-mode pulsed diffraction tomography are discussed. Results of computer simulations and experimental studies of the emission and reception of low-frequency low-mode acoustic signals in a shallow sea are presented. © *2005 Pleiades Publishing, Inc.*

In this paper, we analyze the potential of low-mode pulsed tomography of a shallow sea using echolocation (multistatic in the general case) schemes of observation in shallow water [1, 4, 5, 8–15]. The structure of the signals diffracted by spatially localized inhomogeneities in a waveguide, as applied to the problem of tomographic observations in oceanic underwater channels, was analyzed for the first time in [1, 2] and also in many subsequent publications cited in [13]. In the first part of this paper, we analyze the basic idea of the method and demonstrate the potential of low-mode pulsed tomography for reconstructing the parameters of some specific types of inhomogeneities in a shallow sea on the basis of a computer model developed for this purpose. An important condition for the implementation of low-mode pulsed tomography is the selection of waveguide modes. In the second part, we briefly describe the equipment and some results of experimental studies aimed at the determination of the abilities of selective excitation and reception of waveguide modes. The employment of vertically developed receiving systems in shallow water has its own history. In particular, it is necessary to note the joint experimental studies of the General Physics Institute and the Institute of Applied Physics of the Russian Academy of Sciences that were conducted in 1990 [3]. However, a combined employment of vertical multielement radiating and receiving arrays in the low-frequency tomographic observations on long tracks in a shallow sea was considered for the first time only in [4, 5]. In [6, 7], the abilities of such arrays were examined in application to phase conjugation in an acoustic waveguide for short tracks within a higher frequency range.

BASIC PROPERTIES OF LOW-MODE PULSED TOMOGRAPHY

The idea of the low-mode pulsed tomography is as follows: pulsed signals corresponding to the nth mode and characterized by an ambiguity function that is sufficiently narrow in the frequency–time plane are excited with the help of a set of vertically developed arrays S_i ($i = 1, \ldots, I$, where I is the number of radiating arrays). Here, we assume that the waveguide and mode structures are known. It is necessary to note that it is practically impossible to excite just one mode because of the finiteness of the radiating array aperture and the impossibility of placing the radiator in the soil. We will call a signal low-mode if it is emitted so that all modes are much smaller than one produced by matched excitation [8–12]. The pulses scattered by the inhomogeneity under investigation, which correspond to the modes with the numbers $m = 1, \ldots, M$, where M is the total number of modes propagating in the waveguide, are received by a set of vertically developed receiving arrays R_j ($j = 1, \ldots, J$, where J is the number of receiving arrays). A matched filtration of pulses with sweeping delays τ and Doppler frequency shifts Ω is performed for each of the modes selected at the reception. The number and positions of the sources and receiving systems and the number of the mode tomographic projections corresponding to each source–receiving system pairs may vary. Thus, the received signal for each pair of radiating and receiving arrays is a function of several variables: the numbers of excited and received modes, the delays, and the Doppler frequency shifts. As a result of combined processing of all spatial mode and frequency tomographic projections, the spatial and temporal parameters of inhomogeneities are determined.

Far from the source, in plane-layered waveguides, the field is a finite sum of N propagating modes (for horizontal homogeneous waveguides, the number of modes near the source and the receiver is the same and $N \equiv M$). A mode is characterized by the eigenfunctions $\varphi_n(z)$ and the complex eigenvalues $h_n(\omega)$, with the imaginary parts determined by the mode damping factors $\delta_n(\omega)$. Each ith source of a tomographic system, which is an array of radiators with a length L_1, emits a

sequence of narrowband probe pulses $f_0(t)$ with the pulse spectrum $F(\omega - \omega_0)$, where ω_0 is the carrier frequency. If the depth and dimensions of the radiating arrays are selected optimally, the emitted low-mode signal consists of a mode of number n whose level far exceeds the levels of all other modes [8–12]. In this case, under the assumption of the smallness of the intramode dispersion effects (this imposes limitations on the frequency band of radiated pulses and on the distances at which they are observed), after matched filtration, a direct (nonscattered) pulsed signal from the jth receiving array of length L_j can be represented in the form

$$^0P_{ij}^{nm}(r_{ij}, \tau_{ij}^{nm}, \Omega_{ij}^{nm}) = A_n^i A_n^j \exp[i(h_n r_{ij} - \pi/4)]$$

$$\times (h_n r_{ij})^{-1/2} F_H(\tau_{ij}^{nn}, \Omega_{ij}^{nn}) + \sum_{\substack{\eta \neq n \\ \mu \neq m}}^{M} A_\eta^i A_\mu^j \qquad (1)$$

$$\times \exp[i(h_\eta r_{ij} - \pi/4)](h_\eta r_{ij})^{-1/2} F_H(\tau_{ij}^{\eta\mu}, \Omega_{ij}^{\eta\mu}),$$

where $h_n = h_n(\omega_0)$; $\tau_{ij}^{nm} = r_{ij}/v_n(\omega_0)$ is the delay of the pulse corresponding to the mode with number n in the reception channel that corresponds to the mode with number m; $v_n(\omega_0)$ is the group velocity of the mode with number n; Ω_j^{nm} is the Doppler frequency arising due to the scatterer motion; $A_{n,m}^{i,j} = \int_0^{L_{i,j}} g_{n,m}^{i,j}(z)\varphi_{n,m}(z)dz$ are the coefficients of mode excitation by the radiating and receiving arrays, respectively; $g_{n,m}^{i,j}(z)$ are the weight factors along the apertures of the arrays; $F_H(\tau, \Omega) = 1/2\pi \int_{-\infty}^{\infty} d\omega\, F(\omega)F_0(\omega - \Omega)\exp[i(\omega - \Omega)\tau]$ is the ambiguity function of probe pulses; and $F_0(\omega)$ is the spectrum of the replica of the probing signal. In the case of an ideal spatial filtration, where the conditions of mode orthogonalization are satisfied at the array apertures, the second term in Eq. (1) in the form of a sum of small-value interfering modes vanishes and only the component corresponding to the illuminating field in the form of a single emitted mode remains.

In the course of tomographic observation, the probe pulses subjected to diffraction by waveguide inhomogeneities are measured. In the framework of the mode description, the complex amplitudes of diffracted waveguide modes are determined by the scattering matrix. The matrix depends on the internal structure, shape, and positions of inhomogeneities (for example, see [13–15]). When inhomogeneities are illuminated with a pulsed signal corresponding to the mode with number n, the amplitude of each pulse of the diffracted modes with index m is formed as a result of signal scattering from all inhomogeneities located within a corresponding pulse volume, the points r' of which satisfy the condition $|t - r_{1i} v_n^{-1} + r_{2j} v_m^{-1}| < \Delta\tau/2$, where $r_{1i} = |r_i - r'|$ and $r_{2j} = |r' - r_j|$ are the distances from a scatterer to the

source and the receiver, respectively. In the general case, the inhomogeneities are moving and, hence, the scattered pulses have a Doppler shift. In the case of narrowband illuminating pulses and relatively small velocities of the scatterers V_s, all scatterers satisfying the condition $|\omega_0 V_s(r')(v_n^{-1} \cos\alpha_i(r_i, r') - v_m^{-1} \cos\beta_j(r_j, r'))| < \Delta\Omega$ fall in a separate channel on the axis of the Doppler shifts. Here, $\alpha_i(r_i, r')$ and $\beta_j(r_i, r')$ are, respectively, the angles between the direction of the velocity vector of the velocity for an elementary scatterer at the point r' and the radius vectors constructed from the point of the scatterer position to the source and the receiving system. The quantities $\Delta\tau$ and $\Delta\Omega$ are determined by the width of the ambiguity function $F_H(\tau, \Omega)$ of the probe pulses, respectively, on the axes of time delays and Doppler frequency shifts. In the digital signal processing, in each of the delay–Doppler shift planes corresponding to the pair of radiated modes with the number n and received modes with the number m, it is possible to introduce a set of channels for each source–receiver pair (i, j), which correspond to the interval of the time delays $^0t_{ij}^{nm} + (l - 1)\Delta\tau < t_{ij}^{nm} < {}^0t_{ij}^{nm} + l\Delta\tau$, and the Doppler frequency shifts $(k \mp 1)\Delta\Omega < \Omega_{ij}^{nm} < k\Delta\Omega$, where $l = 1, 2, \ldots, L$ and $k = \pm1, 2\ldots, \pm K$ are the channel numbers and $^0t_{ij}^{nm}$ are the initial values of time delays, which are fixed for each tomographic projection $\{i, j, n, m\}$. After processing consisting of the matched filtration of received mode pulses, taking into account the discretization determined above, we have in the general case $\{IxJxNxMxKxL\}$ tomographic projections, the signals of which are the integral characteristics of all inhomogeneities located within each projection. The combined processing of the signals of these projections yields a reconstruction of the differential characteristics of the inhomogeneities observed, i.e., the distribution of their parameters in the observation region.

Under the assumption of the smallness of multiple scattering effects, the amplitudes of the modes scattered by single elements of the pulse volume are determined by the components of the spatial spectrum of inhomogeneities, which satisfy the condition of resonance scattering $\mathbf{k}_{ij}^{nm} = h_n \mathbf{r}_{1i}/r_{1i} - h_m \mathbf{r}_{2j}/r_{2j}$ [16]. The observed pressure amplitudes of the acoustic field are the sum of the illuminating field $^0p_{ij}^{nm}$, the components $^\sigma p_{ij}^{nm}$ of the field scattered by the inhomogeneity under observation, the field $^R p_{ij}^{nm}$ scattered by all interfering inhomogeneities, and the field of the sources of the additive oceanic noise $^N p_j^m$. In the general case, each component of the received field must be considered as a random signal with certain inherent statistical properties. In this case, it is necessary to assume that the direct illuminating field and the diffracted components of the field are partially coherent, which leads to their inter-

ference. This effect can be used for the reconstruction of inhomogeneities, in particular, in the case of observation of the fields diffracted through small angles. In the scheme of low-mode pulsed tomography, this situation takes place within the first pulsed volume, when the direct pulse and the diffracted pulses are not resolved. A detailed consideration of the influence of the interference effects arising in this case and their use can be found in [1, 13–15]. In this paper, we consider situations where interference effects between the direct illuminating field and the diffracted fields are small; i.e., we analyze the specific features of the tomographic reconstruction of the inhomogeneities located in the pulse volumes, where $l > 1$ and $k > \pm 1$. Assuming the interference effects to be small, we have, for the received signal intensity [13, 14],

$$
\begin{aligned}
\langle |P_{ij}^{nm}(\tau_{ij}^{nm}, \Omega_{ij}^{nm})|^2 \rangle &= \langle |^0P_{ij}^{nm}(\tau_{ij}^{nm}, \Omega_{ij}^{nm})|^2 \rangle \\
&+ \langle |^\sigma P_{ij}^{nm}(\tau_{ij}^{nm}, \Omega_{ij}^{nm})|^2 \rangle \\
&+ \langle |^R P_{ij}^{nm}(\tau_{ij}^{nm}, \Omega_{ij}^{nm})|^2 \rangle + \langle |^N P_j^{nm}(\tau_{ij}^{nm}, \Omega_{ij}^{nm})|^2 \rangle.
\end{aligned}
\tag{2}
$$

The averaging in Eq. (2) is performed over the statistical ensembles of the corresponding random inhomogeneities and noise. If random inhomogeneities are relatively weak or the length of the tomographic tracks is small, the illuminating field can be considered as approximately coherent: $\langle |^0P_{ij}^{nm}(\tau_{ij}^{nm}, \Omega_{ij}^{nm})|^2 \rangle \approx |^0P_{ij}^{nm}(\tau_{ij}^{nm}, \Omega_{ij}^{nm})|^2$. In the case of illumination with the nth mode, the intensities of the signal components from the output of a matched filter, which correspond to the diffracted (by observed (with index σ) and interfering (with index R) inhomogeneities) pulses of the received mode with the number m, are determined by the matrix of mode scattering $(^{\sigma,R}I_{nm}^{\eta\mu})_{ij}$:

$$
\begin{aligned}
&\langle |^{\sigma,R}P_{ij}^{nm}(\tau_{ij}^{nm}, \Omega_{ij}^{nm})|^2 \rangle \\
&= |A_n^i|^2 |A_m^j|^2 (^{\sigma,R}I_{nm}^{mn})_{ij}(\tau_{ij}^{nm}, \Omega_{ij}^{nm}) \\
&+ \sum_{\substack{\nu \neq n \\ \mu \neq m}}^M A_n^i A_\nu^i A_m^j A_\mu^j (^{\sigma,R}I_{nm}^{\nu\mu})_{ij}(\tau_{ij}^{nm}, \tau_{ij}^{\nu\mu}, \Omega_{ij}^{nm}, \Omega_{ij}^{\nu\mu}).
\end{aligned}
\tag{3}
$$

It is necessary to note that, in the case of observation of spatially restricted inhomogeneities, the interference is represented by randomly distributed surface, bottom, and bulk inhomogeneities in the ocean. The intensity of the additive noise $\langle |^N P_j^m(\tau_{ij}^{mm}, \Omega_{ij}^{mm})|^2 \rangle$ can be represented in the form

$$
\begin{aligned}
\langle |^N P_j^m(\tau_{ij}^{mm}, \Omega_{ij}^{mm})|^2 \rangle &= |A_m^j|^2 (N_m^m)^j(\tau_{ij}^{mm}, \Omega_{ij}^{mm}) \\
&+ \sum_{\mu \neq m}^M A_m^j A_\mu^j (N_m^\mu)^j(\tau_{ij}^{\mu m}, \Omega_{ij}^{\mu m}),
\end{aligned}
\tag{4}
$$

where the function $(N_m^\mu)^j(\tau_{ij}^{\mu m}, \Omega_{ij}^{\mu m})$ determines the intensity of the output signal from a matched filter in the absence of the illuminating field, when the receiving array with the index j detects the signals of additive noise in the process of reception of the mode with the number m.

The scattering matrix in Eq. (3) is determined by the spectrum of inhomogeneities [13, 16],

$$
\begin{aligned}
&(^{\sigma,R}I_{nm}^{\nu\mu})_{ij}(\tau_{ij}^{nm}, \tau_{ij}^{\nu\mu}, \Omega_{ij}^{nm}, \Omega_{ij}^{\nu\mu}) \simeq 8/\pi h_0^2 \\
&\times \int_{-\infty}^{\infty} \frac{1}{r_{1i}r_{2j}} \exp[i(h_\nu - h_n)r_{1i} + i(h_\mu - h_m)r_{2j}] \\
&\times \int_{-\infty}^{\infty} {}^{\sigma,R}W_{nm}^{\nu\mu}\left(\frac{h_\nu + h_n}{2}\frac{\mathbf{r}_{1i}}{r_{1i}} - \frac{h_\mu + h_m}{2}\frac{\mathbf{r}_{2j}}{r_{2j}}; \omega', r'\right) \\
&\times \mathrm{F}_H(\tau_{ij}^{nm} - r_{1i}/v_n - r_{2j}/v_m; \omega' - \Omega_{ij}^{nm}) \\
&\times \mathrm{F}_H^*(\tau_{ij}^{\nu\mu} - r_{1i}/v_\nu - r_{2j}/v_\mu; \omega' - \Omega_{ij}^{\nu\mu})d\omega'd^2r',
\end{aligned}
\tag{5}
$$

where h_0 is the value of the wave number at the channel axis for the carrier frequency, $^{\sigma,R}W_{nm}^{\nu\mu}(\mathbf{k}, \omega, r)$ are the corresponding components of the local spectrum for the correlation function of inhomogeneities with respect to differential variables for the sum of the surface, bottom, bulk, and spatially restricted inhomogeneities, and the integration is performed over the horizontal coordinates, the depth of inhomogeneity positions being taken into account in the process of calculation of the components of the local spectrum for inhomogeneities [13, 14, 16, 19].

Tomographic reconstruction of an object consists in the evaluation of the observed parameters of the model describing the object. In particular, in the case of a spatially restricted inhomogeneity, its coordinates, shape, and velocity and direction of motion can be the observed parameters. In the case of wind waves, the parameters of an observed object model can be the velocity and direction of the wind inducing the waves. Let us denote the set of the observed parameters for the object model by the vector $\mathbf{p}$. The components of the vector of observed parameters are evaluated by the method of statistical verification of hypotheses determined by the solution of the direct problem by using *a priori* information in the form of models of the medium, observation object, interference and noise, and configuration of the observation system. The solution corresponds to the global extremum of residual $\Psi(\mathbf{p}) \equiv \|\mathbf{q} - \mathbf{q}^{(\mathbf{p})}\|^\eta \longrightarrow \min_{\mathbf{p}}$ between the vectors of the measured parameters $\mathbf{q}$ and the corresponding sorted hypotheses $\mathbf{q}^{(\mathbf{p})}$. The rule of decision making on the
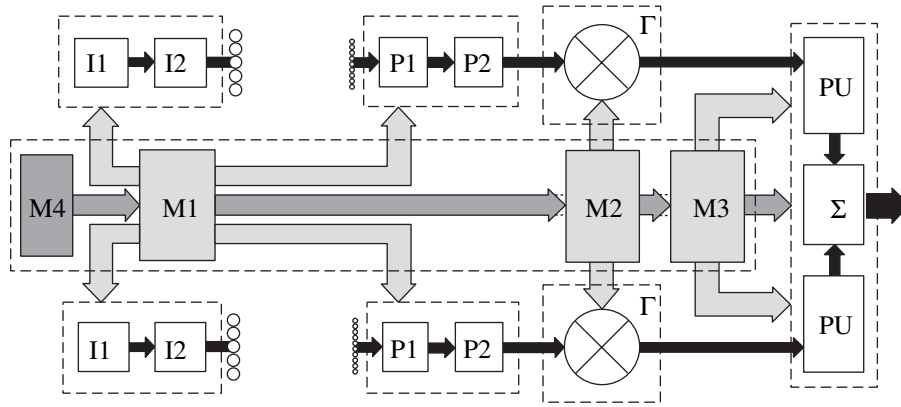
Fig. 1. Block diagram of the algorithm of acoustic observation by the method of low-mode pulsed tomography in a shallow sea.

validity of a hypothesis concerning the value of the vector $\mathbf{q} = \mathbf{q}^{(\mathbf{p})}$ usually has the form

$$\left\| \mathbf{q} - \mathbf{q}^{(\mathbf{p})} \right\|^{\eta} < \boldsymbol{\sigma}, \tag{6}$$

where the norm $\|\cdot\|$, its power index η, and the threshold values $\boldsymbol{\sigma}$ in the general case are determined by the distribution of the probability density for the vector of measured parameters, preset probabilities of errors of the first and second kinds in the process of decision making, noise and interference, and other factors, in particular, the evaluation algorithm for the vector of the conditional probability for the decision on the approval of a hypothesis by an employed measuring device. Under the assumption that the value distributions are normal, using the quadratic metrics $\eta = 2$ and taking into account Eq. (2), for the components of the vector of measuring parameters $\mathbf{q}$ the hypothesis is approved if the difference of the useful signal level and the level of interference and noise exceeds the threshold determined (at the required probabilities of errors) by the statistical distribution of values [17]. In this case, the observation algorithm is determined by the succession of the operations given in Fig. 1, where just two of the $\{I \times J \times N \times M\}$ of jointly processed tomographic projections are given. As follows from Eq. (2) with allowance for Eqs. (1), (3), (4), and (5), the components of the vector of aperture factors for each tomographic projection are determined by the dimensions and positions of the receiving arrays L_j, the frequency band of measurements, the shape of probe pulses, the structure of a hydroacoustic waveguide, and other factors, which are determined by *a priori* information in the form of models of the medium, object, interference, noise, and configuration of the observation system (blocks M1–M4 in Fig. 1). In particular, the aperture factors provide the filtration of mode channels, which is matched to the waveguide, and the compression of probe pulses (blocks I1, I2, P1, and P2). The search for the solution corresponds to the search for hypotheses and, in our case, to the search for discrete channels in the planes

(τ_{ij}^{nm}, Ω_{ij}^{nm}) of separate tomographic projections (blocks G). For each hypothesis, the decision for each tomographic projection is made by the blocks PU, and the resulting solution, obtained by combined processing of all projections in the form of the evaluation of the true values of the observation vector $\mathbf{p} = \tilde{\mathbf{p}}$, is formed by the block Σ. In the case of a change in the observation conditions, the models are corrected (block M4), which can be done by using oceanological models and the hydrological and acoustic data bank for the region of observations. Let us analyze in more detail the specific features of the operation of low-mode pulsed tomography using the examples of observation of wind waves and a spatially restricted inhomogeneity.

RECONSTRUCTION OF THE PARAMETERS OF WIND WAVES

As follows from Eq. (5), the intensity of diffracted low-mode acoustic pulses from the output of a matched filter is determined by the integral equation of convolution of the local spectrum components for inhomogeneities with the squared modulus of the ambiguity function of probing signals. Variation of the delays and Doppler shifts allows us to obtain a set of integral tomographic projections for the spectrum of inhomogeneities and to evaluate their spatial distribution with a resolution determined by the configuration of separate pulse volumes. For different pairs of modes $\{n, m\}$, the spatial structure of pulse volumes may change. Figure 2a shows the structure of these pulse volumes in the horizontal plane (x, y) for $n = 1$ and $m = 3$ for a shallow-water waveguide with a depth of 300 m. In the process of simulation, we adopt the model of a shallow-water sea whose bottom is in the form of two layers of sediments, which lie on an elastic base with the dependence of sound velocity on depth that is typical of winter conditions [4, 5]. The model parameters are conditional and can be easily changed. Selection of mode projections is performed by the blocks I1 and P1 shown in the block diagram in Fig. 1. The positions of radiating $i = 1$

and receiving $j = 1$ arrays located at a distance of 100 km from each other are denoted in Fig. 2a by the letters S and R, respectively, and the digits indicate the positions of pulse volumes with respective numbers. The shapes of pulse volumes, generally speaking, depend on the time of pulse arrival. Their vertical structure is determined by the product of the eigenfunctions $\varphi_{n,m}(z)$ of the modes used.

Let us assume that phase-shift-keyed pulses with a length of 10 s and the modulation law in the form of an M sequence with a carrier frequency of 250 Hz and a frequency band of 10 Hz are used as probing signals [4, 5]. In the case of such probing signals, the central peak of the response in the process of matched filtration performed by the blocks I2 and P2 (Fig. 1) is localized in a narrow interval of the Doppler frequencies and delays. To describe the structure of bottom reverberation, we use the simplest Lommel–Seelinger model [17]. We also assume that nonisotropic wind waves are described by the JONSWAP model [18]. This model can be characterized by the vector of observed parameters, whose components are the wind velocity V and the angle χ determining its direction in the horizontal plane, $\mathbf{p} = \mathbf{p}_R = \{p_1 = V, p_2 = \chi\}$. Further, we assume that the waves are induced by wind with a velocity $V = 5$ m/s directed at an angle $\chi = 5\pi/4$ (the wind direction is indicated in Fig. 2a by an arrow). Calculating the matrices of scattering of waveguide modes from waves at the surface, we use a two-scale model of surface waves, where acoustic field scattering is performed by the resonance harmonic of the waves. The phase velocity of the harmonic is modulated by higher waves [19].

The shape of such a spectrum is shown in Fig. 2b in the form of a brightness distribution on a logarithmic scale. The anisotropy of the spatial spectrum of wind waves causes the shape asymmetry of the matched filter response on the axis of the Doppler frequencies. Since, in each element of the pulse volume, the scattering is performed by a corresponding spatial harmonic satisfying the condition of resonance scattering, a spatial pulse volume can be associated with a pulse volume in the plane of wave numbers. White lines in Fig. 2b show the structure of such volumes in the case of illumination with the first mode and reception of the third mode and the aforementioned parameters of the wind velocity and the shallow-water waveguide. Pulsed volumes for $l = 1$ have the shape of two adjoining circles and, in particular, for $l = 20$, they take on the form of a circle shaped like a dumb bell. The shape of pulse volumes with high numbers tends to a circular ring with the radius $2k$. Note the importance of mutual orientation of pulse volumes and the symmetry axis of the wave spectrum in the space of wave numbers in the process of formation of the response structure of a matched filter, which is evident when comparing the corresponding structures of pulse volumes in the horizontal plane and the wave-number space of (Figs. 2a and 2b). As the analysis shows, a change in the wind direction causes a rise in the asymmetry of the dependence of the matched filter

response (Eq. (5)) at the axis of the Doppler frequency shifts. Figure 2c demonstrates such a response in the brightness form on a logarithmic scale (for a clearer perception of the signal structure, the isolines corresponding to the levels of 80 and 90 dB are given in the brightness field). The search for the values of the delays and Doppler frequency shifts is performed by the block for the verification of hypotheses (block G in Fig. 1). The response values in separate channels of delays from the output of a matched filter correspond to the pulse volumes with the structures shown in Figs. 2a and 2b. The interval of delays that corresponds to the 20th pulse volume is shown in Fig. 2c by two vertical dashed lines. The summary signal in all Doppler frequencies for a fixed value of τ is determined by the distance from all scattering elements of a corresponding pulse volume. The decrease in the response levels of the signals scattered by bottom inhomogeneities located in the resolution elements with a zero Doppler shift (Fig. 2c) is determined by the structure of the model for the spectrum of bottom inhomogeneities and mode decay that is used for calculations.

For each pulse volume, it is possible to construct a dependence of signal decay on the position of a scattering element. Such translational characteristics [20] calculated for the first and third modes demonstrate that there are spatial regions where the signals scattered by relatively low spatial frequencies are weak. This dependence is explained by the fact that the low-frequency spatial components satisfying the conditions of spatial synchronism are located in the elements of the pulsed volumes that are at large distances from the source and the receiver, which leads to their relatively large attenuation because of decay. It is evident that these regions (the pulse volumes and wave-number intervals corresponding to them) must be excluded in the process of solving the inverse problem that corresponds to the regularization of measured data and that is performed by the optimal selection of the components of the vector of the measured parameters $\mathbf{q} = \mathbf{q}_R$ (block M2 in Fig. 1) [4, 19, 20].

Using the minimization of the rms residual as a criterion, the solution $\mathbf{p}_R = \tilde{\mathbf{p}}_R$ corresponding to the global extremum in a two-parameter space (Fig. 3) is determined with the help of the iteration parameters optimized on the basis of *a priori* information concerning the iteration algorithms [4, 20], in particular, using the ravine character of the space of residuals. Since, in the case of bistatic observation, a symmetry axis exists, an observation system consisting of just one tomographic projection is incapable of distinguishing the positive angles of the wind direction from the negative angles. The true position of the global extremum is invariant with respect to the power of the illuminating source and the noise level that represents interference in the process of reconstruction of the parameters of wind waves. However, if the level of additive noise increases and a preset power of the illuminating source is used, the dis-
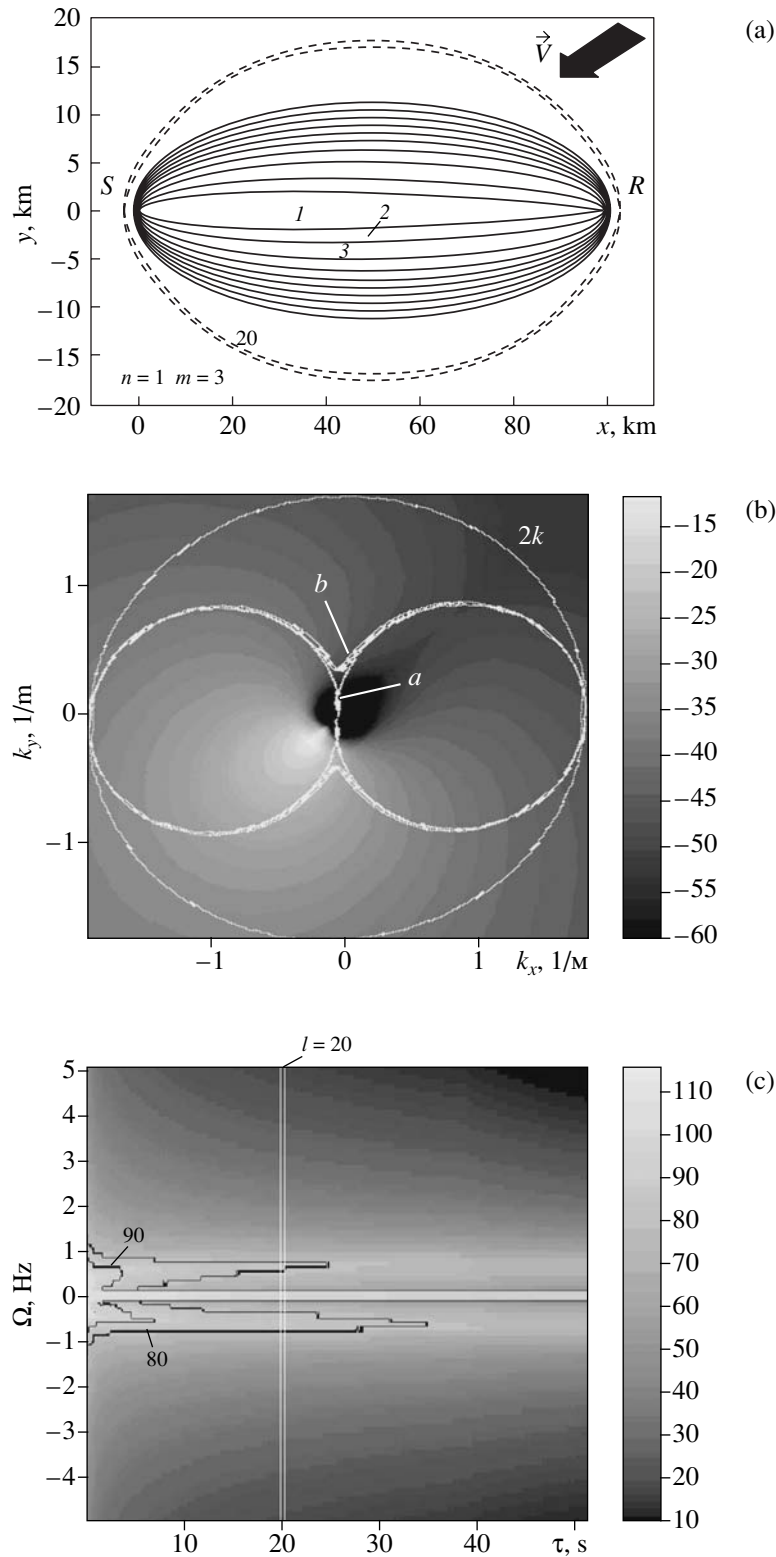
Fig. 2. Formation of the space of residuals in the process of evaluation of the parameters of wind-wave observations. (a) Pulse volumes in the horizontal plane for the first and third modes; (b) the wave spectrum (in a brightness form) and the structure of pulse volumes in the space of wave numbers; and (c) the structure of the matched filter response to reverberation signals from surface waves and the bottom in the process of sorting the hypotheses ($\tau = \tau_{11}^{13}$, $\Omega = \Omega_{11}^{13}$).
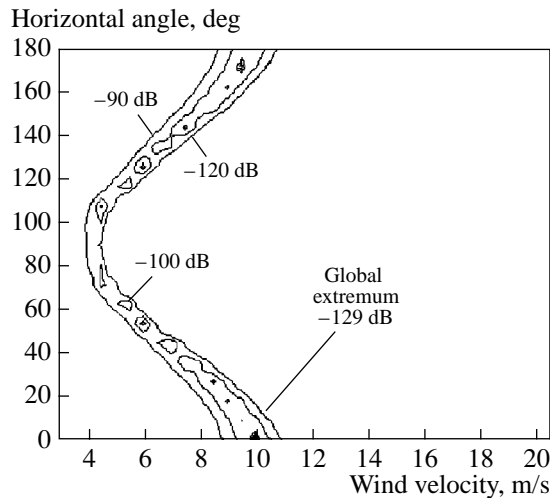
Horizontal angle, deg

Fig. 3. Space of residuals in the process of evaluation of wind parameters.

persion and the shift of the evaluation of the wind wave parameters grow. At a preset required precision of reconstruction, the observation becomes impossible starting from a certain value of the noise level. Using the waveguide model and setting the noise levels, it is possible to indicate *a priori* the regions of the parameters where the reconstruction is possible. These regions can be called the system field of view in the space of the observation parameters $\mathbf{p}_R$.

RECONSTRUCTION OF SPATIALLY LOCALIZED INHOMOGENEITIES

A spatially restricted inhomogeneity in the general case can be characterized by the vector of observation parameters $\mathbf{p} = \{\mathbf{R}, \boldsymbol{\alpha}, \mathbf{V}, \boldsymbol{\sigma}\}$, including, respectively, the three-dimensional vectors of position, orientation, velocity, and extension. Let us consider some specific features of the reconstruction of spatially restricted inhomogeneities for the case of the observation conditions adopted in the previous example. As an observed spatially restricted inhomogeneity, we consider an iceberg, which is simulated by a perfectly rigid body moving along the waveguide surface and partly immersed in the waveguide. To describe diffraction of mode pulses, we assume that the iceberg is shaped like a vertically oriented cylinder with a finite height and dimensions far exceeding the wavelength for the central part of the spectrum of the probe pulse [14, 21]. We assume that the iceberg moves along rectilinear trajectories with equal inclinations with respect to the line between the source and the receiver. The levels and the Doppler shifts of the mode pulses diffracted by this inhomogeneity vary, which determines the efficiency of reconstruction depending on the ratio of useful signals to the level of interference and noise. We assume that, apart from additive noise, the competing scatterers in the form of the wind waves examined in the previous

example also exist. For the observation conditions adopted in the previous section, the pulses scattered by the iceberg are observed after matched filtration against the background of reverberation interference with the structure shown in Fig. 2c. Let us assume that useful signals and interference have a normal statistics. We assume the probability of correct reception of a signal and the probability of false alarms to be set. In this case, the decision on the presence of an iceberg in one of the spatial pulse volumes shown in Fig. 2a, i.e., in a corresponding channel in the plane of time delays and Doppler shifts, is made by a decision device (block PU in Fig. 1). Since the velocity of the moving inhomogeneity is small (0.5–2 m/s), a useful signal is located within the interval of small values of the Doppler shifts, where the interference level is sufficiently high (see Fig. 2c). This situation is mainly characteristic of the iceberg positions near the source–receiver line. In this case, the evaluation of the components of the vector of iceberg parameters, in particular, its coordinates, can be hindered. To increase the spatial resolution, it is necessary to perform observations using several tomographic projections. Let us consider a simple scheme of low-mode pulsed tomography with one illuminating source and two receiving systems, one of them being located near the source, and the other, at a certain distance from it. In this case, one of the tomographic projections corresponds to the monostatic scheme of observation, where all back-scattered signals are detected. The spatial pulsed volumes shaped like concentric circular rings, which correspond to it, are formed by the blocks I1, I2, P1, and P2, and also by the block M1 from the model of the medium (Fig. 1). Verification of hypotheses on the position of the observed inhomogeneity in one of the pulse volumes is performed by the blocks G and PU by searching the channels in the (τ_{11}^{13}, Ω_{11}^{13}) and (τ_{12}^{13}, Ω_{12}^{13}) planes corresponding to the monostatic and bistatic projections in the case of using the model of reverberation interference and noise (block M3 in Fig. 1).

Let us use the numerical model of observation to analyze the efficiency of iceberg observation in the case when some components of the vector of observed parameters, in particular, the velocity and direction of motion, are fixed. In this case, observation is reduced to evaluation of the iceberg position. We assume that the iceberg moves with a velocity of 1.5 m/s along a set of trajectories. Each trajectory makes an angle of $\pi/4$ with the line between the source and the second receiver, located at a distance of 100 km. Calculation of the ratio of the levels of the signal diffracted by the inhomogeneity observed to the level of reverberation from wind waves and the bottom, as well as additive noise, allows us to estimate the probability of the observed object position. Figure 4 gives the spatial distributions obtained in this way for the probability of the approval of a hypothesis on the iceberg coordinates, which determine the fields of view for the monostatic (Fig. 4a) and bistatic (Fig. 4b) projections of low-mode pulsed
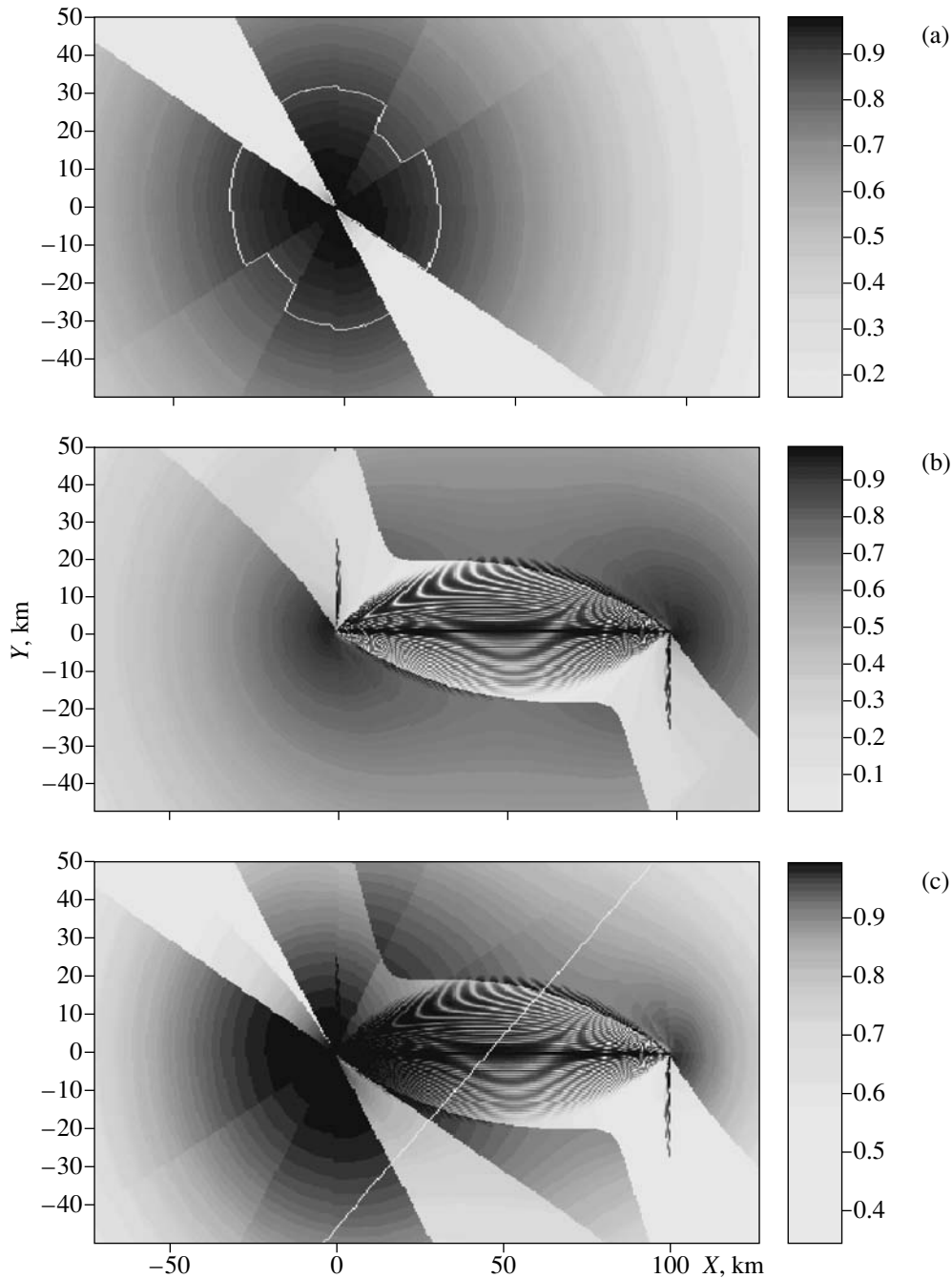
Fig. 4. Structure of the field of view in the case of iceberg observation for the (a) monostatic and (b) bistatic observation schemes and also for (c) a combined processing of two projections. The white line in the lower plot shows one of the trajectories of the iceberg motion.

tomography and also for the case of combined process-
ing of two projections (Fig. 4c). The term "field of
view" is rather conditional. We consider it expedient to
represent the observation capability of the described
tomographic scheme in the form of a brightness distri-
bution of the probability of correct reception in the hor-
izontal plane, to which we relate this concept. The com-
bined processing of the signals from separate tomo-
graphic projections, which is performed by the block Σ

(Fig. 1), consists in the logical accumulation of the
probabilities of separate projections. In the process of
calculation, we assume that the iceberg has the shape of
a cylinder with a diameter of 200 m, which is immersed
in the waveguide for 50 m. The level of additive noise
is taken to be equal to 70 dB relative to 1 μPa. The
power of the illuminating source is selected to be equal
to 100 W. In the case of monostatic observation, the
level of the signals back-scattered by the observed

inhomogeneity only depends on the observation distance. The value of the Doppler shift for the reflected pulses is determined by the angle between the direction of motion and the radius vector from the observation point to the point of the inhomogeneity position (apart from the velocity). The relationship of the values of the Doppler shifts corresponding to iceberg motion with a small velocity and the value of the frequency resolution in the model under consideration is such that the field of view is broken into five pulse volumes corresponding to five channels of the Doppler frequency shifts with different levels of reverberation noise from wind waves and random inhomogeneities of the bottom (Fig. 2c). At small values of the Doppler shifts, the reverberation level is determined mainly by scattering from the bottom. The probability of iceberg observation in the corresponding spatial pulse volumes is close to zero (Fig. 4). The iceberg is also less visible in the case of its motion to the observation point, since, in these regions, the interference is formed by the most intense components of wind waves (Fig. 4a). An analogous structure of the field of view is also formed for a bistatic tomographic projection (Fig. 4b). The maximum interference is formed at small values of Doppler shifts (see Fig. 2c). However, in contrast to the monostatic case, the useful signal level depends on both the illumination angle and on the angle of observation, which leads to a nonuniformity of the field of view (Fig. 4b). In the case of small-angle scattering, where the iceberg is located between the source and the receiving system, the signal level is high, so that the iceberg is visible even against the background of large interference. The spatial distribution of the signal from the iceberg at small scattering angles is of the character of a clearly pronounced interference determined by the scattering pattern of the iceberg, which manifests itself in an irregularity of the field of view in the region between the source and the receiver. The asymmetry of the distribution of interference peaks that is observed in this region is determined by differences in the scattering of modes with different numbers at different angles. Figure 4c shows the field of view in the case of iceberg observation by a tomographic system consisting of two tomographic projections, i.e., the monostatic and bistatic ones. As follows from calculation, the resulting field of view, i.e., the region where it is possible to observe the iceberg, is considerably greater.

The structure of the field of view depends on the observation conditions, such as the level and structure of noise and interference, the waveguide structure, and the parameters of motion of the observed inhomogeneity, which requires the adaptation of the parameters of the observation system to their variation. This adaptation is performed by the block M4 shown in Fig. 1. Most frequently, the external boundary of the field of view is determined by additive noise, while the reverberation interference from random inhomogeneities in the waveguide causes a nonuniformity of the field of view and forms the regions of bad visibility within it. In the case of variation of the parameters of motion, the trajectory of the observed inhomogeneity, and the wave parameters, the field of view may noticeably change. In particular, if the iceberg moves along the track of bistatic observation, the regions where bottom reverberation hinders observation are located at right angles to the source–receiver line.

SELECTIVE EXCITATION AND RECEPTION OF LOW-MODE SIGNALS

An important condition for observation of inhomogeneities in a shallow sea by the method of low-mode pulsed tomography is the selection of mode signals. When implementing low-mode pulsed tomography in practice in shallow water, it is impossible to provide for an ideal selection of waveguide modes, since real radiating and receiving vertically developed arrays always have finite dimensions. Moreover, array deviations from the vertical line are possible, for example, because of the influence of underwater currents, which also affects their selective properties [8, 9, 11, 12].

To verify the possibilities of selective excitation and reception of waveguide modes, a corresponding set of equipment was developed and field experiments were conducted. A radiating array immersed to a preset depth from a research vessel provided the opportunity to emit tone, tone-pulsed, and complex signals with different durations within the frequency range 234–254 Hz. The distance between single radiators in the array (their total number was 16) was 3 m. The position of the radiating array was varied depending on the bottom profile. Two receiving systems were installed at a distance of 1.5 km from each other and operated autonomously. The distance between the hydrophones of each receiving array was 3 m, and the total number of hydrophones in each array was 32. The receiving arrays were held in a vertical position with the help of an anchor and using their flotation ability. The depth at the array sites was 125 m. The level of the signals detected by the receiving arrays in the process of measurements exceeded the noise level by 60–80 dB. The duration of continuous reception was over 48 h. The distance between the source and the receiving systems varied because of the drift of the research vessel from 1 to 22 km. The underwater waveguide depth varied along the trajectory of the vessel motion from 125 to 90 m. A hydrology close to an isovelocity one was observed in the course of measurements. When calculating the mode structure, we adopted the values of the acoustic parameters of the bottom that were characteristic of the region. Effective matching of emitted low-frequency signals, which correspond to the waveguide modes, with a waveguide can be reached by setting the amplitude–phase distribution of pressure at each receiver. Creating such a distribution, it is fundamentally important to take into account the mutual influence of the sources. The preset amplitude–phase distributions were implemented using special iteration algorithms [11]. In the process of mea-

Excitation factor
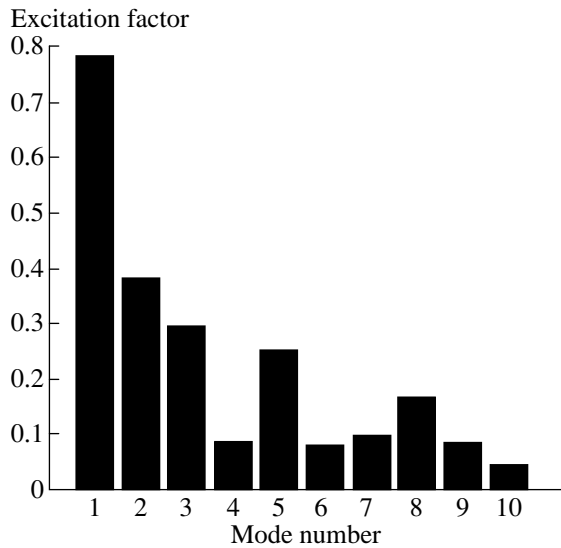
Fig. 5. Mode spectrum of a signal received at a distance of 10 km from a radiating array with a uniform amplitude–phase distribution; the array is positioned in the depth interval from 44 to 89 m.

surements, the distribution that was uniform over the aperture and the distributions corresponding to the first three modes of the waveguide were implemented.

Because of the finiteness of the radiating array aperture, as was indicated before, it is impossible to excite only one specified mode. The level of "parasitic" modes in experiments was determined by the ambiguity in the determination of waveguide parameters and by uncontrolled changes of the array position because of rocking, vessel drift, and currents. One can judge the level of mode selection reached in experiments in the case of combined operation of radiating and receiving arrays by the measured mode spectrum given in Fig. 5.

The measurements demonstrate that the vertical distributions of the acoustic field in both cases are subjected to noticeable time variations caused by the horizontal variability of the parameters of the underwater

sound channel along the track of signal propagation and the spatial variations of the radiating array in the process of research-vessel motion. As a result of these effects and also because of the insufficient track length, it turned out to be impossible to measure with sufficient accuracy the mode attenuation coefficients and some other important parameters of the mode content for different regimes of radiation. At the same time, the acoustic field power summarized over all hydrophones was a very stable quantity at the aperture of the receiving arrays. Figure 6 presents the time variability of the vertical distribution of the field in two radiation regimes. One can see that this distribution is much more stable in the course of the array formation.

In free space or deep ocean, the concentration factor is commonly used as the measure of the array efficiency. In the case of shallow waters, this factor is practically useless, since a layered bottom and surface affect the field formation in the far wave zone. It is suggested to use the ratio of total powers at the aperture of a receiving array covering almost the whole water layer in the case of the field excitation by an array and a single radiator as the measure for the efficiency of a vertical radiating array. Figure 7 shows the dependence of the total powers on the distance for these two radiation regimes in decibels relative to the radiation level of 1 μPa at a distance of 1 m. The difference in these values characterizes the efficiency of an array in a waveguide in comparison with a single radiator. In the described experiment, this value was approximately 7 dB, which agrees well with the calculated data. It corresponds to the array gain at equal radiated powers of a single radiator and an array of radiators. The real level of array radiation can be estimated by adding $10 \log N$ to the given data, where N is the number of radiators in the array. Sometimes, the so-called transition distance, i.e., the distance, starting from which the spherical law of field decay changes to a cylindrical one, is used in engineering calculations. To a certain degree by convention, on the basis of the given experimental data, its value for a single radiator positioned at the array center and for
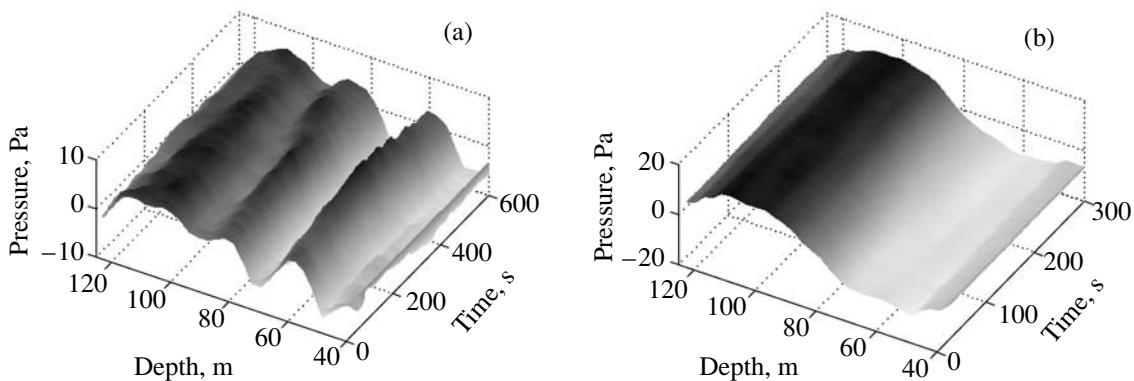
Fig. 6. Field distribution in depth as a function of time in the cases of (a) radiation of a monopole included in the array and (b) a uniform amplitude–phase distribution at the aperture of the radiating array. The observation distance is 4 km.

Pressure, dB/1 μPa
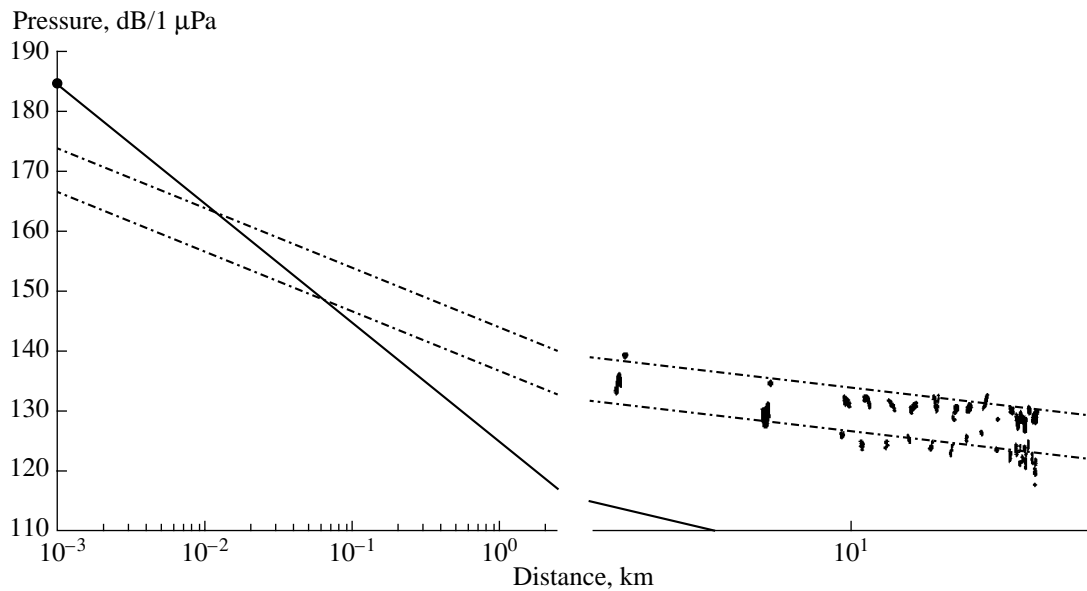
Fig. 7. Dependence of the signal levels on distance for a radiating array (top) and a monopole (bottom). The dashed lines correspond to a cylindrical decay law, and the solid line, to the spherical decay law. The full circle at the left, on the axis, indicates the level of the radiated signal in the case of a monopole and for an array.
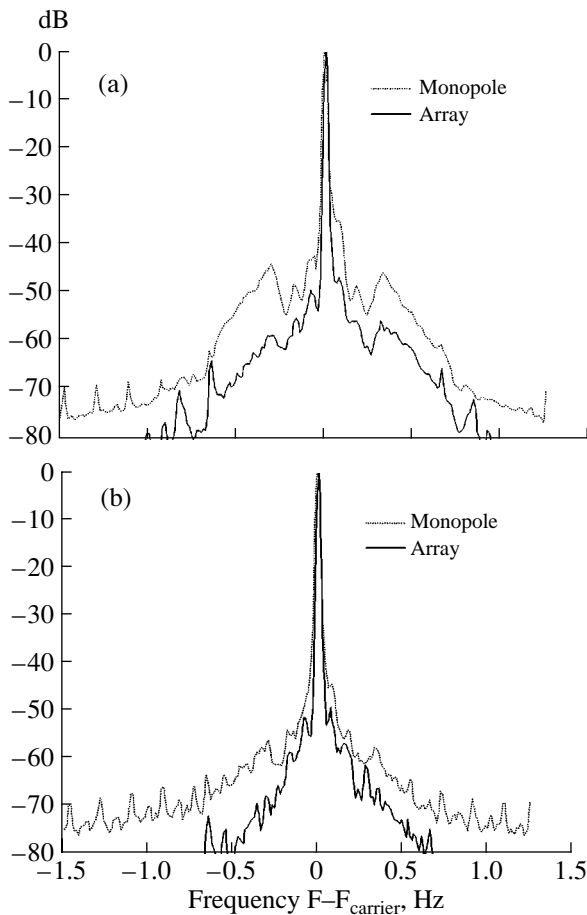
Fig. 8. Spectra of signals scattered by surface waves and received at a distance of 10 km. (a) The spectrum of the total signal at the array and (b) the spectrum of the first waveguide mode.

an array with 16 radiators can be estimated as 100 and 20 m, respectively.

The acoustic field fluctuations in the described measurements were caused by several factors. Low-frequency fluctuations with characteristic scales of about 10 min were apparently connected with the instability of the track length because of the vessel drift. This is confirmed by a comparison of the spectra of signal fluctuations with the fluctuation spectrum of the track length obtained from GPS data. Internal waves as a source of fluctuations can be excluded, since they were not detected in the accompanying measurements by an ADCP Doppler acoustic profiler and an STD probe. The high-frequency fluctuations caused by scattering from surface waves are of most interest. The peak originating from signal modulation by surface waves and fluctuations of the array shape and position is clearly seen in the measured fluctuation spectra of the signal (Fig. 8) from a single source. A comparison of the single source fluctuations with an array demonstrates that the level of the spectral components connected with surface waves in the case of radiation by a vertically distributed source is 10 dB lower than the levels observed in the case of sound radiation by a point source. The major part of the energy of these spectral components is concentrated in the modes with high numbers. These results are explained by the fact that a distributed source almost immediately forms an acoustic field within the water layer, and its region of interaction with the surface decreases, whereas, in the case of a single source, this region is much greater. As a result, the received reverberation level for a single radiator is much higher than the reverberation level observed in the case of radiation by an array of radiators.

Thanks to the experiments conducted up to now, it was possible to establish that the focusing of the acoustic energy flux with the help of a vertically oriented array of radiators in the direction of the waveguide axis reduces the losses connected with the excitation of high-number modes strongly interacting with the layered bottom and, therefore, that are characterized by higher attenuation factors. On account of this effect, in the measurement conditions, it was possible to obtain a gain of about 7 dB in the level of the excited field relative to the case of the field excitation by a single radiator of the same power, which coincides with the theoretical estimates obtained earlier. Moreover, it was experimentally demonstrated that the level of the field fluctuations in the course of the array operation is much lower than in the case of the operation of a single radiator. This is caused by the weaker interaction of the field with the bottom and surface and by the lower sensitivity of the excited low-mode field to variations of the radiating system due to the rocking of the vessel. It was also experimentally found that the level of surface reverberation is more than 10 dB lower in the case of the use of a radiating array with 16 elements in comparison with the use of a single radiator. Thus, the experimental results on the whole confirm the efficiency of selective excitation and reception of low-mode pulsed signals in a shallow sea with the help of vertically developed antenna arrays and allow us to make a conclusion about the possibility of the implementation of low-mode pulsed tomography for solving practical problems. At the same time, the necessity of a stationary mounting of a radiating array follows from the same results.

The experimental studies described above demonstrate that the use of vertical radiating and receiving arrays for low-mode excitation and reception with a subsequent spectral–time processing provides an opportunity to increase the efficiency of tomographic reconstruction and to perform measurements with a comparatively small number of spaced sources and receivers.

ACKNOWLEDGMENTS

REFERENCES

1. N. V. Gorskaya, S. M. Gorskiĭ, V. A. Zverev, and A. I. Khil'ko, Akust. Zh. **34**, 55 (1988) [Sov. Phys. Acoust. **34**, 29 (1988)].

2. Yu. A. Kravtsov, V. M. Kuz'kin, and V. G. Petnikov, Izv. Vyssh. Uchebn. Zaved., Radiofiz. **26** (4), 440 (1983).

3. S. M. Gorskiĭ, V. A. Zverev, A. L. Matveev, and V. V. Mityugov, Akust. Zh. **41**, 223 (1995) [Acoust. Phys. **41**, 190 (1995)].

4. V. G. Burdukovskaya, A. G. Luchinin, and A. I. Khil'ko, in *Proceedings of 4th Scientific Conference on Radio Physics* (Nizhegor. Gos. Univ., Nizhni Novgorod, 2000), pp. 120–137.

5. A. G. Luchinin, A. I. Khil'ko, B. N. Bogolyubov, *et al.*, in *Methods of Acoustical Diagnostics of Inhomogeneous Media*, Ed. by V. A. Zverev (Inst. Prikl. Fiz. Ross. Akad. Nauk, Nizhni Novgorod, 2002), pp. 30–38 [in Russian].

6. W. A. Kuperman, W. S. Hodgkiss, and H. C. Song, J. Acoust. Soc. Am. **103**, 25 (1998).

7. A. L. Matveev, V. V. Mityugov, and A. I. Potapov, Akust. Zh. **47**, 246 (2001) [Acoust. Phys. **47**, 202 (2001)].

8. B. V. Kerzhakov, V. V. Kulinich, A. G. Koshkin, and A. I. Khil'ko, in *Acoustics of the Ocean: Proceedings of X School–Seminar of Academician L.M. Brekhovskikh Combined with XIV Session of the Russian Acoustical Society* (GEOS, Moscow, 2004), pp. 206–210.

9. B. V. Kerzhakov, V. V. Kulinich, A. G. Koshkin, and A. I. Khil'ko, Preprint No. 658, IPF RAN (Inst. of Applied Physics, Russian Academy of Sciences, Nizhni Novgorod, 2004).

10. M. A. Raevskiĭ and A. I. Khil'ko, Preprint No. 620, IPF RAN (Inst. of Applied Physics, Russian Academy of Sciences, Nizhni Novgorod, 2003).

11. A. G. Luchinin, A. I. Khil'ko, B. N. Bogolyubov, *et al.*, in *Methods of Acoustic Diagnostics of Inhomogeneous Media*, Ed. by V. A. Zverev (Inst. Prikl. Fiz. Ross. Akad. Nauk, Nizhni Novgorod, 2002), pp. 30–38 [in Russian].

12. A. G. Luchinin, A. I. Khil'ko, A. A. Stromkov, *et al.*, in *Acoustics of the Ocean: Proceedings of X School–Seminar of Academician L. M. Brekhovskikh Combined with XIV Session of the Russian Acoustical Society* (GEOS, Moscow, 2004), pp. 216–220.

13. V. V. Goncharov, V. Yu. Zaĭtsev, V. M. Kurtepov, A. G. Nechaev, and A. I. Khil'ko, *Acoustic Tomography of the Ocean* (Inst. Prikl. Fiz. Ross. Akad. Nauk, Nizhni Novgorod, 1997) [in Russian].

14. A. G. Nechaev and A. I. Khil'ko, Preprint No. 178, IPF AN SSSR (Inst. of Applied Physics, USSR Academy of Sciences, Gorki, 1987).

15. S. M. Gorskiĭ, V. A. Zverev, and A. I. Khil'ko, in *Formation of Acoustic Fields in Oceanic Waveguides*, Ed. by V. A. Zverev (Inst. Prikl. Fiz. Akad. Nauk SSSR, Gorki, 1991), pp. 82–114 [in Russian].

16. L. M. Brekhovskikh and Yu. P. Lysanov, *Fundamentals of Ocean Acoustics* (Gidrometeoizdat, Leningrad, 1982; Springer, New York, 1991).

17. R. J. Urick, *Principles of Underwater Sound*, 3rd ed. (McGraw-Hill, New York, 1983; Sudostroenie, Leningrad, 1978).

18. K. Hasselman, T. P. Barnet, E. Bouwes, *et al.*, Measurements of Wind–Waves Growth and Swell Decay during the Joint North Sea Wane Project (JONSWAP), Dt. Hydrogr. Z., Reihe, A(8), 12.

19. M. A. Raevskiĭ, V. G. Burdukovskaya, A. G. Luchinin, and A. I. Khil'ko, in *Acoustics of the Ocean: Proceedings of X School–Seminar of Academician L.M. Brekhovskikh Combined with XIV Session of the Russian Acoustical Society* (GEOS, Moscow, 2004), pp. 296–330.

20. I. P. Smirnov, J. W. Caruthers, and A. I. Khil'ko, Preprint No. 550, IPF RAN (Inst. of Applied Physics, Russian Academy of Sciences, Nizhni Novgorod, 1999).

21. I. P. Smirnov, A. I. Smirnov, J. W. Caruthers, and A. I. Khil'ko, Preprint No. 538, IPF RAN (Inst. of Applied Physics, Russian Academy of Sciences, Nizhni Novgorod, 2000).

22. A. I. Belov and A. I. Khil'ko, *Formation of Acoustical Fields in Oceanic Waveguides: Coherence Phenomena* (Inst. of Applied Physics, Russian Academy of Sciences, Nizhni Novgorod, 1997), pp. 240–255.

Translated by M. Lyamshev

Adaptive Active Noise and Vibration Control Systems

A. A. Mal'tsev, R. O. Maslennikov, A. V. Khoryaev, and V. V. Cherepennikov

Lobachevski State University, pr. Gagarina 23, Nizhni Novgorod, 603950 Russia
e-mail: maltsev@rf.unn.ru
Received July 12, 2004

Abstract—A review of research concerned with adaptive noise and vibration control systems and performed under the supervision of Corresponding Member of the Russian Academy of Sciences V.A. Zverev at Nizhni Novgorod State University in the 1980s and 1990s is presented. The history of the subject is briefly outlined, and the theoretical foundations of the design of adaptive active control systems for random wave fields are considered. The main experimental studies performed in this area of research at the Department of Bionics and Statistical Radiophysics of Nizhni Novgorod State University are described. Promising lines of research in this area are indicated, and examples of the practical application of adaptive control systems are given. © 2005 Pleiades Publishing, Inc.

INTRODUCTION

This paper is a review of research conducted at the Radiophysical Faculty of Lobachevski State University, Nizhni Novgorod (NNSU) in the field of adaptive active noise and vibration control systems within the last 20 years. The investigations were performed as research and development works for enterprises and industrial R&D institutes in close collaboration with the Institute of Applied Physics, Russian Academy of Sciences. The supervisor of this work from the Academy of Sciences was Vitaliĭ Anatol'evich Zverev. It can be unquestionably stated that the emergence of this new area of research itself is closely associated with the general approach to the solution of a variety of problems in acoustics, optics, and radio physics that Zverev developed and supported in his publications and reports at seminars. This approach consists in the development and application of ideas and methods elaborated in one branch of radio physics to solving problems that arise in its other branches. Studies carried out by Zverev [1–3] are brilliant examples of the efficiency of the mutual interpenetration of ideas that appeared in radio engineering, optics, and acoustics. We believe that the series of works reviewed here is an illustration of the application of Zverev's approach.

It should be noted that the development of adaptive active control systems (AACSs) was preceded by numerous studies of systems providing for sound and vibration control in a given spatial region by creating a canceling field with the help of active radiators without using the adaptation principle (automatic adjustment of the suppressing radiators). As long ago as in the early 1970s, a possibility of suppressing wave fields of different physical natures by creating a canceling field with the help of a continuous system of monopole or dipole radiators, which realize the Huygens surfaces, was theoretically shown in [4, 5]. Foundations of the theory and experiment concerning nonadaptive systems for the

active control of wave fields were laid in 1971–1982 by G.D. Malyuzhinets, M.V. Fedoryuk, B.D. Tartakovskiĭ, A.A. Mazannikov, V.V. Tyutekin, M. Jessel, G. Mangiante, and other researchers in Russia and abroad [6–14]. The fullest list of publications related to this subject for the period up to 1982 inclusive is given in [15].

However, the practical implementation of the active sound and vibration control technique proved to be rather difficult. Particularly, real active suppression systems encountered computational difficulties in the calculation of Green's operator and in its optimal approximation by discrete radiators [7, 8]. Also, even the first experiments on active sound control in waveguides [9, 10, 13] showed that the system that controls the canceling radiators must be tuned to a very high accuracy. To overcome these difficulties, an adaptive (self-tuning) active wave control system was proposed. This system operates as follows: the adaptive system collects information from sensors of the primary and residual fields and uses it to control the characteristics of the radiators so as to minimize the average power of the residual field.

BASICS OF THE THEORY OF ADAPTIVE CONTROL OF RANDOM WAVE FIELDS

The first publications on AACSs were those by J.C. Burgess [16], S.N. Arzamasov, A.N. Malakhov, A.A. Mal'tsev, and I.E. Pozumentov [17–19], which actually appeared at the same time in 1981 and 1982. The first of the cited papers [16] considered the simplest adaptive canceller containing one active element for solving the one-dimensional sound control problem in a single-mode waveguide. This scheme may be regarded as a straightforward development of the concept of adaptive filters and adaptive cancellers, which was successfully implemented in radar in the late 1960s and early 1970s. For the sake of comparison,

(a)

(b)
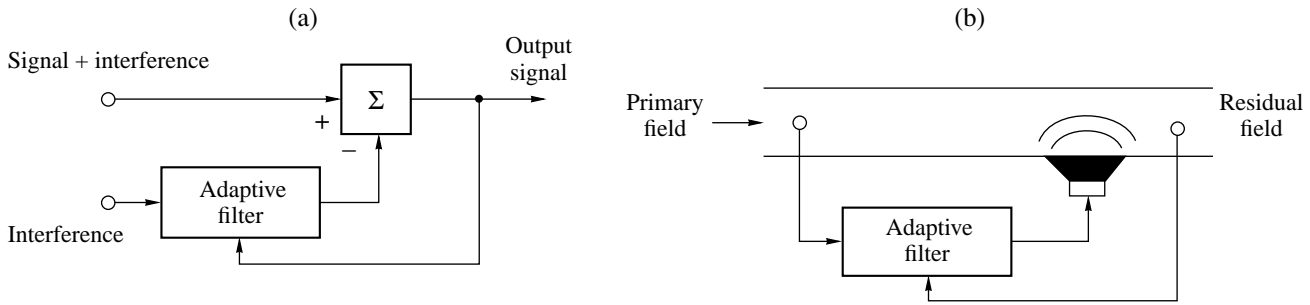
Fig. 1. (a) Adaptive interference canceller and (b) one-dimensional adaptive waveguide sound control system.

(a)

(b)
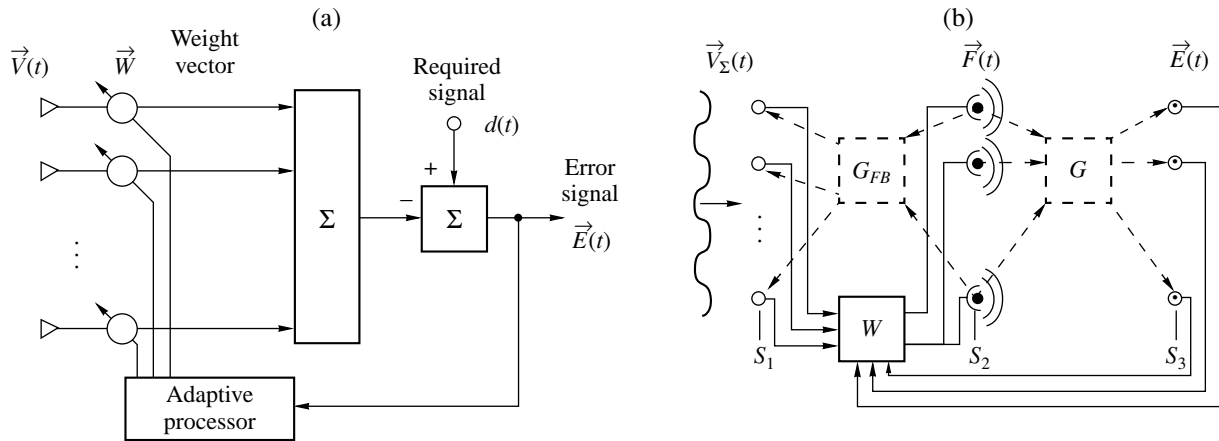
Fig. 2. (a) Adaptive antenna array, which operates by the minimal root-mean-square error criterion, and (b) multidimensional adaptive wave field control system, which operates by the criterion of the minimizing the root-mean-square residual field at several test points.

Fig. 1 shows a structural diagram of adaptive systems used to cancel interference in radar (Fig. 1a) and to suppress a single-mode acoustic field in a waveguide (Fig. 1b). The similarity of these schemes is evident. Their main physical difference is that the radar canceller eliminates interference in the electric circuit (in a wire), while the acoustic adaptive canceller must suppress the field in a certain nonzero region in space (in this example, in the right-hand part of the waveguide).

Adaptive Suppression of Narrowband Random Wave Fields

A more general problem of developing multidimensional AACSs that cancel sound in space and multimode waveguides was considered in [17–19]. In this formulation, the problem can be regarded as a generalization of the structural scheme of an adaptive antenna array to the cancellation of wave fields in space. Since the early 1980s, adaptive arrays have been widely used for spatial signal processing in radar and communications. For the sake of comparison, Fig. 2 shows structural diagrams of signal processing in a narrowband adaptive array, which operates by the minimum root-mean-square (rms) criterion, and in a narrowband

AACS that suppresses acoustic field in space. The narrowband antenna array processes signals produced by field sensors by multiplying them by a vector $\vec{W}$ of weighting coefficients and then summing the results so as to minimize the rms error between the adaptive array output and the required (training) signal. As shown in Fig. 2b, the main elements of the AACS are the sensors (monopoles and dipoles) of the primary field at L points on the surface S_1, M control radiators (monopoles and dipoles) on the surface S_2 characterized by their intensity vector $\vec{F}(t)$, and Q sensors (monopoles and dipoles) of the residual field $\vec{E}(t)$ on the surface S_3. Based on the information collected by the primary field sensors, the adaptive system adjusts the complex weights (entries of the $M \times L$ matrix $\mathbf{W}$) so as to minimize the total power (a sum of mean squares) of the residual field at the points where the secondary measurements are taken.

It can also be seen from the structural diagrams shown in Fig. 2 that, apart from the evident increase in dimension (the number of controlled weights and feedback circuits), the AACS differs from the adaptive array

Comparison of formulas that describe narrowband adaptive arrays and AACSs

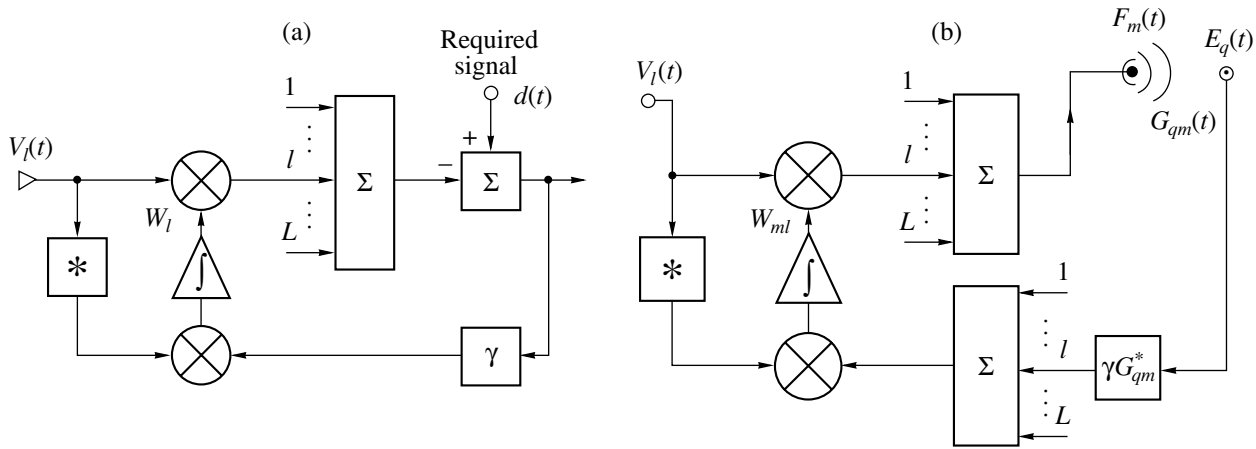| Adaptive array	AACS
Performance criterion	
$J(\vec{W}) = \langle |E(t)|^2 \rangle$	$J(\mathbf{W}) = \sum\limits_{q=1}^{Q} \langle |E(\vec{r}_q)|^2 \rangle$
Adaptive tuning algorithm	
$\dfrac{d\vec{W}}{dt} = \gamma \vec{V}^*(t) E(t)$	$\dfrac{dW_{ml}}{dt} = \gamma V_l^*(t) \sum\limits_{q=1}^{Q} G_{qm}^* E_q(t)$
Optimal weights	
$\vec{W}_{\text{opt}} = \mathbf{R}^{-1} \vec{P}_{Vd}$	Without the wave feedback: $\mathbf{W}_{\text{opt}} = (\mathbf{G}^+\mathbf{G})^{-1}\mathbf{G}^+\mathbf{P}_V\mathbf{R}^{-1}$
	With allowance for the wave feedback: $\mathbf{W}_{\text{st}} = (\mathbf{I} - \mathbf{W}_{\text{opt}}\mathbf{G}_{\mathbf{FB}})\mathbf{W}_{\text{opt}}$
Residual steady-state power	
$J(\vec{W}_{\text{opt}}) = \langle d^2 \rangle - \vec{W}_{\text{opt}}^+\vec{P}_{Vd}$	$J(\mathbf{W}_{\text{opt}}) = \langle \vec{V}^+\vec{V} \rangle - Sp[\mathbf{P}_V^+ \mathbf{G}(\mathbf{G}^+\mathbf{G})^{-1}\mathbf{G}^+\mathbf{P}_V\mathbf{R}_V^{-1}]$
Stability of the steady-state solution	
Global	Local: matrix $\mathbf{B} = \mathbf{I} - \mathbf{W}_{\text{opt}}\mathbf{G}_{\mathbf{FB}}$ must be positive-definite

in that it possesses the following fundamentally new features: it contains a signal transformation (described by the Green's function matrix $\mathbf{G}$) on the path between the suppressing radiators and residual field sensors, and wave feedback (described by the Green's function matrix $\mathbf{G}_{\mathbf{FB}}$) is possible between the canceling radiators and sensors of the primary field. Due to the wave feedback, the vector $\vec{V}_\Sigma(t) = \{V_1(t), V_2(t), \ldots, V_L(t)\}^T$ of signals produced by the primary field sensors (for the narrowband system, all signals are represented by their complex amplitudes) is actually a superposition of the signal produced by the primary field and the feedback signals produced by the canceling radiators. Thus, in the presence of the wave feedback, adaptive algorithms used in active control systems and the optimal weights $\mathbf{W}$, which minimize the total power of the residual field, depend on elements of the Green's matrices $\mathbf{G}$ and $\mathbf{G}_{\mathbf{FB}}$. It is of interest to compare the main analytic expressions that describe operation of narrowband adaptive arrays and AACSs presented in the table.

These expressions use the following designations: $E(\vec{r}_q) \equiv E_q(t)$ is the residual (total) field or its derivative at the sites of secondary sensors $\vec{r}_q$; W_{ml} is the weight (element of matrix $\mathbf{W}$), which determines the contribution of the total signal $V_l(t)$ produced by the lth primary field sensor to the signal of the mth canceling radiator; γ is a constant factor, which determines the convergence rate of the gradient adaptive algorithm; $\vec{P}_{Vq}$ is vector of cross-correlation coefficients between the primary wave field $\vec{V}(t)$ and the required signal $d(t)$; $\mathbf{P}_V$ is the cross-correlation matrix between the primary random fields at the sites of the primary and secondary (monitor) sensors; and $\mathbf{R}$ is the correlation matrix between the random fields at the sites of the primary sensors. The remaining designations are clear from the structural diagrams shown in Fig. 2. The analytical expressions demonstrate a close similarity of the adaptive array and AACS theories. For example, Fig. 3 compares the block diagrams that implement the gradient algorithm that tunes one weight of the adaptive array to that for the AACS. Note that, unlike the adaptive array, to provide stability of the narrowband AACS, the feedback circuit between each qth residual field sensor and the control circuit of each mth canceling radiator must contain a correction filter G_{qm}^*. It can easily be seen that this filter compensates for phase advances of the waves traveling from the mth canceling radiator to the qth control receiver, thereby providing for the stability of the multidimensional control system as a whole. It is clear that, in the narrowband AACS, the correction filters can easily be realized with the help of phase shifters and amplifiers.

Papers [17–19] were the first to report fundamental theoretical results on the narrowband AACSs. Adaptive algorithms for tuning the weights were derived, stability conditions were studied, and analytical expressions for the optimal weights were obtained. It was shown that the wave feedback reduces the convergence rate of the adaptive algorithms and may cause the system as a whole to lose its stability. However, operating by the criterion of the minimum power of the residual field at the sites of the secondary sensors, the AACS automatically accounts for the wave feedback and, with the stability condition of the adaptive algorithm being satis-

Fig. 3. Block diagram of tuning one weighting coefficient for (a) a narrowband adaptive antenna array and (b) a narrowband adaptive active control system.

fied, the average total power of the residual field is independent of the wave feedback.

The analytical results have shown that all averaged AACS characteristics can be expressed through auto- and cross-correlation matrices of the primary field and through the Green's function matrices. Thus, it became possible to analytically study the characteristics of the AACSs in a number of model theoretical problems. Let us illustrate this by two classical theoretical problems.

Cancellation of a Plane Wave Transmitted through a Chaotic Screen [17]

Consider a two-dimensional problem of the active cancellation of random waves behind an infinite chaotic planar screen. Let a monochromatic plane wave $p(x, z, t) = \exp j(kz - \omega_0 t)$, $z < 0$ (see Fig. 4) be normally incident on a screen lying in the plane $z = 0$. Let an
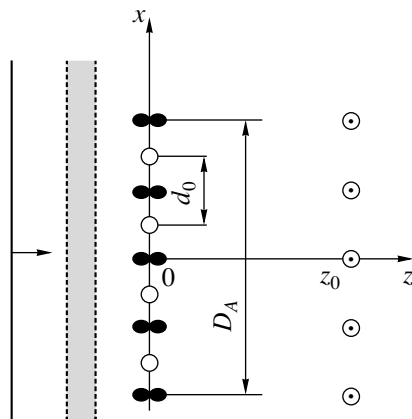
Fig. 4. Arrangement of elements of the AACS for suppressing the plane wave transmitted through an infinite chaotic screen: primary field sensors (open circles), canceling dipole radiators (closed figure-eight-shaped symbols), and monopole monitor receivers (open circles with dots).

active sound control system be used to cancel the random narrowband field $p(x, z, t) = P(x, z)\exp(-j\omega_0 t)$, which is modulated by the screen, in the half-space $z > 0$. Let the primary sensors (monopoles) be arranged uniformly, at a distance d_0 from each other, in the plane $z = 0$ just behind the screen and measure the modulated field $p(x, 0, t)$ at L points. To eliminate the wave feedback, the canceling radiators (dipoles) are also placed in the plane $z = 0$ at M points, and Q secondary sensors (monopoles) of the residual field are located in the far-field zone in the plane $z = z_0$. We assume that the chaotic screen does not affect the field produced by the canceling radiators in the region $z > 0$. For the sake of definiteness, let the number of radiators be equal to the number of secondary sensors: $M = Q$. To obtain analytical expressions and numerically estimate the efficiency of the AACS, assume that the random field in the plane $z = 0$ (just behind the chaotic screen) is stationary, statistically homogeneous, and zero-mean $\langle P(x, 0) \rangle = 0$, and that its spatial correlation function is exponential:

$$\Psi_p(x_1, x_2, 0, 0)$$
$$= \langle P(x_1, 0)P^*(x_2, 0) \rangle = \sigma_p^2 e^{-|x_1 - x_2|/l_p}, \tag{1}$$

where $\sigma_p^2 = \langle |P(x, 0)|^2 \rangle$ is the variance and l_p is the correlation radius of the boundary field behind the chaotic screen. In the case of the large-scale boundary field inhomogeneity ($kl_p \gg 1$), which is most interesting for applications, expressions for the spatial correlation matrix of the initial field $\mathbf{R}$ and the cross-correlation matrix $\mathbf{P}_V$ can easily be found. This allows us to derive analytical expressions for the matrix $\mathbf{W}_{\mathrm{opt}}$ of optimal weights, to find the minimum value of the performance criterion functional $J(\mathbf{W}_{\mathrm{opt}})$ and the residual power of the random field at the sites of the monitor sensors, and, thus, to perform a complete analysis of this model problem.

For example, consider the structure of the residual field in the simplest case, when the system consists of a large number of primary sensors arranged in a uniform array of elements spaced a sufficiently small distance apart ($d/l_p \ll 1$), one canceling radiator at the point with the coordinate x_1, and one secondary sensor at the point with the coordinate x_2. Figure 5 shows the theoretical relative power of the residual field $\langle|E(x)|^2\rangle/\sigma_p^2$ in the plane $z = z_0$ versus the transverse coordinate x for two relative positions of the secondary sensor placed at the point (x_2, z_0) and the canceling radiator placed at the point $(x_1, 0)$. As follows from this plot, the power at the site of the secondary sensor is always zero in this approximation, and the maximum cancellation region (about $2l_p$ long) occurs when the radiator is exactly opposite to the monitor receiver ($x_1 = x_2$). When $|x_2 - x_1| > \lambda_0 z_0/(4l_p)$, intensity oscillations are observed in the residual field, which, presumably, are due to the interference between the spherical wave of the suppressing radiator and the quasi-plane wave of the random field. It is clear that, at long distances $|x - x_2| \gg l_p$ from the monitor sensor, the field of the suppressing radiator and the primary field are incoherently combined and, as one would expect, the total field intensity is twice as high.

This example thus shows that, to efficiently cancel the random field with the help of an active array of adaptively controlled radiators, it is necessary that periods of arrays of the primary and secondary sensors be smaller than the transverse correlation radius l_p of the primary random wave. If the sensors (primary and secondary) and canceling radiators are sufficiently dense, a shadow region is formed behind the active array of radiators (in the far zone with respect to l_p), whose boundaries for different suppression levels are shown in Fig. 6 as a function of dimensionless parameter $\chi^{-1} = 2z_0/(kl_pD)$, which is proportional to the distance z_0 between the plane of the canceling radiators and the secondary sensors.

Cancellation of the Random Wave Field behind a Slot in a Planar Screen [20]

Let a plane wave with the random complex amplitude $P(x, z)$ be incident in the two-dimensional space (x, z) from the region $z < 0$ onto an infinite rigid screen lying in the plane $z = 0$ and containing a slot ($|x| \leq a/2$), as shown in Fig. 7. Let us specify the field and its derivative $\partial P(x, z)/\partial z$ in the plane $z = 0$ behind the screen in terms of Kirchhoff's approximation. It is necessary to cancel the diffraction field $P_d(x, z)$ at $z > 0$. To this end, we place L primary dipole receivers oriented along the z axis, which measure the normal derivative $\partial P(x, z)/\partial z$. Let us relate the intensity vector $\mathbf{F} = \{F_1, ..., F_M\}^T$ of the canceling dipole radiators also placed in the plane of the slot $z = 0$ to the readings of the primary sensors through the matrix $\mathbf{W}$ of adaptive weights (see Fig. 2b). Applying the technique of calculating the optimal
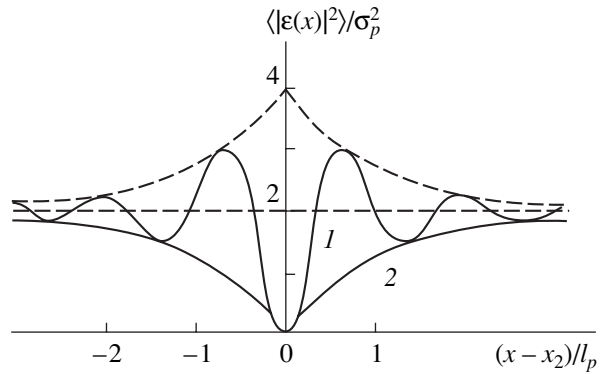

Fig. 5. Power of the residual field near the monitor receiver located at the point (x_2, z_0) when the system contains one suppressing radiator located at the point $(x_1, 0)$: (I) $(x_2 - x_1) = 3z_0\lambda/4l_p$ and (2) $x_2 = x_1$.
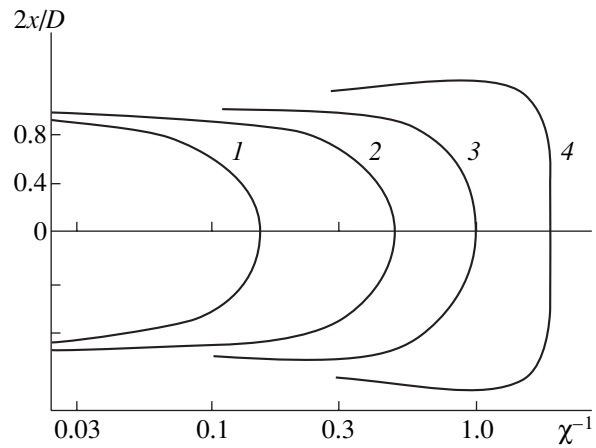

Fig. 6. Boundaries of the shadow zone behind the active array of adaptively controlled radiators.
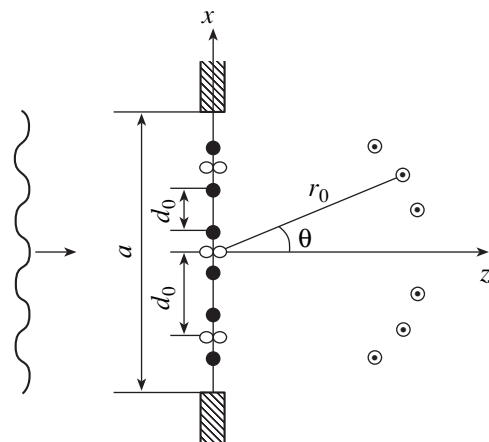
Fig. 7. Arrangement of elements of the adaptive active system, which cancels a random wave field behind a slot in a rigid screen: primary dipole sensors (open figure-eight-shaped symbols), canceling monopole radiators (closed circles), and monopole monitor receivers (open circles with dots).
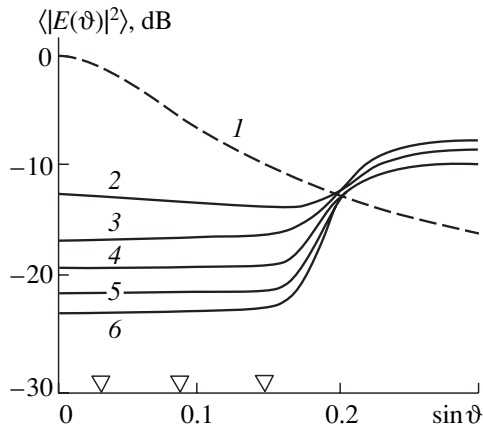
Fig. 8. Power of the (*1*) diffraction and (*2–6*) residual fields behind a slot in a rigid screen versus angle θ for a weakly coherent incident wave ($l_p = 0.5a$, $M = Q = 6$, $L' = 3, 5, 7, 9$, and 11).
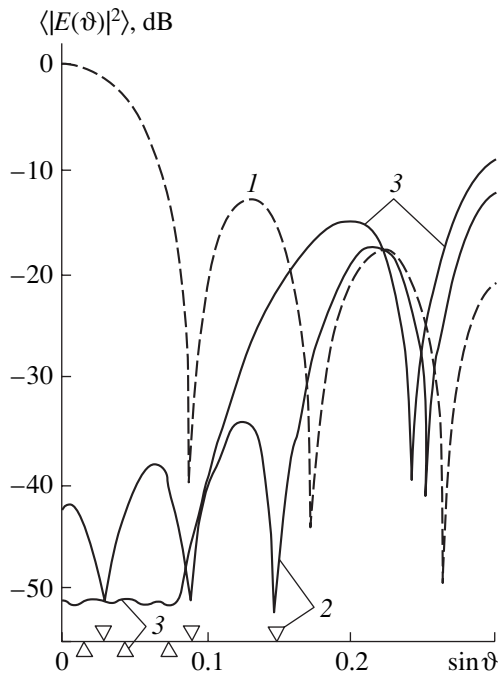
Fig. 9. Angular power spectra of the (*1*) diffraction and (*2*, *3*) residual fields versus the arrangement of the secondary sensors at a high coherence of the incident wave ($l_p = 10^3 a$, $M = Q = 6$, $L' = 5$).

weighting coefficients and the average power of the residual field described above, we can analytically study the characteristics of the AACS in this model problem with any parameters of the random wave incident on the slot and with a different number of elements in the active system.

To illustrate how the degree of canceling the diffraction field depends on the accuracy to which the spatial structure of a weakly coherent incident wave is mea-

sured, Fig. 8 represents the power of the diffraction and residual fields with the number of primary sensors as a parameter (the power of the diffraction field on the *z* axis is taken as reference). The secondary sensor positions were specified by the sine of angle θ and are indicated on the abscissa axis by open triangles. The positions and number of the canceling radiators and secondary sensors were fixed ($M = Q = 6$). A comparison of curves *2–6* shows that the residual field power decreases with an increasing number of primary sensors (and correspondingly decreasing spacing d_0 between them). However, even detailed measurements of the spatial structure of a weakly coherent incident wave ($d_0/l_p = 0.18$, curve *6*) do not reduce the residual field power in the shadow region |sinθ| ≤ 0.15 below –23 dB.

Figure 9 shows the power of the diffraction and residual fields at $l_p/a = 10^3$ with the number of radiators equal to the number of secondary sources ($M = Q = 6$). It can be seen that, due to the high spatial coherence of the primary field, the cancellation of the diffraction field in this case is more efficient. Towards the secondary sensors, the residual field power decreases by 52 dB. However, when the secondary sensors are widely spaced (curve *2*; all six sensors are in the sector of the main lobe and first side lobes of the angular spectrum of the diffraction field), interference maxima appear between them. To reduce the amplitude of these maxima and to create a region of deep shadow (of about –52 dB) over the entire angular sector, the secondary sensors should be placed closer (curve *3*; all sensors are in the sector of the main lobe of the diffraction field) or both their number and the number of suppressing radiators should be increased.

The examples presented above show the efficiency of applying the analytical formalism developed in [17–22] to the analysis of main characteristics of adaptive active systems that cancel random fields. It is well known that direct numerical investigation of solutions to such problems, for example, by the finite element method, requires much computational effort and long processor time.

Adaptive Control of Broadband Wave Fields: Space- and Time-Domain Adaptation [23]

In problems of the active control of broadband random fields in waveguides, it is necessary to model Green's function in both space and time (frequency) domains. One of the methods for approximating the required transfer functions relies on transversal filters. An algorithm based on a multidimensional transversal filter was derived, and characteristics of a broadband adaptive active control system for broadband random wave fields were studied in [23].

Let sources of a broadband random field $p(\vec{r}, t)$ be located in a finite space region. Let it be necessary to suppress the primary field $p(\vec{r}, t)$ in a certain region
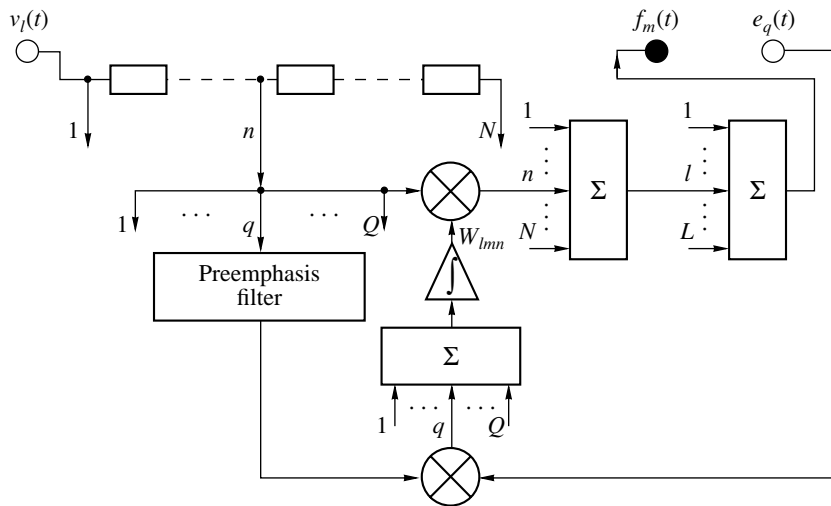
Fig. 10. Block diagram of a tuning circuit of one weighting coefficient of a broadband AACS (preemphasis filters are on the left in the circuits of signals picked up from the primary sensors).

outside a closed surface that includes the sources. To do this, let us use the active control system, the arrangement of the elements of which is illustrated in Fig. 2b. The surface S_1 carries L monopole and dipole sensors of the primary field, and M monopole and dipole canceling radiators lie on the surface S_2. The residual field is measured on the surface S_3 by Q monopole and dipole sensors. All elements of the active control system are assumed to be broadband and perfectly transparent.

Let the broadband device that controls the canceling radiators be an N-stage multidimensional transversal filter, whose inputs are the signals produced by the primary field sensors and whose output signals control the canceling radiators. The structure of the device that controls the weights of this transversal filter can be derived by an element-by-element analysis of the matrix gradient adaptive algorithm. A block diagram of the device that tunes one weight of the matrix adaptive filter is shown in Fig. 10. Note that signals produced by the sensors and radiators of the broadband active control system (output $v_l(t)$ of the lth primary field sensor, output $f_m(t)$ of the mth canceling radiator, and output $e_q(t)$ of the qth monitor sensor of the residual field) are real. As shown in Fig. 10, the weight W_{lmn} (in the nth tap of the transversal filter that links the lth primary field sensor to the mth canceling radiator) is proportional to the current estimate of the cross-correlation function between signals produced by the monitor sensors and primary field sensors, which are preprocessed by linear preemphasis filters. The impulse-response functions $G_{qm}(t, t')$ of these filters are equal to the Green's functions of the wave equation at the corresponding points of the surfaces S_2 and S_3. The purpose of the preemphasis filters is to transform the outputs of the primary field sensors so as to increase their correlation with the corresponding com-

ponents of the error signal $e_q(t)$ and to provide for the stability of the system as a whole.

It is of interest to compare the block diagrams of the weight-control circuits of the narrowband and broadband systems (see Figs. 3b and 10). It can be seen that a significant difference between the narrowband and broadband systems is that the broadband system uses preemphasis filters in the circuits of primary field sensors instead of correction filters (phase shifters) in circuits of the monitor sensors. As a result, the complication of the control system is not simple (about $N/2$-fold, taking into account that weights of the narrowband system are complex) but rather more complex, because each real weight W_{lmn} is now not produced by one multiplier but rather represents a sum of outputs of Q multipliers. Thus, for narrowband fields, when the lag of the envelope of the narrowband signal traveling along the path from a canceling radiator to a control sensor can be neglected, the structure of the adaptive control system can be significantly simplified (in terms of the number of multipliers).

Note that, to implement the gradient adaptive control algorithms, one must specify the elements of the Green's matrix G_{qm} or $G_{qm}(t, t')$ (see Figs. 3b and 10) as *a priori* information about the propagation medium. When the relative positions of canceling radiators and monitor sensors are fixed and the characteristics of the medium do not change, the elements of the Green's matrix can be calculated beforehand or measured experimentally and subsequently used to tune the preemphasis or correction filters. If the functions G_{qm} or $G_{qm}(t, t')$ are unknown or slowly change with time, one can use more complex identification adaptive algorithms or search gradient algorithms instead of the gradient algorithms described by the above block diagrams. The search gradient algorithms use the system that controls the canceling radiators to directly estimate
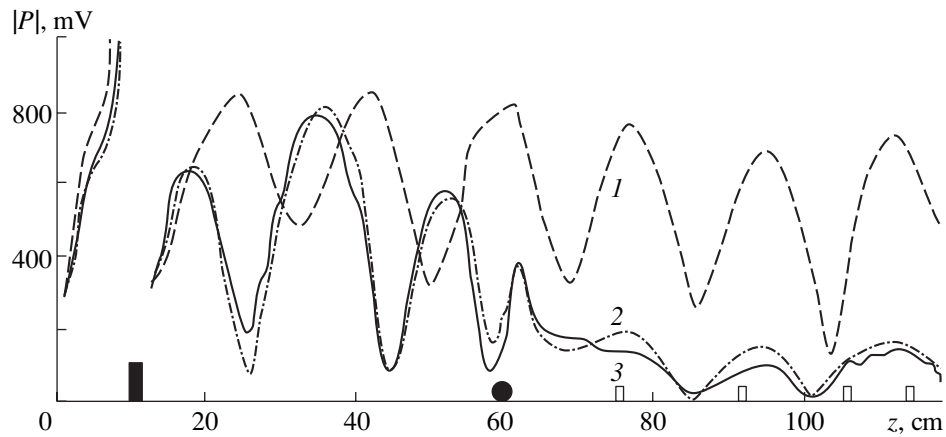
Fig. 11. Acoustic pressure amplitude distribution along the tank axis: (*1*) primary field, (*2*) residual field with one monitor sensor, and (*3*) residual field with four monitor sensors.

the gradient of the goal function through incrementing the weights and measuring the residual field power [24]. Apart from fluctuations in the weighting coefficients and search oscillations, the analysis of AACSs that employ the usual and search adaptive gradient algorithms is completely the same.

It should be noted that results concerning the theory of adaptive random wave field control systems obtained in [17–23] were later repeated in a number of works abroad. Among these, we should primarily mention paper [25], in which the adaptive algorithm for tuning a multielement active sound and vibration control system was derived for the second time. After this paper, a great number of publications on the application of adaptive methods to this problem were published. For example, the fullest Guicking's (1995) reference bibliography of foreign works on the active control included more than 2000 entries [26].

EXPERIMENTAL INVESTIGATIONS
OF ADAPTIVE ACTIVE WAVE FIELD
AND VIBRATION CONTROL SYSTEMS

*Adaptive System for the Active Control
of a Single-Mode Narrowband Acoustic Field
in a Rectangular Tank*

The first adaptive active acoustic control system was intended for laboratory studies of the tuning algorithms and to refine the physical model of processes that evolve therein [27]. The experiment used a tank made of organic glass with 11-mm-thick side walls, a 30-mm-thick bottom, and $118 \times 30 \times 29$ cm inner dimensions; the tank was filled with water to a depth of 16 cm. Piezoceramic radiators and sensors were placed along the axis near the bottom: the source field radiator (a 100-mm diameter disk), canceling radiator (a 50-mm sphere), four residual field monitor sensors (cylinders 30 mm in diameter and 25 mm high), and a monitor hydrophone (a cylinder 5 mm in diameter and 7 mm

high) for measuring the spatial field structure in the tank. The control signal for the canceling radiator was synthesized in the adaptive control unit from signals produced by the four monitor sensors and a harmonic reference signal. The experiment studied the cancellation of harmonic and narrowband noise signals in a frequency band about 100 Hz wide (between 3-dB points). As an example, Fig. 11 shows the pressure amplitude measured along the tank axis at a depth of 14 cm: (*1*) primary field, (*2*) residual field obtained using one (the rightmost) monitor sensor, and (*3*) residual field obtained using all four monitor sensors. The arrangement of the radiators and monitor sensors on the *z* axis is shown schematically. The plots show that, when the control system is on, the field in the cancellation region (behind the canceling radiator) sharply (by 15 to 20 dB) falls off; the amplitude of the standing wave in the region between the source and canceling radiators changes little, but its zeroes and maxima are shifted; and a deep minimum appears in the residual field near the canceling radiator. The changes in the spatial phase structure of the standing wave observed in the region between the radiators allow us to regard the canceling monopole radiator used in this experiment as an equivalent soft wall. A comparison of curves *2* and *3* shows that an increase in the number of monitor sensors (from one to four) makes the residual field smoother and slightly reduced. On the whole, it should be noted that the use of several residual field monitor sensors placed at various points of the cancellation region improved the stability of the AACS and rendered it actually insensitive to positions of the monitor sensors. In contrast, with one monitor sensor placed near a minimum of the primary standing wave, the degree of field cancellation is significantly lower due to the lower correlation feedback factor and signal-to-noise ratio. One should also note that the results of these experiments were actually independent of the type of the radiators and sensors. With one suppressing radiator and one monitor sensor, the adaptive control system canceled the field at the site
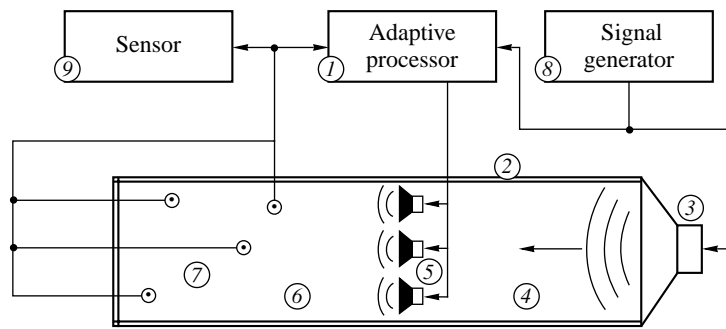
Fig. 12. Block diagram of an experimental setup for studying the possibility of active suppression of intense acoustic radiation by a system of light acoustic radiators.

of the monitor sensor very well. In particular, the signal from the monitor sensor placed near a maximum of the primary field decreased by 45–50 dB when the control system was switched on. We also studied the suppression factor at the site of the monitor sensor as a function of frequency and parameters of the adaptive system for frequency-modulated and narrowband noise acoustic fields in both off line and on line modes of operation.

Adaptive Active Control System
for a Two-Mode Acoustic Field in a Closed Air Space

To study the possibility of the active control of intense acoustic fields with the use of adaptive systems, a special experimental setup was developed [28]. This setup made it possible to experimentally study the cancellation of a two-mode two-frequency acoustic field by a system of light active radiators. A general block diagram of the experimental setup is presented in Fig. 12. The acoustic resonator consisted of two sections: free-propagation region (4) and cancellation region (6). The source of primary field (3) was placed at the end of the free propagation region (4). We used nine canceling radiators 5: one central radiator and eight small-size radiators combined into a circular array necessary for suppressing high-frequency modes with a complex transverse structure. Four monitor sensors (7) were placed in the cancellation region. The radiator was fed by a superposition of two harmonic signals at frequencies f_1 and f_2 produced by signal source (8); these signals were also used as reference ones. The adaptive processor (1) assembled from analog multipliers and adders was used to control three pairs of quadrature circuits of the adaptive gradient algorithm. Two pairs of the circuits fed the central loudspeaker with two reference signals at the frequencies f_1 and f_2. One pair of the circuits independently controlled the circular array at the frequency f_2. Three monitor sensors were placed in the cancellation region. The effective acoustic pressure measured along the axis in the cancellation region is shown in Fig. 13. The experiments showed that an increase in the number of degrees of freedom of the adaptive active control system makes it possible to virtually independently and simultaneously cancel two

modes at two different frequencies. The cancellation efficiency was approximately the same as that obtained for each mode separately.

Adaptive Control System
with an Additional Identification Channel

As we noted above, the preemphasis filters in an AACS with the gradient algorithm must preliminarily be tuned in accordance with values of the Green's function of the wave equation at the sites of the canceling radiators and residual field monitor sensors. If characteristics of the acoustic channels vary in time over a wide range, stable operation of the AACS may only be provided for with the use of a completely adaptive control system with an additional identification unit [29–31]. Figure 14 shows an experimental setup that studies
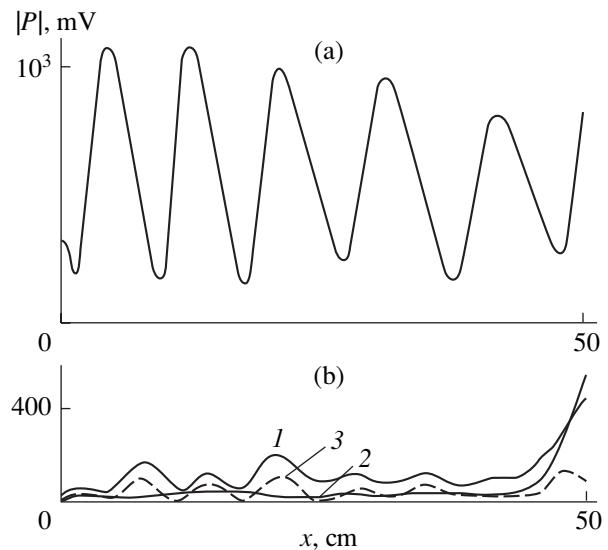
Fig. 13. Acoustic pressure amplitude distribution of a two-mode field (at frequencies of 1020 and 2820 Hz) along the axis of an acoustic resonator: (a) primary two-mode field and (b) the residual field with the control system switched on ((1) total two-frequency residual field, (2) 1020-Hz residual field component, and (3) 2820-Hz residual field component; on the average, the field is suppressed by 17 dB).
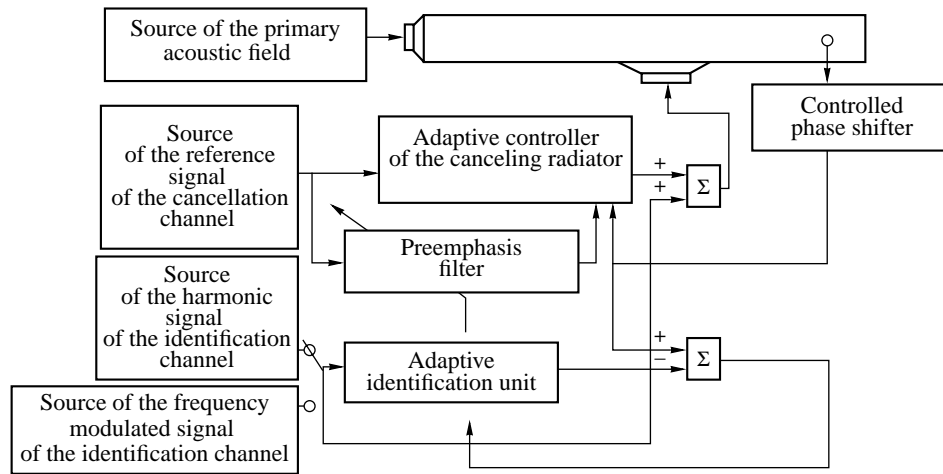
Fig. 14. Block diagram of an adaptive control system with an additional identification channel for suppressing narrowband acoustic fields in a closed air space.

the characteristics of such a completely adaptive narrowband AACS. The narrowband AACS consisted of one canceling radiator and one residual field monitor sensor placed in a pipe 2.5 m long with an inner diameter of 45 mm. The end source radiator was fed with the help of a narrowband (1.5%) noise generator. The nonstationary behavior of the acoustic channel (Green's function) between the canceling radiator and monitor sensor was simulated by a variable phase shifter. The entire electronic control system was built around a TMS320C26 signal processor and contained an adaptive control unit for the canceling radiator (with the reference-signal generator of the cancellation channel and the preemphasis filter) and adaptive identification unit with the reference-signal generator of the identification channel. The adaptive unit that controlled the canceling radiator formed the signal through the quadrature weighting of the harmonic reference signal at a frequency equal to the average frequency of the primary acoustic field. To determine the characteristics of the acoustic-signal propagation channel, a small identification signal (harmonic or phase-shift keyed) was additively applied to the canceling radiator. The active control system was capable of achieving a general field cancellation ratio of about 12 dB; the identification channel was fast enough to follow phase variations in the acoustic channel at a rate of about 6 deg/s without disrupting stable operation of the system as a whole.

Adaptive System of Control over Boundary Conditions in a Waveguide

Reflection of the hydroacoustic wave from the active boundary at the end of the waveguide was studied experimentally in [32]. These studies were used to develop an adaptive active control system over boundary conditions that employed a search gradient tuning

algorithm. The experiments were performed in water-filled duraluminum pipe with a length $l = 2.2$ m, an external diameter $D = 50$ mm, and a wall thickness $d = 6$ mm. As the canceling radiators (used to realize the specified boundary conditions), the system used specially designed acoustically transparent electronic radiators. The signals induced by the incident and reflected waves were separated by digitally processing the signals picked up from two spaced monitor transducers. The adaptive system that controlled the canceling radiators allowed the system to realize the specified boundary conditions (matched, compliant, or rigid boundaries) in the presence of a passive boundary with an arbitrary reflection coefficient slowly varying in time. The tuning accuracy achieved in the experiments was 20 to 25 dB relative to the initial value of the parameter being minimized at a tuning time of 0.5 to 1.5 s.

Active Control of a Broadband Acoustic Field Produced by a Turbulent Jet

In 1991–1993, a series of studies [33–35] on the cancellation of a random broadband acoustic field produced by a turbulent jet in a pipe with unmatched ends were performed at the Department of Statistical Radiophysics of NNSU and experiments were conducted under conditions close to the field conditions. The major part of the hydroacoustic noise was above the critical frequency, and only the waves with a homogeneous cross-sectional structure could be excited in the pipe. A block diagram of the experimental setup is shown in Fig. 15. The pipe was made of stainless steel, had an inner diameter of 100 mm, was 4.7 m long, and was filled with water. The water jet was fed into the pipe by a centrifugal pump through a nozzle mounted on the left end flange. The adaptive control system consisted of two primary field sensors, two canceling radiators, two residual field monitor sensors, wave selectors

(WSs), and a wave former (WF), which were capable of receiving and exciting unidirectional hydroacoustic waves. The systems of receivers and radiators together with the WSs and WF provided for the cancellation (isolation) of waves traveling in the opposite direction by 20 dB in the frequency range from 700 to 2000 Hz. The control signal for the canceling radiators was synthesized by a digital adaptive transversal filter with 32 variable coefficients built around a digital signal processor. The system's efficiency criterion was the power of the residual wave traveling from left to right in the right-hand part of the pipe behind the canceling radiators. The system was tuned by the search gradient algorithm, and, therefore, it was not necessary to additionally identify the signal-propagation channels. Parameters of the adaptive algorithm were optimal in terms of stability, convergence rate, and cancellation efficiency. Characteristics of the adaptive hydroacoustic noise canceling system were studied in the most efficient design version with unidirectional reception and unidirectional radiation (from left to right) of the canceling wave. Figure 16 shows typical power spectrum densities of the primary (curve *1*) and residual (curve *2*) fields in the right-hand part of the pipe. The highest cancellation ratio, about 10 to 25 dB, was achieved over the frequency range from 850 to 2200 Hz. The lower cancellation at the ends of the frequency range is apparently due to the action of inhomogeneous waves on the primary field sensors (at lower frequencies) and due to the degradation of the WS and WF characteristics outside the range 700–2000 Hz. The integral cancellation ratio of the broadband hydroacoustic noise in the frequency band from 500 to 2500 Hz was 12 to 14 dB.

### Adaptive Active Vibration Canceling Systems

Along with research into the active acoustic field cancellation, model experiments were also performed on the active suppression of vibrations in various mechanisms. As the active elements (canceling radiators), these experiments used controlled vibrators (linear motors).

One of these model problems was formulated as cancellation of the field produced by a ship due to low-frequency vibrations of its mechanisms. A block diagram of such a system is shown in Fig. 17. The system has no primary field sensors, because the primary vibration signal is a combination of harmonic signals whose frequencies can be directly measured. The secondary sensors were vibration detectors placed on the ship's hull. As the canceling radiators, the system used 12 active vibrators with inertial masses: three vibrators for each of the four passive supports to cancel their vibrations in three perpendicular directions. In this laboratory prototype, harmonic vibrations were canceled with a ratio of about 20 to 30 dB.

Another problem was to reduce the effect of vibrations produced by the base (ship's hull) on precision
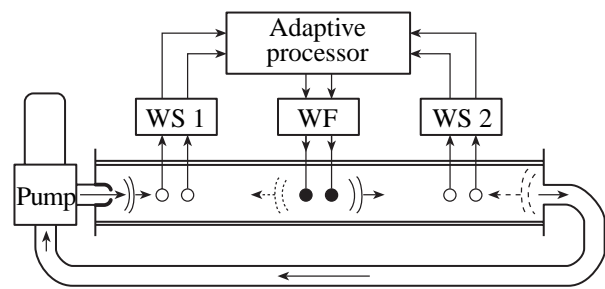

Fig. 15. Block diagram of an experimental setup for the active cancellation of broadband acoustic fields produced by a turbulent jet (WS is the traveling wave selector and WF is the unidirectional wave former).
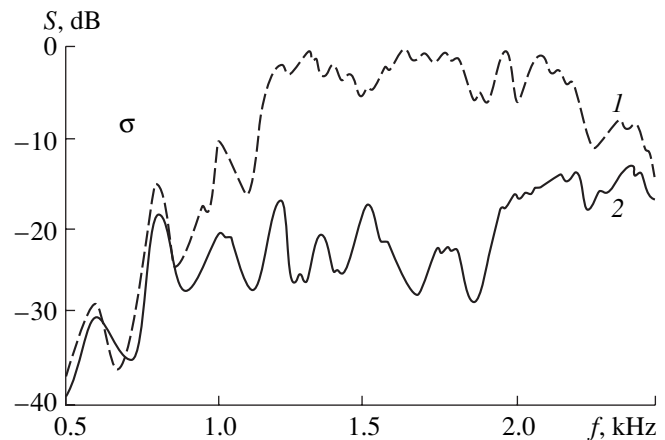
Fig. 16. Power spectrum density of (*1*) the primary hydroacoustic field and (*2*) the residual field. The Reynolds number is above the critical value (Re $\cong$ 5000). The average cancellation ratio within the frequency range from 500 to 2500 Hz is 12 to 14 dB.
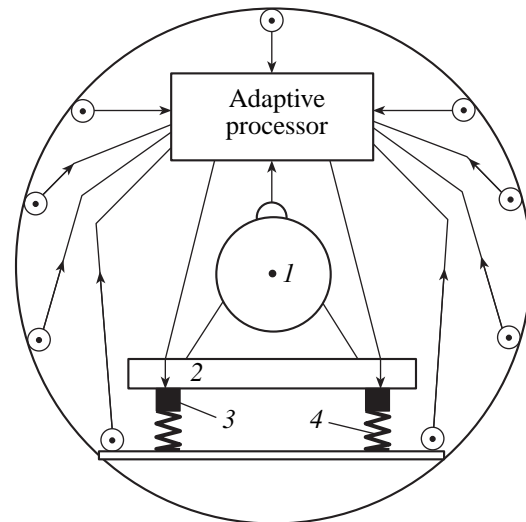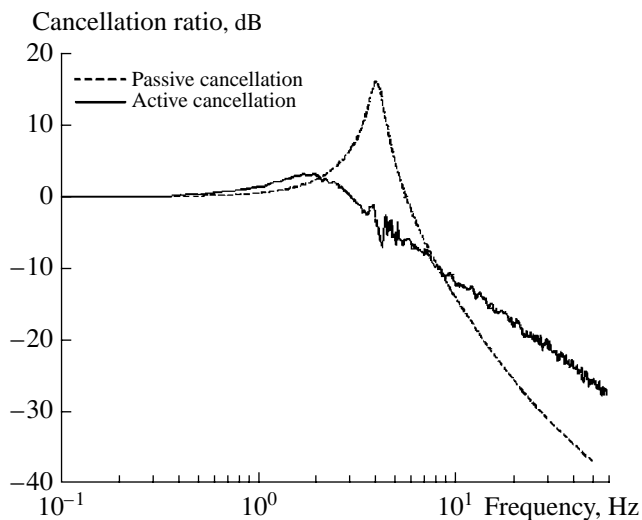

Fig. 17. Block diagram of a prototype canceller of a narrow-band vibration field (at a frequency of about 100 Hz) with an independent harmonic reference signal (12 active vibrators with inertial masses and 9 residual field monitor sensors; the field cancellation ratio is 20 to 40 dB).
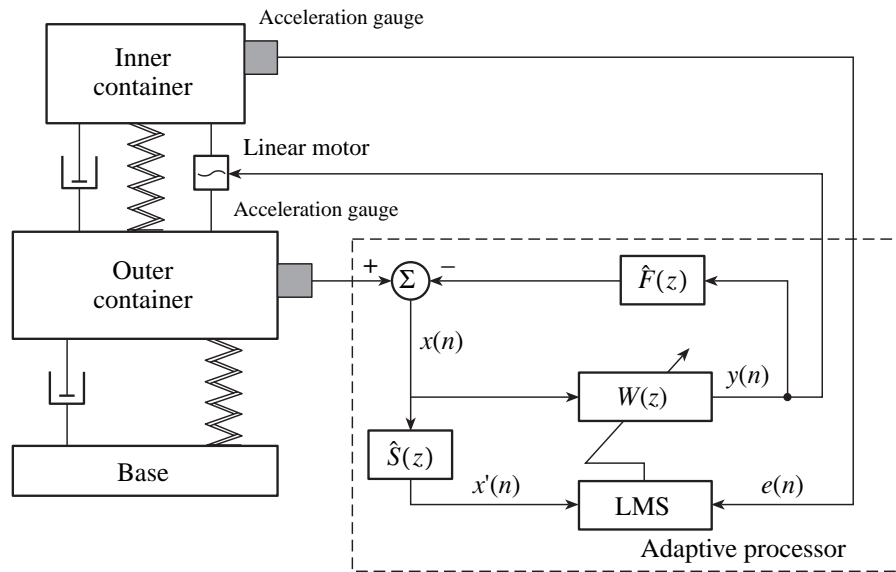
Fig. 18. Block diagram of an active canceling system that protects the inner container from vibrations of the base.

mechanical and electronic devices [36]. In this case, the active elements were linear motors, which allowed the system to eliminate low-frequency resonances in all possible degrees of freedom. A block diagram of the active vibration control system used to suppress the vibrations in one degree of freedom is shown in Fig. 18. For the sake of comparison, Fig. 19 shows the transfer functions of the vibration control system that uses purely passive elements and of the active canceling system.

The reader interested in the experimental works on these problems conducted abroad in the 1980s in paral-

lel to our works should be referred to the review [37] published in 1990.

CONCLUSIONS

Research performed in the 1980s and 1990s showed that modern computers possess enough computational power to allow for the design of adaptive active systems for canceling and suppressing narrowband multimode acoustic and vibration fields of a complex spatial structure or broadband fields of a sufficiently simple spatial structure (for example, a single-mode wave in a pipe). An active planar control system operating on the basis of the extraction and cancellation of particular spatial acoustic modes was developed theoretically in [38–40]. A prototype of this system was built and successfully tested in canceling two horizontal harmonics in a hydroacoustic tank [41]. However, the realization of adaptive control systems for broadband fields of a complex spatial structure described by the above block diagrams is difficult because of the complexity of the sensor–radiator system and due to the very high processor burden imposed by the adaptive control algorithms. Therefore, presently, one of the most promising research directions is the development of so-called local adaptive active control systems, which combine a sensor and a radiator in one element (whose size is about a wavelength), so as to actively absorb the incident waves [42].

Experiments on the active control of the surface acoustic impedance with the help of tile like active elements were performed at one of the US Navy laboratories [43]. Each such tile consisted of several layers, which included a piezoelectric radiating transducer and a piezoelectric pressure sensor, and was supplied with

Fig. 19. Transfer functions of the active and passive canceling systems.

an integrated surface velocity meter. Tests of this system showed that a two-dimensional array of such active elements is capable of controlling the surface impedance in a frequency band from 0.5 to 3.5 kHz.

Theoretical and experimental research into the development of thin (in terms of the incident wavelength) active absorbing coatings based on nonresonant parametric microstructures has been carried out in recent years [44–46]. This approach does not measure the parameters of the wave field being absorbed but transforms its energy into high-frequency oscillations of the active microstructure.

A challenging and rapidly developing area of research is the use of adaptive active vibration control systems for protecting the variety of electronic equipment deployed on ships and other vehicles and subjected to high vibrations and shocks. This idea has recently been embodied in the development of dedicated protective racks for computers and other radio electronic devices that do not comply with special requirements in terms of vibrations and shocks. In spite of their rather high cost, the cost efficiency of these protective racks is very high, because they allow for multiple updates of the equipment and eliminate the necessity of developing expensive electronic devices consistent with special requirements. Realizations of these protective racks based only on passive insulators are vulnerable to unwanted low-frequency resonances and suffer from large shock displacements. Therefore, modern designs usually combine active and passive vibration control elements.

ACKNOWLEDGMENTS

REFERENCES

1. V. A. Zverev, *Radiooptics* (Sovetskoe Radio, Moscow, 1975), p. 304 [in Russian].

2. V. A. Zverev, Akust. Zh. **45**, 74 (1999) [Acoust. Phys. **45**, 65 (1999)].

3. V. A. Zverev, Akust. Zh. **46**, 75 (2000) [Acoust. Phys. **46**, 62 (2000)].

4. G. D. Malyuzhinets, Tr. Akust. Inst. Akad. Nauk SSSR, No. 15, 124 (1971).

5. M. V. Fedoryuk, Tr. Akust. Inst. Akad. Nauk SSSR, No. 15, 169 (1971).

6. B. D. Tartakovskiĭ, Akust. Zh. **20**, 808 (1974) [Sov. Phys. Acoust. **20**, 495 (1974)].

7. M. P. Zavadskaya, A. V. Popov, and B. L. Égel'skiĭ, Akust. Zh. **21**, 882 (1975) [Sov. Phys. Acoust. **21**, 541 (1975)].

8. S. I. Konyaev, V. I. Lebedev, and M. V. Fedoryuk, Akust. Zh. **25**, 887 (1979) [Sov. Phys. Acoust. **25**, 500 (1979)].

9. A. A. Mazannikov and V. V. Tyutekin, Akust. Zh. **22**, 729 (1976) [Sov. Phys. Acoust. **22**, 409 (1976)].

10. A. A. Mazannikov, V. V. Tyutekin, and A. T. Ukolov, Akust. Zh. **23**, 485 (1977) [Sov. Phys. Acoust. **23**, 276 (1977)].

11. M. Jessel and G. Mangiante, J. Sound Vibr. **23** (3), 383 (1976).

12. G. Mangiante, J. Acoust. Soc. Am. **61**, 1516 (1977).

13. S. P. Klimov, A. A. Mazannikov, V. N. Merkulov, and V. V. Tyutekin, Akust. Zh. **26**, 149 (1980) [Sov. Phys. Acoust. **26**, 82 (1980)].

14. V. I. Anfinogenov, G. S. Lyubashevskiĭ, B. D. Tartakovskiĭ, *et al.*, Akust. Zh. **26**, 611 (1980) [Sov. Phys. Acoust. **26**, 340 (1980)].

15. E. M. Babasova, M. P. Zavadskaya, and B. L. Égel'skiĭ, *Active Methods of Acoustic Field Control*, Ed. by V. V. Tyutekin and M. V. Fedoryuk (TsNII Rumb, Leningrad, 1982) [in Russian].

16. J. C. Burgess, J. Acoust. Soc. Am. **70**, 715 (1981).

17. S. N. Arzamasov and A. A. Mal'tsev, Izv. Vyssh. Uchebn. Zaved., Radiofiz. **25** (6), 657 (1982).

18. A. A. Mal'tsev and I. E. Pozumentov, Izv. Vyssh. Uchebn. Zaved., Radiofiz. **25** (8), 668 (1982).

19. S. N. Arzamasov, A. N. Malakhov, and A. A. Mal'tsev, Akust. Zh. **28**, 583 (1982) [Sov. Phys. Acoust. **28**, 346 (1982)].

20. S. N. Arzamasov and A. A. Mal'tsev, Akust. Zh. **30**, 130 (1984) [Sov. Phys. Acoust. **30**, 74 (1984)].

21. A. A. Mal'tsev and I. E. Pozumentov, Akust. Zh. **31**, 77 (1985) [Sov. Phys. Acoust. **31**, 44 (1985)].

22. S. N. Arzamasov and A. A. Mal'tsev, Izv. Vyssh. Uchebn. Zaved., Radiofiz. **28**, 1008 (1985).

23. S. N. Arzamasov and A. A. Mal'tsev, Izv. Vyssh. Uchebn. Zaved., Radiofiz. **29**, 697 (1986).

24. I. A. Korolev, A. A. Mal'tsev, and V. V. Cherepennikov, Izv. Vyssh. Uchebn. Zaved., Radiofiz. **31**, 958 (1988).

25. S. J. Elliott, I. M. Stothers, and P. A. Nelson, IEEE Trans. Acoust., Speech, Signal Process. **35**, 1423 (1987).

26. *Active Noise and Vibration Control. Reference Bibliography*, Ed. by D. Guicking, 3rd ed. (Univ. of Göttingen, 1995), p. 441.

27. I. A. Korolev, V. P. Lependin, A. A. Mal'tsev, and V. V. Cherepennikov, Izv. Vyssh. Uchebn. Zaved., Radiofiz. **30**, 70 (1987).

28. I. A. Korolev, A. A. Mal'tsev, and V. V. Cherepennikov, Izv. Vyssh. Uchebn. Zaved., Radiofiz. **30**, 1141 (1987).

29. A. A. Belyakov and A. A. Mal'tsev, Izv. Vyssh. Uchebn. Zaved., Radiofiz. **38** (3), 196 (1995).

30. A. A. Belyakov, A. A. Mal'tsev, S. Yu. Medvedev, and V. V. Cherepennikov, Akust. Zh. **42**, 860 (1996) [Acoust. Phys. **42**, 762 (1996)].

31. A. A. Maltsev, Active Sound Vibr. Control News **04** (6), 4 (1997).

32. A. N. Malakhov, A. A. Mal'tsev, S. Yu. Medvedev, and V. V. Cherepennikov, Izv. Vyssh. Uchebn. Zaved., Radiofiz. **31** (3), 327 (1988).

33. A. A. Belyakov, A. A. Mal'tsev, and V. V. Cherepennikov, in *Proceedings of XI All-Union Acoustical Conference* (Akust. Inst. Akad. Nauk SSSR, Moscow, 1991), pp. 13–16.

34. A. A. Belyakov, A. A. Mal'tsev, S. Yu. Medvedev, and V. V. Cherepennikov, Izv. Vyssh. Uchebn. Zaved. Radiofiz. **35** (1), 61 (1992).

35. A. A. Belyakov, A. A. Mal'tsev, S. Yu. Medvedev, and V. V. Cherepennikov, Akust. Zh. **39**, 433 (1993) [Acoust. Phys. **39**, 226 (1993)].

36. R. O. Maslennikov, A. V. Khoryaev, and S. V. Purtsezov, in *Proceedings of the Nizhni Novgorod Acoustical Scientific Session* (Nizhegor. Gos. Univ., Nizhni Novgorod, 2002), pp. 340–342.

37. A. Gillespie, H. G. Leventhall, J. Roberts, and M. Ullermose, Probl. Mashinostr. Nadezhnosti Mashin, No. 4, 12 (1990).

38. V. V. Tyutekin, Akust. Zh. **43**, 238 (1997) [Acoust. Phys. **43**, 202 (1997)].

39. A. I. Boĭko and V. V. Tyutekin, Akust. Zh. **45**, 454 (1999) [Acoust. Phys. **45**, 402 (1999)].

40. A. I. Boĭko and V. V. Tyutekin, Akust. Zh. **50**, 5 (2004) [Acoust. Phys. **50**, 1 (2004)].

41. E. V. Korotaev and V. V. Tyutekin, Akust. Zh. **46**, 84 (2000) [Acoust. Phys. **46**, 71 (2000)].

42. A. A. Mazannikov, Akust. Zh. **46**, 89 (2000) [Acoust. Phys. **46**, 76 (2000)].

43. B. Houston, Active Sound Vibr. Control News **02** (7), 5 (1995).

44. V. V. Arabadzhi, in *Proceedings of 10th International Conference on Adaptive Structures and Technologies (ICAST'99)* (Paris, 1999), pp. 626–632.

45. V. V. Arabadzhi, J. Low Freq. Noise Vibr. Active Control **18** (3), 129 (1999).

46. V. V. Arabadzhi, Izv. Vyssh. Uchebn. Zaved., Radiofiz. **44** (3), 270 (2001).

Translated by A. Khzmalyan

Abilities of Nonlinear Acoustic Methods in Locating Gas Bubbles in Biological Tissues

A. D. Mansfel'd, D. A. Mansfel'd, and A. M. Reǐman

Institute of Applied Physics, Russian Academy of Sciences, ul. Ul'yanova 46, Nizhni Novgorod, 603950 Russia
e-mail: mansfeld@appl.sci-nnov.ru
Received October 5, 2004

Abstract—On the basis of a numerical solution to the equation of radial oscillations of a gas bubble in a liquid, the abilities of nonlinear acoustic methods in detecting gas bubbles in biological tissues with the use of pulsed acoustic location are analyzed. It is demonstrated that, with moderate amplitudes of the probing signal, it is possible to detect bubbles whose size is close to resonance. An improved version of the method of paired pulses is proposed, along with a method for detecting the bubbles and measuring their dimensions on the basis of a nonlinear excitation of their natural oscillations. © 2005 Pleiades Publishing, Inc.

INTRODUCTION

The problem of detecting gas bubbles and measuring their concentration and dimensions in blood and in biological tissues is important for aviation and space medicine, for ensuring the safety of underwater and pneumatic works, and also for other human activities under extreme conditions, where a working individual is subjected to strong variations in the external pressure. The detection of gas bubbles in human biological tissues at the stage of their nucleation is important from the point of view of investigating the mechanisms of their formation, as well as for predicting the risk of the decompression disease. Lately, interest has been generated in the employment of contrasts in ultrasonic testing. The basis for these contrasts is particles containing gas bubbles. Another important problem is the monitoring of the nucleation of cavitation bubbles under the effect of intense ultrasonic radiation on biological tissues.

At the same time, the common linear acoustic techniques for bubble detection are efficient only in the case of the location of moving bubbles by the Doppler method [1, 2] or the echolocation of very large bubbles with scattering cross sections sufficiently large to insure their selection against the background of biological tissue layers [3, 4].

One of the problems to be solved is the detection and localization of bubbles with a wide range of radii (1–100 μm). The resonance frequencies for the bubbles in the upper part of this range are so low that it is necessary to apply very low probe frequencies. As is known, the relationship of the resonance frequency of a bubble to its size in a liquid is determined by the expression [5]

$$f_{\text{res}} = \frac{\sqrt{\dfrac{3\gamma P_0}{\rho_0} + \dfrac{(3\gamma - 1)2\sigma}{\rho_0 R}}}{2\pi R}, \qquad (1)$$

where $\gamma = 4/3$ is the adiabatic exponent for the air in a bubble, σ is the coefficient of surface tension of the liquid, ρ_0 is the density of the liquid, and R is the bubble radius. According to Eq. (1), a bubble with a radius of 100 μm has a resonance frequency of about 32 kHz ($\lambda = 5$ cm). Thus, the necessity of detecting relatively large bubbles is at odds with the possibility of their localization.

Another problem involved in detecting motionless bubbles consists in that a bubble is surrounded by layers of biological tissues with different acoustic impedances, which cause a strong reverberation. In the case of the linear pulsed location of biological tissues, a continuous sequence of pulses reflected from the layered structure is recorded, and the pulses from gas bubbles may be indistinguishable against their background. Therefore, of most interest is the development of location techniques based on the nonlinear acoustic properties of bubbles. At the same time, nonlinear effects manifest themselves not only in the signal scattered by a bubble but also in the wave propagation through biological tissues [6].

This paper is devoted to an analysis of the abilities of nonlinear acoustic methods to detect gas bubbles in biological tissues. The techniques based on the second-harmonic generation [7], combination (difference and sum) frequencies (for example, see [7, 8]), subharmonics and ultraharmonics [9, 10], and location by paired pulses with phase keying and alternate-period compensation for the reflected signals [11, 12] will be considered.
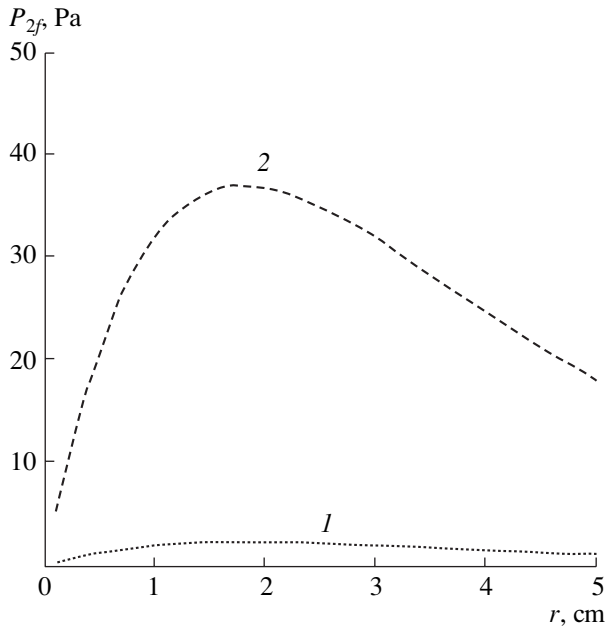
Fig. 1. Dependence of the second-harmonic amplitude on distance at the reflection from a layer with $K_{ref} = 0.1$. The initial pressure amplitude is (*1*) 0.25×10^5 and (*2*) 10^5 Pa.

The basis for all the aforementioned detection techniques is pulsed probing, because, first, a spatial localization is desirable and, in the ideal case, so is the mapping of bubble positions in biological tissues, and, second, the implementation of a nonlinear mode of operation is possible only with the use of location by high-amplitude probe signals while maintaining the average value of radiation intensity at the level permitted for medical diagnostic equipment.

A pulsed location mode has its own special features. As will be demonstrated below, in some cases, the presence of the transient processes inherent in the pulsed location mode leads to the generation of qualitatively different signals, depending on the ratios between the parameters of bubbles and probe pulses. One more specific feature of the techniques under consideration is the use of a single (two at maximum, for the technique with combination frequencies) carrier frequency of location, which corresponds to actual location abilities when it is necessary to detect bubbles in a wide range of sizes.

SECOND-HARMONIC GENERATION

First, let us consider the location of gas bubbles by the method of second-harmonic reception [7]. The major negative factor in this case is the intrinsic nonlinearity of biological tissues, which also leads to the appearance of the second harmonic in the signal propagating through biological tissues. Let us evaluate the amplitude of the signal caused by the intrinsic nonlin-

earity of the medium and reflected from the boundary of the tissue layers.

Let a boundary between different soft tissues with the reflection coefficient $K_{ref} = 0.1$ (for example, the boundary between muscle and fat [6]) lie at a distance r from the tissue surface. For estimates, we use the Burgers equation under the condition of the smallness of the Reynolds number $\mathrm{Re} = \dfrac{\rho_0 V_i \lambda}{2\pi b} \ll 1$ [13], where

$V_i = \dfrac{P_p}{\rho_0 c_0}$ is the initial amplitude of particle velocity, P_p is the pressure amplitude of the emitted wave, λ is the ultrasonic wavelength, c_0 is the sound velocity in the medium, ε is the nonlinear parameter with a value of 4–6 for different biological tissues [6], $b = \rho_0 c_0^3 \alpha / 2\pi f^2$, and α is the coefficient of ultrasonic absorption at the location frequency f. The absorption coefficient in this case includes both viscous and thermal losses (the classical mechanism of absorption) and the relaxation mechanism characteristic of biological tissues. At a frequency of 1 MHz, it is equal to $\alpha_{1\,\mathrm{MHz}} \approx 11.2\ \mathrm{m}^{-1}$ [6]. At the pressure amplitude in the incident wave $P_p = 10^5$ Pa, $\mathrm{Re} \sim 1.6 \times 10^{-2}$. For the wave at the second-harmonic frequency in the case of reflection from a layer located at a distance r from the biological tissue surface, the pressure amplitude is determined by the equation [13]

$$P_{2f} = \frac{K_{ref}\varepsilon P_p^2 f}{2\rho_0 c_0^3 \alpha}(e^{-2\alpha r} - 4^{-4\alpha r}). \qquad (2)$$

Figure 1 shows the dependence of the pressure amplitude P_{2f} on the distance r for two amplitudes of the probe signal at $\varepsilon = 6$.

To evaluate the possibility of bubble detection, we numerically simulate the location process for a medium with gas bubbles by solving the equation for bubble oscillations under the action of a high-frequency (HF) pumping pulse (the frequency $f = 10^6$ Hz and the duration $\tau = 10\ \mu\mathrm{s}$), calculating the time dependence of bubble radius oscillations and (according to it) the pressure in the wave reradiated by a bubble, and simulating the filtration of the acoustic signal by a frequency-selective receiving system. The equation describing the bubble radius oscillations $R(t)$ has the form [14]

$$\rho_0\left[\ddot{R}(t)R(t)\left(1 - \frac{\dot{R}(t)}{c}\right) + \frac{3}{2}\dot{R}(t)^2\left(1 - \frac{\dot{R}(t)}{3c}\right)\right]$$
$$= P(t) + \frac{R(t)}{c}\dot{P}(t), \qquad (3)$$
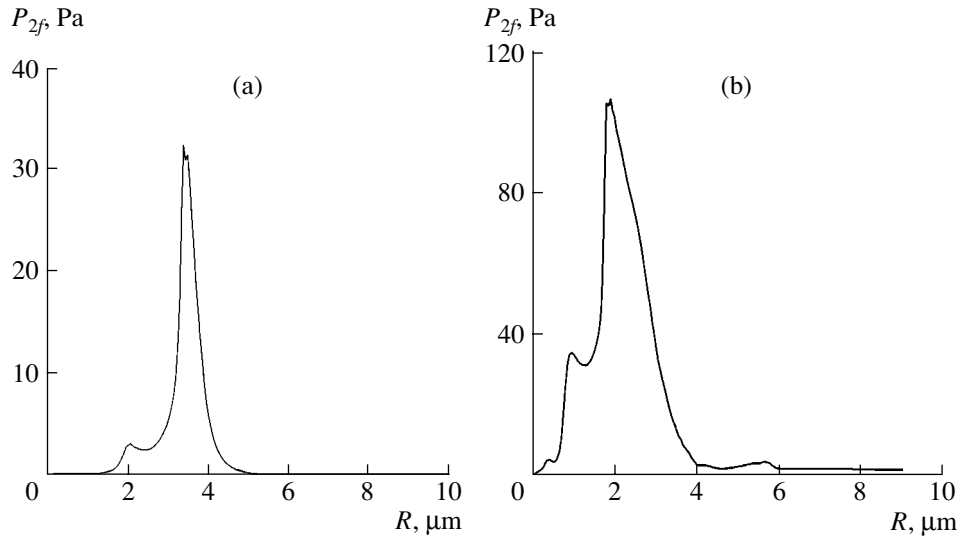
Fig. 2. Dependence of the signal amplitude at the second-harmonic frequency on the radius of a bubble positioned at the distance of 1 cm from the radiator in the case of its excitation by a pulse with an amplitude of 0.25×10^5 Pa.

where $P(t) = \left(P_0 + \dfrac{2\sigma}{R_0} \right)\left(\dfrac{R_0}{R(t)} \right)^{3\gamma} - \dfrac{2\sigma}{R(t)} - P_0 + P_{ac}(t) -$

$4\mu\dfrac{\dot{R}(t)}{R(t)}$, $R(t)$ is the current radius of the bubble, R_0 is the bubble radius, P_0 is the static pressure in the liquid, $P_{ac}(t)$ is the pressure in the incident acoustic wave, and μ is the viscosity of the liquid. The values $\mu = 2$ mN s/m^2 and $\sigma = 52$ N/m used here and below in the calculations related to biological tissues are selected as being typical of the intercellular fluid, and the density ρ_0 for the intercellular fluid is approximately equal to the density of water.

A solution to Eq. (3) with the initial conditions $R(0) = R_0$ and $\dot{R}(0) = 0$ is tried by the Runge–Kutta method of the fourth order. According to the solution determined for the bubble radius, the bulk velocity $V(t) = \displaystyle\iint_s \dfrac{dR(t)}{dt} dS$ is calculated, where S is the area of the bubble surface. Then, we calculate the pressure at the distance r from the bubble, $P(t) = \dfrac{\rho}{4\pi r}\dfrac{dV(t)}{dt}$. After that, we perform the filtration of the pressure signal reflected from the bubble in a frequency band of ± 100 kHz with respect to the central reception frequency (i.e., the second-harmonic frequency, the subharmonic, etc.)

Figure 2 shows the dependence of the second-harmonic amplitude on the bubble radius. Note that, in the case of a small amplitude of the probe signal (Fig. 2a), two resonance peaks are observed at the bubble size corresponding to the resonance at the probing frequency (the right peak, $R = 3.7$ μm) and to the resonance at the second-harmonic frequency (the left peak,

$R = 2$ μm). When the probing-signal amplitude increases, the pronounced resonance peaks vanish (Fig. 2b).

Comparing the curves (Figs. 1 and 2), it is possible to conclude that reliable detection of a bubble is possible only in the case of its excitation near the fundamental resonance. Outside the resonance, in the case of large-size bubbles, the amplitude P_{2f} is small, although it is sufficient for bubble detection in a homogeneous medium. At the same time, at this distance, the second-harmonic signal reflected from the boundary of tissues is on the order of 40 Pa. As the pumping amplitude increases, both the amplitude of the signal reflected from the layer and the amplitude of the signal reflected from a bubble grow. The ratio of these amplitudes considerably increases for the bubbles located at a smaller distance from the surface. For example, when the depth of a bubble in the tissue decreases to 1 mm, the amplitude of the signal from the bubble at the second-harmonic frequency increases tenfold, while the amplitude of the signal from the tissue layers at this frequency noticeably decreases. Thus, using the method of the second harmonic, it is possible to detect bubbles, including nonresonance ones, that occur near the surface of a biological tissue.

COMBINATION FREQUENCY GENERATION

This method is based on the irradiation of the medium under investigation by two HF pulses of different frequencies with the help of radiators positioned at a certain angle to each other and the signal detection at the sum and difference frequencies [8]. Signals at combination frequencies, which are associated with the nonlinearity of the medium, should not be generated in the course of the propagation of probe pulses because
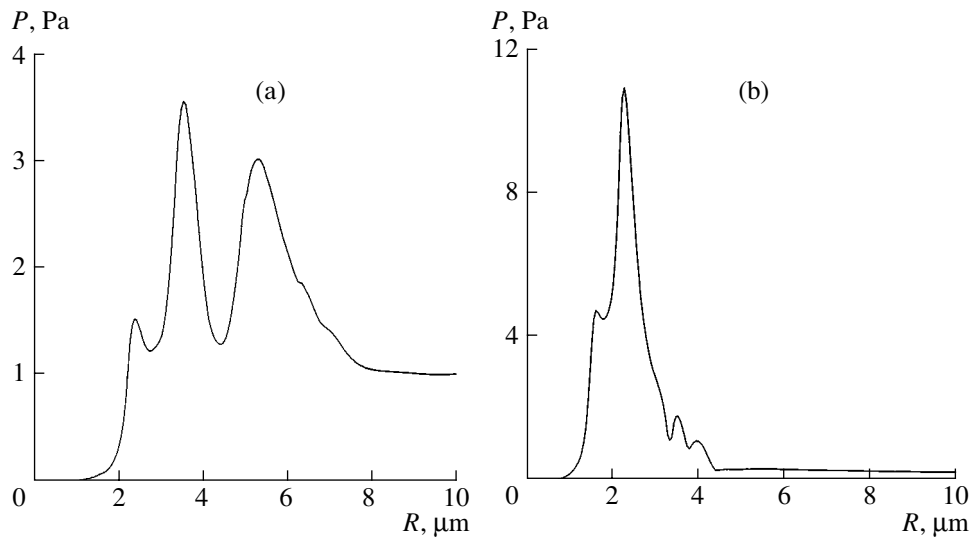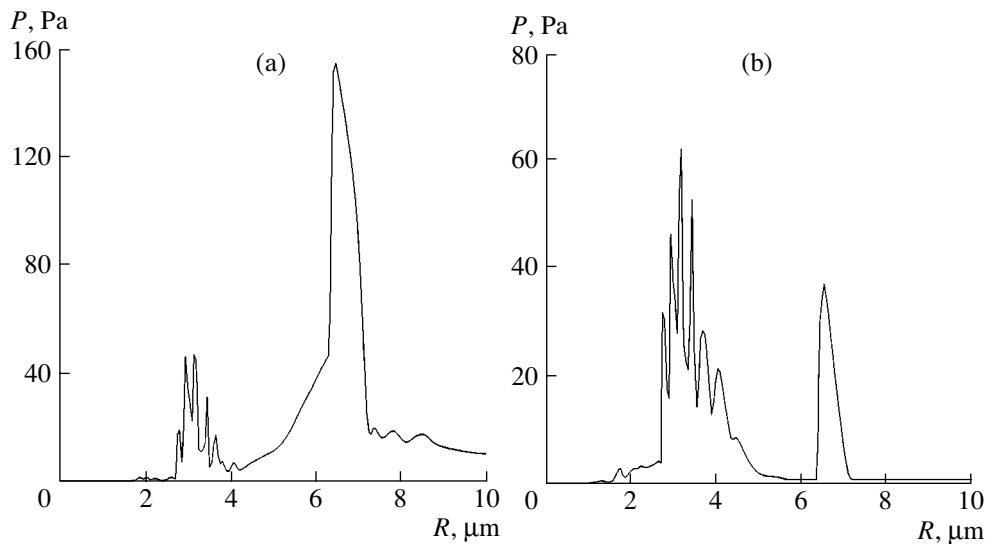
Fig. 3. Dependence of the signal amplitude on the bubble radius at the (a) difference and (b) sum frequencies for a pumping amplitude of 0.25×10^5 Pa, a pulse length of 10 μs, and probing frequencies of 1 and 1.6 MHz.
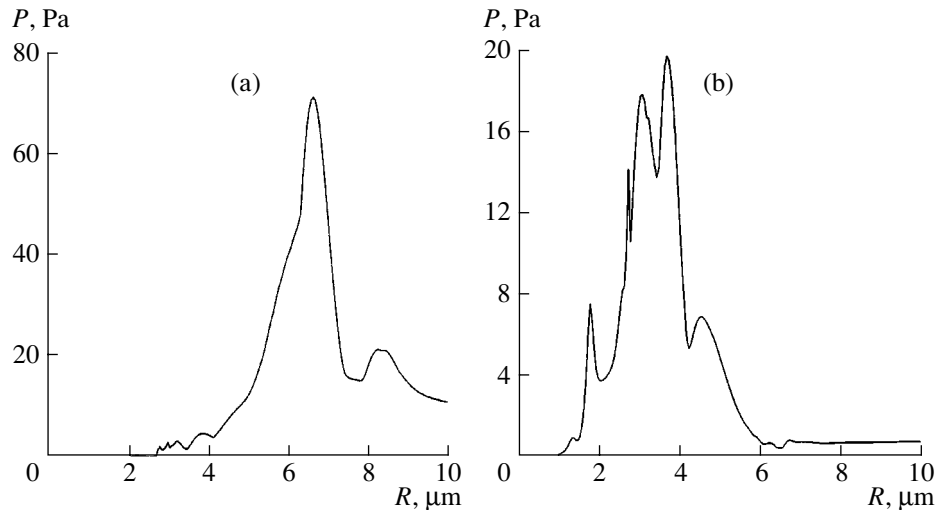
Fig. 4. Dependence of the signal amplitude on the bubble radius at the (a) difference and (b) sum frequencies for a pumping amplitude of 10^5 Pa, a pulse length of 10 μs, and probing frequencies of 1 and 1.6 MHz.

of the very weak dispersion in biological tissues. The possibility of signal detection at the difference frequency, where big bubbles resonate, could also be considered to be an advantage of this method. However, in a real experiment, a certain interaction of probing fields is still observed because of the existence of the collinear components of wave vectors, and detection at the low difference frequency requires the use of long probe pulses. As for the major disadvantages of the combination method, they are the awkwardness of the antenna system (four antennas are needed: two radiating and two receiving antennas tuned to the sum and difference frequencies) and a small location region determined by the zone of intersection of the ultrasonic beams. The

last fact makes it almost impossible to map large regions of tissues, which reduces the probability of bubble detection. It is also possible to demonstrate that, in the case of two-frequency probing, one can reliably detect only those bubbles with dimensions close to the resonance ones at the frequencies of probing or reception. The dependences of the pressure amplitude on the bubble size, which are obtained by numerically solving Eq. (3) at a small pumping pressure $P_p = 0.25 \times 10^5$ Pa, are given in Fig. 3. The results qualitatively coincide with the results obtained in [7] under the approximation of a small quadratic nonlinearity. It is necessary to note the presence of three marked peaks corresponding to

Fig. 5. Dependence of the signal amplitudes on the bubble radius at the (a) subharmonic and (b) ultraharmonic frequencies. The pumping amplitude is 10^5 Pa, the pulse length is 10 μs, and the probing frequency is 1 MHz.

resonances at the pumping, difference, and sum frequencies.

GENERATION OF SUB- AND ULTRAHARMONICS

Let us evaluate the abilities of the detection technique based on the reception of sub- and ultraharmonics at the frequencies $f_p(2n + 1)/2$ ($n \geq 0$). Since the presence of sub- and ultraharmonic signals is connected only with a bubble and is not observed in tissues, this technique suggests a considerable increase in contrast for bubble detection in biological tissues. A possibility of detecting gas bubbles in a pulsed mode of operation at subharmonic and ultraharmonic frequencies was demonstrated experimentally in [9, 10]. The best detection was achieved, as in the case of the second-harmonic generation, when the resonance frequencies of bubbles coincided with the pumping or detection frequencies. The results of numerical calculation by Eq. (3) for the cases of subharmonic and an ultraharmonic $(5/2f_p)$ detection are shown in Fig. 5. The signal amplitudes outside the resonances are small, which makes it difficult to detect nonresonance bubbles with this location method.

It is necessary to note that the amplitude of the pressure signal at ultraharmonics can be comparable with the amplitude of the pressure signal at a subharmonic. This is connected with the fact that pressure is proportional to the second time derivative of the bubble radius and that the frequency of the ultraharmonic is in this case five times higher than the subharmonic frequency.

As in the case of the employment of the second harmonic, in location at a subharmonic, the detection contrast is determined by the ratio of the useful signal and the level of noise not connected with the bubble but caused by the fact that, in a pulsed testing mode, the parasitic signal still can fall within the reception band if the spectral components at the subharmonic frequency are present in the radiated pulse with a broad spectrum; in addition, if these components are suppressed in the radiated pulse, they may reappear due to the propagation of a wideband signal through an acoustically nonlinear medium [13].

We implemented and tested the method of bubble detection at sub- and ultraharmonics in experiments *in vivo*. The device constructed for this purpose used probe pulses with a frequency of 1 MHz, a length of 10 μs, and an amplitude of 10^5 Pa with a cosine envelope; reception was performed at frequencies of 0.5 ± 0.1 and 2.5 ± 0.1 MHz. Figure 6a shows, as an illustration, the results of bubble location in soft tissues of a dog, which was subjected to a pressure change from 10 to 1 atm in a pressure chamber. Figure 6b presents analogous results obtained by locating soft tissues of a human in a pressure chamber under a pressure decrease from 1 to 0.7 atm. As one can see from these figures, signals from bubbles appear for a short time. This is connected with the change in their dimensions (their growth, in this case) and, hence, with a shift of their resonance frequency from the location frequency.

An increase in the amplitude of the probe signal, on the one hand, does not lead to a considerable increase in the signal from nonresonance bubbles; on the other hand, it may lead to an increase in the admissible radiation level for ultrasonic diagnostic devices. It is necessary to note that a probe pulse in medical diagnostic equipment contains only two or three oscillations of the carrier frequency with a total duration not exceeding 1–2 μs. Nonlinear methods of detection by the second harmonic, combination frequencies,
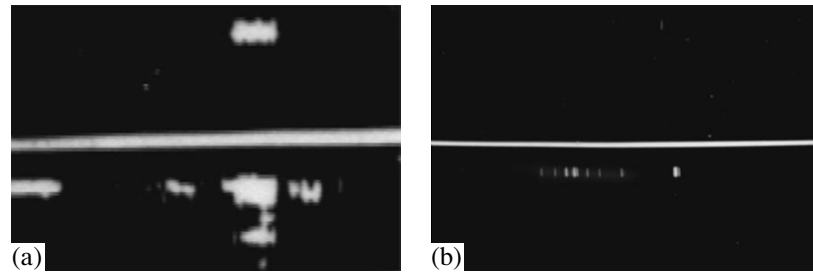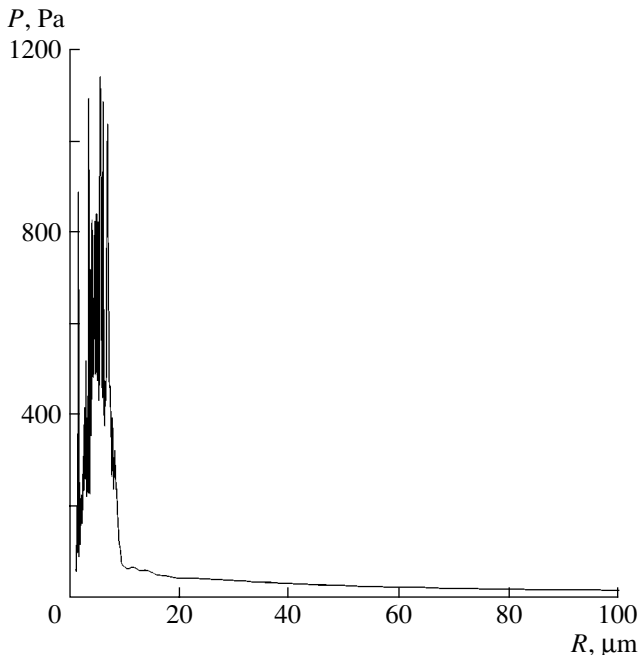
Fig. 6. Appearance of signals from bubbles in the decompression process with signal reception at the ultraharmonic (upper half-frames) and the subharmonic (lower half-frames) frequencies: (a) an experiment with a dog under a pressure drop from 10 to 1 atm and (b) an experiment with a human under a pressure drop from 1 to 0.7 atm. The horizontal axis represents the time within 0–30 s. In the vertical axis, the probing depth is 0–5 cm in each half-frame.

and subharmonics require the employment of longer pulses to "excite" the bubbles at the resonance frequency. Therefore, to maintain the energy of the probing signal at the level permitted for diagnostics, one should make its amplitude smaller than in ordinary medical diagnostic devices.

LOCATION BY PAIRED PULSES

The method of location by paired pulses is based on alternate testing by HF pulses with different initial phases or different types of modulation, storing of the testing results, and their alternate-period subtraction. As a result of this operation, the signals reflected from

Fig. 7. Dependence of the uncompensated signal amplitude at the location frequency on the bubble radius in the nonresonance range in the case of alternate testing by pulses with a phase shift of π. The amplitude of the probe pulse is 4×10^5 Pa, the probing frequency is 1 MHz, the pulse length is 3 μs, and the distance to the bubble in the tissue is 1 cm.

tissue layers must be completely compensated for, while the signals scattered by gas bubbles, because of their nonlinear distortion, are not compensated for. This method is described in [11, 12] and is intended for visualization of contrast particles introduced into a blood vessel. An essential role here is played by the amplitude dependence of the phase shift between the excitation signal and the natural oscillations of a bubble. Naturally, this dependence is most pronounced near the bubble resonance, but the presence of a small amplitude-dependent phase shift, as will be demonstrated below, provides an opportunity to also obtain a certain level of the difference signal outside the resonance.

In [11], the alternate testing of a medium by pulses with initial phases differing by π and with a subsequent summation of the received echo signals was performed to implement the method. Owing to the change in phase relations in signals due to nonlinearity, the sum signal is nonzero. In [12], an analogous alternate location method by the use of three pulses with initial phases differing by 120° and a subsequent summation of echo signals was suggested. In this case, a better suppression of the signal from linear reflectors is achieved. The distinctiveness of our version of such a system consists in that we compare not directly received signals but rather selected signals in the reception band at either the carrier frequency of the locator or the second-harmonic frequency. The results of calculation for the amplitude of the uncompensated signal scattered by bubbles are shown in Fig. 7. One can see that, in the nonresonant region, the signal is sufficient for bubble detection in a wider range of bubble sizes than in the case of other nonlinear methods. It is necessary to note that this compensation method can also be applied in the case of using comparatively short pulses, which provide a higher spatial resolution. A disadvantage of this method is the possible loss of contrast in the case of tissue motion. In this case, no complete compensation of the signals reflected from tissue layers can be achieved.
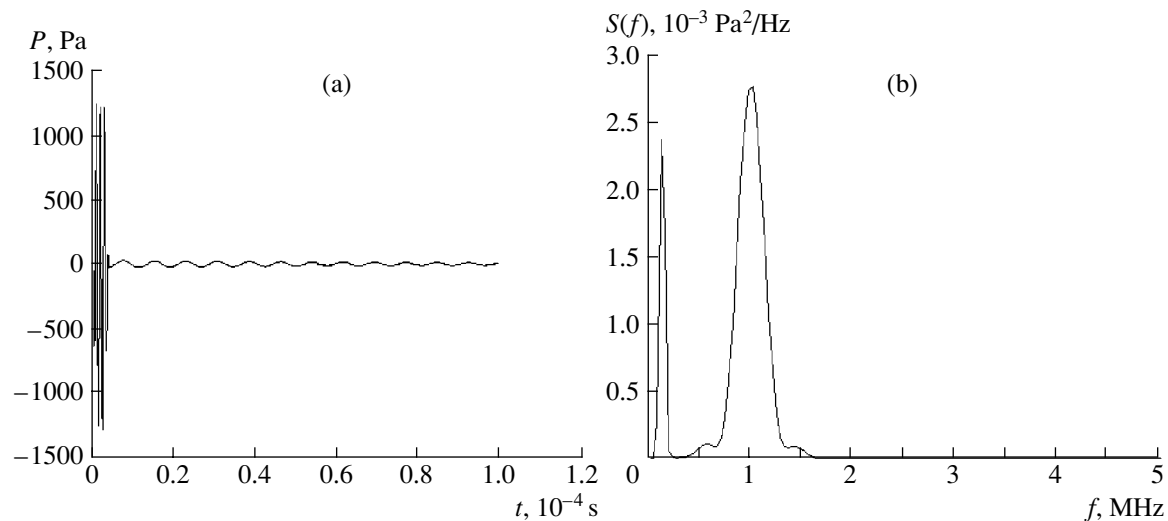
Fig. 8. (a) Oscillogram and (b) the spectral power density of a pressure signal reflected from a bubble with a radius of 25 μm (a pulse amplitude of 5×10^5 Pa, a pulse length of 3 μs, and a frequency of 1 MHz, which corresponds to a bubble resonance radius of 3.7 μm).

NONLINEAR EXCITATION OF NATURAL OSCILLATIONS OF A BUBBLE

Let us consider one more possible version of detection and evaluation of the size of gas bubbles. Location is performed by short HF pulses containing several periods of oscillations. As the result of pulse detection, the natural oscillations of a bubble are excited because of its nonlinear response. Their frequency is directly connected with the bubble size according to Eq. (1). To provide for a contrast against the tissue background, the frequency components falling within the reception band are suppressed in the pumping signal, while, on the contrary, in the signal reflected from a bubble and received from the medium, the signals at the testing frequency are suppressed. For example, in the case of the numerical simulation, the frequencies lower than 500 kHz were suppressed with the help of an HF filter in the spectrum of the probe pulse with the carrier frequency $f_p = 1$ MHz. As one can see from Fig. 8a, after the end of the pumping pulse, the natural oscillations at the frequency determined by the resonance frequency of the bubble are observed in the pressure oscillogram. Figure 8b shows the spectrum of the received signal. A similar procedure is proposed in [16], where spectroscopy based on the excitation of natural low-frequency oscillations of a bubble by high-frequency pulses is suggested. The distinctive feature of the method proposed by us is as follows. In the method described in [16], the driving force contains frequency components at the resonance frequency of a bubble, and, in this case, signals from linear reflectors will not be suppressed. In the version proposed by us, natural oscillations result from the effect produced on the bubble by a "detected" pulse, which results from the acoustic non-

linearity of the bubble. By measuring the frequency of natural oscillations (for example, with the help of a spectrum analysis), it is possible to determine the bubble size. To do this, it is necessary to suppress the probing frequency in the received signal to eliminate signals from linear scatterers (see Fig. 9a). Then, it is possible to analyze the received signal, for example, to alternately calculate the convolution of the received signals with the calibration signals of natural oscillations of bubbles for different dimensions. Figure 9b gives an example of such a convolution, where the solution to Eq. (3) with the suppressed spectrum region around the probing frequency is taken as the basic signal. The first peak is connected with the resonance at the probing frequency (the carrier frequency is filtered out insufficiently), and the second peak is connected with the resonance of the bubble itself.

Substituting functions with different central frequencies and damping factors characteristic of different bubble dimensions into the expression for the convolution, it is possible to determine the resonance frequencies of bubbles and to determine the bubble size according to them. Applying this technique, it is necessary to provide a monotonic frequency characteristic for the receiving antenna in a wide frequency range. This is possible, for example, if one uses a receiving transducer operating within a band lower than the natural resonance.

It is necessary to note that the described procedure of analysis is just a model. Applying the recently developed methods of local time–frequency analysis of pulsed signals (for example, the wavelet analysis or nonlinear spectrum analysis [17]), it is possible to speed up the processing and improve the space–time
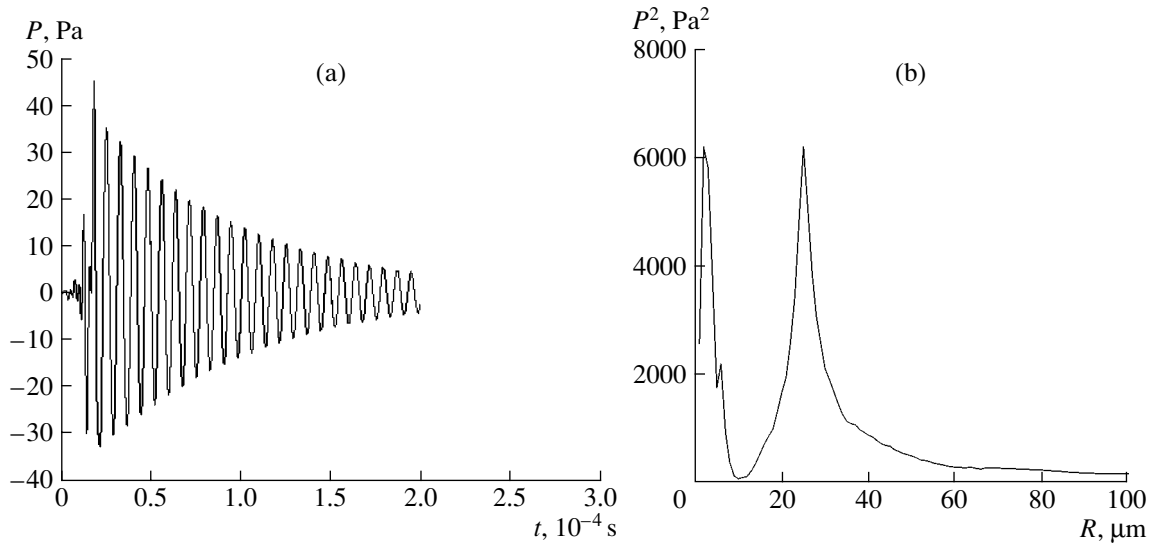
Fig. 9. (a) Filtered response of a signal (the band of the probe signal is suppressed) from a bubble with a radius of 25 μm and (b) the convolution of the solution to Eq. (3) for bubbles 1–100 μm in size with the response from a bubble with a radius of 25 μm.

CONCLUSION

According to the results of the numerical experiments, it is possible to conclude that the nonlinear acoustic detection methods based on the generation and reception of the second harmonic, combination frequencies, and sub- and ultraharmonics in the signal reflected from a gas bubble in biological tissues provide for a high reliability of detection only for the bubbles with dimensions close to the resonance ones at the probing or reception frequencies. The bubbles of other, nonresonance, dimensions at moderate probing amplitudes are almost undetectable by similar techniques because of either echo signals from the layers of biological tissues or reflected signals. Somewhat better capabilities are possessed by the method of paired pulses, which allows one to expand the range of detectable bubbles with a high contrast against the surrounding layers of biological tissues.

The proposed method of nonlinear excitation of natural oscillations provides an opportunity to detect gas bubbles and to measure their sizes in a wide range. Evidently, the echo-signal contrast against the noise from biological tissues in this case must also be high, because the resonance properties of the layers manifest themselves weakly. The application of modern achievements in the field of signal processing will make it possible to improve the localization characteristics of gas bubbles. The described technique evidently needs further study and experimental verification.

REFERENCES

1. K. N. Smith and M. P. Spencer, Aerosp. Med. **41**, 1396 (1970).

2. A. S. Barer, V. P. Katuntsev, A. D. Mansfel'd, *et al.*, in *Medical-Biological Studies for the Nauka–NASA Program* (Slovo, Moscow, 1997), pp. 56–57 [in Russian].

3. G. J. Rubissow and R. S. Mackay, Aerosp. Med. **45**, 473 (1974).

4. V. P. Nikolaev, V. P. Katuntsev, A. M. Reĭman, *et al.*, Kosm. Biol. Aviakosm. Med., No. 3, 52 (1984).

5. M. Plesset and A. Prosperetti, Annu. Rev. Fluid Mech. **9**, 145 (1977).

6. *Physical Principles of Medical Ultrasonics*, Ed. by C. R. Hill (Ellis Horwood, Chichester, 1986; Mir, Moscow, 1989).

7. E. A. Zabolotskaya and S. I. Soluyan, Akust. Zh. **18**, 472 (1972) [Sov. Phys. Acoust. **18**, 396 (1972)].

8. L. A. Ostrovskiĭ and A. M. Sutin, in *Ultrasonic Diagnostics* (Inst. of Applied Physics, USSR Academy of Sciences, Gorki, 1983), pp. 139–150 [in Russian].

9. A. D. Mansfel'd and A. M. Reĭman, in *Ultrasonic Diagnostics* (Inst. of Applied Physics, USSR Academy of Sciences, Gorki, 1983), pp. 151–161 [in Russian].

10. A. G. Kirillov, A. D. Mansfel'd, A. M. Reĭman, and P. K. Chichagov, in *Problems of Nonlinear Acoustics: Proceedings of XI International Symposium on Nonlinear Acoustics* (Novosibirsk, 1987), Part 2, pp. 32–34.

11. P. Burns and D. Hope-Simpson, U.S. Patent No. 6,095,980 (1998).

12. M. A. Averkiou, in *Proceedings of Conference of the IEEE Ultrasonics, Ferroelectrics and Frequency Control Society* (Honolulu, Hawaii, 2003), p. 95.

13. L. K. Zarembo and V. A. Krasil'nikov, *Introduction to Nonlinear Physical Acoustics* (Nauka, Moscow, 1966) [in Russian].

14. J. B. Keller and M. Miksis, J. Acoust. Soc. Am. **68**, 628 (1980).

15. S. Umemura, T. Azuma, H. Kuribara, and H. Kanda, in *Proceedings of Conference of the IEEE Ultrasonics,* *Ferroelectrics and Frequency Control Society* (Honolulu, Hawaii, 2003), pp. 209–210.

16. V. A. Bulanov, *Introduction to the Acoustical Spectroscopy of Micrononhomogeneous Liquids* (Dal'nauka, Vladivostok, 2001) [in Russian].

17. A. G. Kislyakov, A. N. Makarov, A. D. Mansfel'd, and A. M. Reĭman, in *Proceedings of 5th Scientific Conference on Radiophysics*, Ed. by A. V. Yakimov (Nizhegor. Gos. Univ., Nizhni Novgorod, 2001), pp. 136–137.

Translated by M. Lyamshev

Comparative Analysis of Tomographic Methods for the Observation of Inhomogeneities in a Shallow Sea

A. L. Matveev, D. A. Orlov, A. A. Rodionov, B. M. Salin, and V. I. Turchin

Institute of Applied Physics, Russian Academy of Sciences, ul. Ul'yanova 46, Nizhni Novgorod, 603950 Russia
e-mail: matveyev@hydro.appl.sci-nnov.ru
Received October 5, 2004

Abstract—Several procedures are proposed that allow one to determine the parameters of motion of an inhomogeneity crossing the propagation path between a source of an acoustic signal and a receiving array without the use of any detailed description of the medium (the sound velocity profile, the bottom parameters, etc.). The potentialities and characteristic features of the proposed approach are analyzed within the framework of a one-dimensional waveguide propagation model. A comparative analysis of the reliability of inhomogeneity observations is performed on the basis of a representative experimental data set obtained from a lake experiment for the cases of using the procedures of coherent space–time processing of signals in antenna arrays and the procedures with a spatial and temporal incoherent accumulation. © 2005 Pleiades Publishing, Inc.

INTRODUCTION: STATEMENT OF THE PROBLEM

Together with the pulsed location method, which mainly uses backscattered echo signals for the observation of inhomogeneities, the observation method using the forward scattering, where the scattering cross section considerably increases and proves to be close to the geometric area of the inhomogeneity under observation, has been under consideration for a rather long time [1–5]. Observation schemes of this type can be classed with tomographic ones, since the source of acoustic field "illuminates" a certain region of the medium, while the receiver detects the signal variation indicating that the source–receiver path is crossed by an inhomogeneity.[1] By now, a series of sufficiently effective methods have been proposed for inhomogeneity observation against the background of the direct signal fluctuations due to scattering by wind waves and by volume inhomogeneities of the refractive index with the use of both vertical and horizontal receiving arrays [6–8]. Moreover, it was demonstrated that an inhomogeneity can be clearly observed not only at the instant of crossing the source–receiver path but also in a broader region, including the closest sidelobes of the scattering pattern.

This possibility, in particular, results from the specific features of the behavior of the fluctuation spectrum of a direct signal [8]. Naturally, the problem of comparing the efficiencies of different observation methods, including a direct comparison in experiments, seems to be important. The present paper is devoted to this problem.

As the experimental material, we used the data obtained from the lake experiments of 1997–1999 [8]. In these experiments, several types of inhomogeneities with a length of several meters and heights of up to 1 m were towed under the water surface approximately across the sound propagation path between a source (a monopole-type radiator installed near the bottom or a vertical radiating phased array) and a receiver (a vertical or horizontal 64-element equidistant array with a length of 12 m). In the experiment, several (up to five) tone signals were emitted simultaneously in the frequency range of 1–3 kHz. Over one hundred signal records were made, which included the moments of crossing the path 300–450 km in length under identical and different weather conditions, which made it possible to compare different methods. A detailed description of the lake experiment is given in [8].

In the next section, the models of direct and diffracted signals in a plane-layered waveguide are considered from the point of view of the synthesis of signal-processing algorithms in receiving arrays and the understanding of the particular features of inhomogeneity observation in a shallow sea. Below, on the basis of models taking into account the characteristic space–time properties of the interference (first of all, fluctuations of the direct signal), we formulate four methods of inhomogeneity observation: the methods of observation of forward scattering, which employ (a) the combi-

---

[1] We have often encountered the criticism of this classification on the basis of the fact that a certain set of projections is commonly used in tomography, whereas, in the scheme under consideration, only one projection exists (with one source and one receiver). Although, as will follow from the further discussion, there is still a certain set of projections in this scheme, which appears because of the motion of inhomogeneities in a certain vicinity of the source–receiver path, we do not insist on the fact that the term "tomographic" is the most suitable one. It is also possible to use the term "transmission scheme of observation," which is used in practical applications, not only in underwater acoustics but also in radar techniques.

nations of coherent time and incoherent space processing for a vertical array, and (b) space–time coherent processing for a horizontal receiving array and the methods of observation of a scattered signal beyond the main lobe of the scattering pattern, i.e., in the near bistatic region with the use of (c) the space–time processing within a floating time window and (d) incoherent accumulation in time. The last two methods are developed for a horizontal receiving array. The second-to-last section gives the comparison of the efficiencies of methods (a)–(d) on the basis of experimental data, and, in the last section, we formulate our conclusions.

MODELS OF DIRECT AND DIFFRACTED SIGNALS IN A REGULAR PLANE-LAYERED WAVEGUIDE

Figure 1 shows the observation scheme corresponding to the given signal models. The trajectory of inhomogeneity motion lies between the source and the antenna array. The center O of the Cartesian coordinate system (x, y, z) in Fig. 1 is positioned at the water surface. The receiving elements of a vertical array are positioned on the z axis, and, for the case of a horizontal array, they are arranged parallel to the x axis. The z axis crosses the center of the horizontal antenna array. The source emits a continuous tone signal $e^{-2\pi i f_0 t}$.

The sound pressure p measured by an nth element of the array can be described in the form of the sum of the direct field p_0 observed in the absence of the scatterer and the diffracted (scattered) field p_d for the current position of the source:

$$p = p_0 + p_d. \quad (1)$$

In a regular plane-layered waveguide, the direct field has the form

$$p_0 = (2\pi i)^{1/2} \sum_{m=1}^{M} \varphi_m(z_s)\varphi_m(z_n)\frac{e^{i\kappa_m(r - x_n\sin\alpha_0)}}{\sqrt{\kappa_m r}}, \quad (2)$$

where z_s and z_n are the depths of the source and the nth element of the array, respectively; r is the length of the propagation path OS; x_n is the position of the nth element of the array on the x axis; α_0 is the source bearing; $\varphi_m(z)$ is the mth vertical depth eigenfunction corresponding to the mth wave number κ_m; $\kappa_m r \gg 1$; and M is the total number of propagating modes; the factor $e^{-2\pi i f_0 t}$ is omitted.

A diffracted field can be represented with the help of the Kirchhoff approximation. We assume for definiteness that a plane inhomogeneity has a rectangular shape with length l_h and height l_v. The integration over the inhomogeneity aperture performed for Green's function in the form of Eq. (2) and its derivative with respect to the normal to the aperture by taking into account $k_m l_h$,
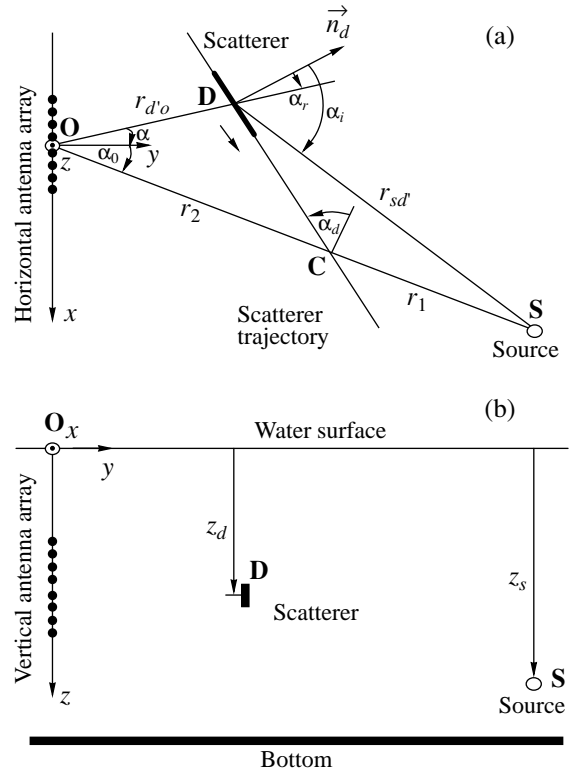

Fig. 1. Experimental geometry in the (a) horizontal and (b) vertical planes.

$k_m l_v \gg 1$ leads to the following representation of the diffracted component:

$$p_d = \frac{D}{\sqrt{r_{sd}r_{d'o}}} \sum_{m'=1}^{M} \sum_{m''=1}^{M} \frac{\kappa_{m'} + \kappa_{m''}}{\sqrt{\kappa_{m'}\kappa_{m''}}}$$
$$\times \varphi_{m'}(z_s)\varphi_{m''}(z_n)f_{m',m''}\Phi_d \quad (3)$$
$$\times \left(\frac{l_h}{2\pi}(\kappa_{m'}\sin\alpha_i + \kappa_{m''}\sin\alpha_r)\right)e^{i\phi_{m',m'',n}},$$

where $D = l_h l_v \cos\alpha_d$ is the area of the "shadow" of the inhomogeneity and Φ_d is the section of the scattering pattern in the horizontal plane:

$$\Phi_d\left(\frac{l_h}{2\pi}\xi\right) = \frac{1}{l_h}\int_{-l_h/2}^{l_h/2} e^{-i\xi x}dx = \text{sinc}(\xi l_h/2\pi), \quad (4)$$

$\text{sinc}\,x = \sin\pi x/\pi x$. The main lobe of the scattering pattern (Eq. (4)) describes the forward scattering, and the sidelobes correspond to the region of bistatic scattering. The matrix $f_{m',m''}$ describes the mode coupling, which is determined by the vertical dimension of the scatterer:

$$f_{m',m''} = \frac{1}{l_v}\int_{z_d-l_v/2}^{z_d+l_v/2} \varphi_{m'}(z)\varphi_{m''}(z)dz, \quad (5)$$

$$\phi_{m',m'',n} = \kappa_{m'}r_{sd'} + \kappa_{m''}r_{d'o} - \kappa_{m''}x_n\sin\alpha, \quad (6)$$

where α is the current bearing of the inhomogeneity. The distances r_{sd} and $r_{d'o}$ and the angles α_i, α_r, and α are determined from elementary geometrical constructions:

$$r_{sd'} = \sqrt{r_1^2 - 2r_1 u \sin\alpha_d + u^2};$$
$$r_{d'o} = \sqrt{r_2^2 + 2r_2 u \sin\alpha_d + u^2};$$
$$\quad (7)$$

$$\sin\alpha_i = \frac{u - r_1 \sin\alpha_d}{r_{sd'}}; \quad \sin\alpha_r = \frac{u + r_2 \sin\alpha_d}{r_{d'o}};$$
$$\sin\alpha = \frac{r_2 \sin\alpha_0 + u \cos(\alpha_d - \alpha_0)}{r_{d'o}},$$
$$\quad (8)$$

where $u = V(t - t_0)$, V is the velocity of the inhomogeneity, t_0 is the instant of its crossing the line OS, and r_1 and r_2 are the distances between the source and the scatterer trajectory and between the scatterer trajectory and the origin of coordinates, respectively, $r_1 + r_2 = r$. In the vicinity of the instant of crossing, the first three terms of the expansions of Eqs. (7) and (8) in u can be used instead of the full expressions. The diffracted component reaches the global maximum when the inhomogeneity crosses the propagation path, i.e., at the instant $t = t_0$. This is true, however, only in the case where the scatterer trajectory is perpendicular to the propagation path OS ($\alpha_d = 0°$). At $\alpha_d \neq 0°$, the global maximum can be located in a certain vicinity of the instant of crossing.

The use of Eq. (3) as a replica while processing the received signals leads to serious difficulties, because Eq. (3) strongly depends on the propagation conditions. Equation (3) can be simplified under the assumption that the difference between the wave numbers κ_m is negligible; i.e., it is possible to assume that $\kappa_m \approx \kappa$ for all $m = 1, \ldots, M$, where κ is a certain average wave number. In the vicinity of the crossing instant, this approximation takes on the form

$$p_d \approx p_d^{(a)} = \frac{D}{\sqrt{r_1 r_2}} a_n S_d(t - t_0) e^{-i\kappa x_n \sin\alpha(t)},$$
$$\sin\alpha(t) = \sin\alpha_0 + \frac{V(t - t_0)}{r_2} \cos\alpha_0 \cos\alpha_d,$$
$$\quad (9)$$

where phase (9) characterizes the constant and time-variable components of the source bearing for a horizontally positioned antenna array and the function

$$S_d(t) = \Phi_d(t/T_d) e^{i\gamma t^2} \quad (10)$$

describes the time shape of the diffracted component, which can be considered as a linearly frequency-modulated pulse with duration T_d and frequency deviation γ:

$$T_d = \frac{\lambda r_e}{V l_n \cos^2\alpha_d}, \quad \gamma = \frac{\pi(V \cos\alpha_d)^2}{\lambda r_e}, \quad (11)$$

where $\lambda = 2\pi/\kappa$ is the wavelength, $r_e = r_1 r_2/r$ is the effective distance, and

$$a_n = \sum_{m'=1}^{M} \sum_{m''=1}^{M} \varphi_{m'}(z_s) \varphi_{m''}(z_n) f_{m', m''} e^{i(\kappa_{m'} r_1 + k_{m''} r_2)}. \quad (12)$$

In the case of a horizontal antenna array, all amplitudes a_n are equal: $a_1 = a_2 = \ldots = a$. Thus, in a plane-layered waveguide, the approximate space–time form of the diffracted signal does not depend on the propagation conditions except for the value of the average wave number; i.e., the form of the approximation given by Eq. (9) coincides with the case of free space with a constant sound velocity. In the case of a vertical antenna array, the dependence of the amplitudes a_n on the profile of sound velocity and the acoustic parameters of the bottom is significant, and only the time shape of diffracted signal component (10) does not depend on the propagation conditions.

Using Eq. (3), it is possible to investigate two basic effects of multimode propagation that affect the observation characteristics. The first effect consists in that the value of the maximum of the diffracted component considerably varies depending on the position of the inhomogeneity trajectory and the depths of the source and the receiving array. In some cases, the diffracted components cannot be observed, namely, when the inhomogeneity is located at the minimum of the incident field or the receiver is located at the minimum of the diffracted field. The second effect consists in the mismatch of the time or space–time shapes (Eqs. (3) and (9)). To describe both these effects qualitatively, it is possible to use a simplified model for an underwater sound channel, e.g., a Pekeris waveguide [9].

The above effects can be illustrated with the help of a numerical simulation for a set of parameters approximately corresponding to the conditions of the lake experiment [8]: $r = 450$ m, depth $H = 15$ m, sound velocity in the water layer $c = 1450$ m/s, sound velocity in the bottom $c_b = 1700$ m/s, density of the bottom $\rho_b = 1.5$ (bottom reflection coefficient $K_b = 0.28$), $z_s = 13$ m, $z_d = 6$ m, $l_h = 5$ m, and $l_v = 1$ m. Figure 2 shows the dependence of the diffracted component maximum at the instant $t = t_0$ for a frequency of 3 kHz and a source amplitude of 1 Pa at a distance of 1 m. The upper plot demonstrates the variation of the maximum for one array element located at the depth $z_1 = 6$ m, and the lower plot represents the amplitude $\bar{p}_d$ averaged over the elements of a vertical antenna array, which are located at the depths $z_n = 2.0 + (n - 1)d$, where $n = 1, \ldots, N$, $N = 64$, $d = 0.19$ m,

$$\bar{p}_d = \sqrt{\frac{1}{N} \sum_{n=1}^{N} |p_d(z_n, t_0)|^2}. \quad (13)$$
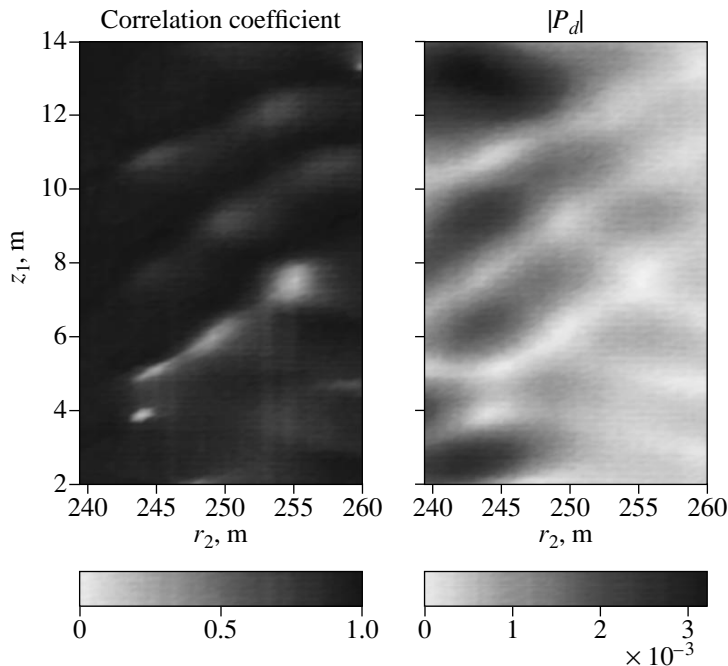
Diffracted component, 10^{-3} Pa
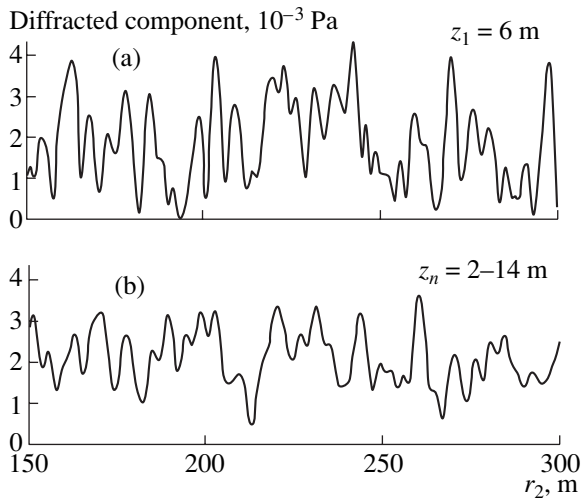
Fig. 2. Dependences of the maximum amplitude of the diffracted component on the distance r_2 determining the position of the trajectory of the inhomogeneity between the source and the receiver (a) for a single receiving element at a depth of 6 m and (b) the result of averaging the amplitudes over the elements of the vertical array at the depths 2–14 m. The frequency is 3 kHz, and the scale is linear.

One can see that the maximum of the diffracted component is subjected to considerable variation already in the case of a change in r_2 by ~5 m. The swing of these oscillations is reduced (from ~47 dB to ~18 dB) as a result of averaging over the elements of the vertical array.

The mismatch of the time shape of diffracted component models (3) and (9) can be characterized by the correlation coefficient C:

$$|C| = \frac{\left|\sum\limits_{j} p_d(t_j) S_d^*(t_j)\right|}{\sqrt{\sum\limits_{j} |p_d(t_j)|^2 \sum\limits_{j} |S_d(t_j)|^2}}, \quad (14)$$

for the time instants t_j in the interval $\pm 2T_d$ at $t_0 = 0$. Figure 3 presents the dependences of $|C|$ and the maximum of the diffracted component on the depth of a receiving element z_1 and the distance r_2. As follows from Fig. 3, the maximum of the diffracted component is subjected to strong variation in the range of ~20 dB, while the modulus of the correlation coefficient varies mainly within ~0.9–1.0 and decreases only in the deepest minima $|p_d|$. Precisely this fact provides an opportunity to perform matched signal processing based on model (9). The latter is characterized by just one parameter determined by the propagation medium, namely, the mean wave number or the average sound velocity in the waveguide c. Calculations for the above group of parameters demonstrated that, in the case of variation of c in the wide range of 1250–1650 m/s, the correlation coefficient may vary within 0.88–1.0 in the frequency range of 1–3 kHz; i.e., for processing, it is sufficient to use an approximate value of sound velocity. The last geometrical parameter that can affect the correlation coefficient is the angle α_d (see Fig. 1). Numerical simulations demonstrated that the correlation coefficient

Fig. 3. Dependences of the modulus of the correlation coefficient (at the left) and the maximum amplitude of the diffracted component (at the right) on the distance r_2 and the receiving-element depth z_1. The frequency is 1 kHz.
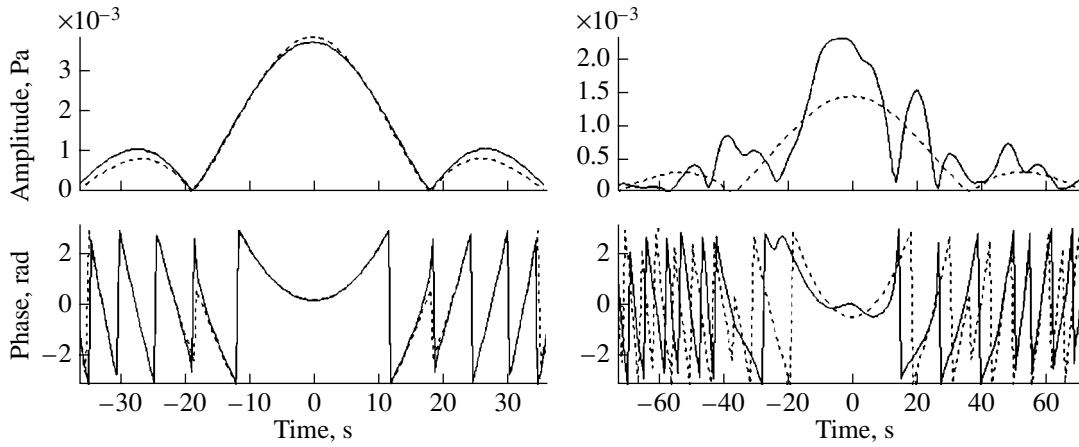
Fig. 4. Examples of the time dependences of the diffracted signal for the inhomogeneity moving perpendicularly to the propagation path ($\alpha_d = 0$, at the left) and at an angle of $\alpha_d = 45°$ to the propagation path (at the right). The solid curve represents exact dependence (3), and the dashed line shows approximation (9).

noticeably decreases with an increase in this angle: for the given set of parameters, the correlation coefficient remains within 1.0–0.8 at $|\alpha_d| < 25°$ and decreases to ~0.4 at $\alpha_d = 60°$. The time dependences of the amplitude and phase of the diffracted signals that were calculated according to Eqs. (3) and (9) for $\alpha_d = 0°$ and $45°$ are given in Fig. 4 as an example.

It is necessary to note that the influence of multimode propagation on the form of the diffracted signal for a horizontal antenna array in a plane-layered waveguide is the same as for a single receiving element, since the factors $\Phi_d e^{i(\kappa_{m'} r_{sd'} + \kappa_{m''} r_{d'\theta})}$ in Eq. (3) are identical for all elements. Additional influence of multimode propagation on the precision of the bearing estimate is well-studied (for example, see [10]). It is inessential for comparatively short arrays and the directions close to the normal to the array.

If the inhomogeneity moves away from the path *OS* (see Fig. 1), the diffracted component is determined by the sidelobes of the scattering pattern. Their description (in contrast to the main lobe) is difficult within the Kirchhoff approximation; it is necessary to take into account the shape of the scatterer edges, the boundary conditions at its surface, etc. Therefore, one has to use a cruder model as a replica in the region of bistatic scattering. For a horizontal array, it can be the time variation of the signal phase that is determined by the Doppler frequency shift and the inhomogeneity bearing, which synchronously vary in time. This approximation can be represented in the form

$$p_d^{(a,b)} = A_d(t)e^{i[\phi_d(t) - \kappa x_n \sin\alpha(t)]}, \qquad (15)$$

where $\phi_d(t) = \kappa[r_{sd'}(t) + r_{d'o}(t)]$; $A_d(t)$ is a certain quasi-random complex-valued function determined by both the sidelobes of the scattering pattern and the interference structure of the field in the waveguide; κ is the

average wave number, as in Eq. (9); and the distances $r_{sd'}$ and $r_{d'o}$ and the sine of the scatterer bearing are determined according to Eqs. (7) and (8). The first derivative of ϕ_d is a current Doppler frequency shift:

$$\omega_d = d\phi_d/dt = \kappa V(\sin\alpha_r + \sin\alpha_i). \qquad (16)$$

The properties of the diffracted component in the region of bistatic scattering can be illustrated by the current estimates for the inhomogeneity bearing, which are obtained using a common procedure of the scattering pattern formation:

$$B(\sin\alpha, t) = \left| \frac{1}{N} \sum_{n=1}^{N} p_d(x_n, t) e^{i\kappa x_n \sin\alpha} \right|, \qquad (17)$$

where p_d is determined by Eq. (3). The two-dimensional representation given by Eq. (17) that is obtained by numerical simulation is given in Fig. 5b for the time interval $t_0 + 4T_d < t < t_0 + 4T_d + 250$ s and the parameters $f_0 = 2$ kHz, $V = 0.6$ m/s, $\alpha_0 = 10°$, and $\alpha_d = 0°$. Figure 5a demonstrates the current estimates of the bearing for free space, where Eq. (15), with $A_d = D\Phi_d(\kappa l_h(\sin\alpha_i + \sin\alpha_r)/2\pi)/(\lambda r_0 \sqrt{r_{sd'} r_{d'o}})$, is taken as p_d. The rate of the diffracted field decrease in this case was taken to be the same as in a waveguide with the transition range r_0 (~12 m). One can see from Fig. 5a that the estimate for the inhomogeneity bearing in the case of free space is modulated by sidelobes (4). This modulation becomes irregular for waveguide propagation (Fig. 5b), since the inhomogeneity also crosses interference maxima and minima in the course of motion. Such irregular modulation can be considered, however, as a positive factor in the case of a sufficiently long trajectory of the inhomogeneity. As we have noted above, in the case of observation of forward scattering, the maximum of the diffracted signal strongly varies depending on the loca-
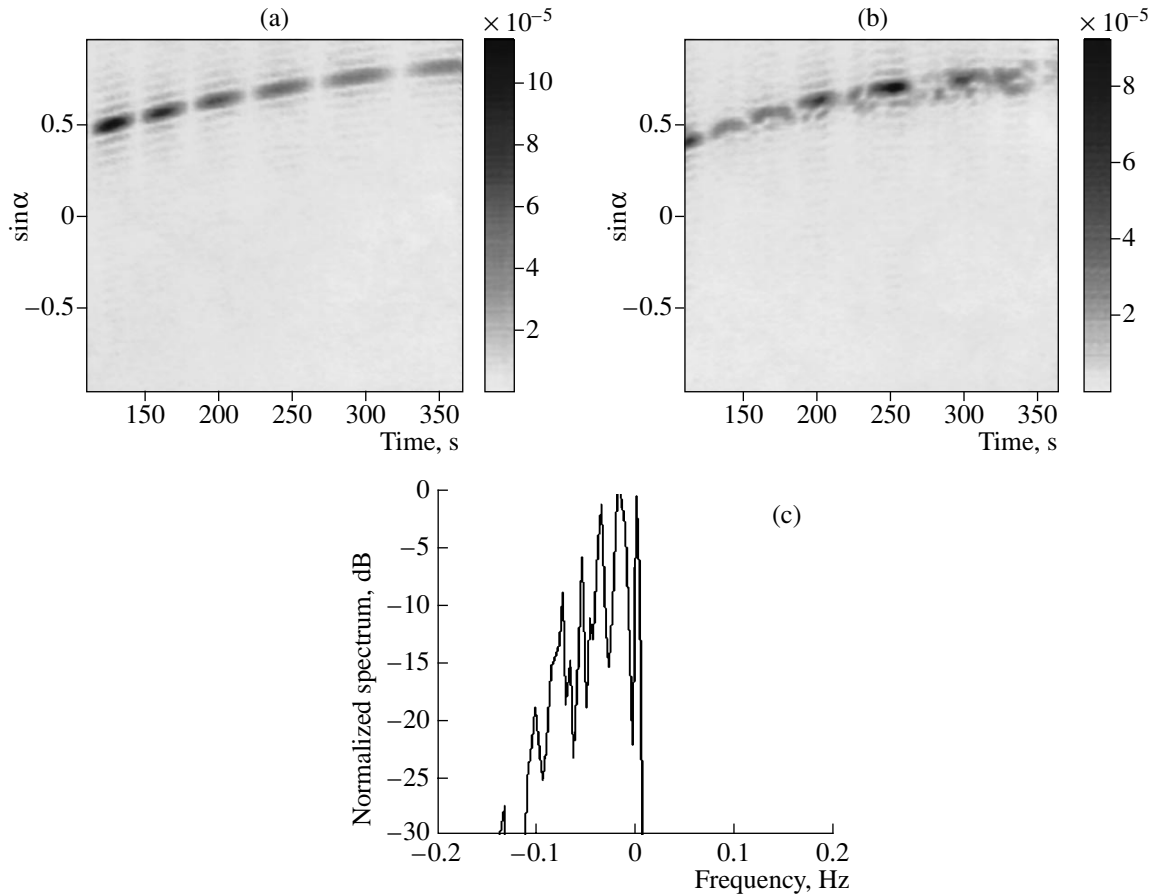
Fig. 5. Time and scan-angle dependences of the amplitude at the output of a horizontal scanning antenna array in the bistatic scattering region for the case of an inhomogeneity moving away from the point of crossing the propagation path (a) in free space and (b) in a waveguide; (c) the spectrum of the complex amplitude of the signal at the array output in the case of monitoring the inhomogeneity by the main lobe of the scattering pattern.

tion of the inhomogeneity trajectory between the source and the receiving array (see Fig. 2), so that, at certain values of the distance r_2, the inhomogeneity may be unobservable. Although the average amplitude of the diffracted signal in the region of bistatic scattering is smaller in comparison with the forward scattering, the observation of a moving scatterer becomes more stable at the trajectory length comparable to the length of the propagation path. At least several maxima of the diffracted signal can be observed for any distance r_2.

The spectrum of the function $A_d(t)$ determined from Eq. (3) is shown in Fig. 5c for the same parameters as in Fig. 5b. The width of this spectrum determines the admissible duration of the temporal coherent processing of a signal in the region of bistatic scattering (in the given example, this duration is ~20 s).

The models of replicas given above (Eqs. (9) and (15)) will be used below for the synthesis of signal-processing procedures aimed at the detection and estimation of the parameters of moving inhomogeneities.

ESTIMATION OF THE PARAMETERS OF A MOVING INHOMOGENEITY

As we have mentioned above, inhomogeneities are characterized by a sufficiently large number of parameters, which, as a rule, are unknown: the time of crossing t_0, the velocity V, the distance r_2, the length l_h, and the angle α_d between the trajectory and the normal to the propagation path. Therefore, the observation procedure itself must consist in the estimation of these parameters with allowance for the fact that the diffracted signal is observed against a noise background. Assuming that the observation is conducted with an antenna array, the set of signal snapshots, i.e., the vector $\mathbf{p}(t)$ with the dimension $N \times 1$, where N is the number of receiving elements, after a complex demodulation at the radiated signal frequency, low-pass filtration, and decimation, can be represented according to Eq. (1) in the form

$$\mathbf{p}(t) = \mathbf{p}_d(t, \boldsymbol{\theta}) + \mathbf{p}_0(t) + \boldsymbol{\xi}(t),$$

where the vector $\boldsymbol{\theta}$ denotes the set of the unknown parameters listed above and $\boldsymbol{\xi}(t)$ is the noise back-

ground. In a natural underwater channel, both the diffracted component and the direct signal fluctuate due to scattering by random inhomogeneities. We assume that these fluctuations are comparatively small; e.g., for the direct signal, the average value is much greater than the fluctuating part. At the same time, because of the smallness of the diffracted component in comparison with the direct signal, the fluctuating part of the direct signal is comparable with the diffracted component and interferes with its observation. At least in the lake experiment [8], precisely the fluctuations of the direct signal were the major interference in the observation of the diffracted component. Under this approximation, the diffracted component can be treated as a regular signal with a known structure, and the direct signal together with the background noise, as a random additive interference $\varsigma(t) = \mathbf{p}_0(t) + \boldsymbol{\xi}(t)$.

As is known, a classical method for the determination of the unknown parameters of a deterministic signal observed against the background of additive noise is the maximum likelihood technique (for example, see [11]). Further, we assume that interference is a process stationary in time; i.e., its covariance matrix $\mathbf{K}$ can be represented in the form $\langle \varsigma(t_1)\varsigma^H(t_2) \rangle = \mathbf{K}(t_1 - t_2)$, where $(\cdot)^H$ means Hermitian transpose. We represent the diffracted component model (a replica) in the form $\mathbf{p}_d(t, \boldsymbol{\theta}) = \theta_0 \mathbf{s}_d(t, \boldsymbol{\theta}_1)$, where θ_0 is an unknown complex amplitude and $\boldsymbol{\theta}_1 = (t_0, V, \ldots)^T$ is the vector of the parameters nonlinearly involved in the diffracted component model. The components of the vector $\mathbf{s}_d$, for example, in the case of a horizontal receiving array and observation of forward scattering, are determined according Eq. (9):

$$\mathbf{s}_d(t, \boldsymbol{\theta}_1) = S_d(t - t_0)\mathbf{a}(t, \boldsymbol{\theta}_1), \quad a_n = e^{-i\kappa x_n \sin\alpha(t)}. \quad (18)$$

In this case, the maximum likelihood estimate of unknown parameters in the case of the normal distribution of noise is determined in the form [12]

$$\hat{\boldsymbol{\theta}}_1 = \underset{\theta_1}{\arg\max} F(\boldsymbol{\theta}_1);$$

$$F(\boldsymbol{\theta}_1) = \frac{\left| \int\limits_{-f_s/2}^{f_s/2} \mathbf{u}_d^H(f, \boldsymbol{\theta}_1)\mathbf{W}^{-1}(f)\mathbf{q}(f)df \right|^2}{\int\limits_{-f_s/2}^{f_s/2} \mathbf{u}_d^H(f, \boldsymbol{\theta}_1)\mathbf{W}^{-1}(f)\mathbf{u}_d(f, \boldsymbol{\theta}_1)df}, \quad (19)$$

where $\mathbf{u}_d$, $\mathbf{q}$, and the matrix of the cross-spectral densities of interference $\mathbf{W}$ are the discrete Fourier transforms of the replica $\mathbf{s}_d$, the input signal vector $\mathbf{p}$, and the matrix of interference covariance $\mathbf{K}$, respectively; f_s is the sampling rate. It is necessary to note that Eq. (19) is also a detection procedure: according to the excess of max F over a certain threshold, it is possible to judge the presence of a moving inhomogeneity.

In the case of a vertical receiving array, the replica is represented in the form $\mathbf{s}_d = S_d(t - t_0)\mathbf{a}$, where $\mathbf{a}$ is the

constant vector characterizing the diffracted field distribution over the array aperture. As was noted before, its structure depends on the propagation conditions; therefore, the simplest way is to consider it to be an unknown parameter. A maximization of Eq. (19) with respect to this vector leads to the replacement of Eq. (19) by a quadratic form:

$$F(\boldsymbol{\theta}_1) = \mathbf{v}^H\mathbf{Q}^{-1}\mathbf{v}, \quad (20)$$

where

$$\mathbf{v} = \int\limits_{-f_s/2}^{f_s/2} U_d^*(f, \boldsymbol{\theta}_1)\mathbf{W}^{-1}(f)\mathbf{q}(f)df,$$

$$\mathbf{Q} = \int\limits_{-f_s/2}^{f_s/2} |U_d(f, \boldsymbol{\theta}_1)|^2\mathbf{W}^{-1}(f)df, \quad (21)$$

and U_d is the discrete Fourier transform of $S_d(t - t_0)$. However, the experiment demonstrated that the structure of processing algorithms (19) and (20) can be considerably simplified. Figure 6 shows one of the experimental dependences of the cross-spectrum density matrix averaged along the diagonals:

$$W_n(f) = \frac{1}{N-n}\sum_{l=n}^{N-1} W_{l,l-n}(f), \quad n = 0, \ldots, N-1.$$

As follows from Fig. 6, the cross-spectrum density matrix has a complex spatial structure in a narrow frequency range with a width of several tens of millihertz, but, as the frequency grows, the spatial correlation vanishes (the correlation scale becomes $\sim\lambda/2$). Since Eqs. (19) and (20) include inverse filtration, it is evident that this narrow frequency interval will be "cut out" by the inverse filter. In this case, the spatial structure of the matrix within the "cut-out" range does not play a significant role. This structure of interference provides an opportunity to use the diagonal representation of the cross-spectrum density matrix in Eqs. (19) and (20). Taking into account the fact that the shape of the power spectral densities (diagonal elements) is almost the same, it is possible to proceed to the representation $\mathbf{W}(f) \longrightarrow \mathbf{I} \cdot W(f)$, where $\mathbf{I}$ is the unit matrix and $W(f)$ is the spectral density of the interference power that is averaged over the array elements. In this case, Eqs. (19)–(21) transform into Eqs. (22)–(24), respectively:

$$F(\boldsymbol{\theta}_1) = \frac{\left| \int\limits_{-f_s/2}^{f_s/2} \mathbf{u}_d^H(f, \boldsymbol{\theta}_1)\mathbf{q}(f)\frac{df}{W(f)} \right|^2}{\int\limits_{-f_s/2}^{f_s/2} \mathbf{u}_d^H(f, \boldsymbol{\theta}_1)\mathbf{u}_d(f, \boldsymbol{\theta}_1)\frac{df}{W(f)}}, \quad (22)$$

$$F(\boldsymbol{\theta}_1) = \mathbf{v}^H\mathbf{v}/Q(f), \quad (23)$$
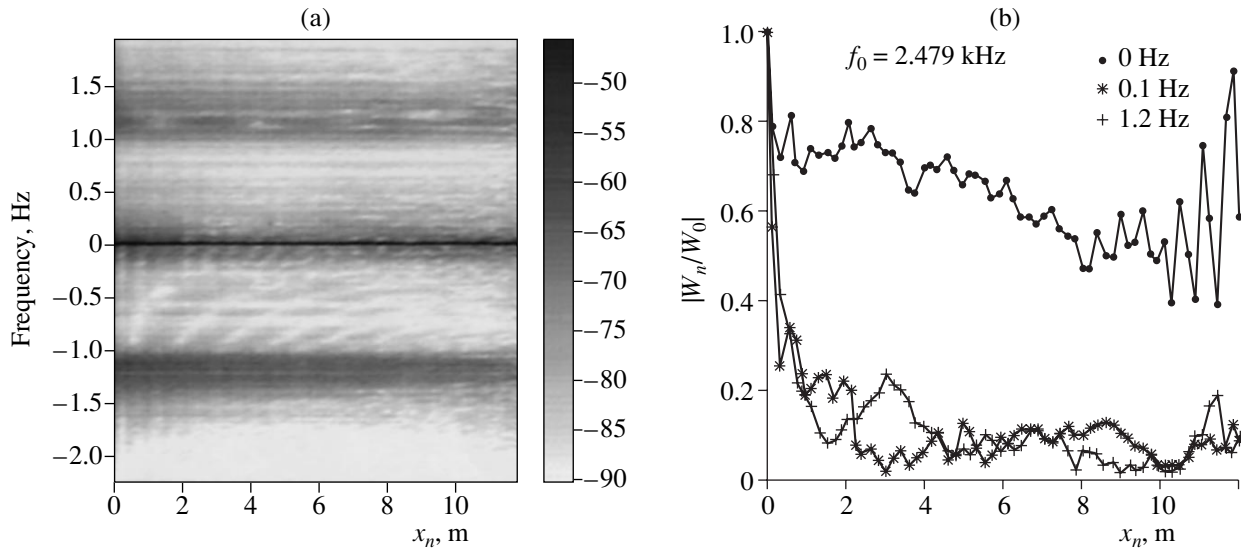
Fig. 6. An example of (a) the power cross-spectrum density for a fluctuating direct signal in the lake experiment as a function of frequency and distance between receiving elements on a logarithmic scale in decibels and (b) its section at zero frequency and frequencies of 0.1 and 1.2 Hz on a linear scale with normalization by $W_0(f)$ (correlation coefficients) as a function of the distance between receiving elements. The wavelength is 0.59 m.

where

$$\mathbf{v} = \int_{-f_s/2}^{f_s/2} U_d^*(f, \boldsymbol{\theta}_1)\mathbf{q}(f)\frac{df}{W(f)},$$

$$Q(f) = \int_{-f_s/2}^{f_s/2} |U_d(f, \boldsymbol{\theta}_1)|^2 \frac{df}{W(f)}. \tag{24}$$

Expressions (22)–(24) determine the procedures of detection and estimation of the parameters of motion of an inhomogeneity according to the forward-scattering data in the case of the use of a horizontal or vertical receiving array, respectively. The practical implementation of Eqs. (22) and (23) basically depends on the selection of the inverse filter $W^{-1}(f)$. For example, the time sequence of $\mathbf{p}(t)$ can be initially high-passed using a finite impulse response filter, which has coefficients determined with the help of the estimation of the power spectral density within the framework of the autoregressive model of a fixed order (for example, see [11]). This adaptive filtration is sufficiently convenient from a practical point of view, since it does not need any preliminary estimation of the parameters of the high-pass filter. In processing the results of the lake experiment, we used filter orders lying within the range 5–12. For other techniques of filtration of upper frequencies in estimating the parameters of a signal scattered forward, see [5, 6].

As has been noted above, in the case of the estimation of inhomogeneity parameters in the region of bistatic scattering with a horizontal receiving array, two strategies were used.

The first was based on the fact that, when the inhomogeneity passes along the trajectory approximately equal in length to the propagation path, clear peaks of the diffracted signal may form on one or several local sections of the trajectory. In this case, it is possible to conduct matched processing within a certain time window by simultaneously moving this window in such a way that the maximum of the function $F(\boldsymbol{\theta}_1, t_c)$,

$$F(\boldsymbol{\theta}_1, t_c)$$
$$= \left| \sum_{-T_0/2 < t_j - t_c < T_0/2} \mathbf{a}^H(t_j, \boldsymbol{\theta}_1)e^{-i\phi_d(t_j, \boldsymbol{\theta}_1)}\mathbf{p}^{(f)}(t_j) \right|^2 \tag{25}$$

(see Eqs. (7), (8), (15), and (18)), is achieved with respect to the parameters $\boldsymbol{\theta}_1$ and the position of the time window center t_c. Here, T_0 is the length of the time window, and $\mathbf{p}^{(f)}(t)$ is the time sequence of signal vectors after a high-pass filter. As has been shown in the previous section, the length of the time window must be selected for each specific waveguide and dimensions of the inhomogeneity proceeding from the spectrum width of the time factor $A_d(t)$ in Eq. (15), as follows from Fig. 5c. For the lake data, this value was determined experimentally. The cut off band of the high-pass filter was taken to be approximately equal to the minimum Doppler frequency shift (Eq. (16)) corresponding to the preset variability range of the parameters $\boldsymbol{\theta}_1$. It also was assumed that, in the range of the Doppler frequency shifts, which is determined by the dimension of the time window, the fluctuation spectrum of the direct signal can be taken as approximately constant (as is demonstrated in [8], this spectrum flattens out with fre-
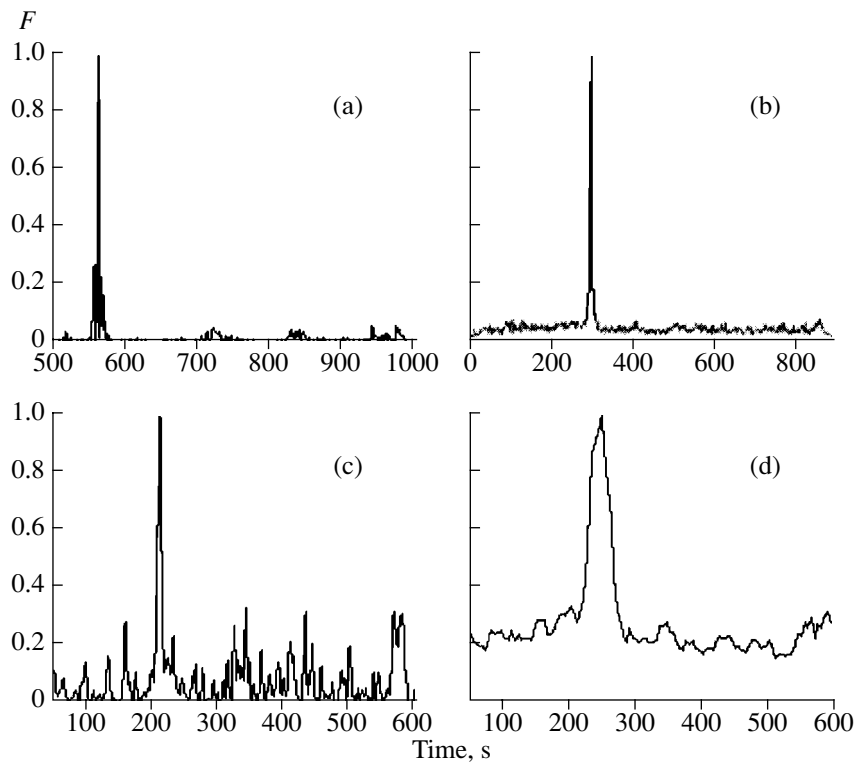
Fig. 7. Dependences of the results of the experimental signals processing on the parameter t_0 (the instant at which the inhomogeneity crosses the propagation path): (a) forward scattering and a horizontal array (Eq. (22)), (b) forward scattering and a vertical array (Eq. (23)), (c) bistatic region and coherent processing (Eq. (25)), and (d) bistatic region and incoherent accumulation (Eq. (26)).

quency growth); therefore, the operation of interference "whitening" was not included in Eq. (25).

The second strategy consisted in the accumulation of Eq. (25) in time windows with a certain weight. In this case, the dimension of the time window was selected in such a way that, within each lth window with the center $t_{c, l}$, it was possible to consider the bearing α_l and the Doppler frequency shift $\omega_{d, l}$ to be constant. The calculation in this case was reduced to the determination of the function

$$F(\boldsymbol{\theta}_1) = \sum_{t_{c, l} \notin [t_0 - \Delta t, t_0 + \Delta t]} g_l$$
$$\times \left| \sum_n \sum_j p_{jn, l} e^{-i\omega_{d, l}(\boldsymbol{\theta}_1)t_j + i\kappa x_n \sin\alpha_l(\boldsymbol{\theta}_1)} \right|^2, \quad (26)$$

where n is the element number and j is the snapshot number within the window. In the process of summation, we excluded the windows adjoining the current value of the instant of crossing t_0. The terms in Eq. (26) have different dispersions, because the two-dimensional spectral power density of direct signal fluctuations $P(\omega, \kappa \sin\alpha)$ determining the dispersion of each term changes noticeably in the variation range of $\omega_{d, l}$ and α_l used; this fact was taken into account with the

help of the weights g_l. While processing, we assumed $g_l = 1/\hat{P}(\omega_{d, l}, \kappa \sin\alpha_l)$, where $\hat{P}$ is the estimate of the two-dimensional spectral power density P, which is made according to the realization of the received signal. Selecting the statistical weight, we took into account the fact that responses to the diffracted component for different windows decrease on the average with an increase in the Doppler frequency shift and the bearing (it is possible to demonstrate rigorously that, for constant responses, in the case of the Gaussian fluctuations, the dispersion F is minimal at $g_l = 1/P^2$). Explicit dependences of the Doppler frequency shift and the bearing on the parameters $\boldsymbol{\theta}_1 = (t_0, V, \ldots)^T$ are determined by Eqs. (7), (8), and (16).

Examples of the experimental dependences (22), (23), (25), and (26) on the parameter t_0, i.e., the instant of crossing the propagation path by an inhomogeneity, are given in Fig. 7. Other parameters (the inhomogeneity velocity, the distance r_2, etc.) in this case were assumed to be known. In the case of using Eq. (25), the time window was taken to be equal to 40 s, according to the preliminary experimental estimation of the optimal value for this parameter. The procedure of Eq. (22) was implemented using adaptive time filtration.

COMPARISON OF THE CHARACTERISTICS OF OBSERVATIONS PERFORMED BY DIFFERENT METHODS

In total, according to the results of the experiments conducted in 1997–1998, the analysis of more than 120 crossings of the signal propagation path by different inhomogeneities was carried out. Signals from a vertical and/or horizontal receiving array were recorded usually during ~10 min, while an inhomogeneity moved from one shore of the lake to another. Signals were detected simultaneously at several (from three to five) discrete radiation frequencies from the range 0.6–3.5 kHz. Inhomogeneities of four types were used. The first and second types were hollow metal cylinders with a diameter of 0.45 m and lengths of 6 and 3.5 m, respectively; the third type was a short cylinder equipped with an additional plastic foam screen of 0.7×2 m. A plastic foam screen with dimensions of 5×1 m was used as the fourth-type inhomogeneity. The inhomogeneities were most often towed at a depth of 6 m with a velocity of 0.6 m/s. The processing of these data demonstrated that, as a rule, in the case of observation by vertical and horizontal arrays, the crossing was detected for all types of inhomogeneities at at least one frequency. However, the crossing was not always observed at all of the radiated frequencies. In all series, for a vertical receiving array, the results were more stable, which also follows from Fig. 2.

The estimation of a successful observation of the crossing of the signal propagation path by an inhomogeneity was performed proceeding from the noticeable prevalence of the global maximum over the fluctuating background in the process of estimation of the crossing instant (see Fig. 7). It is natural to use a well-known criterion, namely, the signal-to-noise ratio after processing, as the quantitative characteristic of the success in the observation of crossing:

$$ SNR = 10\log \frac{\max\{F\} - \bar{F}}{\sqrt{\mathrm{disp}\{F\}}} [\mathrm{dB}], \qquad (27) $$

where $\bar{F}$ is the average value of the random background beyond the vicinity of the global maximum and $\mathrm{disp}\{F\}$ is the background variance in the same region. The value of Eq. (27) for each experiment can be determined empirically from the realizations of F. In this case, we assume that, beyond a certain vicinity of the global maximum F, the ambiguity function rapidly decreases and does not contribute to the estimation of the background mean and variance. Note that, in comparing the results obtained by different methods, the use of Eq. (27) is not quite correct, since, for coherent processing (22), (25) and procedures (23), (26) using incoherent accumulation, the random quantity F has different probability-density distributions and, therefore, different detection probabilities at the same signal-to-noise ratio. Therefore, a more correct quantity for the comparison is the difference Δ_{SNR} between the

empirically determined signal-to-noise ratio SNR and its threshold value SNR_0 corresponding to the fixed probabilities of detection of the diffracted component P_D and false alarm P_F. The threshold value SNR_0 was determined theoretically for the normal interference distribution $\varsigma(t)$ and, correspondingly, the central or noncentral distribution χ_n^2 for F in the presence or absence of the diffracted component [12]. For the coherent processing, the number of the degrees of freedom n was taken to be equal to two. For the procedures with incoherent accumulation, the number of degrees of freedom must correspond to twice the number of independent accumulated blocks. Its precise estimation for experimental conditions is difficult, but we demonstrated that, for sufficiently large P_D and $P_F = 10^{-2}$–10^{-4}, the difference in SNR_0 at $n = 16$–128 for fixed P_D and P_F does not exceed 1 dB, which corresponds to the accuracy of the empirical estimation of SNR. In what follows, for the coherent processing, we took $SNR_0 = 11.5$ dB and, for incoherent processing, $SNR_0 = 8$ dB, which corresponds to $P_D = 0.95$ and $P_F = 10^{-3}$.

A detailed comparison of the above-mentioned differences Δ_{SNR} was conducted for the most representative series of experiments with the inhomogeneity of the third type (a cylinder with an additional screen). The series included 18 crossings observed simultaneously with the help of vertical and horizontal arrays positioned at a small distance from each other. Figure 8 shows four frequency dependences of Δ_{SNR} for procedures (22), (23), (25), and (26), respectively. It is necessary to note that the results for a horizontal receiving array (procedures (22), (25), and (26)) were obtained with the same initial data.

From Fig. 8 and from the results of processing of other experiments, we draw the following conclusions:

(i) At given characteristics of the fluctuations of the direct signal and a uniform rectilinear motion of the inhomogeneity, the methods developed for estimating the parameters of the diffracted signal in the bistatic region provide a slightly higher signal-to-noise ratio in comparison with the estimation of the parameters for forward scattering. Method (26) using incoherent accumulation along the whole motion trajectory, on the average, gives higher values of SNR in comparison with purely coherent space–time processing (25), designed for detecting "bright" spots of the diffracted signal along the trajectory of the inhomogeneity motion. It is necessary to note that bistatic methods use a longer rectilinear section of the trajectory, as compared to the methods based on forward-scattering observations.

(ii) The estimation of the parameters of forward scattering with the help of a vertical receiving array yields a smaller variation of Δ_{SNR}, whereas, in the case the use of a horizontal array, greater values of Δ_{SNR} may be observed.

(iii) The detection characteristics for all methods deteriorate at the edges of the selected frequency range.
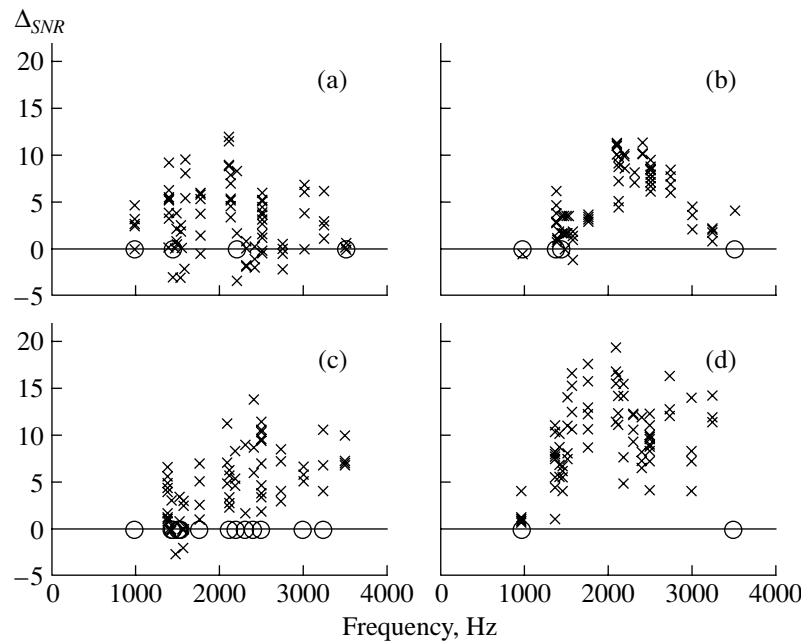
Fig. 8. Frequency dependence of Δ_{SNR}: (a) forward scattering and a horizontal array (Eq. (22)), (b) forward scattering and a vertical array (Eq. (23)), (c) bistatic region and coherent processing (Eq. (25)), and (d) bistatic region and incoherent accumulation (Eq. (26)). Symbols "×" indicate the cases of successful detection (the estimates obtained for the parameters are close to the expected parameter values); symbols "○" indicate the cases of no detection; for the latter cases, the value of Δ_{SNR} was conditionally selected to be equal to 0 dB.

This may be cased by both technical factors (the frequency dependences in Fig. 8 closely coincide with the frequency characteristic of the radiator used in the experiment) and the existence of a certain optimal frequency range for inhomogeneity observation: at low frequencies, the target strength decreases, and, at high frequencies, the correlation between the replica and the actual shape of the diffracted signal is reduced. The experiments gave no definite answer to this question.

The experiment also demonstrated that, at least in the case of a horizontal receiving array, it is expedient to use a group of processing methods in parallel, by analogy with many applications where the filter-bank technique is used.

CONCLUSIONS

Several methods for estimating the parameters of motion of an inhomogeneity from its field scattered both forward and in the bistatic region are developed for the case of observation by antenna arrays and a simultaneous emission of several tone signals at different frequencies. A sufficiently representative experimental sample is obtained, which allows one to draw a conclusion concerning the statistical characteristics of the observation results for signals scattered by a moving inhomogeneity under the conditions of waveguide propagation of sound and fluctuations of the direct signal because of random scattering by wind waves and volume inhomogeneities of the refraction index. In par-

ticular, it is demonstrated that the reliability of observations strongly depends not only on the fluctuations of the direct field but also on the interference effects, which are regular but poorly predictable because of the indeterminacy in the description of the propagation medium. The after fact must be taken into account in the theoretical estimation of the reliability of inhomogeneity observations under preset conditions together with such characteristics as the space–time scales and the values of fluctuations of the direct signal.

REFERENCES

1. N. V. Gorskaya, S. M. Gorskiĭ, V. A. Zverev, *et al.*, Akust. Zh. **34**, 55 (1988) [Sov. Phys. Acoust. **34**, 29 (1988)].

2. S. M. Gorskiĭ, V. A. Zverev, A. L. Matveev, and V. V. Mityugov, Akust. Zh. **41**, 223 (1995) [Acoust. Phys. **41**, 190 (1995)].

3. V. A. Grigor'ev and V. M. Kuz'kin, Akust. Zh. **41**, 410 (1995) [Acoust. Phys. **41**, 359 (1995)].

4. V. A. Zverev, A. L. Matveev, and V. V. Mityugov, Akust. Zh. **41**, 591 (1995) [Acoust. Phys. **41**, 518 (1995)].

5. A. L. Matveev and V. V. Mityugov, Akust. Zh. **46**, 94 (2000) [Acoust. Phys. **46**, 80 (2000)].

6. A. L. Matveev, V. V. Mityugov, and A. I. Potapov, Akust. Zh. **47**, 246 (2001) [Acoust. Phys. **47**, 202 (2001)].

7. A. L. Matveev and V. V. Mityugov, Akust. Zh. **48**, 653 (2002) [Acoust. Phys. **48**, 576 (2002)].

8. V. A. Zverev, P. I. Korotin, A. L. Matveev, *et al.*, Akust. Zh. **47**, 227 (2001) [Acoust. Phys. **47**, 184 (2001)].

9. L. M. Brekhovskikh and Yu. P. Lysanov, *Fundamentals of Ocean Acoustics* (Gidrometeoizdat, Leningrad, 1982; Springer, New York, 1991).

10. T. C. Yang and T. Yates, J. Acoust. Soc. Am. **104**, 1316 (1998).

11. V. I. Tikhonov and V. N. Kharisov, *Statistical Analysis and Synthesis of Radio Engineering Devices and Systems* (Radio i Svyaz', Moscow, 1991) [in Russian].

12. S. M. Kay, *Fundamentals of Statistical Signal Processing*, Vol. 2: *Detection Theory* (Prentice Hall, Englewood Cliffs, N.J., 1998).

Translated by M. Lyamshev

Wave Processes in Microinhomogeneous Elastic Media with Hysteretic Nonlinearity and Relaxation

V. E. Nazarov and A. V. Radostin

Institute of Applied Physics, Russian Academy of Sciences, ul. Ul'yanova 46, Nizhni Novgorod, 603600 Russia
e-mail: nazarov@hydro.appl.sci-nnov.ru
Received July 22, 2003

Abstract—The nonlinear propagation of an initially harmonic acoustic wave in a microinhomogeneous medium containing defects with quadratic hysteretic nonlinearity and relaxation is studied by the perturbation method. The frequency dependences of the effective nonlinearity parameters are determined for the self-action of the quasi-harmonic acoustic wave and the higher harmonic generation processes. © *2005 Pleiades Publishing, Inc.*

INTRODUCTION

Hysteretic equations of state are commonly used to explain the phenomenon of amplitude-dependent internal friction (ADIF) in solid materials with imperfect elasticity. Earlier [1–7], different types of inertialess hysteretic equations, i.e., dependences of the type of $\sigma = \sigma(\varepsilon, \text{sgn}\dot{\varepsilon})$ (where σ is the stress and ε is the strain), were obtained to describe the deformation of such materials at low frequencies. The absence of inertia in these equations means that the stress σ at a given point of the medium at a given instant t is determined by the strain ε and the sign of the strain rate $\dot{\varepsilon}$ at the same point at the same instant of time. For media with inertialess nonlinearity, the effective nonlinearity parameters (which, generally speaking, are different for different wave processes) are constant and independent of the frequencies of the interacting acoustic waves. The results of experimental studies of the ADIF effects (such as nonlinear loss, resonance frequency shift, and higher harmonic generation) testify that the nonlinearity parameters of some polycrystalline metals and rocks are frequency-dependent. To explain these results, a rheological model of a microinhomogeneous medium was proposed and studied in [8, 9]. The model had the form of a one-dimensional chain of linear elastic elements and relatively soft nonlinear viscoelastic (relaxation) defects. In the cited publications, three-wave processes in media containing defects with a quadratic elastic nonlinearity were considered and it was shown that, because of the nonlinear relaxation of defects at the frequencies of initial and nonlinearly generated waves, the quadratic nonlinearity parameters of microinhomogeneous media are frequency dependent; i.e., such media exhibit a dispersion of their nonlinear elasticity. Evidently, rheology alone cannot completely elucidate the physical nature of this phenomenon: its mechanisms may be different for different media. However, the proposed rheological model adequately describes the behavior of linear and nonlinear acoustic properties of a wide class of microinhomogeneous media (in particular, polycrystalline metals and rocks) and qualitatively accounts for the results obtained from the experimental studies of nonlinear effects in such media. For each specific medium, the amplitude–frequency characteristics of nonlinear effects manifest themselves in an individual manner, and, therefore, along with the nonlinear properties, the relaxation properties of microinhomogeneous media can also be used for their classification and diagnosis.

In this paper, we present a theoretical analysis of nonlinear effects accompanying the propagation of an initially harmonic acoustic wave in a microinhomogeneous medium containing defects with a quadratic hysteretic nonlinearity and relaxation. We determine the frequency dependences of the effective nonlinearity parameters for the wave self-action and higher harmonic generation processes.

EQUATION OF STATE OF A MICROINHOMOGENEOUS MEDIUM WITH QUADRATIC HYSTERETIC NONLINEARITY AND RELAXATION

As in the previous publications [8, 9], we consider a rheological model of a medium in the form of a one-dimensional chain of linear elastic elements and relatively soft nonlinear viscoelastic defects characterized by a hysteretic stress–strain (σ–ξ) dependence:

$$\sigma(\xi, \text{sgn}\dot{\xi}, \dot{\xi}) = \zeta E[\xi - f(\xi, \text{sgn}\dot{\xi})] + \eta\dot{\xi}, \quad (1)$$

$$f(\xi, \text{sgn}\dot{\xi})$$

$$= \frac{1}{2} \begin{cases} \gamma_1 \xi^2, & \xi > 0, \quad \dot{\xi} > 0; \\ -\gamma_2 \xi^2 + (\gamma_1 + \gamma_2)\xi_m \xi, & \xi > 0, \quad \dot{\xi} < 0; \\ -\gamma_3 \xi^2, & \xi < 0, \quad \dot{\xi} < 0; \\ \gamma_4 \xi^2 + (\gamma_3 + \gamma_4)\xi_m \xi, & \xi < 0, \quad \dot{\xi} > 0. \end{cases} \quad (2)$$

Here, E is the elastic modulus of stiff elements, ζ is the relative elasticity of a defect with respect to the elasticity of a linear stiff element ($\zeta \ll 1$), η is the viscosity coefficient, ξ_m and $\dot{\xi}$ are the strain amplitude and the strain rate, γ_{1-4} are the hysteretic nonlinearity parameters, $|\gamma_{1-4}|\xi_m \ll 1$, and $|\gamma_{1-4}| \gg 1$. For definiteness, we consider defects described by a quadratic elastic hysteresis [10] (or the separation hysteresis [3]), but the expressions obtained below for the nonlinearity coefficients $A_p(\omega)$ and $B_p(\omega)$ are also valid for defects with an inelastic but also quadratic hysteresis [10] (or a friction hysteresis [3]).

When the concentration of defects is small, the equation of state of a microinhomogeneous medium has the form [8, 9]

$$\sigma(\varepsilon) = E\left[\varepsilon - \int_0^\infty\int_0^1 R(\varepsilon)N(\zeta, W)d\zeta dW\right.$$

$$\left. - \int_0^\infty\int_0^1 \zeta R[f(R(\varepsilon), \text{sgn}\dot{R}(\varepsilon))]N(\zeta, W)d\zeta dW\right], \quad (3)$$

$$\left|\int_0^\infty\int_0^1 \zeta R[f(R(\varepsilon), \text{sgn}\dot{R}(\varepsilon))]N(\zeta, W)d\zeta dW\right|$$

$$\ll \left|\int_0^\infty\int_0^1 R(\varepsilon)N(\zeta, W)d\zeta dW\right| \ll |\varepsilon|, \quad (4)$$

where $R(\varepsilon) = \dfrac{W}{\zeta}\int_{-\infty}^t \varepsilon(\tau)e^{-W(t-\tau)}d\tau$, $W = \zeta E/\eta$ is the defect relaxation frequency, and $N = N(\zeta, W)$ is the function describing the defect distribution in the parameters ζ and W.

Equation of state (3) takes into account the relaxation and contains both linear and nonlinear relaxation terms. The linear and nonlinear relaxations of this medium are caused by the relaxation of defects, and the nonlinear relaxation manifests itself twice: first, owing to the linear relaxation, because the nonlinear correction is determined by the linear response of the defects, and, second, owing to the relaxation of the nonlinear correction itself. In the low-frequency approximation, i.e., for $\omega/W \ll 1$ (where ω is the frequency of the acoustic wave), Eq. (3) is reduced to a simple inertialess equation:

$$\sigma(\varepsilon)$$

$$= E\left[\varepsilon\left(1 - \int_0^1\frac{N(\zeta)}{\zeta}d\zeta\right) - f(\varepsilon, \text{sgn}\dot{\varepsilon})\int_0^1\frac{N(\zeta)}{\zeta^3}d\zeta\right]. \quad (5)$$

The propagation of a quasi-harmonic wave in a medium with inertialess hysteretic nonlinearity (2) was studied in [10, 11].

NONLINEAR PROPAGATION OF A QUASI-HARMONIC WAVE

We set a boundary condition in the form of $\varepsilon(x = 0, t) = \varepsilon_0\sin\omega t$ and consider the nonlinear effects that accompany the propagation of a longitudinal (along the x axis) acoustic wave in the medium. Substituting equation of state (3) into the equation of motion $\rho U_{tt} = \sigma_x$ (where $\varepsilon = U_x$, U is the displacement, and ρ is the density) and solving the latter by the perturbation method, we obtain expressions for the wave (in the form of a Fourier series), the nonlinear damping decrement $\delta(\varepsilon_1)$, and the nonlinear variation of the propagation velocity $\Delta C(\varepsilon_1)/C$ of the wave at the fundamental frequency ω:

$$\varepsilon(x, t) = \sum_{p=1}^\infty \varepsilon_p(x)\sin[\omega_p t - k_p x - \varphi_p(x)],$$

$$\sum_{p=2}^\infty \varepsilon_p(x) \ll \varepsilon_1(x), \quad (6)$$

$$\varepsilon_1(x) = \frac{\varepsilon_0\exp[-A_{l,1}k_1 x]}{1 + \dfrac{A_1}{A_{l,1}}\varepsilon_0[1 - \exp(-A_{l,1}k_1 x)]},$$

$$\varphi_1(x) = B_{l,1}k_1 x \quad (7)$$

$$- \frac{B_1}{A_1}\ln\left(1 + \frac{A_1}{A_{l,1}}\varepsilon_0[1 - \exp(-A_{l,1}k_1 x)]\right),$$

$$\varepsilon_p(x) = \sqrt{A_p^2 + B_p^2}\varepsilon_0^2 k_p x,$$

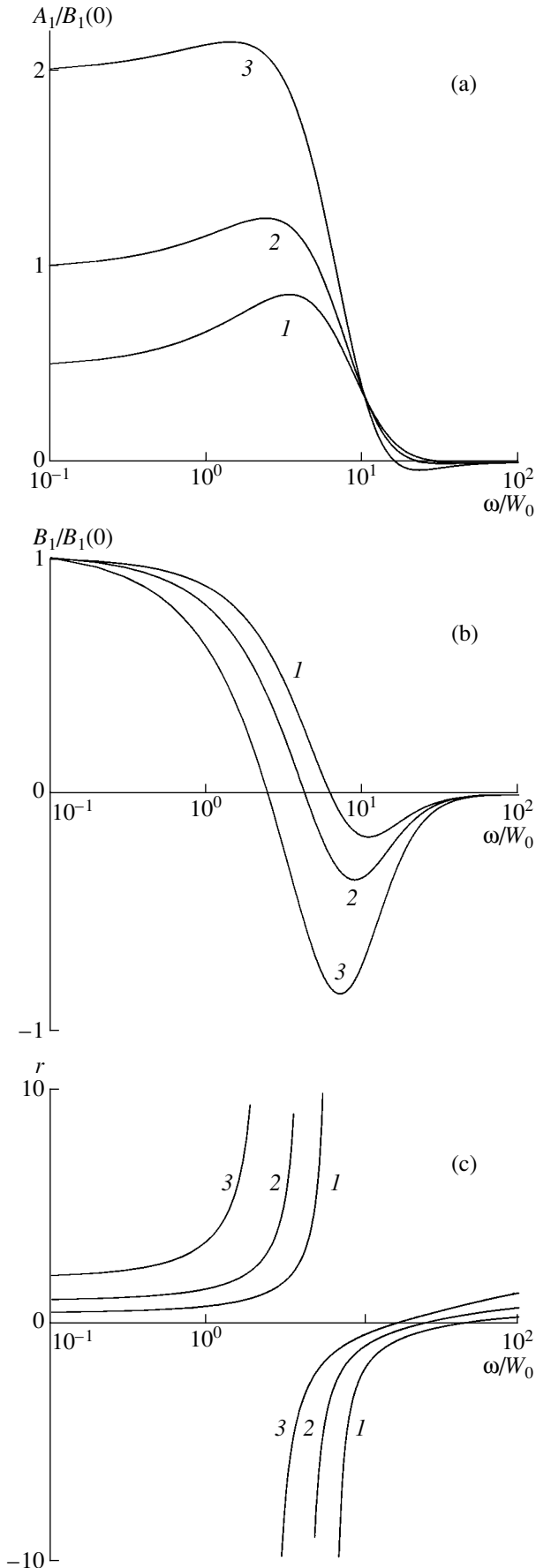$$\varphi_p(x) = p\varphi_1(x) - pB_{l,p}k_1 x + \arctan(B_p/A_p), \quad (8)$$

$$|\varphi_p(x) - p\varphi_1(x)| \ll \pi,$$

$$\delta(\varepsilon_1) = A_1(\omega)\varepsilon_1(x), \quad \frac{\Delta C(\varepsilon_1)}{C} = B_1(\omega)\varepsilon_1(x), \quad (9)$$

$$A_{l,p}(\omega) = \int_0^\infty\int_0^1\frac{p\omega W N(\zeta, W)}{2\zeta(p^2\omega^2 + W^2)}d\zeta dW,$$

$$B_{l,p}(\omega) = \int_0^\infty\int_0^1\frac{W^2 N(\zeta, W)}{2\zeta(p^2\omega^2 + W^2)}d\zeta dW, \quad (10)$$

$$\left\{\begin{matrix} A_1(\omega) \\ B_1(\omega) \end{matrix}\right\} = \int_0^\infty\int_0^1\frac{N(\zeta, W)}{\zeta^2[1 + (\omega/W)^2]^{5/2}}$$

$$\times\left[\left\{\begin{matrix} a_1 \\ b_1 \end{matrix}\right\}[1 - (\omega/W)^2] \pm 2\left\{\begin{matrix} b_1 \\ a_1 \end{matrix}\right\}(\omega/W)\right]d\zeta dW, \quad (11)$$

$$\left\{ \begin{array}{c} A_p(\omega) \\ B_p(\omega) \end{array} \right\}$$

$$= \sqrt{a_p^2 + b_p^2} \int_0^\infty \int_0^1 \frac{N(\zeta, W)}{\zeta^2[1 + (\omega/W)^2][1 + (p\omega/W)^2]^{1/2}} \quad (12)$$

$$\times \left\{ \begin{array}{c} \cos[p\Psi + \arctan(b_p/a_p)] \\ \sin[p\Psi + \arctan(b_p/a_p)] \end{array} \right\} d\zeta dW,$$

where $\omega_p = p\omega$, $k_p = \omega_p/C$, $C = (E/\rho)^{1/2}$, $\Psi = 2\arctan(\omega/W)$,

$$a_1 = \frac{1}{24\pi}(\gamma_1 + \gamma_2 + \gamma_3 + \gamma_4) \ge 0,$$

$$b_1 = \frac{1}{16}(\gamma_1 + \gamma_2 + \gamma_3 + \gamma_4) + \frac{1}{6\pi}(\gamma_1 - \gamma_2 + \gamma_3 - \gamma_4),$$
$$(13)$$
$$a_2 = \frac{1}{24\pi}(\gamma_1 + \gamma_2 - \gamma_3 - \gamma_4),$$

$$b_2 = \frac{1}{12\pi}(\gamma_1 + \gamma_2 - \gamma_3 - \gamma_4) + \frac{1}{32}(\gamma_1 - \gamma_2 - \gamma_3 + \gamma_4),$$

and $A_p(\omega)\varepsilon_1^2(x)$ and $B_p(\omega)\varepsilon_1^2(x)$ are the Fourier coefficients of the nonlinear function of equation of state (3). (Expressions for the coefficients a_p and b_p for media with elastic and inelastic hysteresis are given in [11].)

From Eqs. (7)–(12), it follows that the relaxation of hysteretic defects has two consequences: first, the coefficients $A_p(\omega)$ and $B_p(\omega)$, which determine the nonlinear loss, the wave velocity variation, and the higher harmonic amplitudes and phases in the microinhomogeneous medium, become frequency-dependent (with any sign); second, each of these coefficients is a linear combination of the coefficients a_p and b_p. From Eqs. (8) and (12), one can see that the excitation of a harmonic wave of frequency ω in a microinhomogeneous medium with hysteretic nonlinearity and relaxation gives rise to waves with frequencies $p\omega$. The amplitude of each of these higher harmonics exhibits a quadratic dependence on both the initial wave amplitude and the distance traveled by the wave and is proportional to the effective nonlinearity parameter $D_p(\omega) = \sqrt{A_p^2(\omega) + B_p^2(\omega)}$, which depends on the initial wave frequency ω and the number p of a given harmonic:

Fig. 1. Frequency dependences of the coefficients (a) $A_1(\omega/W_0)/B_1(0)$ and (b) $B_1(\omega/W_0)/B_1(0)$ and (c) the parameter $r(\omega/W_0)$ for a medium containing identical defects; $r_0 = $ (1) 0.5, (2) 1, and (3) 2.

$$D_p(\omega) = \sqrt{a_p^2 + b_p^2}$$

$$\times \int\limits_0^\infty \int\limits_0^1 \frac{N(\zeta, W)}{\zeta^2 [1 + (\omega/W)^2][1 + (p\omega/W)^2]^{1/2}} d\zeta dW. \quad (14)$$

In the quasi-static approximation, i.e., for $\omega/W \longrightarrow 0$, expressions (7)–(12) and (14) are simplified by transforming to expressions for a medium with an inertialess (i.e., frequency-independent) hysteretic nonlinearity [10, 11]. In this case, the nonlinearity coefficients $A_p(0)$ and $B_p(0)$ are determined by the coefficients a_p and b_p (separately) and the defect concentration:

$$\left\{ \begin{array}{c} A_p(0) \\ B_p(0) \end{array} \right\} = \left\{ \begin{array}{c} a_p \\ b_p \end{array} \right\} \int\limits_0^1 \frac{N(\zeta)}{\zeta^2} d\zeta. \quad (15)$$

Now, we determine the parameter $r = r(\omega)$ representing the ratio of the damping decrement $\delta(\varepsilon_1)$ to the relative variation of the wave velocity, $\Delta C(\varepsilon_1)/C$. This dimensionless parameter, which is independent of the wave amplitude, is an important characteristic of the ADIF [1–3, 5]:

$$r(\omega) = \frac{A_1(\omega)}{B_1(\omega)}. \quad (16)$$

In the low-frequency region ($\omega \ll W^*$, where W^* is the effective frequency of defect relaxation), we have $r(0) = r_0 = a_1/b_1 = \text{const}$, while for $\omega \geq W^*$, the parameter $r(\omega)$ may be arbitrary in the general case. Its value and sign are determined by the wave frequency ω and the defect distribution function $N = N(\zeta, W)$. Below, to simplify the calculations, we consider different distributions of defects in relaxation frequencies W under the assumption that $\zeta = \text{const}$.

FREQUENCY DEPENDENCES OF NONLINEAR COEFFICIENTS FOR IDENTICAL AND DISTRIBUTED DEFECTS

The simplest expressions for the coefficients $A_p(\omega)$ and $B_p(\omega)$ and the parameter $r(\omega)$ are obtained in the case of a monodisperse distribution of defects in relaxation frequencies: $N(W) = N_0\delta(W - W_0)$. For example, the expression for $r(\omega/W_0)$ has the form

$$r(\omega/W_0) = \frac{r_0(1 - (\omega/W_0)^2) + 2(\omega/W_0)}{1 - (\omega/W_0)^2 - 2r_0(\omega/W_0)}. \quad (17)$$
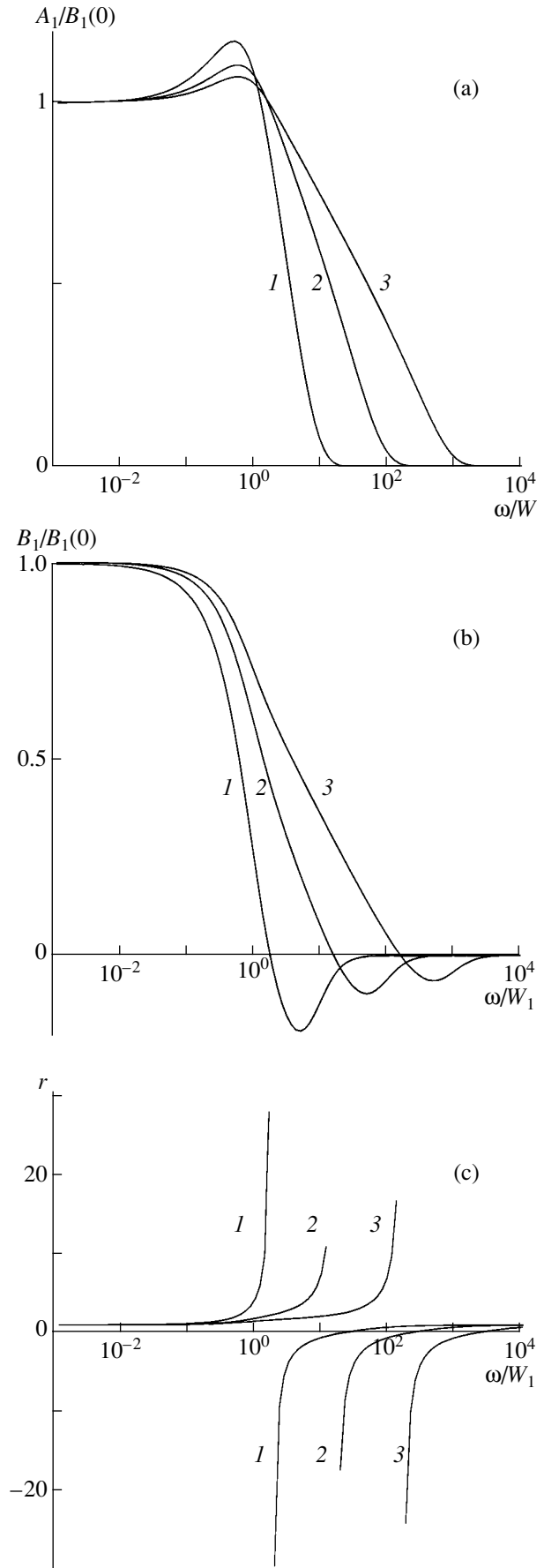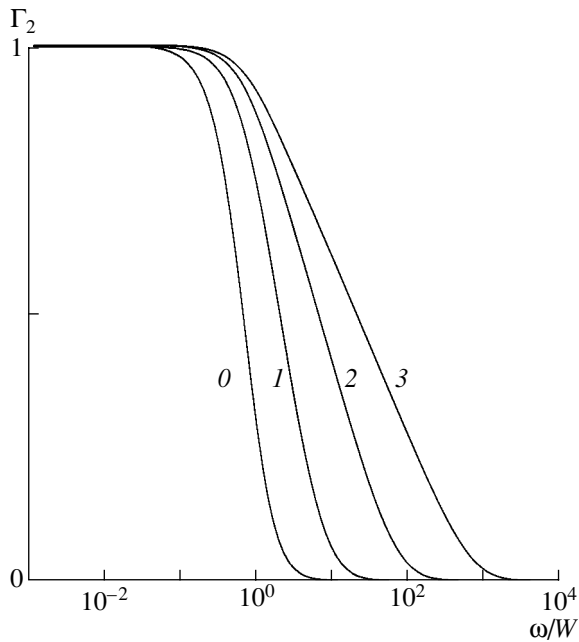

Fig. 2. Frequency dependences of the coefficients (a) $A_1(\omega/W_1)/B_1(0)$ and (b) $B_1(\omega/W_1)/B_1(0)$ and (c) the parameter $r(\omega/W_1)$ at $r_0 = 1$ for media with different distributions of defects in relaxation frequencies: $W_1 = 10^2$ s^{-1} and $W_2 = $ (1) 10^3, (2) 10^4, and (3) 10^5 s^{-1}.

Fig. 3. Frequency dependences of the coefficient $\Gamma_2(\omega/W_1)$ for media with (0) identical and (1–3) distributed defects: $W_1 =$ (1–3) 10^2 s^{-1} and $W_2 = $ (1) 10^3, (2) 10^4, and (3) 10^5 s^{-1}.

From Eq. (11), it follows that (for $r_0 > 0$) the coefficients $A_1(\omega)$ and $B_1(\omega)$ are positive in the frequency regions $\omega/W_0 \le \mu_1 = r_0^{-1} + (1 + r_0^{-2})^{1/2}$ and $\omega/W_0 \le \mu_2 = -r_0 + (1 + r_0^2)^{1/2} < \mu_1$, respectively, so that the parameter $r(\omega/W_0)$ is positive at low frequencies ($\omega/W_0 \le \mu_2$) and at high frequencies ($\omega/W_0 > \mu_1$), while in the frequency range $\mu_2 < \omega/W_0 < \mu_1$, it is negative. Figures 1a–1c show the coefficients $A_1(\omega/W_0)/B_1(0)$ and $B_1(\omega/W_0)B_1(0)$ and the parameter $r(\omega/W_0)$, respectively, as functions of the ratio ω/W_0 for a medium containing identical defects; the curves are plotted for different values of r_0. From these plots, one can see that, in the low-frequency range ($\omega \ll W_0$), we have $A_1(\omega/W_0)/B_1(0) \simeq r_0$ and $B_1(\omega/W_0)B_1(0) = 1$; in the high-frequency range ($\omega \gg W_0$), these coefficients tend to zero (as ω^{-3}); and in the intermediate frequency region ($\omega \approx W_0$), the coefficient $A_1(\omega/W_0)/B_1(0)$ slightly exceeds r_0, while the coefficient $B_1(\omega/W_0)/B_1(0)$ decreases to zero and changes sign. The parameter $r(\omega/W_0)$ exhibits a corresponding behavior: at low and high frequencies, $r(\omega/W_0) \simeq r_0$, while at intermediate frequencies, it exhibits changes in its value and sign.

Figures 2a–2c show the coefficients $A_1(\omega/W_1)/B_1(0)$ and $B_1(\omega/W_1)/B_1(0)$ and the parameter $r(\omega/W_1)$, respectively, as functions of the ratio ω/W_1 for a medium with defects distributed in relaxation frequencies (at $r_0 = 1$):

$$N(W) = \frac{N_0}{\ln(W_2/W_1)W}, \quad W_1 \le W \le W_2. \quad (18)$$

With this distribution of defects in relaxation frequencies, the medium possesses a frequency-independent linear damping decrement in the frequency range $W_1 \le \omega \le W_2$. In this case, the frequency dependences of the coefficients $A_1(\omega/W_1)/B_1(0)$ and $B_1(\omega/W_1)/B_1(0)$ and the parameter $r(\omega/W_1)$ qualitatively coincide with those shown in Fig. 1.

Figure 3 represents the dependences of the normalized quadratic nonlinearity coefficient $\Gamma_2(\omega/W_1) = \dfrac{D_2(\omega/W_1)}{D_2(0)}$ on ω/W_1 for media with identical defects ($W_0 = W_1$) and with defects distributed according to law (18). In the low-frequency region, this coefficient is equal to unity, and, as the frequency increases, it decreases and tends to zero. If the upper bound W_2 of distribution function (18) increases, the aforementioned decrease in the nonlinearity coefficient becomes slower because of the increase in the effective relaxation frequency W^*. Similar frequency dependences occur for other nonlinearity coefficients $\Gamma_p(\omega/W_1) = \dfrac{D_p(\omega/W_1)}{D_p(0)}$, where $p > 2$.

CONCLUSIONS

Thus, in this paper, in terms of the rheological model of a microinhomogeneous medium containing viscoelastic defects with quadratic hysteretic nonlinearity, we studied the effects of both the self-action of an initially harmonic wave and the higher harmonic generation. We derived analytical expressions for the nonlinear coefficients $A_p(\omega)$ and $B_p(\omega)$ responsible for these processes. We have shown that, unlike the medium with the same hysteretic nonlinearity but without relaxation, where the nonlinearity of the medium does not depend on the frequency of the acoustic wave, the hysteretic nonlinearity of a microinhomogeneous medium with relaxation is frequency-dependent; as the frequency of the acoustic wave increases, the effective nonlinear parameters of such a medium asymptotically tend to zero. Although, in this paper, we considered a definite class of media with a quadratic elastic hysteresis, the expressions obtained for the nonlinearity coefficients $A_p(\omega)$ and $B_p(\omega)$ are also valid for media with an inelastic quadratic hysteresis [10], because the dependences of the nonlinear effects on the wave amplitude are determined by the degree of the nonlinear equation of state of a single defect (for both types of hysteresis, the degree is equal to two), while the dependences on the wave frequency are determined by the distribution of defects in relaxation frequencies (and elasticities).

We believe that the study described above and the analysis of the measured amplitude–frequency dependences of different nonlinear effects accompanying the propagation and interaction of elastic waves in a relaxing microinhomogeneous medium demonstrate the

possibility of determining the general form of the non-linear equation of state of this medium, the parameters of this equation, and the distribution function describing the distribution of defects in relaxation frequencies and elasticities.

ACKNOWLEDGMENTS

REFERENCES

1. N. N. Davidenkov, Zh. Tekh. Fiz. **8**, 483 (1938).
2. A. V. Granato and K. J. Lucke, J. Appl. Phys. **27**, 583 (1956).
3. S. Asano, J. Phys. Soc. Jpn. **29**, 952 (1970).
4. V. E. Nazarov, L. A. Ostrovsky, I. A. Soustova, and A. M. Sutin, Phys. Earth Planet. Inter. **50** (1), 65 (1988).
5. A. B. Lebedev, Fiz. Tverd. Tela (St. Petersburg) **41**, 1214 (1999) [Phys. Solid State **41**, 1105 (1999)].
6. V. Gusev, W. Lauriks, and J. Thoen, J. Acoust. Soc. Am. **103**, 3216 (1998).
7. R. A. Guyer and P. A. Johnson, Phys. Today, No. 4, 30 (1999).
8. V. E. Nazarov, V. Yu. Zaitsev, and I. Yu. Beliaeva, Acoust. Lett. **22** (12), 236 (1999).
9. V. E. Nazarov, V. Yu. Zaitsev, and I. Yu. Beliaeva, Acust. Acta Acust. **88** (1), 40 (2002).
10. V. E. Nazarov and A. M. Sutin, Akust. Zh. **35**, 711 (1989) [Sov. Phys. Acoust. **35**, 410 (1989)].
11. V. E. Nazarov, A. V. Radostin, L. A. Ostrovskiĭ, and I. A. Soustova, Akust. Zh. **49**, 405 (2003) [Acoust. Phys. **49**, 344 (2003)].
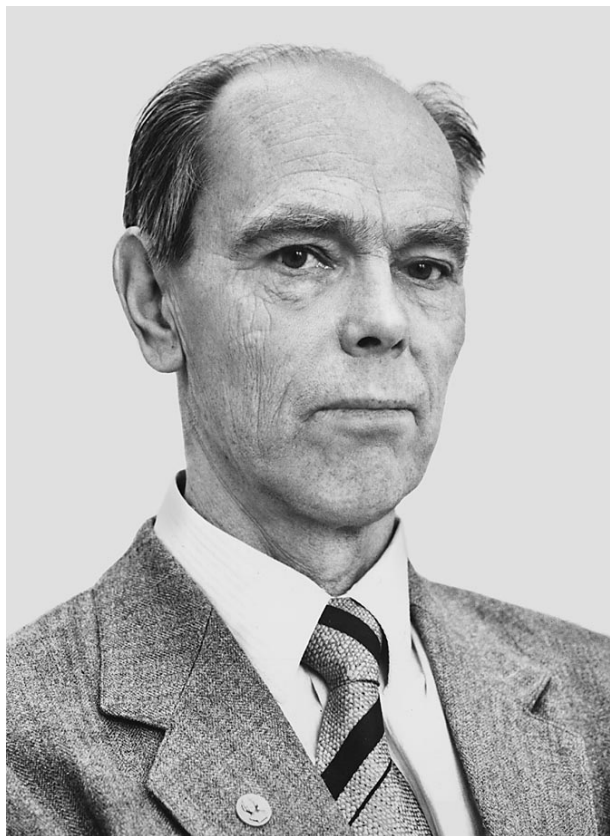
Translated by E. Golyamina

═══ **CHRONICLE** ═══

Vitaliĭ Anatol'evich Zverev

(On His 80th Birthday)

November 3, 2004, marked the 80th birthday of the prominent scientist, Corresponding Member of the Russian Academy of Sciences, Doctor of Physics and Mathematics, Professor Vitaliĭ Anatol'evich Zverev.

Zverev is a well-known specialist in radiophysics and acoustics. He is the author of more than 200 scientific works, including four monographs and 30 inventions. He made a substantial contribution to the development of acoustics; he was one of the first to lay the foundations of nonlinear acoustics, which has become a rapidly developing area of research.

Zverev's youth fell within the period of the Second World War. From 1942 to Victory Day in 1945, he served in the army, specifically in the air-defense forces. As a young soldier, Zverev demonstrated his talent for research and invention: he successfully fixed and tuned new complicated radar systems that were appearing at that time in air defenses. Zverev's occupation in the army determined his civilian profession. In 1945, he left the army and became a student in the newly founded Radiophysical Faculty of Gorki State University. In 1950, Zverev graduated from the university and became a postgraduate student of Professor G.S. Gorelik.

Zverev's first research project was based on the idea put forward by M.A. Isakovich regarding the dispersion of acoustic waves in emulsions. To implement this idea, Zverev studied the characteristic features of the propagation of modulated waves in dispersive media. He found that the propagation of a modulated wave in a dispersive medium can be described by a single parameter—the phase invariant. Zverev developed a method for measuring this parameter and designed the corresponding equipment. This work resulted in his candidate dissertation, which he defended in 1953. The further development of these studies offered the possibility of using the same approach and equipment for studying the spatial spectra of random inhomogeneities. This possibility was realized in acoustics.

In the following years, Zverev's scientific activity was related to the formation of images by wave fields. All four monographs written by Zverev are devoted to this subject. The first of them, entitled *Optical Analyzers*, was published in 1971 (in co-authorship with E.F. Orlov), and the second, *Radio-Optics*, in 1975. The last two monographs were written in recent years: *Physical Foundations of the Formation of Images by Wave Fields* appeared in 1998, and *Extraction of Signals from Noise by Numerical Methods* was published in 2001 (in co-authorship with A.A. Stromkov). Zverev was one of the first to propose and develop the optical methods of spectral and correlation analysis. Based on these methods, unique instruments for spectral and correlation analysis were designed under his supervision. The instruments have found applications in radar, acoustics, and medicine.

The book *Radio-Optics* published by Zverev in 1975 and his monographs published in 1998 and 2001 are unique editions that contain a unified description of all known features of image formation. To consider all possible cases, it was necessary to combine optics, acoustics, and radiophysics, because no single area covers the whole variety of image-formation conditions.

The simplest and most illustrative example of the image formation by wave fields is our vision. Waves arriving at the pupil of the eye are processed so as to allow us to reconstruct (to see) their sources. To see

objects, we do not need to understand the mechanism of the phenomenon. However, to see objects with some other waves, e.g., acoustic ones that cannot be perceived with our eyes or ears, a corresponding scientific description of the phenomenon is necessary with allowances made for the specific conditions of the image formation. The variety of the image-formation conditions can be illustrated by hearing and sight. We perceive the images with our ears in a completely different way than with our eyes. Zverev proposed a mathematical model describing how we "see" with our ears. The proposed procedure was close to the aperture synthesis widely used in radio astronomy. The determination of this procedure allowed Zverev to explain the characteristic features of the perception of monophonic and stereophonic sound and to propose an original method of volume sound reproduction. This method is now successfully used in industry.

Zverev's studies in nonlinear acoustics were also related to the problems of acoustic vision. Zverev proposed and implemented the parametric transmission and reception of sound. Parametric antennas possess some specific features of image formation. A parametric acoustic array has a directional pattern close to an ideal one. Similar systems were proposed by Westervelt two years later, and his publications marked the beginning of nonlinear acoustics in Western countries. For their studies in nonlinear acoustics, Zverev and his colleagues received a USSR State Award in 1985.

Currently, Zverev is involved in both scientific and tutorial activities. In the past five years, he has submitted for publication 19 scientific works, including one monograph. Most of his papers were published in the *Akusticheskii Zhurnal* (*Acoustical Physics*). Zverev continues working on the problems of vision in acoustic fields. Many media that are opaque to other types of waves prove to be transparent to acoustic waves. However, conventional ways of image formation are not always appropriate in acoustics. The factors that hinder image formation and ways to overcome these difficulties are currently studied by Zverev. In the last ten years, he has proposed and developed the acoustic dark-field method, which allows one to select the objects of interest against scattered and direct intense radiation. Zverev's most recent studies are concerned with the problems of acoustic vision by the so-called time-reversal method. This subject is now being actively investigated by M. Fink and other scientists from Western countries. In this area of research, Zverev has found a number of new solutions, which, in particular, have made it possible to interpret some experimental results.

Zverev developed original lecture courses on statistical radiophysics, acoustics, and physical foundations of the image formation by wave fields (radio-optics).

For years, these lectures were delivered to the students of Nizhni Novgorod State University.

Zverev's working activity has always been related to Nizhni Novgorod. Over a period of seven years, he chaired the department of General Physics at the Radiophysical faculty of Nizhni Novgorod State University. Starting in 1956, he headed the department of Statistical Radiophysics and Acoustics of the Radiophysical Research Institute, and, in 1977, he became head of the department of Physical Acoustics at the newly established Institute of Applied Physics of the Russian Academy of Sciences. Today, Zverev is councilor of the Russian Academy of Sciences.

In 1964, Zverev defended his doctoral dissertation, which included the results of his research in modulated waves, optical signal processing, nonlinear acoustics, and some applications. In 1979, he was elected as corresponding member of the Russian Academy of Sciences for the Division of General Physics and Astronomy. For his achievements in science, Zverev was awarded an Order of the Red Banner of Labor and several medals.

While celebrating his 80th birthday, Zverev is deeply involved in his creative endeavors. As always, he is full of new ideas and plans. He spends much of his time working with his personal computer verifying new concepts and algorithms of signal selection against background noise. In the aforementioned monograph published in 2001, Zverev considered some characteristic features of programming for wave problems and included a great number of specific computer codes, which clarify the principles of image formation under different conditions. He shares his enthusiasm for work with his students and colleagues. Zverev is an interesting story teller; he has written memoirs about different people and about his childhood, studies, and work. Part of the stories were written as lectures for schoolchildren with the aim of showing them the attractiveness of scientific studies.

Zverev's hobby is classical music, which he has loved since childhood. At the age of 23, he started playing piano, and, today, he can easily play his favorite pieces by Liszt, Beethoven, Rachmaninov, Schubert, and other composers. Though 80 years old, Zverev remains tireless in his many-sided activities and creative abilities, with which nature has generously endowed him. He demonstrates a wonderful example of vitality and devotion to science and human ideals.

The friends, students, and colleagues of Vitaliĭ Anatol'evich Zverev wish him good health and further success in his creative endeavors.

Translated by E. Golyamina